Univerzita Karlova v Praze

1. lékařská fakulta

Studijní program: Biomedicína

Studijní obor: Biologie a patologie buňky

Mgr. Veronika Mistríková

ELEKTRON KRYO-MIKROSKOPICKÉ TECHNIKY V BIOLOGICKÉM VÝZKUMU A NANOTECHNOLOGIÍCH

ELECTRON CRYO-MICROSCOPY TECHNIQUES IN BIOLOGICAL RESEARCH AND NANOTECHNOLOGIES

Disertační práce

Vedoucí závěrečné práce/Školitel: Doc. RNDr. Jan Bednár, PhD.

Praha, 2011

Prohlášení

Prohlašuji, že jsem závěrečnou práci zpracovala samostatně a že jsem řádně uvedla a citovala všechny použité prameny a literaturu. Současně prohlašuji, že práce nebyla využita k získání jiného nebo stejného titulu.

Souhlasím s trvalým uložením elektronické verze mé práce v databázi systému meziuniverzitního projektu Theses.cz za účelem soustavné kontroly podobnosti kvalifikačních prací.

V Praze, 14. 10. 2011 VERONIKA MISTRÍKOVÁ

Identifikační záznam

MISTRÍKOVÁ, Veronika. *Elektron kryo-mikroskopické techniky v biologickém výzkumu a nanotechnologiích* [*Electron cryo-microscopy techniques in biological research and nanotechnologies*]. Praha, 2011. 182 s., 0 příl. Disertační práce (Ph.D.). Univerzita Karlova v Praze, 1. lékařská fakulta, Ústav buněčné biologie a patologie. Vedoucí závěrečné práce/Školitel Bednár, Jan.

Acknowledgements

I would like to thank everyone who has supported me and believed in me during the period of my doctoral studies.

My special thanks go to my supervisor, dr. Jan Bednár for his continuing support, guidance and patience given during these years. Thanks for giving me the opportunity to study and work in your laboratory, to work on interesting projects, fruitful scientific discussions and help during the preparation of this thesis.

I am also deeply grateful to dr. Ivan Raška for providing me the opportunity to work at the Institute of Cellular Biology and Pathology, for his tireless guidance and permanent encouragement.

I would especially like to thank dr. Dušan Cmarko for providing valuable advice, discussions and introducing me to the field of science.

I would like to express my thanks to present and former laboratory members for their great help, contribution to a nice atmosphere and all the good advice they gave me over the years, Jane, Paul, Adriana, Eugen, Alexej, Filipa, Guy, Kate, Radka, Helena, Zdenka and many others. Special thanks belong to Ľubomír for the stimulation of every-day work and ongoing assistance with images analysis and processing.

Last but not least, I am especially grateful to my parents, sisters and friends for their understanding, patience and encouragement throughout my study and all my life. Most importantly I wish to thank my husband Robert for his love, tolerance and continued support.

The financial support from the Ministry of Education, Youth and Sports of the Czech Republic (MSM0021620806 and LC535), the Academy of Sciences of the Czech Republic (AV0Z50110509), the Grant Agency of the Czech Republic (303/03/H065) and the Grant Agency of Charles University (grant No. 13308) is gratefully acknowledged.

Abstrakt

Příprava biologických vzorků pro transmisní elektronovou mikroskopii není triviální úkol. Vzorky musí odolat vakuu přítomném v mikroskopu, a proto je často nutné uplatnit nefyziologické postupy při jejich zpracování. Tyto postupy obvykle zahrnují fixaci na bázi aldehydů, nahrazení vody alkoholem (t.j. dehydrataci/substituci), a zalití do pryskyřice, která vytváří podporu pro následnou přípravu tenkých řezů, které pak mohou být vloženy do mikroskopu. V posledním desetiletí získala dominantní postavení v oblasti výzkumu buněčné biologie metoda kryo-fixace (vitrifikace) za pomoci ultrarychlého vysokotlakého zmrazování a následná kryo-substituce a zalití vzorků do pryskyřice při nízkých teplotách. Tímto způsobem byli úspěšně vitrifikovány různé biologické vzorky s tloušťkou až několik stovek mikrometrů do stavu, který byl srovnatelný s jejich *in vivo* strukturou. Kryo-fixace izolovaných biologických objektů (s omezenou tloušťkou do několika mikrometrů) je možná i v tenké vrstvě vitrifikované vody za pomoci imerzní kryo-fixace při normálním tlaku. V kombinaci s kryo-elektronovou mikroskopií se tato metoda stala nejefektivnejším a základním principem pro tvorbu elektron kryo-mikroskopických obrázků plně hydratovaných vzorků s velmi vysokým rozlišením na úrovni několika desetin nanometrů. Obě tyto metody jsou prezentovány v této práci. Pučící kvasinky *Saccharomyces cerevisiae* zpracované kryo-fixací za pomoci vysokotlakého zmrazování a následné kryo-substituce byly vybrány jako biologický objekt pro jemné ultrastrukturální a immunocytochemické studie s využitím klasické transmisní elektronové mikroskopie; liposomy a jiné typy vezikulárních struktur zpracované imerzní kryo-fixací byly vybrány jako nanoobjekty pro elektron kryo-mikroskopické studie.

Klíčová slova: elektronová kryo-mikroskopie · imerzní kryo-fixace · kryo-fixace · mrazová substituce · transmisní elektronová mikroskopie · vitrifikace · vysokotlaké zmrazování

Abstract

Preparation of biological samples for transmission electron microscopy is not a trivial task. The samples must withstand a vacuum environment present inside a microscope, and it is often necessary to use non-physiological procedures for their processing. These procedures usually involve aldehyde-based fixation, replacing water with alcohol (i.e. dehydration/substitution), and embedding into a resin, which creates support for the subsequent preparation of thin sections that can be placed into the microscope. In the last decade, the method of cryo-fixation (vitrification) using ultra-fast high-pressure freezing followed by freeze substitution and low-temperature resin embedding gained a dominant position in the cell biology research. In this way, a range of biological samples with a thicknesses up to several hundreds of micrometers was successfully vitrified to a state that was closely related to their *in vivo* structures. The cryo-fixation of isolated biological objects (with a limited thickness up to several micrometers) is possible in a thin layer of vitrified water by plunge freezing at ambient pressure. In combination with electron cryo-microscopy, this method has become the most effective and fundamental principle for the high-resolution studies and image analysis of fully hydrated samples breaking the sub-nanometer limit. These methods are presented in this thesis. The budding yeast *Saccharomyces cerevisiae* processed by high-presure freezing and freeze substitition was selected as a biological object for both fine ultrastructural and immunocytochemical studies using conventional transmission electron microscopy; the liposomes and other types of vesicular structures vitrified by plunge freezing were selected as nanoobjects for electron cryo-miscroscopic studies.

Keywords: cryo-fixation · electron cryo-microscopy · freeze substitution · high-pressure freezing · plunge freezing · transmission electron microscopy · vitrification

TABLE OF CONTENTS

Title page 1
Prohlášení 2
Identifikační záznam 3
Acknowledgements 4
Abstrakt / Klíčová slova 5
Abstract / Keywords 6
TABLE OF CONTENTS 7
LIST OF ABBREVIATIONS AND SYMBOLS 12
LIST OF TABLES 15
LIST OF FIGURES 16

OUTLINE OF THE THESIS 19

Chapter 1 THEORETICAL BACKGROUND 21
1.1 RESOLVING POWER OF TRANSMISSION ELECTRON MICROSCOPE 22
1.2 PREPARATION OF BIOLOGICAL SAMPLES FOR TEM ANALYSIS 23
1.2.1 CONVENTIONAL FIXATION AND PROCESSING FOR FINE STRUCTURE PRESERVATION AND IMMUNOCYTOCHEMISTRY 24
1.2.1.1 Immunoelectron microscopy 28
1.2.1.2 Viewing sample under TEM and contrast enhancement 29
1.2.1.3 Main drawbacks of conventional TEM procedures 30
1.2.2 PROGRESSIVE LOWERING OF TEMPERATURE EMBEDDING 32
1.2.3 CRYO-SECTIONING ACCORDING TO TOKUYASU 33
1.2.4 CRYO-FIXATION 35
1.2.4.1 Theory of freezing 35
1.2.4.1.1 Freezing of pure water 37
1.2.4.1.2 Freezing of solutes 39
1.2.4.1.3 Freezing of a biological material 40
1.2.4.1.4 Vitrification 41
1.2.4.1.5 Freezing with cryo-protectants 42
1.2.4.1.5.1 Classification of cryo-protectants 42
1.2.4.1.5.1.1 Extracellular cryo-protectants (Non-penetrating) 43
1.2.4.1.5.1.2 Intracellular cryo-protectants (Penetrating) 43

1.2.4.1.6 Freezing with liquid cryogens 45
1.2.4.2 Rapid freezing methods 46
1.2.4.2.1 Plunge freezing 46
1.2.4.2.2 Cold metal block freezing 48
1.2.4.2.3 Jet freezing 48
1.2.4.2.4 Spray freezing 49
1.2.4.3 High-pressure freezing 50
1.2.4.4 Follow-up procedures 53
1.2.4.4.1 Cryo-sectioning of vitreous sections 53
1.2.4.4.2 Freeze fracturing 55
1.2.4.4.3 Freeze etching 57
1.2.4.4.4 Freeze drying 57
1.2.4.4.5 Freeze substitution and low-temperature resin embedding 58
1.2.4.5 Cryo-methods versus conventional way of sample processing for TEM 60
1.3 TRANSMISSION ELECTRON CRYO-MICROSCOPY 62
1.3.1 PREPARATION OF SAMPLES FOR CRYO-TEM ANALYSIS 63
1.3.2 THE VITREOUS STATE OF ICE AND ICE CONTAMINATION 65
1.3.3 LOW DOSE IMAGING IN CRYO-TEM 66
1.3.4 CONTRAST IN CRYO-TEM 67
1.3.5 CRYO-NEGATIVE STAINING 68
1.3.6 THE (BIOLOGICAL) APPLICATIONS OF CRYO-TEM 70
1.3.7 BENEFITS OF CRYO-TEM COMPARED TO OTHER APPROACHES 71
1.3.8 PERSPECTIVES OF CRYO-TEM 73

Chapter 2 AIMS OF THE THESIS 75

Chapter 3 MATERIALS AND METHODS 77
3.1 PROCESSING OF S. CEREVISIAE FOR IMMUNOELECTRON MICROSCOPY 77
3.1.1 YEAST STRAIN 77
3.1.2 RECIPES FOR SELECTED BUFFERS / SOLUTIONS 77
3.1.3 CHEMICAL FIXATION OF S. CEREVISIAE 79
3.1.4 PROTOCOLS FOR LOW-TEMPERATURE DEHYDRATION AND EMBEDDING OF HP-FROZEN S. CEREVISIAE CELLS 80
3.2 CRYO-TEM OF LIPOSOMES AND OTHER VESICULAR STRUCTURES 84

3.2.1 NANOSCOPIC VESICULAR STRUCTURES....84
3.2.2 PREPARATION OF THE HOLEY-CARBON GRIDS FOR CRYO-TEM IMAGING
....84
3.2.3 PLUNGE FREEZING....86
3.2.4 LOW DOSE IMAGING....86
3.2.5 DATA TREATMENT....87

Chapter 4 RESULTS....88
4.1 PUBLICATION No.1 *Saccharomyces cerevisiae* nuclear and nucleolar antigen preservation for immunoelectron microscopy....88
4.1.1 ABSTRACT....89
4.1.2 INTRODUCTION....89
4.1.3 MATERIALS AND METHODS....91
4.1.3.1 Yeast strain, media and cultivation conditions....91
4.1.3.2 Preparation of *S. cerevisiae* cells for immunoelectron microscopy....91
4.1.3.2.1 High-pressure freezing....91
4.1.3.2.2 Freeze substitution....92
4.1.3.2.3 Chemical fixation....92
4.1.3.2.4 Microtomy, staining and electron microscopy....93
4.1.3.2.5 Immunolabeling....93
4.1.3.3 Immunofluorescence microscopy....94
4.1.3.4 Antibodies....94
4.1.4 RESULTS....95
4.1.4.1 Chemically fixed cells....95
4.1.4.1.1 Formaldehyde-fixed cells....95
4.1.4.1.2 Formaldehyde/Glutaraldehyde-fixed cells....95
4.1.4.2 High-pressure freezing and freeze-substitution....96
4.1.4.2.1 FS medium 1: acetone alone....96
4.1.4.2.2 FS medium 2: acetone with 0.1% glutaraldehyde....96
4.1.4.2.3 FS medium 3: acetone with 0.1% uranyl acetate....96
4.1.4.2.4 FS medium 4: acetone with 0.1% uranyl acetate and 0.1% glutaraldehyde....97
4.1.4.3 Immunofluorescence and immunoelectron microscopy....98
4.1.4.3.1 Nop1 protein....98
4.1.4.3.2 Nsr1 protein....98
4.1.4.3.3 Nsp1 protein....99

4.1.4.3.4 α-Tubulin 99
4.1.5 DISCUSSION 100
4.1.5.1 *S. cerevisiae* nuclear ultrastructure 102
4.1.5.2 *S. cerevisiae* nucleolar ultrastructure 103
4.1.5.3 Immunocytochemistry 104
4.1.6 ACKNOWLEDGEMENTS 105
4.1.7 FIGURE LEGENDS 106
4.1.8 FIGURES 108
4.2 PUBLICATION No.2 Silicone-stabilized liposomes 113
4.2.1 ABSTRACT 114
4.2.2 INTRODUCTION 114
4.2.3 EXPERIMENTAL SECTION 115
4.2.3.1 Materials 115
4.2.3.2 Synthesis of the monomer 116
4.2.3.3 Preparation of cationic liposomes 116
4.2.3.4 Covering with silicone 117
4.2.3.5 Calcein-release studies 117
4.2.3.6 Cryo-transmission electron microscopy (cryo-TEM) 117
4.2.3.7 Light scattering and zeta potential measurements 118
4.2.3.8 FTIR and NMR spectroscopy 118
4.2.4 RESULTS AND DISCUSSION 118
4.2.4.1 The monomer synthesis 118
4.2.4.2 Characterization of the cationic liposomes 119
4.2.4.3 Preparation of silicone-coated liposomes 121
4.2.5 CONSLUSIONS 124
4.2.6 ACKNOWLEDGEMENTS 125
4.2.7 FIGURE AND TABLE LEGENDS 125
4.3 PUBLICATION No.3 Bilayer structures in dioctadecyldimethylammonium bromide/oleic acid dispersions 131
4.3.1 ABSTRACT 132
4.3.2 INTRODUCTION 132
4.3.3 MATERIALS AND METHODS 134
4.3.3.1 Materials 134
4.3.3.2 DODAB/OA dispersion 135
4.3.3.3 Differential Scanning Calorimetry (DSC) 135

4.3.3.4 Cryo-Transmission Electron Microscopy (cryo-TEM) 135
4.3.3.5 Differential interference contrast (DIC) microscopy 136
4.3.3.6 Fluorescence anisotropy measurements and microviscosity calculations 136
4.3.3.7 Langmuir monolayer measurements 137
4.3.4.1 Cryo-TEM and DIC microscopy studies 138
4.3.4.2 Differential scanning calorimetry studies 139
4.3.4.3 Fluorescence anisotropy measurements 140
4.3.4.4 Langmuir monolayer measurements 141
4.3.5 DISCUSSION 143
4.3.6 CONCLUSIONS 146
4.3.7 ACKNOWLEDGEMENTS 146
4.3.8 FIGURE AND TABLE LEGENDS 147
4.3.9 FIGURES AND TABLES 148

CHAPTER 5 GENERAL DISCUSSION 154

CHAPTER 6 CONCLUSIONS 160

CHAPTER 7 REFERENCES 162

LIST OF ABBREVIATIONS AND SYMBOLS

This is a list of abbreviations and symbols that are commonly used in this thesis and submitted publications:

°C:	Celsius
µm:	Micrometer
µM:	MicroMolar
2D:	Two-dimensional
3D:	Three-dimensional
***A*:**	Area
Å:	Ångström
BAM:	Brewster angle microscopy
BC:	Large ice crystals
BSA:	Bovine serum albumine
BU:	Bubbles
C:	Chloroplast
$CaCl_2$:	Calcium chloride
CCD:	Charged coupled device
CEMOVIS:	Cryo-electron microscopy of vitreous sections
CL:	Calcein-loaded
CLEM:	Correlative light electron microscopy
cm:	Centimeter
Cryo-ET:	Cryo-electron tomography
Cryo-TEM:	Cryo-electron microscopy; Cryo-transmission electron microscopy; Cryogenic tranmission electron microscopy
C_S^{-1}:	Compression
CSC:	Calorimetry sciences
	corporation
Cy:	Cytoplasm
CW:	Cell wall
$D_4^{ethyl\text{-}D}$:	Tetra(methyldimethoxy silethyl)-tetramethyl cyclotetrasiloxane
D_4^H:	1,3,5,7-Tetramethyl cyclotetrasiloxane
DABCO:	1,4-Diazabicyclo[2.2.2] octane
DAPI:	4',6-Diamidino-2-phenylindole
DFC:	Dense fibrillar component
DIC:	Differential interference contrast; Differential interference microscopy (microscope)
DLS:	Dynamin light scattering
DMF:	*N*,*N*-dimethylformamide
DMSO:	Dimethylsulfoxide
DNA:	Deoxyribonucleic acid
DODAB:	Dimethyldioctadecyl ammonium bromide
DPH:	1,6-diphenyl-1,3,5-hexatriene
DSC:	Differential scanning calorimetry

dz: Hydrodynamic mean diameter

EC: Euchromatin

EM: Electron microscopy; Electron microscope

ER: Endoplasmatic reticulum

FA: Formaldehyde

FC: Fibrillar center

FM: Fluorescence microscopy; Fluorescence microscope

FS: Freeze substitution

FTIR: Fourier transform infrared spectroscopy

***G*:** Instrumental correction factor

GA: Glutaraldehyde

GC: Granular component; Golgi cisternae

***h*:** Horizontal orientation

HC: Heterochromatin

HP-: High-pressure-

HPF: High-pressure freezing

***I*:** Fluorescence intensity

IEM: Immunoelectron microscopy; EM immunocytochemistry

IF: Immunofluorescent; Immunofluorescence

IR: Infrared

K: Kelvin

K_2HPO_4: Dipotassium phoshate

KBr: Potassium bromide

KCl: Potassium chloride

kDa: KiloDalton

KH_2PO_4: Potassium dihydrogen phosphate

$KMnO_4$: Potassium permanganate

KPi: Potassium phosphate buffer

kV: Kilovolt

LB: Lamellar body

LC: Liquid condensed

LDV: Laser Doppler velocimetry

LE: Liquid expanded

LM: Light microscopy

m: Meter

M: Mitochondria, Mitochondrion

MD: Molecular dynamics

$MgCl_2$: Magnesium chloride

MHz: Megahertz

mM: MilliMolar

MPa: MegaPascal

Mt: Microtubule

mV: MilliVolt

MVB: Multivesicular body

n.d.: No date

N_2: Nitrogene

$Na_2HPO_4x7H_2O$: Disodium hydrogen phosphate heptahydrate

$Na_3(C_6H_5O_7)x2H_2O$: Sodium citrate dihydrate

NaCl: Sodium chloride

$NaIO_4$: Sodium periodate

NaOH: Sodium hydroxide

NE: Nuclear envelope

NGS: Normal goat serum

NH_4Cl: Ammonium chloride

nm: Nanometer

NMR: Nuclear magnetic resonance

Np: Nucleoplasm

NPC: Nuclear pore complex

Nu: Nucleolus

OA: Oleic acid

OsO_4: Osmium tetroxide

$Pb(NO_3)_2$: Lead nitrate

PBS: Phosphate buffered saline

PC: Phosphatidylcholine

PDI: Polydispersity

PIPES: 1,4-Piperazine bis [2-ethanosulfonic acid]

p*Ka*: Physiological salt concentration

PLT: Progressive lowering of temperature

PM: Plasma membrane

***r*:** Steady state anisotropy

rER: Rough endoplasmatic reticulum

rRNA: Ribosomal ribonucleic acid

RNA: Ribonucleic acid

RT: Room temperature

Saccharomyces cerevisiae: *S.cerevisiae*

***S*:** Packing diameter

SP: Splotchy ice

SPA: Single particle analysis

SPB: Spindle pole body

TEM: Transmission electron microscope (microscopy)

T_{end}: Temperature at the end of FS step

TI: Thick ice

T_m: The melting temperature

T_{start}: Temperature at the beginning of FS step

UA: Uranyl acetate, $[UO_2(OCOCH_3)_2x2H_2O]$

UV: Ultraviolet

***v*:** Vertical orientation

V: Vacuole

VMS: Vinylmethyldimetho-xysilane

X_{OA}: The mole fraction of OA

XRC: X-ray crystallography

YPD: Yeast extract, peptone, glucose

Δ G: Gibbs energy of mixing

ΔH_m: Enthalpy of transition

***ζ*:** Zeta potential

***η*:** Microviscosity

***π*:** Surface pressure

LIST OF TABLES

Table 1: *List of conventional cryo-protectants, which should be used to accomplished successful cryo-fixation. ..* 43

Table 2: *List of selected liquid cryogens with corresponding values of melting and boiling points at atmospheric pressure.* 45

Table 3: *Properties of solvents generally used for freeze substitution.*.....58

Table 4: *Summary of main differences between the conventional and cryo-way of sample processing for TEM.* 62

Table 5: *Summary of advantages over disadvantages of cryo-TEM procedure*.....72

Table 6: *Composition of fixative solutions used for yeast cells preservation.* 80

Table 7: *The protocol used for freeze substitution and Lowicryl HM20 low-temperature embedding of HP-frozen S. cerevisiae yeast cells by manual reagent handling.* 81

Table 8: *The protocol used for freeze substitution and Lowicryl HM20 low-temperature embedding of HP-frozen S. cerevisiae yeast cells using an automatic reagent handling system (Leica EM FSP) .* 82

Table 9: *The protocol used for freeze substitution and LR White resinembedding of HP-frozen S. cerevisiae yeast cells.* 83

Table 10: *The values of mean hydrodynamic diameter (dz), polydispersity (PDI) and the zeta potential (ζ).* 126/130

Table 11: *Thermodynamic data obtained by micro-DSC analysis for 10 mM mixture DODAB/OA in water; the melting temperature, T_m, the melting enthalpy, ΔH_m.* 147/151

Table 12: *Experimentally measured the fluorescence anisotropy of DPH and the calculated microviscosity.*.....148/152

LIST OF FIGURES

Chapter 1

Figure 1-01: *Resolving power*.....22
Figure 1-02: *Reactions involved in fixation by aldehydes*.....25
Figure 1-03: *Mammalian tissue culture cells prepared by conventional procedure for TEM analysis*.....27
Figure 1-04: *Schematic illustration of un-direct labeling protocol using gold-conjugated secondary antibodies*.....29
Figure 1-05: *Example of a post-staining procedure*.....30
Figure 1-06: *Immunogold labeling of cryo-sections of filamentous funghi*.....34
Figure 1-07: *A phase diagram showing the pressures and temperatures at which the different states of water exist* 36
Figure 1-08: *Three different physical forms of cooled water* 38
Figure 1-09: *Ice formation in the presence of solute* 39
Figure 1-10: *Ice crystal growth in the concentrated medium of a cell.* 40
Figure 1-11: *Schematic diagram illustrating the method of plunge freezing*.....47
Figure 1-12: *Schematic diagram illustrating the method of cold metal block freezing*.....48
Figure 1-13: *Schematic diagram illustrating the method of jet freezing*.....49
Figure 1-14: *Schematic diagram illustrating the method of spray freezing.*.....50
Figure 1-15: *The influence of solute concentration and pressure on the crystallization window for cryo-fixation* 51
Figure 1-16: *High-pressure freezer*.....52
Figure 1-17: *Frozen hydrated yeast cells* 54
Figure 1-18: *Freeze fracturing* 56
Figure 1-19: *Example of the timing of freeze substitution followed by low-temperature resin embedding*.....59
Figure 1-20: *Comparison of HP-frozen/FS type II alveolar epithelial cells (a, c) with chemically fixed samples (b, d)*.....61
Figure 1-21: *Schematic illustration of the method of plunge freezing and the embedding of samples into a thin layer of vitreous water, followed by cryo-TEM observation*.....64
Figure 1-22: *Types of cryo-TEM contamination* 65

Figure 1-23: *Low dose imaging* 67
Figure 1-24: *Contrast in the cryo-TEM micrographs* 68
Figure 1-25: *An outline of the cryo-negative staining procedure* 69
Figure 1-26: *Cryo-negative staining* 69
Figure 1-27: *Cryo-TEM micrographs of silica-silicone nanocapsules prepared by template polymerization* 73

Chapter 3

Figure 3-01: *A metal support with arranged copper EM grids covered with perforated cellulose film, after drying* 85

Chapter 4

Figure 4-01: *Morphology of chemically fixed and LR White embedded S. cerevisiae cells* 106/108
Figure 4-02: *Morphology of Lowicryl HM20 embedded S. cerevisiae cells after high-pressure freezing and freeze-substitution in different media* 106/109
Figure 4-03: *Details of various cell components preserved in S. cerevisiae cells after high-pressure freezing and freeze-substitution* 106/109
Figure 4-04: *Details of selected nuclear structures demonstrating fine ultrastructure preservation obtained by high-pressure freezing and freeze-substitution of S. cerevisiae cells, embedded in Lowicryl HM20* 106/110
Figure 4-05: *Nucleolar ultrastructure preservation of high-pressure frozen S. cerevisiae cells substituted in different media* 106/111
Figure 4-06: *Comparative immunolocalization of the nucleolar markers Nop1 and Nsr1 in S. cerevisiae cells at the LM and EM levels* 107/110
Figure 4-07: *Comparative LM and EM mapping of Nsp1 in S. cerevisiae cells* 107/118
Figure 4-08: *Immunolocalization of α-tubulin in S. cerevisiae cells* 107/118
Figure 4-09: *Synthesis of the monomer* 125/126
Figure 4-10: *Distribution profiles of the hydrodynamic diameters obtained from DLS*

measurements for the different system 125/127
Figure 4-11: *The cryo-TEM micrograph and the diameter profiles of the initial liposomes obtained by extrusion* 125/127
Figure 4-12: *FTIR spectra of the polymeric material extracted from the liposomes after heating (solid line) and* $D_4^{ethyl\text{-}D}$ *(dotted line)* 125/128
Figure 4-13: *Polymerization / condensation processes of* $D_4^{ethyl\text{-}D}$ *catalyzed by hydroxide anion at the liposome surface* 125/128
Figure 4-14: *The cryo-TEM micrographs of the silicone-coated liposomes obtained at pH 10.2 (a) and 8.5 (b) and the appropriate distribution profiles of the vesicle diameter* 125/129
Figure 4-15: *Optical density traces for the surfactant titration of the liposome dispersions* 125/129
Figure 4-16: *Changes in fluorescence intensity of calcein during titration of the liposome dispersions at pH 8.5* 126/130
Figure 4-17: *Chemical structure of dioctadecyldimethylammonium bromide (DODAB) and oleic acid (OA)* 142/148
Figure 4-18: *Cryo-TEM micrographs of vitrified extruded DODAB/OA dispersions* 147/149
Figure 4-19: *Differential interference contrast (DIC) images of structures formed in the DODAB/OA dispersions at* $X_{OA} = 0.4$ *(A) and* $X_{OA} = 0.6$ *(B)* 147/148
Figure 4-20: *DSC thermograms (second upscans) for 10 mM DODAB/OA aqueous dispersions as a function of OA mole fraction* 147/150
Figure 4-21: *The effect of the OA mole fraction on the fluorescence anisotropy of the DPH probe incorporated into bilayer* (λ_{exc} = 350 nm, λ_{em} = 428 nm, $c_{DPH} = 1.4 \times 10^{-7}$ M) 147/150
Figure 4-22: *The surface pressure (π)–area (A) isotherms of DODAB/OA mixed monolayers formed at the air/water interface at 20 °C* 147/151
Figure 4-23: *(A) The compression modulus versus surface pressure for the DODAB/OA mixed monolayer. (B) The changes of the compression modulus values at* $\pi = 32.5$ *mN/m vs. composition of DODAB/OA monolayers* 147/152
Figure 4-24: (A) *The mean area per molecule (*A_{12}*) vs. composition plots for DODAB/OA mixed monolayers at various surface pressures. (B) The excess Gibbs energy of mixing vs. Composition plots for DODAB/OA mixed monolayers at various surface pressures* 147/153

OUTLINE OF THE THESIS

Research presented in this thesis is focused on two main objectives: i) specification of the protocol for the preparation of the yeast *Saccharomyces cerevisiae* (as a biological object) for both ultrastructural and immunocytochemical electron microscopic studies; with the aim to preserve the cellular ultrastructure as close as possible to *in vivo* state, and ii) exploring the application of the electron cryo-microscopy techniques in the study of the liposomes and other vesicular structures (as nanoobjects).

The first chapter, which is preceded by the statement (prohlášení), identification tag (identifikační záznam), acknowledgements, abstract/keywords (both in Czech and English), table of contents, list of abbreviations and symbols, list of tables and by list of figures, delineates outline of the thesis. Chapter 1 presents a general introduction to transmission electron microscopy. Emphasis is given on a biological sample processing using conventional methods and advanced microscopy methodologies, including progressive temperature lowering embedding and cryo-sectioning according to Tokuyasu. Some specific aspects of cryo-fixation are discussed subsequently. At the same time an overview is also provided of the methods of rapid freezing (plunge freezing, slam freezing, jet freezing and spray freezing), as well as the method of high-pressure freezing and follow-up procedures. Merits and limitations of each method are discussed in detail in parallel with their area of application and implementation presented previously in the literature. The final section of Chapter 1 is devoted to electron cryo-microscopy technique. Overall view of the methodology, main pitfalls and advantages are discussed in detail. In Chapter 2, the specific aims of our work are formulated. In Chapter 3, the material and methods employed in this thesis are shortly commented. The results of our experimental work are finally shown in Chapter 4. Three publications divided into separate subchapters are enclosed. The first publication is dedicated to *Saccharomyces cerevisiae nuclear and nucleolar antigen preservation for immunoelectron microscopy*. Conventional methods of fixation, drying and embedding are compared with the method of high-pressure freezing, freeze substitution and low-temperature embedding. Moreover, the immunofluorescence microscopy and on-section immunogold labeling were also performed. This study was published in Folia Biologica 2010, (Praha) 56(3), 97-109. The *S. cerevisiae* haploid strain NOY 886 was a kind gift of Yvonne S. Osheim from the University of Virginia Health System in USA. In the second publication entitled *Silicone-stabilized liposomes* we try to address the question of utilization and advantage of plunge

freezing technique and electron cryo-microscopic imaging in the study of liposomes, compared with alternative methods that could be used for the characterization of such vesicles. As described in detail, our method allows direct imaging of frozen hydrated samples in the most natural environment currently possible. This study was published in Colloid & Polymer Science 2010, 288, 37-45. The third publication is dedicated to *Bilayer Structures in Dioctadecyldimethylammonium Bromide/Oleic Acid Dispersions*. The morphology and properties of dioctadecyldimethylammonium bromide-oleic acid bilayers were inspected using electron cryo-microscopy and differential interference contrast microscopy. This study has recently been published in Chemistry and Physics of Lipids 2011, 164(5), 359-367. My contribution to both of these works therefore included, in particular, the processing of objects for electron cryo-microscopy by plunge freezing, the examination and evaluation of cryo-electron microscopic images and determination of their essential morphological properties. These two studies arose from the collaboration with the research group of Mariusz Kepczynski at the Faculty of Chemistry, Jagiellonian University in Krakow, Poland. The figures accompanying publications in Chapter 4 are provided at the end of subchapters 4.1, 4.2 and 4.3, respectively. The consecutive Chapter 5 discusses the results presented in Chapter 4. In Chapter 6, the summary of experimental studies of this thesis and suggestions for future work are provided. The closing chapter, Chapter 7, contains the list of references.

This work represents a research performed at the Institute of Cellular Biology and Pathology, First Faculty of Medicine of Charles University in Prague.

Chapter 1 THEORETICAL BACKGROUND

The transmission electron microscopy (TEM) has become one of the most powerful techniques used in the ultrastructural studies of cells, their compartments and other biological objects since its invention in 1931 by Max Knoll and Ernst Ruska (Ernst Ruska – Autobiography, n.d.). The main interest of life scientists, among other investigations, was to develop methods capable to arrest biological samples in their 'close-to-native' state for their 'close-to-real' electron microscopic investigations. In early days, the methods based on conventional chemical fixation followed by dehydration, resin embedding and sectioning used to result in numerous cases in poorly-preserved biological samples. Nevertheless, these old classical embedding procedures have paved the way for the development of structural cell biology and are still widely used in many laboratories, not loosing their importance (Deerinck, 2006; Glauert, 1974; Griffiths, 1993). In recent years, with a boom in the development of new instruments, cryo-preparation techniques gained a dominant position in the processing of various biological samples. Among them, the cryo-fixation by high-pressure freezing and freeze substitution has become the method of choice for superior preservation of both fine cellular ultrastructure and immunoantigenicity (Moor & Riehle, 1968; Studer *et al*, 2001). These processing methods have enabled the successful cryo-fixation to be accomplished not only for samples such as tissues, cell cultures, etc., but also for those generally considered to be 'problematic' for the electron microscopic processing, such as plants, fungi, insects and nematodes (Hess, 2007; Kang, 2010; McDonald, 2007; Murray, 2008; Studer *et al*, 2001; Vanhecke *et al*, 2008). Simultaneously with the progress of molecular biology in recent decades the transmission electron microscopy has begun to be widely used for the visualization and analysis of biological and biochemical processes and pathways at the molecular level. A pre-requisite for these structure-function studies was a development of a simple method by Marc Adrian and Jacques Dubochet in 1984 (Adrian *et al*, 1984; Dubochet *et al*, 1988), which allowed the preservation of molecules in their native hydrated conformation by embedding in a thin layer of vitreous water using plunge freezing and their direct observation in the so-called transmission electron cryo-microscope.

All of these cryo-preparation techniques are currently making valuable contributions to research and development in many fields of cell biology, structural biology, biomedical science and nanotechnology-based biomedical science, etc., and this trend is expected to continue.

1.1 RESOLVING POWER OF TRANSMISSION ELECTRON MICROSCOPE

Light microscopy (LM) and fluorescence microscopy (FM) are the most commonly used imaging techniques in biological and biomedical studies. Both represent excellent tools for studying living cells in a real time; however, they cannot give a detailed view of structures, which is readily achievable by transmission electron microscope (TEM) (Figure 1-01).

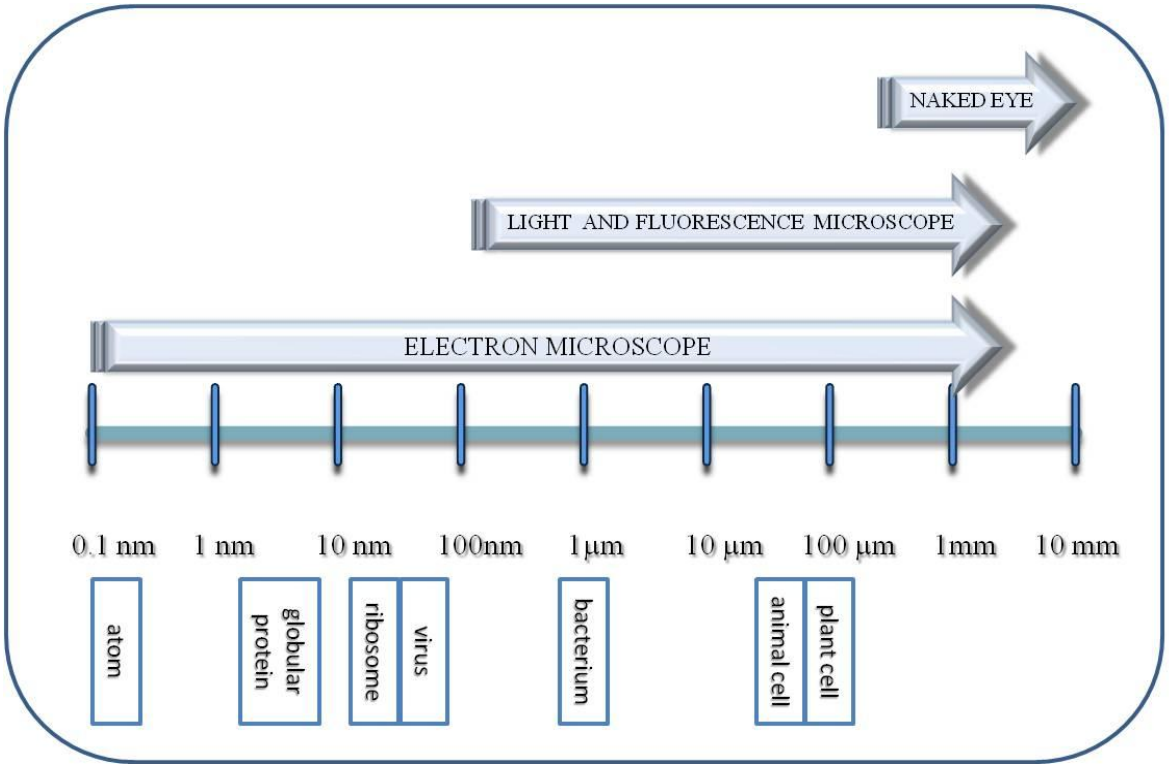

Figure 1-01: *Resolving power.* Sizes of cells and their components are drawn on a logarithmic scale, indicating what can be resolved by the naked eye and in the light and electron microscopes. The following units of lenght are commonly employed in microscopy: μm (micrometer) = 10^{-6} m (meter); nm (nanometer) = 10^{-9} m; Å (Ångström unit) = 10^{-10} m. Figure adapted with modifications from Alberts *et al* (2008).

Unlike TEM, conventional light microscopes are limited by the physical limits to a lower magnification and under optimal conditions to a resolution of about 0.2 μm in practice (Alberts *et al*, 2008; Cox & Sheppard, 2004; Griffiths, 2001). This resolution limit has been recently reduced below 0.1 μm with a newly developed fluorescence techniques capable of nanometer-scale resolution ('fluorescence nanoscopy') that offers the possibility to localize a

single fluorescently-labeled protein molecule using a confocal laser-scanning microscope (Cox & Sheppard, 2004). However, there is still fundamental limitation in relating that signal to the context of a cell (Betzig *et al*, 2006; Cox & Sheppard, 2004; Hell, 2003; Watanabe *et al*, 2011). Such ultrastructural studies require nanometer resolution that at present can be achieved by TEM. Currently, the practical resolving power of most TEMs can reach 0.1 nm (1 Å). This is especially true for non-biological objects (Alberts *et al*, 2008; Conway *et al*, 1997). For biological objects, TEM can achieve a resolution in 1 nm (10 Å) range, and even better in the case of isolated complexes (Grigorieff & Harrison, 2011). This is about 200 times better than the resolution of the light instrument, and therefore TEM can reveal far greater details of subcellular structures, such as membranes, filaments, ribosomes, etc. (Alberts *et al*, 2008). This higher resolution, however, comes at a cost: the sample preparation for TEM observation is much more complex and together with the contrast and radiation damage, has a potential to induce significant modifications of the sample (structure, content, spatial distribution of components) – the artifacts.

1.2 PREPARATION OF BIOLOGICAL SAMPLES FOR TEM ANALYSIS

The greatest obstacles to examine a biological material inside TEM are the non-physiological conditions it is exposed to. As the name 'TEM' implies, these microscopes transmits a high energy electron beam through a sample in a high vacuum environment. The sample must therefore tolerate the vacuum of TEM (about 10^{-5} to 10^{-8} Torr; 1 Torr = 133.322 Pascals), required to prevent the scattering of electrons by the gas molecules. If an untreated biological sample is exposed to the vacuum inside a TEM column at room temperature, the contained water immediately evaporates destroying completely its structure, and also TEM (Griffiths, 1993; Robards & Sleyter, 1985). Biological sample must therefore be prepared in a particular way, which ensures the removal of water without leading to significant structural alterations. In the simplest case, as in negative staining technique used for small biological objects with resistant structure (e.g., viruses or phages) or isolated complexes, the dehydration of the sample is accopmplished by simple air-drying (Harris, 2007). Bigger and more complex samples are first chemically-fixed before the water is replaced by an organig solvent that allows the infiltration with a plastic resin (Deerinck, 2006; Glauert, 1974; Griffiths, 1993). Unfortunatelly, when using these methods, it is unknown how much water remained around proteins in the preparation (Dubochet *et al*, 1988; Glauert, 1974; Robards & Sleyter, 1985). Furthermore, the samples must be extremely thin due to the limited penetrating power (mean

free path) of electrons for conventional TEM observations. Only small objects can be directly viewed. Larger samples need to be sectioned after resin embedding. Typical thickness of sections used for routine observation should be in the order of 50 to 100 nm for TEMs operating at accelerating voltages of 60 - 80 kV (kiloVolt). For thicker samples a significant part of electrons would suffer from multiple scattering events, or a substantial loss of energy at this accelerating voltage, and thus the resolution would be severely degraded. Therefore, a higher accelerating voltage (100 - 200 kV) should be used for the samples with a thickness of about 250 nm (or even more if the electron energy filtering is used). On the other hand, increasing the thickness of the sample leads again to a loss of resolution, which is usually limited to 2 nm at best in the case of samples prepared as described above (Ellisman, 2006; Glauert, 1974; Robards & Sleyter, 1985). The only way to break that resolution limit is the use of alternative methods such as very rapid freezing of biological samples (McDonald, 1999), negative staining (Harris, 2007), and/or transmission electron cryo-microscopy (Conway *et al*, 1997; Dubochet *et al*, 1988). Furthermore, digital image analysis can be used to reconstruct three-dimensional (3D) objects by combining information either from many individual particles or from a set of tilted views of a single object (Chiu, 2006; Marko & Hsieh, 2007; Pierson *et al*, 2009). Together, these approaches extend the resolution and scope of TEM to the point, at which we can reliable image the biological sample.

1.2.1 CONVENTIONAL FIXATION AND PROCESSING FOR FINE STRUCTURE PRESERVATION AND IMMUNOCYTOCHEMISTRY

Generally, a standard preparation of biological material for TEM study includes three principal steps: i) chemical fixation using buffered aldehydes, ii) dehydration in graded alcohol series, iii) resin embedding and polymerization, and iv) ultrathin sectioning (Deerinck, 2006; Glauert, 1974; Griffiths, 1993).

The goal of fixation in any TEM procedure is to maintain the maximal degree of morphological preservation by rapidly terminating all enzymatic activities in order to minimize the post-mortem changes and to prevent the redistribution of cellular content during further processing (Deerinck, 2006; Glauert, 1974; Griffiths, 1993). In the case of immunocytochemical studies it should also allow specific antibody labeling without denaturation of antigens in a question (Griffiths, 1993).

Preferred fixatives for TEM are buffered solutions of formaldehyde and/or glutaraldehyde; aldehydes which readily react with various functional groups of biological

macromolecules in a cross-linking fashion (Figure 1-02), creating thus inter- and intra-locking structures (Fox *et al*, 1985; Glauert, 1974; Kiernan, 2000).

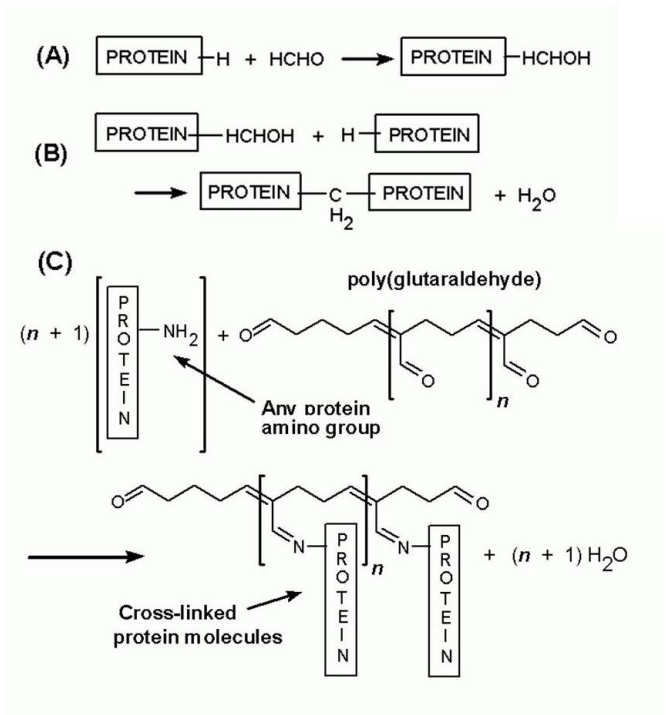

Figure 1-02: *Reactions involved in fixation by aldehydes.* (A) Addition of a formaldehyde (FA) molecule (HCHO) to a protein. (B) Reaction of bound FA with another protein molecule to form a methylene cross-link. (C) Reaction of poly (GA) molecule with amino groups of proteins. Figure adapted from Kiernan (2000).

The dialdehyde glutaraldehyde (GA) is generally the fixative of choice for the ultrastructural studies. GA cross-links irreversibly proteins (Figure 1-02C), most commonly by reacting with α-amino groups of lysine. GA can also react with nucleic acids and carbohydrates, though it shows limited reactivity with lipids (Glauert, 1974; Griffiths, 1993). Formaldehyde (FA) is a monoaldehyde and it is a less effective cross-linker than GA. FA reacts with free amino groups in proteins to form amino-methyl groups (Figure 1-02A and B), which can, in turn, form methylene bridges with other functional groups (Fox *et al*, 1985; Griffiths, 1993; Kiernan, 2000). These reactions are usually reversible, so the majority of FA can be washed out by subsequent exposure of the sample to aqueous solutions. This implies that the overall morphology is not well preserved if FA is used alone. Hence, a combination of FA/GA fixation solutions is often employed, especially in TEM immunocytochemical

analysis (Deerinck, 2006; Fox *et al*, 1985). Contrary to LM preparations of biological samples, alcohols (e.g., methanol, ethanol) are generally unusable as fixatives for TEM because these organic solvents fix proteins in place by precipitation (Deerinck, 2006).

Several different buffers may be used to protect the cells and to counter rapid drops in pH that should occur during the fixation process (Webster & Webster, 2007). The most commonly used buffers are phosphate, cacodylate and organic buffers such as PIPES (1,4-Piperazine bis [2-ethanosulfonic acid]). Though their usage is essential, buffers are not entirely innocuous as some fine detail may be altered. For example, high concentrations of phosphates may damage mitochondria; consequently, one should keep the buffer concentration as low as possible while still maintaining the pH within the desired range. On the other hand, organelles such as microfilaments and microtubules are better preserved, and the increase in the overall density of the cell suggests that extraction is minimized with the organic buffers (Bozzola, 2007; Webster & Webster, 2007).

After fixation, the sample is usually embedded in a plastic resin (embedding medium) to provide solid support for the sectioning procedure and stability under the electron beam. With few exceptions, most of the embedding media are not soluble in water. Therefore, the fixed samples must be first dehydrated in an organic solvent miscible with the embedding medium (Bozzola, 2007; Deerinck, 2006). Two most widely used dehydrating agents are ethanol and acetone. Acetone causes less shrinkage than ethanol. It is therefore the solvent of choice for most applications (Deerinck, 2006; Glauert, 1974), except the cases when the acrylic resin LR White is used. This embedding medium does not polymerize in the presence of acetone and the use of ethanol is thus the only option (Deerinck, 2006).

Infiltration with the resin is the next step in the preparation of biological samples for TEM observation (Figure 1-03). The choice of resin depends on the type of sample and the intended procedure. Two main classes of resins in use today for the embedding of samples are epoxides (Epon 812, Araldite, Spurr`s) and acrylics (LR White, LR Gold, and Lowicryls). The epoxy resins are more stable under the electron beam than acrylics, and they show less shrinkage. These resins are capable to form covalent bonds with biological material and biological material is then easy to section (Brorson *et al*, 1994; Finck, 1960). Therefore epoxides are the resins of choice for TEM ultrastructural studies providing excellent morphology, though often the antigenicity is affected. Since they are fairly impermeable to aqueous solutions, it is more difficult to use them for post-embedding on-section immunogold labeling or histochemical studies (Deerinck, 2006; Finck, 1960; Schwarz & Humbel, 2007). Contrary to epoxides, the acrylic resins polymerize via free radical chain reaction (only the

acrylic monomers polymerize) so that the biological components are not covalently bind to a resin but they are enmeshed in a network of polymers (Schwarz & Humbel, 2007). Hence, these resins offer higher degree of hydrophilicity and better yield of immunolabeling (Biggiogera & Fakan, 2008; Brorson *et al*, 1994; Schwarz & Humbel, 2007). These are the resins of choice of sample preparation for TEM immunocytochemical studies (Deerinck, 2006; Griffiths, 1993).

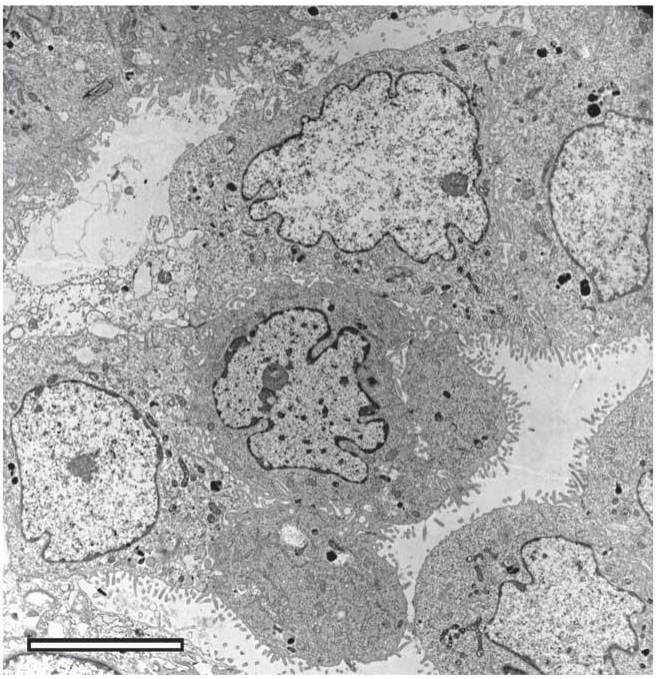

Figure 1-03: *Mammalian tissue culture cells prepared by conventional procedure for TEM analysis.* The cells were fixed in 4% FA / 2.5% GA in PIPES buffer, dehydrated in ethanol and finally embedded in Epoxy 812. Bar = 7.5 μm. Figure adapted from Bozzola (2007).

After infiltration with the resin, the samples are let to polymerize (usually at higher temperatures) to produce a solid block. This makes the sample suitable for thin sectioning. Ultra-thin sections (50 – 100 nm thick) are cut using an ultramicrotome with a glass or diamond knife. Sections are floated on the water surface of the boat attached to a knife, and subsequently transformed to a 3-mm diameter EM (electron microscopic) grid coverred with a supporting film (Hagler, 2007). Type of grids and films used is usually determined by the sample preparation technique required and the nature of sample. For standard work, copper grids with a fine mesh are generally used. Nickel or gold grids are better suited for the requirements of immunocytochemical procedures. Grids are usually coated with plastic film

(e.g. Formvar) and a thin layer of evaporated carbon (Webster & Webster, 2007). It is only at this point that the thin sections can be introduced into the electron microscope for observation and study.

1.2.1.1 Immunoelectron microscopy

Often, EM immunocytochemistry (IEM; immunoelectron microscopy) is the final step of sample preparation. It offers a unique possibility to localize antigens with high resolution in the context of intact cellular ultrastructure and to provide a better understanding of cellular functions (Griffiths, 1993). Immunocytochemical reaction can be carried out following either pre-embedding or post-embedding technique. The former method is preferred when the antigen can be altered or damaged by procedures other than fixation, such as dehydration or resin embedding and sectioning. For details of this procedure see, e.g., Griffiths (1993), Morphew (2007), Ochs (2006). Here, I will briefly comment on the second procedure; the on-section immunogold labeling.

As known, the specificity is one of the basic concepts for cytochemistry: an ideal reaction should be specific for a single reactive group or for a single component – an antigen. Antibodies are proteins produced by the immune system of vertebrates as a defense against infection. They are unique among proteins because they are made in billions of different forms, each with a different binding site that recognizes a corresponding antigen (Alberts *et al*, 2008; Griffiths, 1993). Monoclonal antibodies have the advantage (or sometimes disadvantage) of recognizing a single epitope, whereas polyclonal antibodies are often of higher titer and avidity, and may recognize multiple epitopes, some of which may be more resistant to denaturation by fixation (Griffiths, 1993). When dealing with antigens for which antibody production is difficult or impossible (because the immunogen is unvailable or antigen is not very immunogenic), autoantibodies are sometimes the method of choice. This is especially true for many nuclear proteins (Hemmerich & von Mikecz, 2000; Raska *et al*, 1990). At EM level, the usual procedure to locate the antigen-antibody complex involves the blocking, incubation of a thin section with a specific primary antibody and then with a secondary antibody marked with colloidal gold particle (Alberts *et al*, 2008; Schwarz & Humbel, 1993). The reaction is schematically shown in Figure 1-04. Colloidal gold is the most often used particle marker for IEM, mainly because the gold particles of defined size are easy to produce and can be attached to a number of affinity molecules such as immunoglobulins and protein A. In general, the use of 5 - 10 nm gold particles is

recomended; although smaller particles (down to 1 nm) can also be used. Moreover, dense gold particles are recognized easily in TEM and resemble no natural cellular structure (Griffiths, 1993). Using antibodies conjugated to different sizes of colloidal gold particles permits the high-resolution detection, localization, and quantification of one or more defined antigens in cellular compartments at EM level (Griffiths, 1993; Mayhew, 2007).

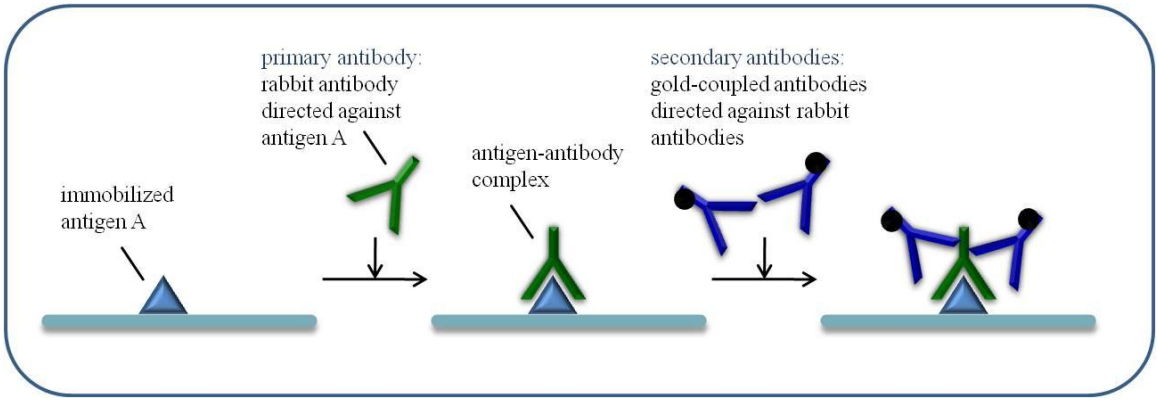

Figure 1-04: *Schematic illustration of un-direct labeling protocol using gold-conjugated secondary antibodies.*

In a conventional procedure, the FA/GA-based fixation and embedding into LR White resin is employed for IEM studies (Biggiogera & Fakan, 2008; Brorson *et al*, 1994; Deerinck, 2006; Griffiths, 1993; Schwarz & Humbel, 2007). However, this method is often compromised by technical issues including the destruction of antigens, inaccessibility of antigens by excessive cross-linking of the surrounding biological matrix, the lack of suitable antibodies and non-specific binding of antibodies (Biggiogera & Fakan, 2008; Deerinck, 2006; Griffiths, 1993; Morphew, 2007; von Schack & Fakan, 1993).

1.2.1.2 Viewing sample under TEM and contrast enhancement

The contrast in TEM is formed by the scattering of electrons on atoms of the sample. The amount of scattering on a given atom is proportional to its atomic number Z. The higher the atomic number, the more electrons are scaterred and the higher contrast is generated (Alberts *et al*, 2008). As both biological sample and embedding media are mostly composed of atoms with low Z (carbon, oxygen hydrogen, and nitrogen), the contrast formed by a thin section is very low. Thus, prior to viewing the sample under TEM (however after on-section

immunogold labeling), it is usually stained with exogenous electron-dense substances to increase the contrast of certain cellular structures. Most of the stains employed are the salts of the metals with high Z (Deerinck, 2006; Ellis, 2007). Aqueous solutions of uranyl acetate (Watson, 1958) and/or lead citrate (Reynolds, 1963) are the most frequently used contrasting agents (Figure 1-05) (Yamaguchi *et al*, 2010).

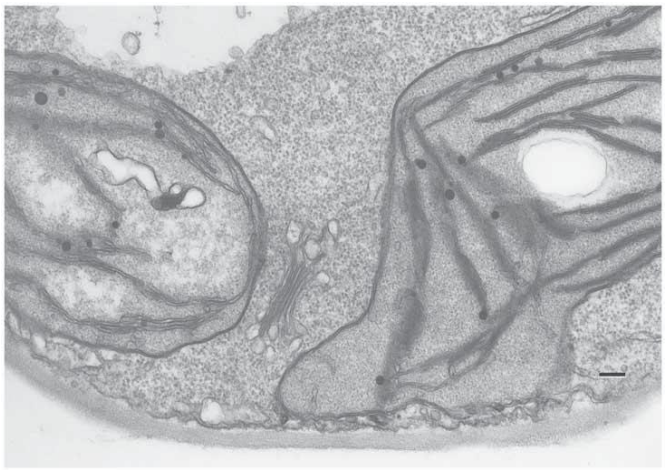

Figure 1-05: *Example of a post-staining procedure.* Section through a cotyledon of *Arabidopsis* stained for 5 s in 2% aqueous uranyl acetate in the microwave at 250 watts followed by 1 min in lead citrate on the bench. The grid was examined and photographed at 100 kV accelerating voltage. Bar = 200 nm. Figure adapted from Ellis (2007).

Uranyl ions react strongly with phosphate and amino groups so that the nucleic acids and certain proteins are highly stained; lead ions bind to negatively charged components such as hydroxyl, carboxyl, and sulfhydryl groups, membranes, ribosomes, and glycogen (Deerinck, 2006; Ellis, 2007).

Unfortunately, no contrasting agent currently in use stains all structures equally well (Biggiogera & Fakan, 2008).

1.2.1.3 Main drawbacks of conventional TEM procedures

Although chemical fixation is the most widely employed type of fixation, there are several significant disadvantages of this procedure. Not all chemical fixatives (aldehydes or other) react equally well with all cellular components. For example, nucleic acids are most effectively stabilized with FA (Deerinck, 2006). However, in the case of GA, there is no

convincing evidence for apparent reaction with nucleic acid molecules. Any stabilization of these components is probably due to the cross-linking of proteins (histoproteins) that are firmly bound to them (Bozzola, 2007; Deerinck, 2006; Griffiths, 1993). Both GA and FA can react with, and in principle cross-link, primary amino groups of amino lipids, such as phosphatidyl ethanolamine and phosphatidyl serine, to each other or to amino groups in proteins (Bozzola, 2007; Deerinck, 2006; Glauert, 1974; Griffiths, 1993). Other phospholipids, however, should not be cross-linked and as such may be lost or re-arranged during further preparation. An example is the considerable loss of phospholipids, when tissues are left in FA for a long time. Likewise, membrane lipids, which interact poorly with GA, remain mobile long after other cellular components have been stabilized (Glauert, 1974). To solve this problem, a secondary fixation with a metallic oxide fixative such as osmium tetroxide can be applied. Osmium tetroxide is a heavy-metal compound that reacts with unsaturated fatty acids and is the best fixative to preserve the structure of membranes (Bozzola, 2007; Riemersma, 1968). However, osmium penetrates tissues extremely slowly, and extracts proteins and RNA (ribonucleic acid). It is able to destroy enzymatic activity and antigenicity; therefore the osmium-fixed samples are generally not suitable for IEM (Bozzola, 2007; Deerinck, 2006; Riemersma, 1968). Next, the use of GA may even favor membrane interactions, such as fission or fusion, which would not occur otherwise. A typical example after GA fixation is a mesosome formation in bacteria, membrane blisters (nuclear equivalent in bacteria), proteolysis, etc. (Ebersold *et al*, 1981). The action of osmium tetroxide on bacteria cells can have a similar effect (Dubochet *et al*, 1983; Hobot *et al*, 1985).

Other limitation of aldehyde-based fixation is that the completion of FA/GA fixation reaction can take several seconds to minutes depending upon the nature of proteins and the proximity of organelles involved (Glauert, 1974; Griffiths, 1993; Hayat, 1989). GA could relatively fast establish irreversible and extensive 3D network of cross-links throughout the cytoplasm, but its rate of penetration into the soft tissues at room temperature was shown to be slow: 1.5 mm/24 hours (Griffiths, 1993; Hayat, 1989). This is mainly because of its high molecular weight. On other hand, small molecular weight allows FA to penetrate cells and tissues more rapidly (Kiernan, 2000). However, its reaction with proteins, especially cross-linking and formation of methylene bridges, occurs more slowly (Glauert, 1974; Kiernan, 2000; Webster & Webster, 2007). Due to the velocity of aldehyde-based fixation these samples are not suitable for the investigation of many dynamic subcellular processes (Deerinck, 2006; Griffiths, 1993; Hayat, 1989).

The preservation of morphology and the retention of antigenicity are the goals that often conflict with each other (Griffiths, 1993). Although the GA-based fixation gives better structural preservation, it leads to a weaker (up till none) antibody labeling of target antigens, if GA is used in a higher concentration. Too much cross-linking of cellular components may result in antigens being embedded in a dense matrix that is impermeable to antibodies. However, there are certain 'insensitive' antigens that appear to remain unaffected even at concentrations up to 1% GA. Conversely, the so-called 'sensitive' antigens, could tolerate the FA concentrations of up to 8%. However, milder fixation (FA < 4%) often results in substantial extraction of the cytoplasm. It is very possible that antigens of interest are part of the extracted material and important information is then washed away (Deerinck, 2006; Webster & Webster, 2007). It is for these reasons that each antibody–antigen reaction will have its own unique fixation conditions that have to be determined empirically (Griffiths, 1993; Webster & Webster, 2007).

Beside fixation, dehydration may also result in swelling or shrinkage artifacts that would distort the fine structure. Many molecules, including lipids, primarily at higher concentrations of solvent, and also of proteins, primarily at lower concentrations of solvent would be extracted (Glauert, 1974). As reported, as much as 95% of lipids (Glauert, 1974; Korn & Weisman, 1966) and about 4% of proteins may be lost from the sample (Glauert, 1974). This is accompanied by a significant loss of sample volume, rearrangement of the native subcellular environment and distortions of the cell structure.

Altogether, fixation conditions, dehydration procedures, even the resin properties (Subchapter 1.2.1) and the high resin polymerization temperature have cumulative denaturing effects on the epitopes.

1.2.2 PROGRESSIVE LOWERING OF TEMPERATURE EMBEDDING

The method of progressive lowering of temperature embedding (PLT) is an alternative to conventional dehydration and embedding process of aldehyde-fixed samples as described above (Subchapter 1.2.1). The procedure was originally developed by Fernandez-Moran in the 1950s, and with the development of methacrylate/acrylate based low-temperature embedding resins it was reintroduced by Carlemalm group in the 1980s (Carlemalm *et al*, 1982; Carlemalm *et al*, 1985).

In the PLT method, a chemically-fixed sample is dehydrated with increasing organic solvent concentration in combination with decreasing temperature (Cavalier, 2008; Gounon,

1999). As reported, dehydration performed at low temperatures causes less conformational changes to the tertiary structure of protein molecules, reduces the extraction of lipids and significantly minimizes structural alterations that occur when the process is carried out at room temperature (Gounon, 1999). The sample is then infiltrated with the acrylic resin (usually lowicryls) at low temperatures. Lowicryl embedding can be performed between -70 °C (203 K; Kelvin = °C + 273.15) to -30 °C [243 K] depending on the type of resin (e.g., Lowicryl K4M, Lowicryl HM20); and their polymerization is initiated by UV (ultraviolet) light (Carlemalm *et al*, 1985; Cavalier, 2008; Gounon, 1999) instead of high temperature. The advantages of these resins are multiple: lowicryls are the only low-temperature embedding resins (below -30 °C [243.15 K]); they have a low viscosity, therefore they infiltrate rapidly into samples; they are fluid at low temperatures, some of them are miscible (at least partly) with water; they are hydrophilic when polymerized so that they have no non-specific affinity for immunoreagents; they have good stability under the electron beam and enable optimal ultrastructural preservation (Carlemalm *et al*, 1985; Cavalier, 2008). Unfortunately they are also strong alergenes, which imposes strict precautions during their use.

The method described above has been shown to improve ultrastructural and immunocytochemical preservation in a wide variety of samples of both mammalian and plant origin (Armbruster *et al*, 1983; Gounon, 1999; Hobot *et al*, 1984; Robertson *et al*, 1992).

1.2.3 CRYO-SECTIONING ACCORDING TO TOKUYASU

Alternative choice of sample preparation for TEM is the Tokuyasu method of cryo-sectioning (Tokuyasu, 1973). The method usually involves a mild fixation with a low concentration of aldehydes, and impregnation of the sample with a high-molar (2.3 *M*) sucrose solution. Sucrose infiltration is one of the most critical steps of the Tokuyasu method because the cryo-protective properties of the sugar allow the freezing of biological material without crystal formation (Subchapter 1.2.4) that damage morphology. Sample is then made solid by freezing in an ordinary cryogen (liquid nitrogen) and sectioned at low temperatures (usually between -80 °C [193 K] to -140 °C [133 K]), without using resin for embedding. Sections are then collected from the knife surface, transferred to room temperature (thawed), and placed on a Formvar/carbon coated EM grid (Liou *et al*, 1996). Thawed cryo-sections can be labeled with specific antibodies and colloidal gold probes and stained with a contrasting agent. The grid is then embedded in a thin film of methylcellulose usually containing uranyl

acetate. After drying, the sections are ready for TEM analysis (Humbel & Stierhof, 2008; Webster & Webster, 2007).

The morphology of samples prepared by Tokuyasu method is strikingly different to that of resin-embedded samples (see Figure 1-06). The contrast of cryo-sections is low and often reversed with membranes appearing light (electron transparent) against a darker (electron dense) background of cytoplasm (Griffith *et al*, 2011; Webster & Webster, 2007).

Advantages of the Tokuyasu cryo-sections are probably related to the absence of harsh organic solvents, which are routinely used for dehydration and resin embedding, so that the molecules remain in their natural aqueous environment until immunolabeling. As reported, 20% to 30% water remains in the sample (Humbel & Stierhof, 2008). This amplifies the result of better preservation of ultrastructure compared to that achieved by other sample preparation methods (see previous subchapters). Thawed cryo-sections have, moreover, a rough surface topology exposing more antigens than their resin counterparts. Partial penetration of antibodies and ultra-small gold markers into the section of weakly fixed material is also possible (Humbel & Stierhof, 2008).

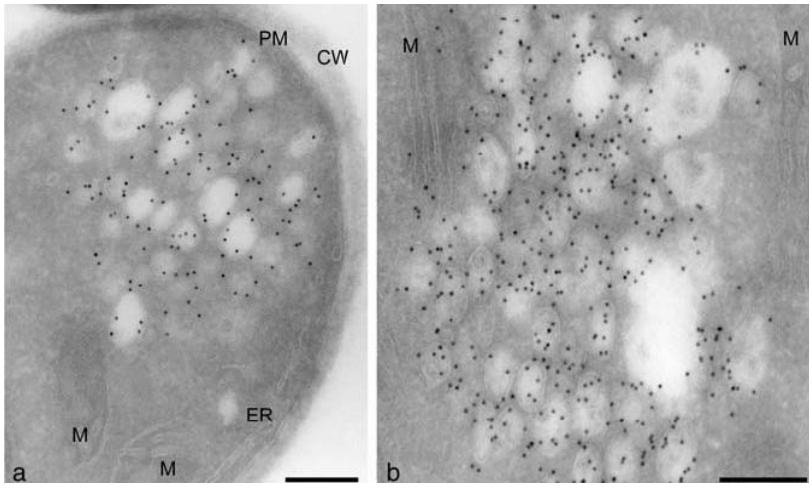

Figure 1-06: *Immunogold labeling of cryo-sections of filamentous funghi.* Figure shows immunolabeling of *Aspergillus nidulans* cryo-sections. (a,b) Compartments are specifically labeled by the antibody, e.g. clusters of endosomes and multivesicular bodies are shown. CW, cell wall; ER, endoplasmic reticulum; M, mitochondrion; PM, plasma membrane. Bar = 200 nm. Figure adapted from Griffith *et al* (2011).

The Tokuyasu method, therefore, has become one of the most sensitive preparation methods for high resolution detection of antigens at the subcellular level (Peters & Pierson,

2008; Slot & Geuze, 2007; Webster & Webster, 2007). This method has been successfully adapted for numerous biological objects including fungi (Bleck *et al*, 2010; Griffith *et al*, 2011), yeast (Griffith *et al*, 2008), etc., though the cryo-sectioning of these samples is more difficult due to the presence of extracellular cell walls. Therefore, a common feature is for example detachment of the cell wall and/or its flipping over the sections of yeast cells (Griffith *et al*, 2008). Likewise, problems such as low-quality sections, high background labeling, dirty grids and weak contrast are commonly encountered (Humbel & Stierhof, 2008; Liou *et al*, 1996; Peters & Pierson, 2008; Slot & Geuze, 2007; Webster & Webster, 2007).

1.2.4 CRYO-FIXATION

Biological samples consist of about 80% water or more, and it is essential for most living processes that this water remains in a liquid state (Griffiths, 1993). Ideally, the electron microscopists would like to observe these samples in TEM under conditions resembling a living state as closely as possible, i.e., when they are fully hydrated. One of the possible solutions is to use cryo-fixation instead of chemical fixation (Dubochet, 2007). Nowadays, it is well accepted that cryo-fixation is the best available method for optimal preservation of the cell ultrastructure without introducing significant structural alterations. However, appropriate freezing of living material is difficult. Low cooling rates (e.g., in a freezer) have disastrous effects on the cellular ultrastructure and integrity due to the ice crystal formation (Dubochet, 2007). To be successful, the process of freezing has to be ultra-rapid (fixation time in a range of few miliseconds) in order to prevent the ice crystals formation, which damages cellular material and can hinder TEM imaging of fine ultrastructural details (Studer *et al*, 2001; Vanhecke *et al*, 2008). Knowledge of water behavior at low temperatures and conditions of freezing are fundamental requirements to a proper understanding of cryo-fixation. However, the process of freezing water in a biological system is in fact a complex series of events, and only a general outline of the principles of processes involved will be given below. For deeper understanding see, e.g., Dubochet (2007). A variety of methods of cryo-fixation will be described in the subchapters following the theory of freezing.

1.2.4.1 Theory of freezing

Freezing (crystallization) is the process of the conversion of water from a liquid to a solid state by cooling (Crucifix, 2008; Dubochet, 2008; Robards & Sleyter, 1985; Vanhecke

et al, 2008). The process of freezing involves two major events: the ice crystal nucleation, and the rapid growth of ice crystals. The nucleation is the step where the water molecules begin to gather into clusters (nuclei; nucleation centers) on the nanometer scale to form a crystal. These clusters need to reach a critical size in order to become stable nuclei (Crystallization, 2011; Dubochet, 2007), otherwise they re-dissolve. Such critical size is dictated by the operating conditions, i.e., temperature, supersaturation, etc. The crystal growth is the subsequent growth of the nuclei that succeeded to reach the sufficient cluster size (Robards & Sleyter, 1985). When liquid water has to go through the nucleation process without help from another structure (i.e., the only molecule found in the crystal nucleus is water), the first stage of freezing is referred to as homogeneous nucleation. If other molecules (nucleators) are present in solution, the process is called heterogenous nucleation (Dubochet, 2007; Robards & Sleyter, 1985).

Under normal conditions (1 atmosphere), water freezes at 0 °C [273.15 K]. This temperature is referred to as the freezing point of water and the melting point of ice (Figure 1-07).

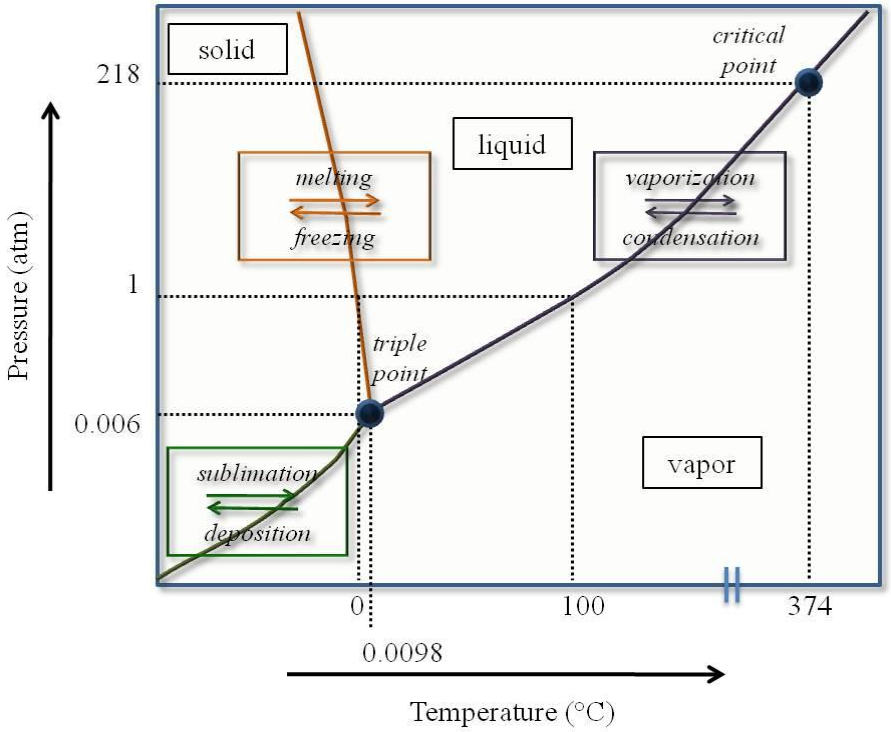

Figure 1-07: *A phase diagram showing the pressures and temperatures at which the different states of water exist*. At 1 atmosphere of pressure, water freezes at 0 °C ([273.15 K], the melting/freezing point), changing from a liquid to a solid. Water boils i.e. changes from liquid

to vapor state at 100 °C [373.15 K]. At lower pressure a direct transition from solid to gas occurs. This process is called sublimation.

As long as solid and liquid coexist, the equilibrium temperature of the system remains constant and equal to the melting/freezing point. When the equilibrium is disrupted, the freezing of water can be superior to melting of ice. Conversely, the melting of ice can be superior to freezing of water (Freezing, 2011). The continuation of crystal growth can only takes place below 0 °C [273.15 K]. This is because each molecule 'falling' on the crystal brings it share of energy – enough to warm the crystal molecule by 80 °C [353.15 K]. Heat energy is used to break the hydrogen bonds that hold the molecules in the crystal together. Below 0 °C [273.15 K], the heat generation is compensated by external cooling, stable nuclei are forming and the crystal growth continues (Dubochet, 2007; Robards & Sleyter, 1985).

1.2.4.1.1 Freezing of pure water

When pure water is cooled under normal pressure, one of three different physical state of solid water may be obtained depending on the rate of cooling (Figure 1-08). When the cooling rate is relatively slow, hexagonal ice crystals form. This is the ice of glaciers, frozen ponds and snow (Griffiths, 1993). Hexagonal crystals are relatively large and they usually appear in the form of grains with regular polygonal contours, which can be as small as 20 - 30 nm if they originate from the condensation of atmospheric water vapor on a cold sample. When small volumes of water (in the form of minute droplets or suspended films) are cooled more rapidly, an intermediate form of ice known as cubic ice may form. Cubic ice appears as a mosaic of small crystals with dimensions of approximately 0.1 mm. Both hexagonal and cubic ice crystals give characteristic X-ray and electron-diffraction patterns (Griffiths, 1993). When small volumes of water are cooled very rapidly (cooling rates $\geq 10^5$ °C/s), the liquid-like 'vitreous' or 'amorphous' state may be obtained. This is defined as solid water that is devoid of crystalline structure, and has an extremely high viscosity. It may help to think of the water molecules being arrested in positions that they occupied in the liquid at the moment of cooling (Dubochet *et al*, 1988; Dubochet & Sartori Blanc, 2001; Griffiths, 1993).

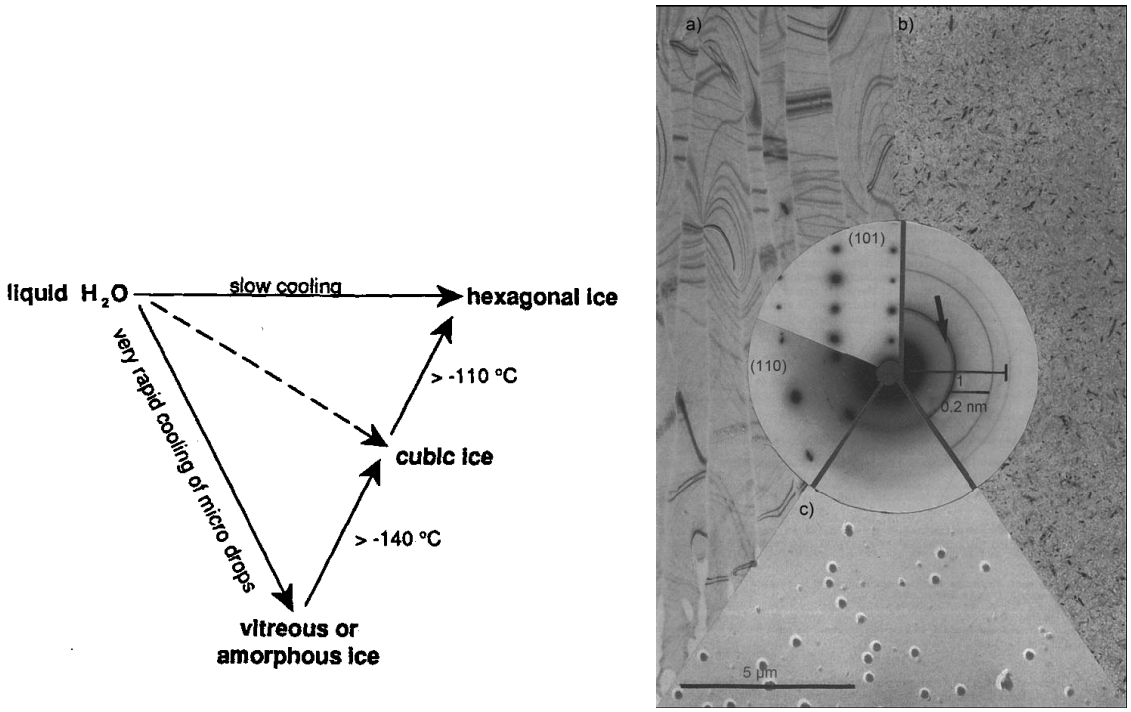

Figure 1-08: *Three different physical forms of cooled water.* On the left, the theoretical diagram illustrates the relationship between liquid water and three forms of ice found at normal pressure. Dashed line indicates the possibility to freeze directly to the cubic ice form at intermediate rates of cooling. On the right side, the cryo-EM images and the diffractograms of a) hexagonal ice, b) cubic ice, and c) a vitreous ice and polystyrene spheres. Figure on the left adapted from Griffiths (1993), figure on the right from Dubochet *et al* (1982).

As indicated, upon slow cooling of pure water at an ambient pressure, ice crystals can form from 0 °C [273.15 K]. However, the effect of so-called supercooling can postpone the process of freezing to -42 °C [231.15 K]. This temperature is reffered to as homogeneous nucleation temperature, when pure water becomes solid (the freezing/melting point of water is thus lowered). The ice crystals will thus form below -42 °C [231.15 K]; and the ice crystallization process will be halted at temperatures below -137 °C [136.15 K]. This temperature is reffered to as the recrystallization temperature. Under high pressure (~2,000 atmospheres), the melting point and the homogeneous nucleation temperature will be further lowered; and supercooling will take place down to temperatures as low as -92 °C [181.15 K] (Freezing, 2011; Vanhecke *et al*, 2008).

1.2.4.1.2 Freezing of solutes

When a solution is frozen (that is a mixture of water and solutes) at low rates of cooling, either hexagonal or cubic ice crystals are formed. In this process, following the initial nucleation step, ordered microcrystal structures grow by the addition of water molecules from the relatively disordered liquid state. The molecules of solute are thus excluded from these crystals. As freezing continues, the concentration of solutes in the liquid phase increases until the residual mixture becomes solid without crystallization (the latter may be referred to as the eutectoid between ice crystals) (Griffiths, 1993). The process of freezing in the presence of solute is shown in Figure 1-09.

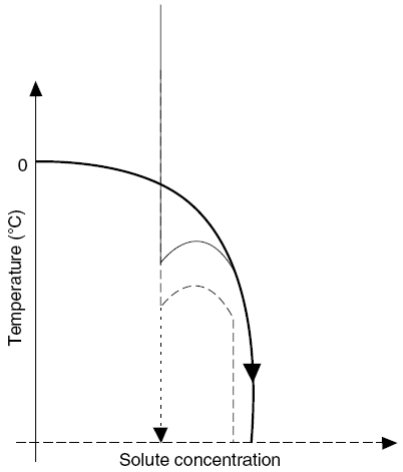

Figure 1-09: *Ice formation in the presence of solute.* The equilibrium temperature of water-ice, which is 0 °C [273.15 K] for a dilute solution, decreases with the concentration of solute until there is no water left free for the crystallization. On freezing, nothing happens to a solution of defined solute concentration until a nucleation event initiates the process of crystallization (black vertical line). From this instant, the heat generated by ice formation opposes further cooling, while the concentration of residual solutes increases. The process ends when the ice crystal leaves only an un-freezable, concentrated solution. The dashed line represents the case of ice crystal formation under higher rates of cooling. The dotted line represents the case when the rate of cooling is so high that vitreous state is obtained. In this case, the concentration of the solution remains constant at each point. Figure adapted from Dubochet (2007).

1.2.4.1.3 Freezing of a biological material

Freezing of water in a biological system is much more complicated. The first obstacle is the presence of semi-permeable membranes inside cells that enclose different intracellular compartments (endoplasmatic reticulum, Golgi complex, mitochondria, peroxisomes, lysosomes, endosomes, etc.), in addition to the multitude of carrier vesicles. It is possible that water and ions may be heterogeneously distributed among these different compartments: certainly their protein and to some extent, their lipid composition is different. The second complication comes from the fact that a significant proportion of cellular water is associated with molecular surfaces in the so-called hydration shell ('bound water'). This water is considered to behave differently from the rest of water upon freezing, because it is not available for the ice crystal growth (Griffiths, 1993). The third complication is the presence of a variety of solutes, i.e., ions, soluble molecules and macromolecules, which are only rarely trapped in the crystal lattice (Dubochet, 2007; Hayat, 1989). Figure 1-10 illustrates the process. The growing ice crystal absorbs available water it comes into contact with. Around the ice surface the cytoplasm material become dehydrated and highly concentrated.

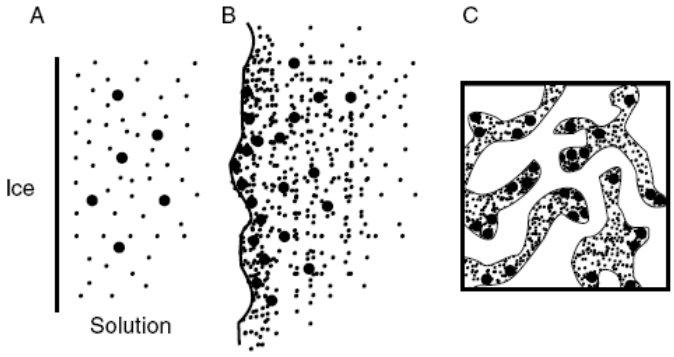

Figure 1-10: *Ice crystal growth in the concentrated medium of a cell.* (A) In the initial state, a hypothetical flat ice crystal is adjacent to an aqueous solution that contains various solutes and macromolecules. (B) Depending on their size and diffusion properties, solutes are concentrated at the surface of the progressing ice crystal. (C) In the final state, the ice crystal extends over the whole volume of the solution leaving concentrated, dehydrated solutes between its tortuous ramifications. Figure adapted from Dubochet (2007).

Apart of the nature of the cell (its composition), the process of freezing is highly dependent on the rate of cooling applied. Generally, when the cells and tissues (uncryo-

protected samples) are frozen slowly (cooling rate < 1 ºC/s), the hexagonal ice crystal first appears in the extracellular matrix, and concentrates salt in the remaining liquid (Dubochet, 2007; Dubochet *et al*, 1988; Griffiths, 1993). The resulting increase in osmolarity draws water from cells, causing a shrinkage and intracellular structures are damaged due to high salt content (Dubochet, 2007; Dubochet *et al*, 1988; Griffiths, 1993). At intermediate cooling rates of 1 ºC/s – 1,000 ºC/s, hexagonal ice crystal forms extracellularly, and before water has time to diffuse out, the nucleation of ice crystal starts intracellularly. This gives rise to the formation of a large hexagonal ice crystal in the cytoplasm, which destroys the cell membranes and cell interior (Dubochet *et al*, 1988; Griffiths, 1993). It should be noted that in most cases there is only one crystal per cell; sometimes there are few, never very many (Dubochet, 2007). At cooling rate exceeding 1,000 ºC/s, cubic ice crystals may be formed. Cells survive, but such preparations are not suitable for ultrastructural TEM studies. Ice forming in the cytoplasm induces the phase segregation between water and solutes with the effect that cellular components are concentrated and precipitated between ice crystal ramifications. In TEM micrographs, the so-called segregation pattern becomes visible (Dubochet, 2007; Studer *et al*, 2008). Rapid freezing (cooling rate >> 10,000 ºC/s) suffices to cool the sample so rapidly that water molecules are practically immobilized in a vitreous state, both intracellularly and extracellularly, before they have time to nucleate an ice crystal (Crucifix, 2008; Dubochet, 2008). As the ice crystals formation is prevented, they do not interfere with TEM ultrastructural analysis. The structure of vitrified biological samples could be preserved down to the atomic scale.

1.2.4.1.4 Vitrification

It is obvious that successful cryo-fixation should always result in vitrification, and this state should always be the goal of electron microscopists for the optimal preservation of biological samples (Dubochet, 2007). It is unlikely that a significant redistribution of ions, molecules and macromolecular assemblies could occur and therefore they are supposed to be arrested in their *in vivo* hydrated states (Dubochet *et al*, 1988). Water becomes solid while remaining in a liquid-like vitreous state ('vitrification' from Latin vitreum – glass; (Vitrification, 2011)), which can be preserved indefinitely, provided the temperature is kept below the recrystalization temperature (Dubochet, 2007), which is about -137 °C [136.15 K] for pure water (Vanhecke *et al*, 2008).

In practice, however, vitrification of living cells and tissues is extremely difficult to achieve because of high rates of cooling required (see Subchapter 1.2.4.1.3) (Dubochet *et al*, 1988). A thickness of about 100 - 200 nm of water suspension may be easily converted into a vitreous state (depending also on the exact composition of the aqueous solution and the pressure applied), which is largely sufficient for high-resolution imaging of isolated particles that should not exceed 100 nm in size (Crucifix, 2008; Dubochet, 2007; Dubochet, 2008). However, eukaryotic cells and tissue samples are much larger, and vitrification in at least the 100 μm scale is needed. The limiting factor is also the heat (thermal) diffusivity of water, i.e. the thermal conductivity divided by density and thermal capacity (Dubochet, 2008; Studer *et al*, 1995). Bad thermal diffusivity of water prevents efficient heat extraction over a large distance. Even at an extremely high rates of cooling (> 500,000 K/s, at atmospheric pressure), the rate of cooling drops below 1,000 K/s within 150 μm from the surface of a 600 μm thick aqueous sample (Studer *et al*, 1995). Two other parameters depress the freezing point of water (-42 °C; [231.15 K]) by several degrees, thereby favoring successful vitrification: an addition of a cryo-protectant and/or a high pressure (Moor, 1987). Combining these two approaches, samples 100 to 300 μm thick can be vitrified (Dubochet, 2007; McDonald, 1999; Moor, 1987).

1.2.4.1.5 Freezing with cryo-protectants

One of the way to achieve successful vitrification is to use a small amount of anti-freeze agents, the cryo-protectants (Echlin *et al*, 1977; Franks *et al*, 1977; Griffiths, 1993; Yakovlev & Downing, 2011). Directly, they alter the properties of water in such a way that they reduce the ability of its molecules to nucleate ice crystals (Griffiths, 1993; Hayat, 1989). Indirectly, they are able to reduce the amount of heat released by the crystallization process, and thus increase the overall rate of cooling (Dahl & Staehelin, 1989). However, it should be noted that cryo-protectants might introduce artifacts of their own, either by segregation from the aqueous solution during freezing or by their toxic effects on the biological system.

1.2.4.1.5.1 Classification of cryo-protectants

Depending on the interaction of cryo-protectants with cells, they are classified as either extracellular (non-penetrating) or intracellular (penetrating) compounds (Moor, 1987; Morphew, n.d.). Their overview is given in Table 1.

1.2.4.1.5.1.1 Extracellular cryo-protectants (Non-penetrating)

These compounds do not pass through membranes of living cells and they do not mix with water. Non-penetrating cryo-protectants are partly effective because ice forms much more readily outside of cells than inside cells due to the fact that nucleating agents are much more prevalent outside of the cells than inside (Griffiths, 1993; Yakovlev & Downing, 2011). They are characterized by low osmotic activity, and they work by binding up water outside the cell inducing cell dehydration. The group comprises many of well-known cryo-protectans (see Table 1) such as polyvinylpyrrolidone, 1-hexadecene, dextran, and various high molecular weight compounds (Griffiths, 1993; Studer *et al*, 1989; Yakovlev & Downing, 2011).

Extracellular cryo-protectants (non-penetrating)	***Intracellular cryo-protectants (penetrating; in some tissues)***
1-Hexadecene	Glycerol (5 - 15%)
Yeast paste / *Escherichia coli* paste	Methanol (8 - 10%)
Cold water fish gelatin (50 - 100%)	Ethanol
Polyvinylpyrrolidone (15%)	Dimethyl sulfoxide (DMSO)
Serum albumin (10 - 20%)	Ethylene glycol
Ficol (5 - 15%, MW 70,000)	Propylene glycol
Low-melt agarose (0.5 – 2.0 %)	Sucrose (150 *mM*)
Dextran (15 - 25%, MW 39,000)	Other sugars (mannitol, sorbitol)

Table 1: *List of conventional cryo-protectants, which should be used to accomplished successful cryo-fixation*. The concentrations of individual compounds usually depend on the sample under study. Table adapted with modifications from Hayat (1989) and Morphew (n.d.).

1.2.4.1.5.1.2 Intracellular cryo-protectants (Penetrating)

These compounds are less desirable as they have a potential to affect the physiology of cells by causing osmotic and other changes, as they could penetrate cell membranes and

reduce the water content of cells (Hayat, 1989; Schwarz & Humbel, 1993). The most commonly used low molecular weight penetrating cryo-protectants are glycerol and dimethylsulfoxide (DMSO). DMSO passes through cell membranes more readily than glycerol, and it may be more toxic at higher temperatures (Best, n.d.). Glycerol penetrates cells very slowly at 0 °C [273.15 K] but rapidly at 20 °C [293.15 K], therefore it can be considered to be either penetrating or non-penetrating compound. It penetrates animal tissues, but generally does not penetrate plant tissues; however DMSO does (Hayat, 1989). Both could introduce significant alterations to the cell ultrastructure. As reported, DMSO induces a large increase in the volume of the mitotic apparatus in living marine eggs (Rebhun & Sawada, 1969). Glycerol causes, e.g., the re-arrangement of microtubules, reduction in the number of microvilli, blebbing and vesiculation of internal membranes (Hayat, 1989; Indi *et al*, 1986). Further penetrating cryo-protectants such as methyl and ethyl alcohols, ethylene glycol (automobile anti-freezer) and propylene glycol (formerly used to reduce ice formation in ice cream) were shown to be effective cryo-protectants (Best, n.d.).

Since most of the cells survive freezing and thawing after proper cryo-protectant treatment, this widely used method allows keeping single cell suspensions, small organisms, tissue pieces, even embryo viable for storage (Dubochet, 2007; Studer *et al*, 2008). However, as mentioned above, all cryo-protectants are at least to some extent toxic to cells due to their dehydrating activity, and thereby introducing various alterations in cellular structure, such as severe shrinking and specific responses to osmotic stress (Studer *et al*, 2008). Although these types of changes are not lethal and are reversible, the ultrastructure of such cryo-protected samples is changed. Generally, non-penetrating cryo-protectants are much less toxic than the penetrating ones. Interestingly, certain cells that contain relatively small amount of water and have high surface-to-volume ratio can be frozen with minimal damage by ice crystals in the absence of cryo-protection (Hayat, 1989). Other cells can actually produce chemicals that act as natural cryo-protectants, and thus in some situations, to allow them to function normally at sub-zero temperatures (Dubochet, 2008). There are, for example, high levels of sugars and sugar alcohols in many polar plants, insects, fungi, etc., which act as non-toxic natural cryo-protectants in response to low temperature (Conlon *et al*, 1998; Dubochet, 2007; Dubochet, 2008).

1.2.4.1.6 Freezing with liquid cryogens

The only way to preserve the fine ultrastructure of the sample close to the living state is to freeze it in such a way that its intrinsic water turns into vitreous ice even in the absence of cryo-protectants. This is achieved by very high rates of cooling as mentioned previously (Dubochet, 2007; Studer *et al*, 2008). For the given sample, the rate of cooling is determined by the method applied (see Subchapter 1.2.4.2 and 1.2.4.3), and the type of used cryogen (Frederik *et al*, 2008). An effective liquid cryogen must have special characteristics, such as: high thermal conductivity and heat capacity, low melting point at atmospheric pressure, high specific heat, and a significant difference between the freezing and boiling points (Hayat, 1989).

Liquid cryogen	***Melting point***	***Boiling point***
Nitrogen	-210 °C [63.15 K]	-195.8 °C [77.36 K]
Ethane	-181.76 °C [91.39 K]	-88.6 °C [184.55 K]
Propane	-187.7 °C [85.45 K]	-42.1 °C [231.15 K]
Helium	-272.20 °C [0.95 K] (at 2.5 MPa)	-268.93 °C [4.22 K]
Isopentane	-159.9 °C [113.25 K]	27.7 °C [300.9 K]
Argon	-189.35 °C [83.80 K]	-185.85 °C [87.30 K]
Hydrogen	-259.14 °C [14.01 K]	-252.87 °C [20.28 K]
Oxygen	-218.79 °C [54.36 K]	-182.95 °C [90.20 K]
Methane	-182.5 °C [90.7 K]	-161.6 °C [111.6 K]

Table 2: *List of selected liquid cryogens with corresponding values of melting and boiling points at atmospheric pressure*. The table was created based on data obtained from Wikipedia (2004).

Liquid nitrogen is generally not recommended for routine vitrification. Due to the small difference between melting/boiling points (see Table 2), the gas formation around the sample rapidly occurs when it is plunged into liquid nitrogen (the so called Leidenfrost phenomenon). This significantly slows the freezing and leads to the formation of ice crystals. Nitrogen slush provides faster cooling than liquid nitrogen does at its boiling point. For the

same reasons, the liquid helium is also not recommended. Liquid propane and ethane cooled by liquid nitrogen are very good cryogens for general use. They both have low melting points, high boiling points (see Table 2), and good thermal conductivity and specific heat. When propane is supercooled at -194 °C [79.15 K], it cools very fast. However, ethane when supercooled cools even faster and gives the best measured rates of cooling – of about 10,000 ºC/s (Crucifix, 2008; Dubochet, 2008; Hayat, 1989).

Thermal properties of metals are also very important for successful cryo-fixation. They differ with temperature. For example, the transfer of heat by copper (and other metals) improves significantly when the temperature is lowered. At -254 °C [19.15 K], both copper and silver are superconductors of heat (Hayat, 1989). For more details, see Hayat (1989).

1.2.4.2 Rapid freezing methods

Nowadays, there are several rapid freezing methods operating at atmospheric conditions that can adequately cryo-immobilize biological samples up to a thickness of about 5 to 20 μm without detectable ice-crystal formation (Hayat, 1989; Pierson *et al*, 2009) without any cryo-protection. These are: plunge freezing, cold metal block freezing (slam freezing), jet freezing, and spray freezing. With any of these methods, the actual depth of appropriate vitrification vary with the nature, size and composition of particular cell type, depth of region of interest in the sample, the initial temperature of the sample, the presence (or absence) of high concentration of salts and natural organic cryo-protectants in the cytoplasm, the type of cryogen used and the rate of sample entry into the cryogen (Dubochet, 2008; Hayat, 1989).

1.2.4.2.1 Plunge freezing

The principle of plunge freezing is simple: to quickly dip (plunge) the sample into a liquid cryogen (Figure 1-11). Once the sample has been vitrified, it can be stored under liquid nitrogen until used for further processing. A variety of freezing apparatuses, from simple hand-operated devices to a commercially available automated devices capable of computer-controlled vitrification, has been successfully used for plunge freezing. Cryogens such as liquid propane, a mixture of propane and isopentane, liquid nitrogen slush, ethane, and freons have been tested (Hayat, 1989). Among them, the liquid ethane slush cooled by liquid nitrogen to about –182 ºC [91.15 K] has been the most efficient cryogen. At an ambient pressure, the rate of cooling of about 10,000 ºC/s is usually obtained by plunging the sample

into ethane slush (Crucifix, 2008; Dubochet, 2008). This method is suitable for the cryo-immobilization of samples with limited thickness of about 5 to 20 μm, e.g., small structures like different macromolecular complexes (Hayles *et al*, 2010), viruses (Dubochet *et al*, 1988), isolated cellular organelles (Nicastro *et al*, 2006), and thin rims of larger cells grown directly on EM grids (Kurner *et al*, 2004; Lucic *et al*, 2008; Medalia *et al*, 2002). The method of plunge freezing is currently widely used in the so-called thin vitreous layer embedding method in electron cryo-microscopic studies. The method allows direct examination of frozen hydrated macromolecules and complexes in their near-native states (Adrian *et al*, 1984; de Carlo, 2008; Dubochet *et al*, 1988). Details of the procedure will be described in Subchapter 1.3.1.

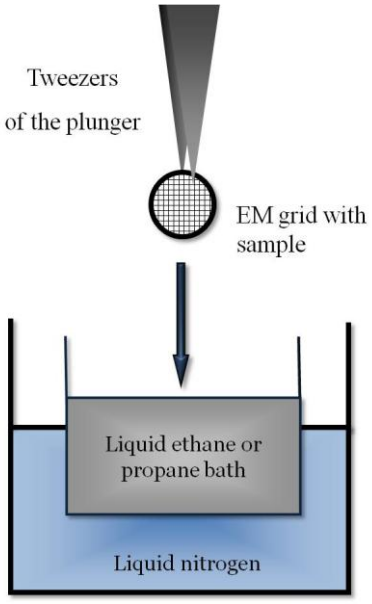

Figure 1-11: *Schematic diagram illustrating the method of plunge freezing*.

The so-called self-pressurized rapid freezing has been recently introduced as a new application of this method. It employs plunge freezing of sample in a sealed capillary tube into a cryogen (Leunissen & Yi, 2009). The success of this method depends on generating pressure inside the clamp-sealed sample capillary tube and holding that pressure for the time it takes to cryo-preserve the sample. Bacteria, yeast and nematodes have been adequately vitrified using this method. The preservation of these uncryo-protected samples was comparable to that achieved with high-presure freezing (see Subchapter 1.2.4.3) in the presence of cryo-protectants.

1.2.4.2.2 Cold metal block freezing

Cold metal block freezing (also called slam freezing) is the process of rapidly projecting (slamming) the cells or tissue slices against a polished metal surface (e.g., copper, silver or gold) or diamond block that was previously cooled with a liquid cryogen to corresponding temperature (Hayat, 1989; Spehner & Edelmann, 2008). Despite the fact that the method produces one of the fastest heat transfers, is technically simple and the apparatus is inexpensive, it is used only rarely. The main limitation is the fact that only a small portion of the sample could be properly cryo-fixed (Hayat, 1989). Though it is possible to freeze, for example, large tissue fragments of up to 2 cm in diameter, only the superficial layers 10 μm in depth (30 μm in the best case) could represent well-vitrified material (Spehner & Edelmann, 2008; Yakovlev & Downing, 2011). The basic principle of the method is shown in Figure 1-12.

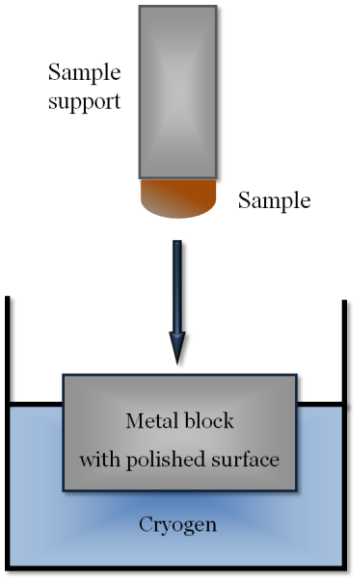

Figure 1-12: *Schematic diagram illustrating the method of cold metal block freezing.*

1.2.4.2.3 Jet freezing

In the jet freezing method (Figure 1-13), the sample is pelleted and suspended on a 200- to 400-mesh copper or gold EM grid, and placed between two metal plates to form a sandwich. A special holder adjusts the sandwich between the spraying nozzles of the apparatus. Liquid propane cooled by liquid nitrogen to about -190 °C [83.15 K] is generally

used and sprayed through the nozzles at high speed (~100 m/s) under 10 atmospheres synchronously from two sides onto the sandwiched sample. Frozen sample is then separated from the holder and transferred into liquid nitrogen (Hayat, 1989; Schwarz & Humbel, 1993).

The advantage of this method is that the high velocity propane jet provides the rate of cooling ~30,000 °C/s. The heat exchange, when a jet of liquid cryogen is shot on the surface of a bulk sample, is therefore ~ 2 - 3 times faster than that provided by plunge freezing. The rate of cooling close to the surface of the sample surface is 4 times superior for jet freezing compared with that of plunge freezing. Because heat is withdrawn simultaneously and rapidly from both sides of the sample, the depth of frozen region in the sample is greater than the one achieved with another freezing method performed at an atmospheric pressure. Theoretically, the entire volume of the sample up to 40 µm thick can be rapidly frozen with this method. However, in practical terms, propane jet freezing shows satisfactory freezing to a depth of about 15 µm (Hayat, 1989).

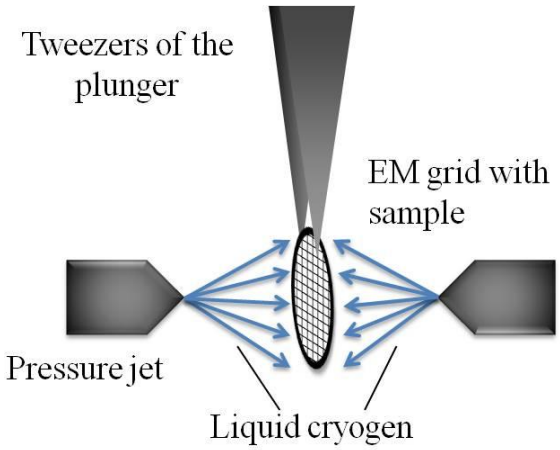

Figure 1-13: *Schematic diagram illustrating the method of jet freezing.*

1.2.4.2.4 Spray freezing

Spray freezing is based on the fact that: i) the sample splitted into very small droplets (10 – 50 µm in diameter) has the optimal (high) surface-to-volume ratio, ii) vigorous injecting of the spray droplets into a cryogen increases the heat convection, and iii) very low heat content of the sample droplets encourages higher rates of cooling (Bachmann & Schmitt, 1971; Hayat, 1989). The rate of cooling of droplets may be higher than 100,000 °C/s (Hayat, 1989).

Schematic diagram illustrating the method of spray freezing is shown in Figure 1-14. Briefly, a cryogen (liquid propane) is held in a cavity (cryo-chamber) in a copper block cooled with liquid nitrogen. The sample is filled in an air brush and sprayed in the form of fine droplets at high velocity into this cooled propane. After transfer of the block into a cryostat inside a glove box, the propane is evaporated under prevacuum conditions (0.1 to 0.01 Torr) at about -85 °C [188.15 K] (Schwarz & Humbel, 1993). Fine powder of frozen samples is then found on the bottom. Inert organic medium such as *n*-butylbenzene is added at the same temperature to make a paste with samples. Because of its low freezing point (-95 °C [178.15 K]), *n*-butylbenzene does not penetrate the frozen samples. Small aliquotes of the paste are then transferred into liquid nitrogen until further processing (Bachmann & Schmitt, 1971; Hayat, 1989).

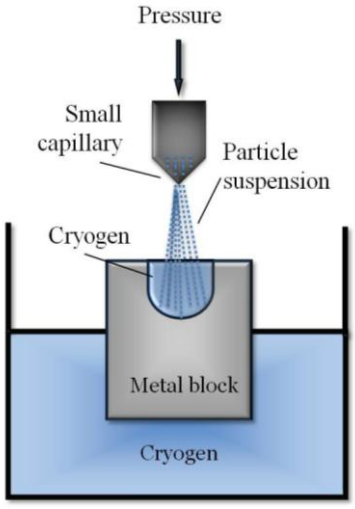

Figure 1-14: *Schematic diagram illustrating the method of spray freezing.*

The main limitation of this method is that it can be applied to very small samples (e.g., bacteria), subcellular fractions, and other particulates no larger than ~10 μm in diameter. For these samples, the quality of ultrastructural preservation is satisfactory (Hayat, 1989).

1.2.4.3 High-pressure freezing

Mammalian cells, tissues, and larger bacteria cells are too large to be vitrified *in toto* by any of the methods mentioned above. At present, high-pressure freezing (HPF) is the only practical way that allows such a bulk biological samples to be successfully vitrified (Hess,

2007; Kang, 2010; McDonald, 2007; Murray, 2008; Studer *et al*, 2001; Vanhecke *et al*, 2008). The original concept of HPF was introduced by Hans Moor and collaborators in 1968 (Moor & Riehle, 1968), and about 20 years ago, the first high-pressure (HP-) freezer - HPM 010 - was commercialized by Balzers Company. Currently, there are four commercially available HP-freezers: the Wohlwend Compact HPF01 (Wohlwend Engineering, Switzerland), the LEICA EM PACT2 and the LEICA EM PACT2 with rapid transfer system (Verkade, 2008) and the LEICA EM HPM100 (Leica Microsystems, Vienna, Austria). Except few minor differences the mechanism of these four instruments is practically identical. Detailed information can be found for example in McDonald *et al* (2007), McDonald (2009), Verkade (2008). Generally, the method of HPF is based on the principle of Le Chatelier and Braun, which postulates that if a system at thermodynamic equilibrium experiences a change in one of the physical parameters involved, then the equilibrium is shifted in order to minimize that change. In HPF this principle explaines how an externally applied pressure of between 200 - 210 MPa (MPa, megapascal; 1 atmosphere = 0.1013 MPa) prevents water from expanding into low-density ice upon cooling (Figure 1-15).

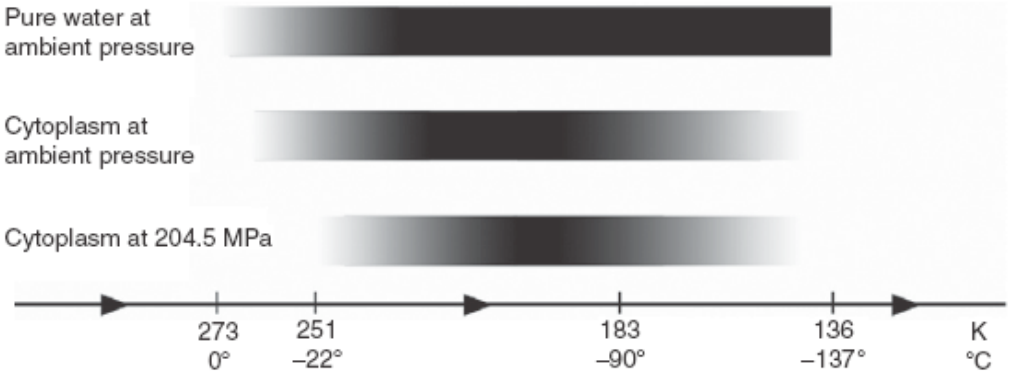

Figure 1-15: *The influence of solute concentration and pressure on the crystallization window for cryo-fixation.*Upon slow cooling of pure water, ice crystals can form from 0 °C [273.15 K], but the effect of supercooling can postpone this process up to the homogeneous nucleation temperature of -42 °C [231.15 K]. The increasing probability that ice crystals are formed at decreasing temperatures is represented by the grayscale gradient. Below -42 °C [231.15 K], ice crystals will form (*black region*). The ice crystallization process is halted at temperatures below the recrystallization temperature of -137 °C [136.15 K]. The typical solute concentration of the cell cytoplasm will lower the melting/freezing point (concentration depending) and will elevate the recrystallization temperature. Applying a pressure of 204.5

MPa will further lower the melting point and the homogeneous nucleation temperature. As a result, the temperature range suitable for ice crystal formation is decreased. The arrows indicate the direction of cooling. Figure adapted from Vanhecke *et al* (2008).

The application of this pressure at the moment of freezing (while the sample is cooled at a maximal speed to liquid nitrogen temperature) changes the freezing behavior of water enough to cryo-preserve biological samples up to a thickness of about 200 μm (from the surface of the sample) with minimal or no ice crystal formation and optimum heat transfer (Studer *et al*, 2008; Vanhecke *et al*, 2008) (Figure 1-16). This is approximately 10 times better depths of vitrification than it is possible to achieve by other freezing methods operating at an ambient pressure (see Subchapter 1.2.4.2). Moreover, the effective advantage of HPF is that the rate of cooling required for the vitrification is significantly reduced to about 5,000 K/s that is ~10times smaller than at ambient pressure (Vanhecke *et al*, 2008). Thus, the cellular water is vitrified and macromolecules remain in a close proximity to where they were located in a living cell, i.e. they are not extracted as they can be by conventional methods of sample preparation based on chemical fixation. The highest level of ultrastructural preservation is therefore achieved (McDonald *et al*, 2007; Studer *et al*, 2001; Studer *et al*, 2008).

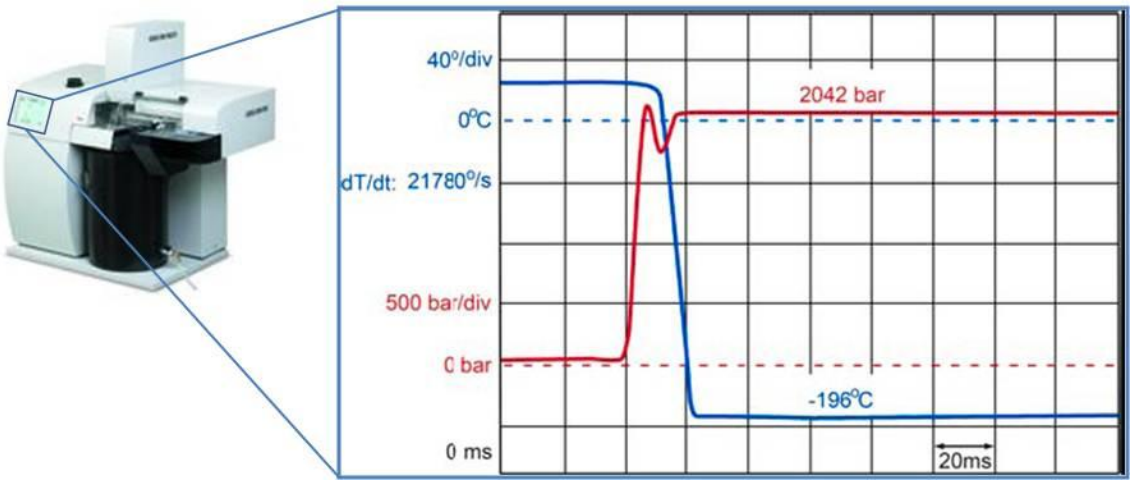

Figure 1-16: *High-pressure freezer.* Record of temperature (*blue line*) and pressure (*red line*) changes during freezing (total time = 200 ms) in the EM PACT 2 HPF machine (Leica Microsystems). The temperatures and as a result the cooling rates are measured with a thermocouple located just below the sample carriers. The pressure is measured in the pressure

system that is connected to the sample. As a consequence, the pressure measured is the one that really acts on the sample, whereas the temperature record just tells us that pressure and temperature have been synchronized correctly and that the freezing cycle was technically working. Figure adapted with modifications from Studer *et al* (2008).

Interestingly, the increase in the pressure to about 200 - 210 MPa during freezing has a similar effect as an increase in solute concentration of the sample (Figure 1-15). Practically, this means that ice crystal formation can be prevented in 100 - 200 μm thick samples with a typical biological solute concentration and distribution (Studer *et al*, 1995; Vanhecke *et al*, 2008), without additional cryo-protection. However, in many published applications HPF is combined with the use of non-penetrating cryo-protectants such as dextran, 1-hexadecene or serum albumin to further support the cryo-preservation (Dubochet, 1995; Leunissen & Yi, 2009; Pierson *et al*, 2009; Studer *et al*, 1995). As recently shown by Yakovlev & Downing (2011), the complete vitrification of the medium surrounding the cells is not essential for good structural preservation. Crystallization of the medium, for example due to low cryo-protectant content, may even improve cryo-preservation of some samples in a near native state. Vitrification of the cell interior in crystallized medium is thus possible for most bacteria and yeast that contain about 20% protein which acts as a cryo-protectant.

1.2.4.4 Follow-up procedures

After cryo-fixation (vitrification), the frozen samples are transferred into liquid nitrogen for storage and further they may be processed in many different ways, such as vitreous cryo-sectioning followed by direct observation in their native state by transmission electron cryo-microscope, or they could be freeze fractured, freeze dried or freeze substituted and resin embedded for room temperature sectioning and convenional TEM examination.

1.2.4.4.1 Cryo-sectioning of vitreous sections

As mentioned above, HPF is the only method, which enables the vitrification of larger samples, e.g., whole mammalian cells or even tissues. As these are generally too thick to be directly observed in TEM, the preparation of thin sections is necessary. The most straightforward way is to prepare ultrathin sections under cryogenic conditions (Al-Amoudi *et al*, 2004) and to observe them in their native hydrated state in the so-called transmission

electron cryo-microscope (Vanhecke *et al*, 2007). In principle, the electron cryo-microscopy of such vitreous sections (CEMOVIS; cryo-electron microscopy of vitreous sections) is free of any aggregation artifacts since the material remains fully hydrated and is free of chemical fixation and staining (Dubochet & Sartori Blanc, 2001). The procedure itself is technically quite demanding, though it has been used to examine various biological samples such as bacteria, insect flight muscle, culture cells and yeasts (see Figure 1-17) (Al-Amoudi *et al*, 2005; Vanhecke *et al*, 2007). The necessity to work during the whole procedure at temperatures below -140 °C [133.15 K] induces some difficulties, including the cryo-section transfer from the knife edge to EM grid; grid handling in the cryo-chamber and grid transfer into the cryo-holder of a microscope (Vanhecke *et al*, 2007).

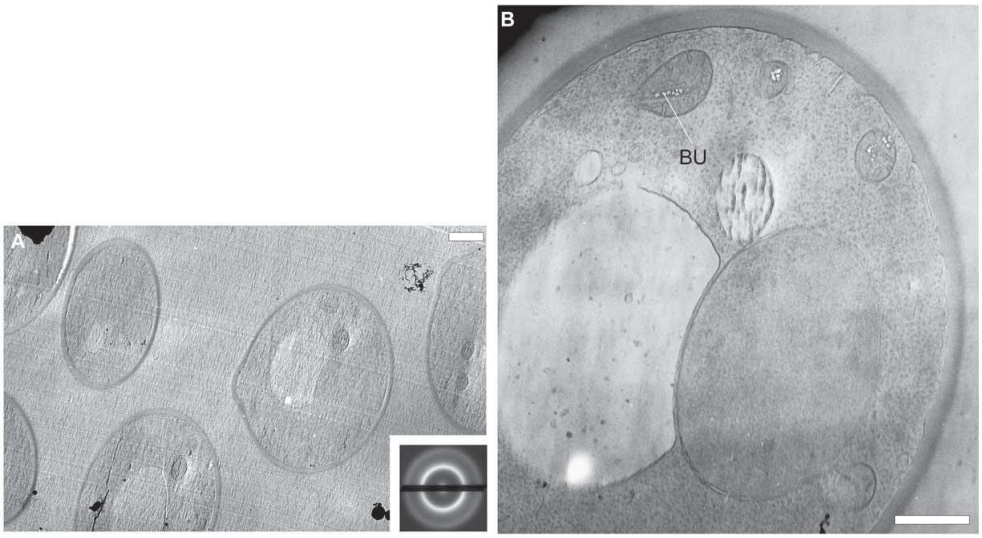

Figure 1-17: *Frozen hydrated yeast cells.* (A) An overview with a few cells is shown. (B) Magnification of one of the cells. The bubbles (BU) in the mitochondria illustrate beam damage. It is obvious that not all structures are at the same amount sensitive to beam damage; beside the mitochondria, all structures are well preserved. Note that membranes and cell organelles are well preserved. The diffraction pattern with its blurred rings (insert in A) shows that the section derived from a vitreous sample. Bars: A = 1 μm; B = 500 nm. Figure adapted from Vanhecke *et al* (2007).

Furthermore, sectioning is an extremely difficult task, and cutting artefacts are found on most vitrified sections (Al-Amoudi *et al*, 2005; Hsieh *et al*, 2006). The resulting vitrified sections suffer from severe distortions like compression (from 30% to more than 60%) in the cutting direction, crevasses and suitable limited thickness of about 100 nm (Al-Amoudi *et al*,

2005; Dubochet & Sartori Blanc, 2001; Hayles *et al*, 2010; Hsieh *et al*, 2006).Another limitation is an extreme caution that must be taken during image acquisition. Beam induced alterations in the sample are well-known to be a problem during CEMOVIS image recording. It is known that the vitreous sections 'flow' during image acquisition. It is therefore important to 'learn' how to read vitreous sections with respect to their structural integrity and preservation (Dubochet, 2007). One should note for example that in the vitreous section, observed at low or medium electron optical magnification, the whole cell and its surrounding are uniformly gray. Whereas the contrast in the micrographs of stained sections indicates the ability of the structure to bind heavy-metal stains, the density of the vitreous section images is directly and quantitatively related to the local mass thickness of the sample, namely to the actual amount of material in the observed region (Dubochet & Sartori Blanc, 2001).

Anyway, HPF and vitreous sectioning is currently the only way to visualize and investigate cells and tissues larger than 0.5 μm, directly in the absence of chemicals, heavy-metals and hypertonic cryo-protectants (Al-Amoudi *et al*, 2004; Dubochet, 2007; Peters & Pierson, 2008; Vanhecke *et al*, 2007). Now, it is even possible to reconstruct the 3D distribution of material in vitreous cryo-sections by means of computerised cryo-electron tomography (Dubochet, 2008; Lucic *et al*, 2008). Though these samples cannot be used for on-section immunogold labeling, the procedure can be combined with methods, in which markers such as gold are introduced into cells (e.g. by endocytosis) prior to the vitrification step (Bleck *et al*, 2010). Diamond knives and accessory tools used for cryo-sectioning are also considerably improving and in the near future both the quality of vitreous sections and subsequently the quality of imaging will significantly improve (Dubochet & Sartori Blanc, 2001; Pierson *et al*, 2009). For example, the focused ion beam milling - an alternative approach to cryo-sectioning, which bypasses the cutting artifacts associated with mechanical sectioning of frozen-hydrated samples - has recently been introduced by Hayles research group (Hayles *et al*, 2010).

1.2.4.4.2 Freeze fracturing

In this technique (Figure 1-18), a rapidly frozen biological sample is physically broken apart (fractured) with a cold 'knife' at -100 °C [173.15 K] or lower temperature (Steere, 1957). The fracture path generally takes the route of the lowest mechanical resistance in the hydrophobic interior of frozen membranes, splitting them into half-membrane leaflets following the contours of the nanostructures present in the fracture plane. These contours can

be further accentuated by etching through the sublimation of a thin layer of ice; features of the embedded objects then stand out more clearly. The fracture plane is generally not observed directly; rather a replica (or a cast) is made of the fractured surface by 'shadowing' it at an angle of about 45° with the heavy-metal deposition (platinum and carbon) under a vacuum. The resulting metal replica is retrieved, placed on an EM grid and viewed like a section with TEM (Severs, 2007; Severs & Robenek, 2008). Contrast results from different thicknesses of heavy-metal producing a 3D-like image corresponding to a template of the original fractured surface (Dahl & Staehelin, 1989).

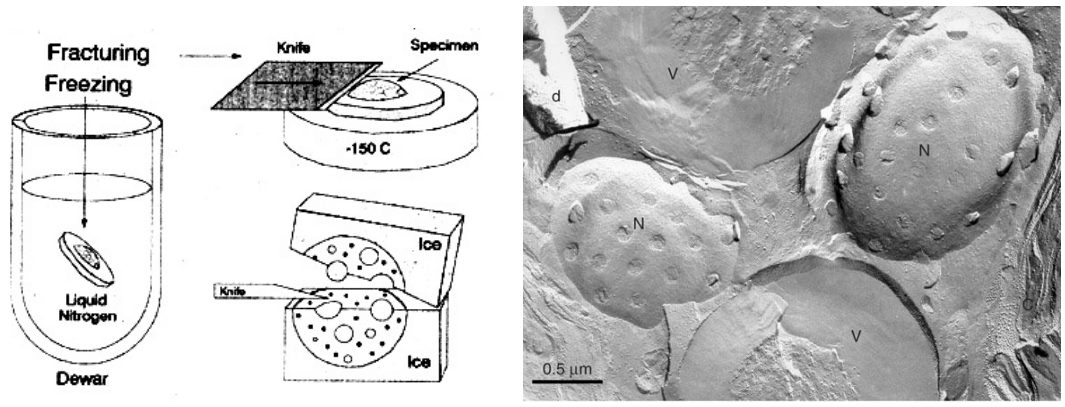

Figure 1-18: *Freeze fracturing***.** (left) Schematic diagram illustrating the basic principle of freeze fracturing procedure. (right) Freeze fracture view of the interior of a Chlorella cell. Two nuclei (N) have been convexly fractured along the outer nuclear membrane to display face views of nuclear pores. Two cross-fractured vacuoles (V) and part of a chloroplast (C) are also seen. A piece of debris (d) that has fallen onto the sample after fracture casts a long white absence of platinum shadow, providing a marker for orientation of the image. Figure on the left adapted from Freeze-fracturing and Etching (n.d.); figure on the right adapted from Severs (2007).

Freeze fracture is unique among EM techniques in providing planar views of the internal organization of membranes. In particular, the distribution and spatial organization of integral membrane proteins (seen as intramembrane particles) are visible in the membrane plane (Severs & Robenek, 2008).

1.2.4.4.3 Freeze etching

Freeze etching is a modification of the method of freeze fracturing. The frozen sample is fractured and then the fractured surface is either replicated immediately, or is etched first to remove some ice from non-membraneous regions of the fracture face. Etching removes a layer of ice by sublimation thereby exposing true membrane surfaces embedded in ice and hidden from the cleavage surfaces. Parts of the cell exposed by fracturing and etching process are shadowed with a metal, e.g., platinum; organic material is dissolved away, and the replica is floated off for viewing in TEM. Extracellular details, such as membrane surfaces and intracellular details (e.g., cell cytoskeleton) can be studied with this method. Thus, the real membrane surface and intracellular and extracellular structures that would otherwise be hidden can be viewed (Hayat, 1989).

1.2.4.4.4 Freeze drying

Freeze drying involves dehydration of frozen samples through the sublimation of ice. Frozen sample is allowed to dry under vacuum (10^{-3} Torr), accompanied by temperature rise (until it reaches room temperature). Any contact with an organic solvent is avoided during the process of dehydration (Edelmann, 2008; Hayat, 1989). Finally, the samples are fixed by osmium tetroxide (or FA) vapours, embedded in a resin and used for a conventional thin sectioning at room temperature (Edelmann, 2008; Glauert, 1974; Hayat, 1989). Variable quality of sample preservation is usually observed after freeze drying; depending highly on the quality of cryo-fixation and physiological state of the biological material (Edelmann, 2008). The production of ice-crystal relation may even occur during freeze drying when it is not carefully controlled. The well-preserved area is generally restricted to ~15 μm in thickness in the periphery of tissue sample. Another undesirable effect of freeze drying is intracellular, whole cell and entire tissue shrinkage (from 7 to 20 %), and in the case of relatively large samples, undried portions that can cause rehydration of the whole sample, including peripheral regions (Hayat, 1989). Consequently, this method of preparation has generally been replaced by freeze substitution and/or cryo-sectioning.

1.2.4.4.5 Freeze substitution and low-temperature resin embedding

Freeze substitution (FS) is the most common way to process samples rapidly frozen by some of the techniques of cryo-fixation mentioned above. During the procedure, the frozen cellular water is replaced (substituted) with a liquid organic solvent (substitution medium) at low temperatures, typically around -90 °C [183.15 K] (Steinbrecht & Müller, 1987). This temperature is thought to be low enough to avoid disruptive ice formation by devitrification (recrystallization) while still being above the melting point of the solvent used (see Table 3) (Buser & Walther, 2008; McDonald & Webb, 2011; Pierson *et al*, 2009).

Solvent	***Melting point***
Methanol	-98 °C [175.15 K]
Ethanol	-117 °C [156.15 K]
Acetone	-95 °C [178.15 K]
1-Propanol	-127 °C [146.15 K]
2-Butanol	-115 °C [158.15 K]
n-Hexadecene	-95 °C [178.15 K]

Table 3: *Properties of solvents generally used for freeze substitution.* The melting points (temperatures) of selected solvents are shown. Table adapted from Buser & Walther (2008).

The recrystallization temperature for amorphous ice is -137 °C [136.15 K], however it should be noticed that this value is valid for pure water. The natural cryo-protective effect of the protein and ionic content in cellular interior, as well as the use of external cryo-protectants may well increase the real recrystallization temperature for a biological material. It is presumed that the transformation from cubic to hexagonal ice probably takes place at around -80 °C [193.15 K]; therefore it is still arguable whether the water is in vitreous state or has transformed into cubic ice during substitution (Dubochet, 2007). In fact, the aggregation of macromolecules, inorganic solvents, and changes of hydration shells surrounding biological molecules can also occur even at low temperatures. Neverthelles these structural changes created by recrystallization at these temperatures are negligible and the information obtained from well-frozen samples can be considered as an accurate representation of the living cell (Dubochet, 2007; Humbel, 2008; McDonald & Webb, 2011; Pierson *et al*, 2009).

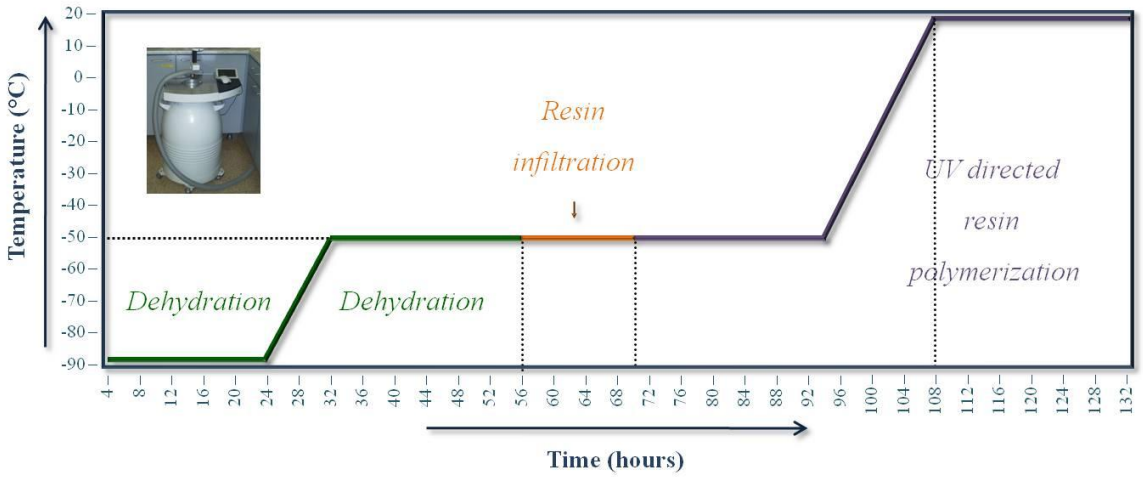

Figure 1-19: *Example of the timing of freeze substitution followed by low-temperature resin embedding.* Note that times required for dehydration and polymerization are significantly prolonged compared to a conventional ways of sample preparation after aldehyde-based fixation.

Generally, the timing of FS procedure varies considerably and may depend to some extend on the size, nature and hydratation of the sample being processed and the quality of cryo-fixation (Nicolas & Bassot, 1993). Diffusion at low temperatures is very slow and complete procedure, including resin embedding, usually takes several days to complete (Figure 1-19). Recently published improvement in the FS procedure shorten this time to few hours (quick FS as the 3-hours method, and super quick FS as only the 90-minutes method) with excellent ultrastructural preservation for a variety of cell types (McDonald & Webb, 2011). A variety of solvents can be used to substitute water of cryo-fixed biological samples (see Table 3). The two most commonly used are organic solvents such as methanol or acetone. In addition, the cryo-fixed samples can be simultaneously fixed/stained by adding different substances to FS media (Fernandez-Moran, 1960). Usually, osmium tetroxide, uranyl acetate, aldehydes and even water are added separately or in combination to FS media, and a variety of protocols can be found in the literature (Buser & Walther, 2008; Walther & Ziegler, 2002). The activity of fixatives is temperature-dependent: osmium starts to react at -70 °C [203.15 K], uranyl acetate is supposed to react at even lower temperatures and GA begins to cross-link macromolecules at -50 °C [223.15 K]. However, it is suggested to remove osmium at -40 °C [233.15 K] before further processing (Schwarz & Humbel, 2007). At temperatures higher than 0 °C [273.15 K], osmium reacts proteolytically, so it should not be used in combination with immunolabeling (Humbel *et al*, 2001). It is still also questioned

whether the dehydration of cryo-fixed samples (starting at – 90 °C [183.15 K]) before they are additionally chemically fixed (see the data above) allows extraction of lipids or promotes the aggregation of proteins. However, as the viscosity of the solvent increases with decreasing temperature it stabilizes the sample, and thus limits the mobility of proteins and their capability to form aggregates (Humbel *et al*, 2001; Schwarz & Humbel, 2007). The HPF/FS samples often have less contrast, especially for membranes compared with conventionally prepared samples (Walther & Ziegler, 2002). One possible explanation for this phenomenon can be the good preservation of proteins surrounding the membranes that inhibit the access of the stain. Addition of small amount of water to the FS media was shown to enhace the contrast of membranes of HPF/FS samples (Buser & Walther, 2008; Walther & Ziegler, 2002).

Once the substitution is complete, the samples are gradually warmed-up and embedded in either epoxy or methacrylic resins (Figure 1-19). A better FS approach, at least theoretically, is to maintaint the sample at sub-zero temperatures during embedding using Lowicryl resins and polymerizing by UV light (see Subchapter 1.2.2) (Carlemalm *et al*, 1985). Though even here the effect of polymerized resin on the dehydrated sample at the molecular level is difficult to predict, this approach is theoretically the best for preserving structure under conditions compatible with immunogold labeling. During the low-temperature embedding, total or partial loss of the hydration shell can be further reduced so that aggregation and redistribution of diffusible elements can be minimized (Bleck *et al*, 2010; Pierson *et al*, 2009).

1.2.4.5 Cryo-methods versus conventional way of sample processing for TEM

Cryo-fixation of biological samples as performed by HPF and followed by low-temperature dehydration and embedding has several distinct advantages over conventional methods of sample preparation for TEM analysis. Unlike the duration of aldehyde-based fixation (see Subchapter 1.2.1.3), cryo-fixation by HPF is achieved within milliseconds and it ensures simultaneous immobilization of all macromolecular components (Hurbain & Sachse, 2011; McDonald, 2007; McDonald, 2009). Many protein networks are very labile and fall apart with the slightest osmotic or temperature changes. These unwanted effects are minimized with cryo-fixation. Thus it is possible to study dynamic cellular processes, which can not be 'fixed' by conventional slow chemical fixation (Deerinck, 2006; Hayat, 1989; Pierson *et al*, 2009). Moreover, since the dehydration is performed at low temperatures, the

artifacts induced by the solvent are also greatly reduced. Even when the fixative is added to FS media, it is inactive during substitution at -90 °C [183.15 K], but it penetrates the sample and reacts simultaneously as soon as the temperature is raised. In this way the gradient of fixative during conventional preparation is avoided. The importance of this for morphological preservation is demonstrated by the formation of mesosomes in bacteria. This membrane compartments form when bacteria are fixed at room temperature with osmium, whereas it is absent when osmium is used at low temperatures during FS (Hurbain & Sachse, 2011). Another example is shown in Figure 1-20. As shown, the appearance of HP-frozen/FS samples is very different from that observed after conventional preparations.

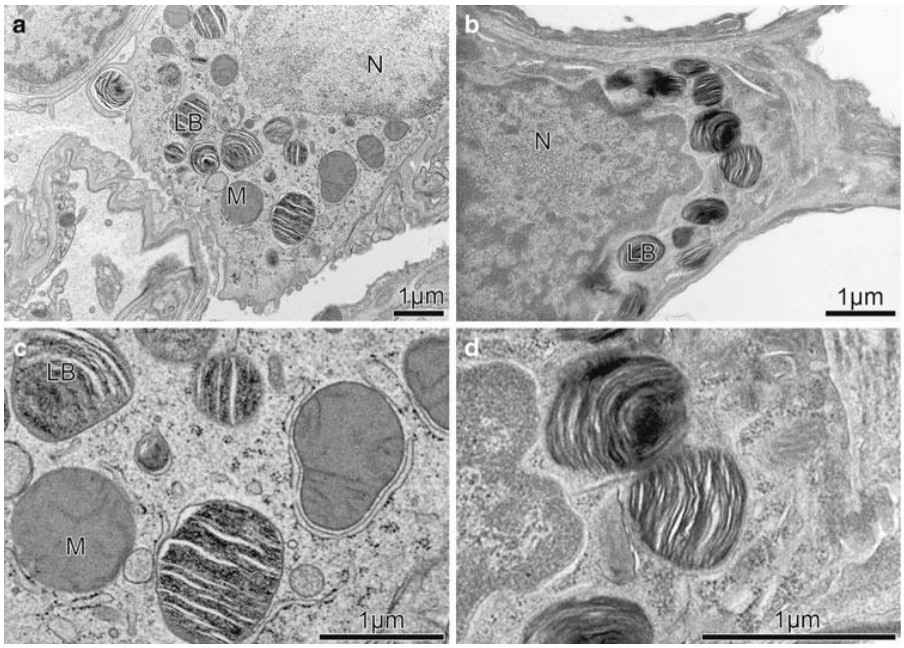

Figure 1-20: *Comparison of HP-frozen/FS type II alveolar epithelial cells (a, c) with chemically fixed samples (b, d).* The cryo-fixed samples show smooth membranes of lamellar bodies (LB) and mitochondria (M). Burst mitochondria are absent. Weighted against the cytoplasm, the matrix of HP-frozen/FS mitochondria demonstrates more electron scattering events, resulting in a darker appearance; an indication of improved retention of material in these organelles. Figure adapted from Vanhecke *et al* (2010).

Moreover, the efficient and fast chemical fixation is generally deficient in the samples containing air or large vacuoles (leaves), cell walls, cuticles (plants, fungi) or hydrophobic surfaces (insects, nematodes) (Humbel & Stienhorf, 2008). Especially in these cases, the cryo-fixation by HPF followed by FS is the method of choice for the excellent ultrastructural

preservation (Buser & Walther, 2008; Hawes *et al*, 2007; McDonald, 2007; Vanhecke *et al*, 2008). The hybrid approach of HPF combined with FS and low-temperature plastic embedding also gives a possibility to examine thick samples (200 - 300 nm thick sections) by electron tomography, so that relatively large cellular volumes can be studied in 3D (Pierson *et al*, 2009). There are numerous examples where HPF/FS combined with electron tomography have changed our understanding of cellular structure and dynamics (Pierson *et al*, 2009). During the past few years, protocols were also developed to adapt HPF/FS for subsequent immunolabeling according to the Tokuyasu technique (Griffith *et al*, 2008; Slot & Geuze, 2007; Stierhof *et al*, 1991; van Donselaar *et al*, 2007).

The main differences between both methods are summarized in Table 4.

	Chemical fixation, dehydration and embedding	***Cryo-fixation, low-temperature dehydration and embedding***
Duration	Seconds / minutes / hours	Milliseconds
Fixation	Selective fixation	Non-selective fixation
Dehydration	Increased extraction of cell constitutents	Extraction of materials is significantly decreased
Embedding	Shrinkage during polymerization	Reduced shrinkage
TEM observation	Ultrastructure alterations	Close-to-live ultrastucture preservation
Immunolabeling	Not Compatible / Compatible	Compatible

Table 4: *Summary of main differences between the conventional and cryo-way of sample processing for TEM.*

Altogether, HPF followed by FS and plastic embedding is becoming the most widely used method for TEM sample preparation.

1.3 TRANSMISSION ELECTRON CRYO-MICROSCOPY

The use of frozen-hydrated techniques to study biological samples in TEM was first proposed in 1952 by Fernandez-Moran (Fernandez-Moran & Dahl, 1952). Unfortunately, his results were not convincing. In early 80's, Dubochet and his colleagues demonstrated that it is possible to produce thin layers of vitrified water that contain an unfixed and unstained

biological samples, which could then be examined directly in their native hydrated state in the so-called transmission electron cryo-microscope (cryo-TEM; also known as cryo-electron microscope, electron cryo-miscroscope) (Adrian *et al*, 1984; Dubochet *et al*, 1988). This method, currently known as the 'thin ice embedding method' or 'bare grid method', has become a basic principle for the high-resolution cryo-TEM studies and image analysis, breaking the sub-nanometer limit (Dubochet *et al*, 1988). It is now possible to study isolated biological (and non-biological) objects up to the size of about 100 nm, and even more. Cryo-TEM therefore found its application in a numerous scientific disciplines, including structural and molecular biology, cell biology, medicine, nanobiology and even nanotechnology research.

1.3.1 PREPARATION OF SAMPLES FOR CRYO-TEM ANALYSIS

As mentioned above (see Subchapter 1.2.4.2), there are different ways to obtain vitrified samples for TEM, as well as for cryo-TEM analysis. Among them, the method of plunge freezing has been considered to be the most suitable one for the preparation of samples embedded in a thin layer of vitreous water (Adrian *et al*, 1984). Typically, a drop of an aqueous suspension containing the sample particles is placed on an EM grid with 'pre-treated' perforated supporting film, mounted in a tweezers of the plunger (Figure 1-21). Excess fluid is then blotted off with filter paper and the grid is immediately plunged into the cryogen at a high velocity (Adrian *et al*, 1984). Thin film of solution, spanning the holes, is formed after blotting. As the thickness is typically 50 - 100 nm and the hole diameter is in the range of microns, the surface-to-volume ratio is extremely high and therefore the heat extraction is very efficient. A high freezing velocity (10^4 ºC/s) is typically reached with ethane slush. Though other types of cryogens can be also used, plunging blotted samples into liquid ethane cooled close to its melting point become the most standard for this technique today. Once the sample has been vitrified, it can be stored almost indefinitely under liquid nitrogen until examined in cryo-TEM. Contrary to conventional TEM procedure, a special cryo-transfer holder has to be used to introduce the sample grid into cryo-TEM and inspect the sample. The temperature at which the sample is to be maintained during the observation and image recording should be below the recrystallization temperature (-137 °C [136.15 K]), but typically temperatures between -180 °C [93.15 K] and -160 °C [113.15 K] are used (Marko & Hsieh, 2007).

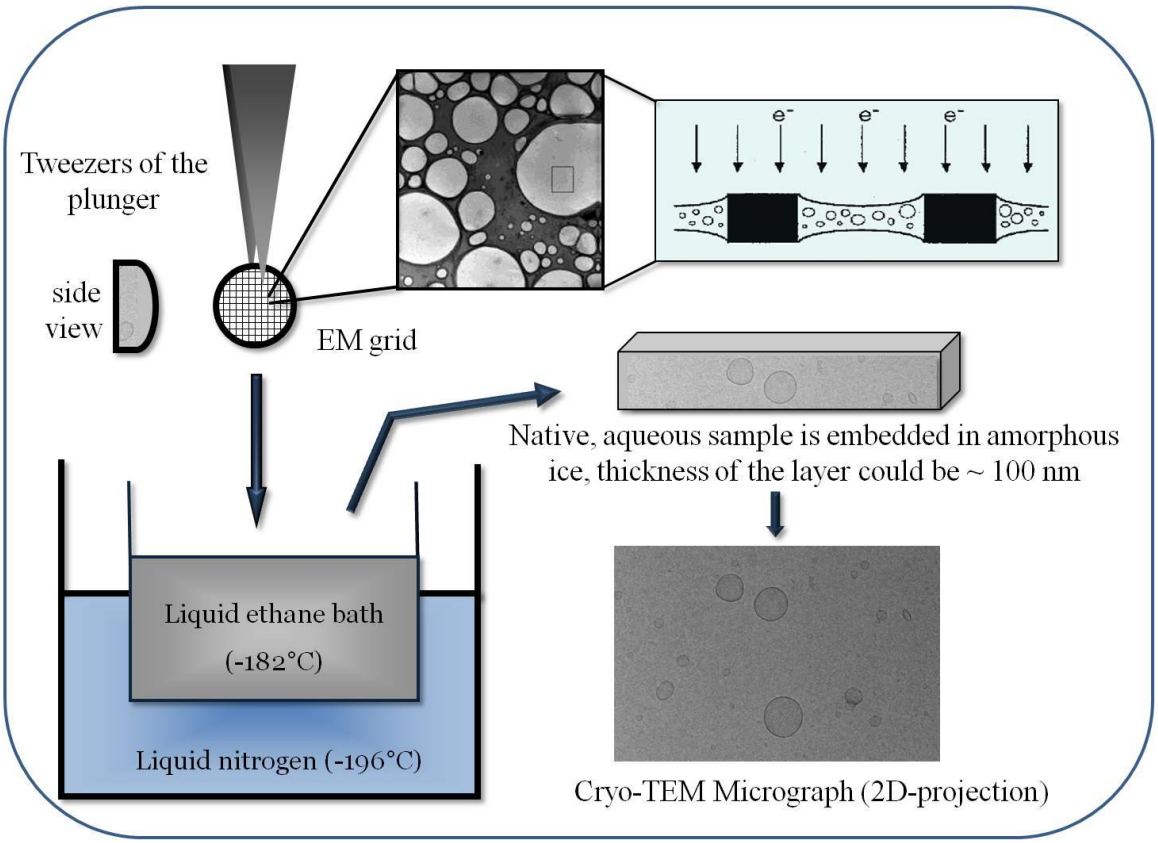

Figure 1-21: *Schematic illustration of the method of plunge freezing and the embedding of samples into a thin layer of vitreous water, followed by cryo-TEM observation.*

Preparing a 'representative' thin vitrified sample in a controlled and reproducible manner is an important step for each cryo-TEM experiment. Forces that the sample is subjected to in an aqueous suspension when it is being transferred via a pipette to the surface of the grid are many and may affect the native structure. For example, the structure of some molecules was observed to be affected (displaced and even crushed) during the formation of thin layer of ice through the surface effects considering the high surface tension of water, which tends to minimize the surface-to-volume ratio (Crucifix, 2008; Dubochet *et al*, 1988). This difficulty can be overcome, if appropriate surface property is given to the supporting film (Adrian *et al*, 1984). A droplet of applied solution should behave as one entity and spread out across holes in the carbon support (de Carlo, 2008; Frederik *et al*, 2008). Therefore, often the grids should be glow-discharged, prior to applying the sample, in order to increase the surface hydrophilicity of the supported film (de Carlo, 2008). The higher the quality of the support film, the better results are obtained.

The sample can be further subjected to local charge changes, dipoles, van der Waals interactions and hydrodynamic effects which can disrupt the sample (Frederik *et al*, 2008; Marko & Hsieh, 2007). For any sample it is therefore necessary to identify suitable conditions for obtaining a sufficiently thin layer of ice (typically less than 100 nm thick), yet maintaining a reasonable number of randomly orientated particles across the holes of the film. Often the variables such as sample concentration, buffer, blot time, waiting time, temperature and humidity, must be empiricaly determined in order to achieve optimal imaging conditions (Frederik *et al*, 2008; Chiu *et al*, 2006).

1.3.2 THE VITREOUS STATE OF ICE AND ICE CONTAMINATION

In cryo-TEM, the vitreous status of ice needs to be maintained. Its state can be verified by electron diffraction (see Figure 1-08), recognized as two-dimensional (2D) circular diffraction pattern displaying the typical diffuse ring (Dubochet *et al*, 1988; Hayles *et al*, 2010).

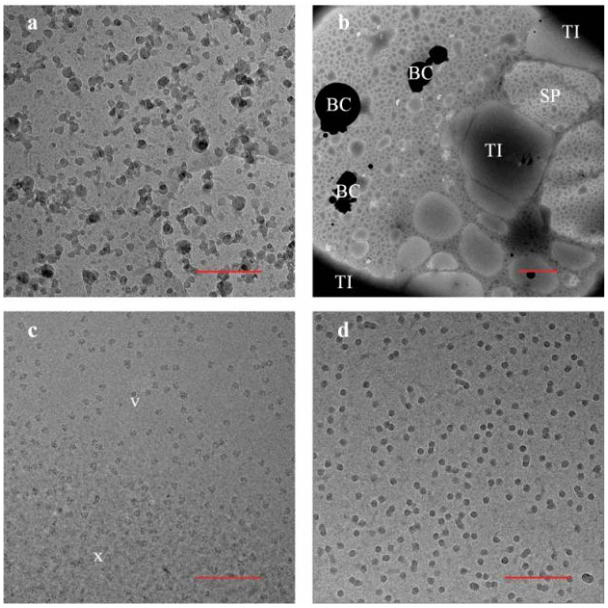

Figure 1-22: *Types of cryo-TEM contamination.* Images show various problems that can occur when preparing frozen-hydrated grids: (a) Ethane contamination. (b) Low-magnification cryo-TEM image of a bad grid. BC indicates large ice contaminants that are usually the result of poor handling. SP indicates the 'splotchy' appearance of ice that occurs when the substrate is not hydrophilic. TI indicates thick ice. (c) Cryo-TEM micrograph showing the appearance of vitreous ice (v) and crystalline ice (x). (d) Cryo-TEM micrograph

showing the high-contrast appearance of particles that have been freeze dried. Bars = 250 nm in a, c, and d; 2 μm in b. Figure adapted from Grassucci *et al* (2007).

On the other hand, the presence of Bragg peaks could indicate contamination by hexagonal ice crystals. Ice contamination is often encountered in cryo-TEM (Frederik *et al*, 2008; Grassucci, 2007). This could appear as a dark round balls or hexagonal tablets of varying sizes dispersed randomly over the grid surface, sometimes in chain formation (Figure 1-22). They may be a result of water trapped in liquid nitrogen or may have condensed during the grid transfer. Working in a dry atmosphere and possibly emptying and drying liquid nitrogen container generally limits this problem (Crucifix, 2008). The impurities present in the ethane can be another source of contamination. In this case, the grid surface may be covered with long filamentous aggregates, which tend to be more numerous when the grid is covered with a thick layer of solid ethane.

1.3.3 LOW DOSE IMAGING IN CRYO-TEM

One of the most important causes of artifacts, and sometimes misinterpretations of TEM micrographs, is the electron-beam-induced radiation damage. All biological samples, and under high magnification most inorganic samples, are highly sensitive to electron-beam radiation. These samples suffer from degradation as a result of the impact of high-energy electrons from the focused electron beam. The concomitant dissipation of energy gives rise to chemical reactions and rearrangements that lead to the loss of structural details during the image acquisition (Glaeser & Taylor, 1978; Chiu *et al*, 2006). This is especially true for the examination of samples embedded in a thin layer of vitrified ice. Due to the absence of protection by chemical cross-links or the stabilization by the stain molecules, samples are more easily damaged in comparison with other preparation techniques. Special conditions are therefore necessary to substantially reduce electron beam induced damage of these samples and to record the high quality cryo-TEM micrographs. So far, the low dose electron imaging has been the most effective approach for overcoming these difficulties (Chiu *et al*, 2005; Chiu *et al*, 2006). In the low dose mode (Figure 1-23), the total imaging electron dose is limited to the range of 10 – 20 electrons per square Ångström (compare to ~100 to ~1000 in conventional TEM) (Dubochet *et al*, 1988; Glaeser & Taylor, 1978; Chiu *et al*, 2006). The number of inelastically scattered electrons that often leads to radiation damage is thus significantly reduced (Dubochet *et al*, 1988). Exceeding this dose will generally result in a

change of biological structure and 'bubbling', thus compromising high resolution imaging (Lucic *et al*, 2008). Electron doses are limited not only during the actual exposure, but also during the search for suitable objects or area. As the sample is usually found in only a few regions on the grid, the low magnification is used for their identification, to minimize the amount of radiation on the sample before studying it more closely.

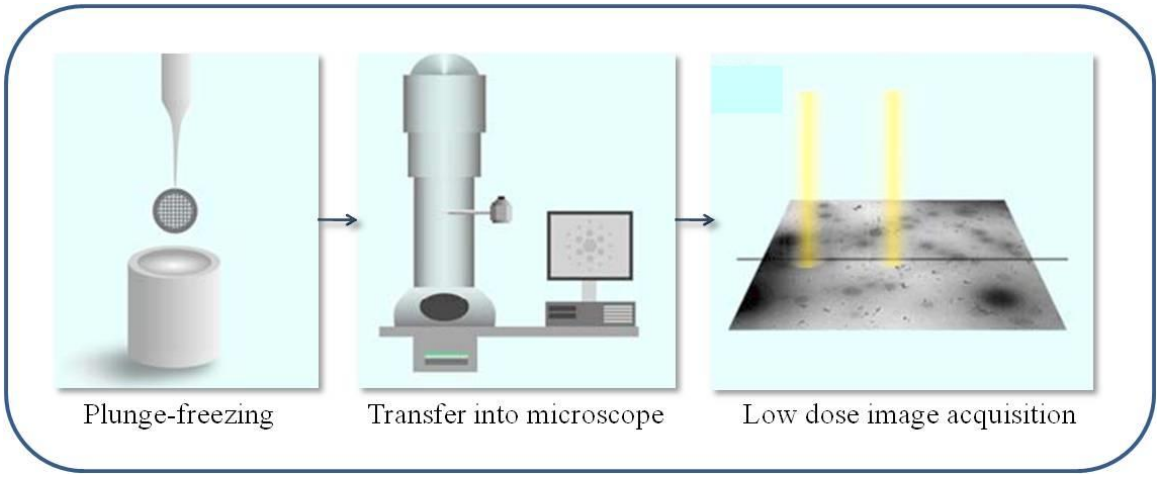

Figure 1-23: *Low dose imaging.* Plunge-frozen samples are transferred into cryo-TEM without re-warming. Low dose imaging is then used to minimize radiation damage. Images are focused (left yellow electron beam) on the tilt axes (black line) at a different position than used for imaging (right yellow electron beam). Figure adapted with modifications from Koning & Koster (2009).

1.3.4 CONTRAST IN CRYO-TEM

Unstained vitreous samples suffer from limited contrast. A poor signal-to-noise ratio of recorded images is one of the basic problems in cryo-TEM imaging (Lucic *et al*, 2008; Pierson *et al*, 2009). The contrast of sample depends on the sample itself, the defocus value of the objective lens and the thickness of ice. The ability of sample to provide contrast cannot be altered, however, the sufficient phase contrast can be obtained using an appropriate objective lens underfocus setting (Marko & Hsieh, 2007). Usually the images are recorded at a 1 - 3 µm underfocus in order to enhance the visibility of low-resolution structural details (Chiu *et al*, 2006). An example is shown in Figure 1-24. The image on the left was captured in a near focus mode, while the image on the right was recorded using a moderate underfocusing.

With increasing ice thickness, the background noise increases as well. It is therefore preferable to record images in areas with a thinner layer of ice, though its thicknes must imperatively be superior to the particle size.

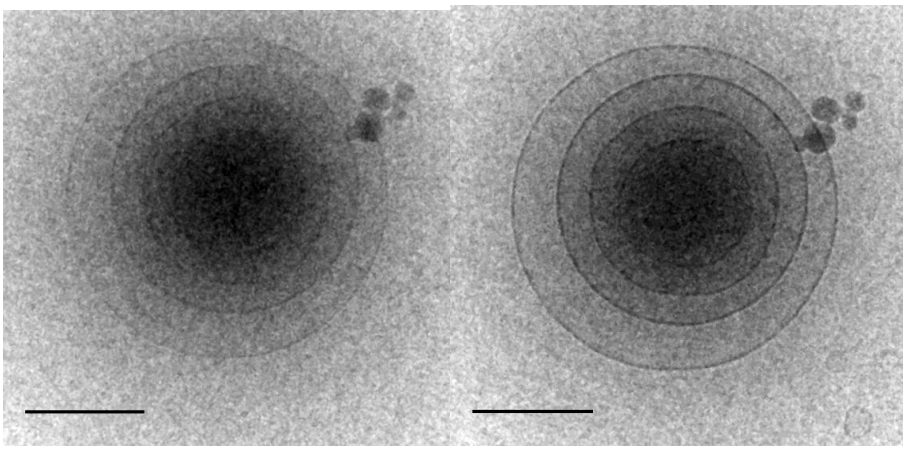

Figure 1-24: *Contrast in the cryo-TEM micrographs.* Cryo-TEM image of liposomes on left is in the focus. The second one is in ~ 2 μm underfocus. Note the small liposome particles in the lower right corner, not visible in the micrograph, which was recorded in the focus mode. Bars = 200 nm.

1.3.5 CRYO-NEGATIVE STAINING

Negative staining in TEM is often the first step to check the quality and suitability of the sample by its embedding in a layer of the metal ions (phosphoric tungsten acid, uranyl acetate, uranyl formiate, ammonium molybdate and others) (Brenner & Horne, 1959; Harris, 2007; Hayat, 1989; Pierson *et al*, 2009). Cryo-negative staining is a rapid, practical method that combines negative staining and cryo-TEM (Adrian *et al*, 1998). Unlike conventional air-drying negative staining, in cryo-negative staining method the aqueous buffer surrounding biological particles is replaced by a higher density heavy metal salt (Figure 1-25).

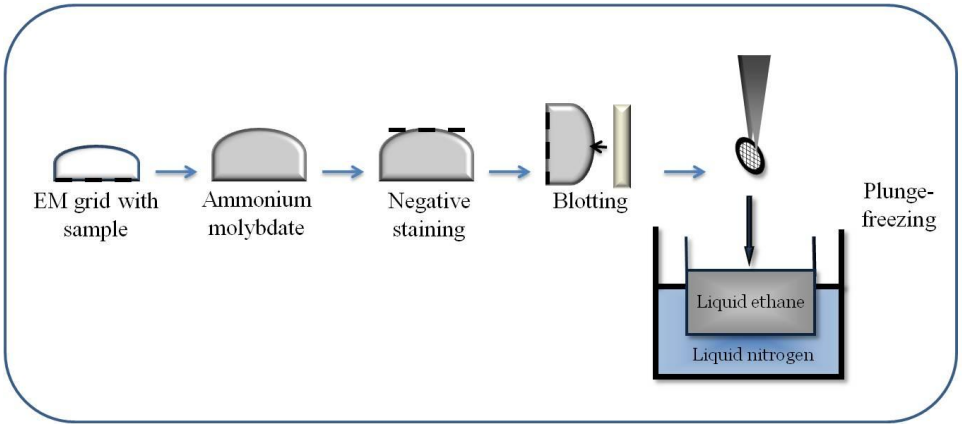

Figure 1-25: *An outline of the cryo-negative staining procedure.* The biological sample is mixed with a stain prior to blotting and is rapidly vitrified by plunge freezing.

The contrast of image is then produced as a result of differences in scattering density of the buffer and the sample. That is why biological samples appear light in a dark background in TEM micrographs of a cryo-negatively stained preparation using, e.g., ammonium molybdate (de Carlo, 2008). An example is shown in Figure 1-26.

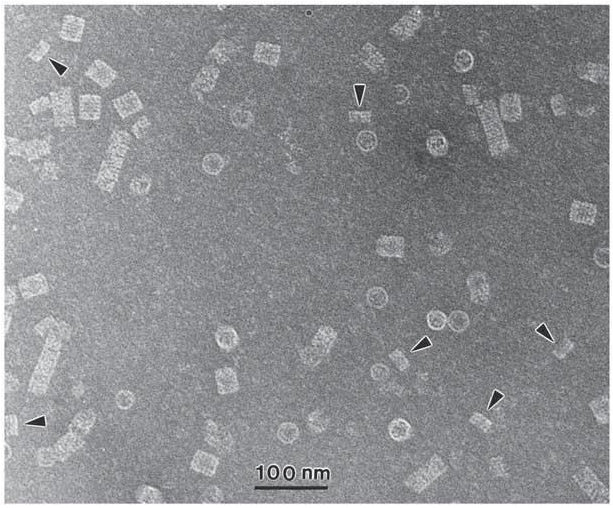

Figure 1-26: *Cryo-negative staining.* Reassociated keyhole limpet hemocyanin type 1 revealed by cryo-negative staining with 15% (w/v) ammonium molybdate. Note the presence of decamers (arrowheads), didecamers and longer tubular structures. Figure adapted from Harris (2007).

The method of cryo-negative staining is currently widely used to increase the signal-to-noise ratio of small biological complexes that are difficult to visualize in a standard cryo-TEM. Some macromolecular assemblies, however, do not withstand the high salt concentration (2% w/v and higher) and may dissociate (Harris, 2007; Mears & Hinshaw, 2008). Moreover, each negative stain salt is characterized with slightly different chemical properties and varying interaction with biological material (Harris, 2007). Staining of the sample can therefore potentially alter its fine structural details and extreme care should be taken in the interpretation of such electron micrographs (Friedrich *et al*, 2010). In some cases, the sensitivity of biological samples exposed to the electron beam is also decreased (de Carlo, 2008). Under optimal conditions, and depending on the precise experimental procedure, a resolution of 2 nm can be attained. However, the grain size of staining agent generally precludes the sub-nanometer resolution (Pierson *et al*, 2009).

1.3.6 THE (BIOLOGICAL) APPLICATIONS OF CRYO-TEM

When imaging of a frozen-hydrated material is complete, computational techniques are used to transform 2D images of randomly oriented objects (particles) into 3D structure (model) (Chiu *et al*, 2006). These 3D data are generally based on types of applications: the single-particle analysis (SPA; resolution better than 1.0 nm), and/or the cryo-electron tomography (cryo-ET; resolution better than 3 nm) (Frederik *et al*, 2008). SPA and additional well-defined computational protocols are capable to computationally purify and identify variety of macromolecules and biological nanomachines from the low dose cryo-TEM images (Pierson *et al*, 2009).

The cryo-ET reconstruction is computed from a tilt series of projections from a single structure (particle) embedded in a thin vitrified ice layer of ice (Marko & Hsieh, 2007). Just in the last 10 years, structures studied include for example: i) macromolecules such as the nuclear pore complex (Beck *et al*, 2004; Stoffler *et al*, 2003), viruses (Cyrklaff *et al*, 2005), ribosomal subunits (Zhao *et al*, 2004), and immunoglobin (Sandin *et al*, 2004); ii) isolated organelles such as mitochondria, axonemes (McEwen *et al*, 2002; Nicastro *et al*, 2005), and triad junctions (Wagenknecht *et al*, 2002); and iii) small cells such as *Pyrodictium* (Nickell *et al*, 2003), and others (Baumeister, 2002; Kurner *et al*, 2004; Lucic *et al*, 2008; Medalia *et al*, 2002). Now it is even possible to correlate tomograms obtained from imaging of the same EM grids in cryo-TEM, as well as in LM at liquid nitrogen temperature (cryo-fluorescence) (Gruska *et al*, 2008; Lucic *et al*, 2008; Sartori *et al*, 2007; Schwartz *et al*, 2007). In

combination with conventional TEM or cryo-TEM, correlative cryo-LM-TEM offers a promising opportunity to investigate cellular organization (Pierson *et al*, 2009; Plitzko *et al*, 2009; Sartori *et al*, 2007; Schwartz *et al*, 2007). Of particular interest is a labeling of intracellular epitopes for cryo-approaches with a fluorescent tag (Sartori *et al*, 2007) and quantum dots (Dahan *et al*, 2003; Lucic *et al*, 2008; Mercogliano & DeRosier, 2007; Nisman *et al*, 2004; Pierson *et al*, 2009).

1.3.7 BENEFITS OF CRYO-TEM COMPARED TO OTHER APPROACHES

Not so long ago, X-ray crystallography (XRC) and/or nuclear magnetic resonance (NMR) spectroscopy have been the primary tools used for complete characterization of the overall structural organization of individual protein complexes (Crucifix *et al*, 2008). Both approaches offer atomic-level spatial resolution, but require a relatively large amount of intact complexes. Contrary to them, cryo-TEM offers a distinct advantage, as it requires significantly less material (10 $\mu g.ml^{-1}$ versus 10 $mg.ml^{-1}$) (Grassucci *et al*, 2007; Chiu *et al*, 2005). XRC further requires that the protein must be crystallized. Crystallization conditions are typically not physiological and may well introduce changes in the structure. Some macromolecules, however, can not be crystallized, or when crystallized, they diffract poorly, as only large, well-ordered crystals diffract. These macromolecules can then only be captured in their free single-particle form by rapid freezing and direct visualization using cryo-TEM (Grassucci *et al*, 2007; Chiu *et al*, 2005). NMR avoids the requirements for crystallization, but it is difficult to use with large molecules and complexes (the size of protein complex is limited to approximately <100 kDa; kiloDalton) (Pierson *et al*, 2009). As obvious, neither technique provides easily interpretable, intuitive results. Moreover, it is not unusual for complete determination of a protein structure, including expression, purification, crystallization and analysis, to take several months using XRC. NMR, though it eliminates the requirement for crystallization, is computationally more complex and NMR structural analysis times are also typically measured in months. In contrast, cryo-TEM provides structural information within a single day. Cryo-TEM offers an alternative technique that avoids the requirement for crystallization, and complementary to NMR, is best suited for the analysis of secondary, tertiary, and quartery structure – levels at which structure-activity-relationships operate (Elands & Hax, 2004).

To summarize: though there are some disadvantages possible to meet during the sample preparation and cryo-TEM imaging (as mentioned above), cryo-TEM is the most

appropriate imaging technique for biological nanomachines. The main reasons are highlighted in Table 5.

Advantages of cryo-TEM	***Disadvantages of cryo-TEM***
No artifacts due to fixation, dehydration or staining	Possible freezing artifacts
Preservation of native conformation	Difficult to distinguish between different orientations versus conformations
Random orientation	Low contrast
Works well on a homogeneous sample	Low signal-to-noise ratio
Good contrast at high defocus	Sensitive to radiation
Higher resolution information than negative staining	Technically demanding
	Can not visualize smaller than 100kDa

Table 5: *Summary of advantages over disadvantages of cryo-TEM procedure.* Table adapted from Beginning an electron microscopy project (2009).

Briefly, cryo-TEM bypasses the need for conventional fixatives, dehydration and staining, so that a biological object is observed directly and a 'close-to-native' environment is retained (Pierson *et al*, 2009). Unlike conventional TEM techniques, where the objects are flattened by adsorption onto the supporting film and covered with heavy-metal staining material, cryo-TEM allows the analysis of dynamic behavior of unfixed and freely suspended samples within the layer of vitrified solution. Frozen-hydrated sample is therefore observed by its own contrast in the absence of stain, avoiding problems in interpretation caused by an unpredictable accumulation of staining material (Lucic *et al*, 2008). An example is shown in Figure 1-27.

Moreover, SPA processing techniques, and additionally, cryo-ET in combination with 3D reconstruction can determine 3D structure of a sample directly from a low dose electron imaging conditions. Currently, the resulting reconstructions of conformationally rigid and uniform machines have achieved sub-nanometer (6-10 Å) resolution (Chiu *et al*, 2005; Jiang & Ludtke, 2005). In this resolution range, secondary structure elements can be identified and high-resolution structures can be fitted to provide an understanding of the biological machine and its components (Chiu *et al*, 2006).

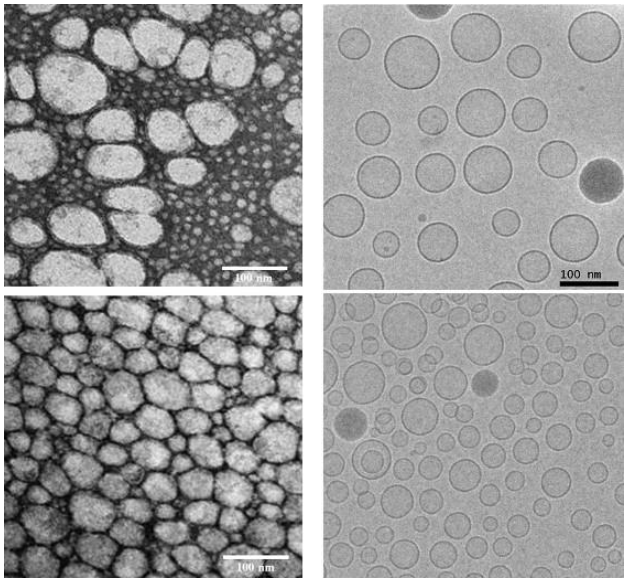

Figure 1-27: *Cryo-TEM micrographs of silica-silicone nanocapsules prepared by template polymerization.* On the left: Conventional TEM micrographs of negatively stained samples. The right panel shows native, rapidly frozen samples in cryo-TEM micrographs. Capsules embedded in a vitreous ice are imaged very close to their native state. Each row contains images of identical samples. It is obvious that conventional TEM imaging does not enable imaging of the native state. Bar = 100 nm. Figure courtesy of J. Bednár.

1.3.8 PERSPECTIVES OF CRYO-TEM

Evidently cryo-TEM is nowadays the imaging method of choice for structural and morphological analysis of a different macromolecular complexes and nanomachines at the sub-nanometer level (Friedrich *et al*, 2010; Nickell *et al*, 2006). It is complemetary to existing techniques such as NMR and XRC, offering less resolution but avoiding the requirement for crystallization and works well with larger molecules and molecular complexes. Most importantly, it can determine higher-level structure in a fraction of time required by conventional techniques and promises to play a key role in a structure-based drug discovery in recent years (Elands & Hax, 2004). It should however be mentioned that one of the most promising approaches for protein structural analysis seems to be a hybrid analysis that fits atomic-resolution structures determined by XRC and/or NMR to lower resolution cryo-TEM images to create a multi-resolution map of large, uncrystallized protein structures (Sali *et al*, 2003). Such bridging techniques will be instrumental in providing a complete understanding

of the structure and function of molecular complexes as can be possible with a stand-alone technique (Nicastro *et al*, 2006; Pierson *et al*, 2009).

Chapter 2 AIMS OF THE THESIS

There were several objectives in this thesis:

- to install and to establish cryo-preparation methods at the Institute of Cellular Biology and Pathology of the First Faculty of Medicine of Charles University in Prague, namely: i) the method of high-pressure freezing, freeze substitution and low-temperature embedding, and ii) the thin ice embedding method followed by electron cryo-microscopic imaging,
- to demonstrate their usability and powerfulness by applying them on particular biological and biomedical objects, which included the budding yeast *Saccharomyces cerevisiae*, and different nanovesicular structures such as the liposomes, cationic liposomes, etc.,
- to establish an optimized protocol for the immunolocalization of the nuclear and nucleolar antigens of *Saccharomyces cerevisiae,* which also involve an optimization of the preparation of the cells for both ultrastructural and immunocytochemical TEM studies with the best possible 'close-to-live' preservation.

It is well known that the preparation of yeast cells for TEM study is rather problematic, mainly because of the presence of a rigid cell wall. Chemical fixation using 'strong' fixatives may result in adequate ultrastructural preservation, but at the expense of preservation of sensitive antigens. Therefore, the use of alternative methods had to be considered. Development of new tools such as high-pressure freezers and low-temperature processing systems provided new opportunities for the processing of yeast and other biological objects for the high-resolution ultrastructural and immunocytochemical TEM analysis. We therefore aimed to establish an optimized protocol for the cryo-fixation of yeast *S. cerevisiae* followed by low-temperature dehydration, embedding and advanced TEM imaging, in order to study selected nuclear and nucleolar antigens.

Next, we aimed to use the technique of a thin vitreous layer for detailed morphological characterization of various nanostructures, potentially convenient to serve as carriers of biologically active molecules in the processes of targeted drug delivery. This method is able to produce very thin vitrified aqueous films with the hydrated samples embedded in them. In combination with cryo-TEM analysis it allows direct examination of frozen-hydrated samples in their near-native state with a fully preserved structure. This method is practically unique,

which can be used for the analysis of one of the most intensively studied nanosystems at the present time – the liposome - without disturbing its structure and directly visualize its morphological features.

Chapter 3 MATERIALS AND METHODS

Detailed description of the materials and methods used in this thesis is provided in Publications No.1 to No.3 presented in Chapter 4, in the separate Subchapters 4.1.3, 4.2.3 and 4.3.3, respectively. Therefore, the following chapter concentrates mostly on some comments explaining in more details some of the procedures used.

3.1 PROCESSING OF *S. CEREVISIAE* FOR IMMUNOELECTRON MICROSCOPY

Approaches presented in this thesis are mainly focused on the preservation of the yeast *S. cerevisiae* for both fine ultrastructural and immunocytochemical studies performed at EM level. These approaches encompass mainly: i) aldehyde-based fixation, dehydration in alcohol, resin embedding and ultra-thin room temperature sectioning, ii) cryo-fixation by high-pressure freezing, and freeze substitution, resin embedding and ultra-thin sectioning as mentioned above, iii) EM immunocytochemistry, and/or iv) post-staining procedures. In addition to TEM observation, the immunofluorescence microscopy was also performed.

Publication No.1 of Chapter 4 (Subchapter 4.1.3) offers a detailed description of the implemented procedures. Therefore, only supplementary information will be mentioned in the following section.

3.1.1 YEAST STRAIN

The *S. cerevisiae* haploid strain (a kind gift of Yvonne S. Osheim, University of Virginia Health System, USA) with the following genotype was used in this study:
NOY 886: MAT α rpa135Δ::LEU2 ade 2-1 ura 3-1 his 3-11 trp 1-1 leu 2-3,112 can 1-100 foblΔ::HIS 3, pNOY 1I7 [CEN, RPA135, TRP1]

3.1.2 RECIPES FOR SELECTED BUFFERS / SOLUTIONS

Recipes for buffers that were used in the preparation of yeast cells for LM and/or TEM analysis, and were not included in Publication No.1, are additionally provided here:

Phosphate-buffered saline (PBS), pH 7.4

To prepare 10x stock solution (1 Liter), 80g of sodium chloride [NaCl], 2.0g of potassium chloride [KCl], 2.0g of potassium dihydrogen phosphate [KH_2PO_4] and 11.5g of disodium hydrogen phosphate heptahydrate [$Na_2HPO_4x7H_2O$] were dissolved in 800 ml of double-distilled water. The pH was adjusted to 7.4, and the final volume was brought to 1 Liter with double-distilled water. The solution was filtered, sterilized by autoclaving and stored at room temperature. The final working dilution of this buffer was 1:10.

Potassium phosphate buffer (KPi), pH 6.8

To prepare 1 *M* KPi buffer, 49.7 mL of 1 *M* dipotassium phosphate [K_2HPO_4] buffer was mixed with 50.3 mL of 1 *M* potassium dihydrogen phosphate [KH_2PO_4] buffer to obtain the desired pH 6.8. The combined 1 *M* stock solution was prepared each time on the day of the experiment. The final working concentration of this buffer was 0.1 *M*.

Lowicryl HM20 resin

Crosslinker D	2.98g
Monomer E	17.02g
Initiator C	0.10g

All components of the resin (HM20 kit, Cat# 14340, Electron Microscopy Sciences, Hatfield, Pennsylvania, USA) were weighed into a glass vial on the day of the experiment and mixed together according to manufacturer's instructions: a continuous stream of dry nitrogen gas was used to mix the resin with a Pasteur pipette for about 5 min to remove oxygen. The resin was then placed into a FS machine (Leica EM AFS2, Leica Microsystems, Vienna, Austria) set to -90 °C (to cool down), at the begining of FS procedure. The resin was kept protected from direct light during handling. Pre-mixed Lowicryl HM20 MonoStep (Cat.# 14335, Electron Microscopy Sciences) was also used as an embedding medium (not mentioned in Publication No.1). This 'ready-to-use' resin was also mixed using a stream of dry nitrogen before the use, kept protected from light and pre-cooled in the FS machine before each processing.

Uranyl Acetate solutions

For the post-staining of ultra-thin sections of aldehyde-fixed yeast cells, 2% (w/v) aqueous solution of uranyl acetate [$UO_2(OCOCH_3)_2x2H_2O$] was prepared. For the post-staining of HP-frozen/FS yeast cells, 2% (w/v) uranyl acetate in 70% (v/v) methanol was prepared. For the FS media, 10% (w/v) uranyl acetate in methanol was prepared as a stock each time prior to

experiment. The final working dilution used was 0.1% uranyl acetate in acetone. Each solution was filtered three times through a syringe filter (0.22 μm) after preparation and once prior to experiment. The solutions were stored in the syringe at 4 °C, kept protected from light.

Lead Citrate solution

The stain solution was prepared by mixing of 1.33g of lead nitrate [$Pb(NO_3)_2$] and 1.76g of sodium citrate dihydrate [$Na_3(C_6H_5O_7)x2H_2O$] in 30 mL of double-distilled water. The solution was shaked vigorously for 1 min, and then intermittently for 30 min until obtaining milky aspect of the solution. The pH was adjusted to 12.0 by addition of 1 *N* sodium hydroxide [NaOH] (the solution became clear). The final volume of the solution was brought to 50 mL with double-distilled water. The solution was stored in a 50 mL Falcon conical tubes, kept protected from light at 4 °C.

3.1.3 CHEMICAL FIXATION OF S. CEREVISIAE

Yeast cells were prepared according to (Mulholland & Botstein, 2002) with the following modifications: 2x fixative (see Table 6) was added directly to the yeast culture (1:1, v:v) to reach a final concentration of 4% (w/v) FA (Fluka, Ronkonkoma, NY) in 0.1 *M* PIPES (pH 6.8), 1 *mM* calcium chloride [$CaCl_2$], 1 *mM* magnesium chloride [$MgCl_2$] and 0.1 *M* D-Sorbitol. Each time, FA was prepared freshly just before use by dissolving the solid paraformaldehyde in a buffer (16% (w/v) FA in 0.4 *M* PIPES as a stock solution). Additionally, GA in final concentrations of 0.05% to 0.5% was used in combination with the fixative mentioned above. The cells were first fixed for 5 min at room temperature, pelleted and subsequently resuspended in a 1x fixative (see Table 6) to complete the fixation for additional 1 hour. Gentle agitation with orbital shaker was applied during the fixation procedure and centrigufation at 1500g for 5 min was used for pelleting the cells. Thereafter, the cells were washed twice in 0.1 *M* PIPES (pH 6.8) with 0.1 *M* D-Sorbitol and once in 0.1 *M* PIPES (pH 6.8) alone. The cells were then transferred into a glass test tubes, treated with 1% (w/v) sodium periodate [$NaIO_4$] (Sigma, St. Louis, USA) for 15 min, washed in double-distilled water and subsequently treated for additional 15 min with 50 *mM* ammonium chloride [NH_4Cl] (Sigma) and washed again in water. The samples were dehydrated successively in a graded ethanol series (25%, 50%, 75%, and 95% ethanol) in 5 min steps. Dehydration was performed on ice to minimize the extraction of the material. Each step was

followed by centrifugation at 1500g for 1 min at 4 °C. Three changes of 100% ethanol were additionaly applied (5 min steps) and final dehydration step was performed at room temperature using a freshly opened bottle of ethanol in order to have anhydrous solutions. The dehydrated cells were then infiltrated with 2:1 (v:v), 1:1 (v:v) and 1:2 (v:v) ethanol:LR White resin mixtures and twice with pure LR White (Medium grade, kit, Cat.# 14380, Electron Microscopy Sciences). Each step was carried out at room temperature for 1 hour using a gentle agitation with orbital shaker. The third infiltration step with pure resin was performed overnight at 4 °C. Next day, the resin was exchanged for a fresh one and left incubated for additional 30 min at room temperature. Finally, the samples were transferred into gelatin capsules (size 1, Cat.# 16702745, Leica Microsystems) containing fresh resin, allowed to settle for 15 min, and polymerized at 47 °C for 2 or 3 days.

	2x Fixative	**1x Fixative**
PIPES, pH 6.8	0.2 *M*	0.1 *M*
D-Sorbitol	0.2 *M*	0.1 *M*
$MgCl_2$	2 *mM*	1 *mM*
$CaCl_2$	2 *mM*	1 *mM*
FA	8%	4%
GA	0 %, 0.1% - 1%	0 %, 0.05% - 0.5%

Table 6: *Composition of fixative solutions used for yeast cells preservation.*

3.1.4 PROTOCOLS FOR LOW-TEMPERATURE DEHYDRATION AND EMBEDDING OF HP-FROZEN S. CEREVISIAE CELLS

As described in detail in Publication No.1, the *S. cerevisiae* cells were cryo-fixed using the Leica EM PACT2 HP-freezer equipped with the rapid transfer system (Leica Microsystems, Vienna, Austria). Freeze substitution was performed using the Leica EM AFS2 FS instrument, equipped with an automatic reagent handling system (Leica EM FS processor) and integrated UV LED lamp (Leica Microsystems).

Here, the summary tables of preparation steps in the FS procedure are only provided. It should be mentioned that both a manual reagent handling (Table 7) and an automatic

reagent handling (using the Leica EM FS processor) (Tables 8 and 9) were tested (not mentioned in Publication No.1).

Step	T_{start}	T_{end}	Time (in hour)	Reagent	UV
1.	-90 °C	-90 °C	24.00	FS solution	
2.	-90 °C	-50 °C	08.00	FS solution	
3.	-50 °C	-50 °C	24.00	FS solution	
4.	-50 °C	-50 °C	00.01	Acetone	
5.	-50 °C	-50 °C	00.01	Acetone	
6.	-50 °C	-50 °C	00.01	Acetone	
7.	-50 °C	-50 °C	02.00	Acetone:HM20 (3:1)	
8.	-50 °C	-50 °C	03.00	Acetone:HM20 (1:1)	
9.	-50 °C	-50 °C	03.00	Acetone:HM20 (1:3)	
10.	-50 °C	-50 °C	02.00	HM20	
11.	-50 °C	-50 °C	02.00	HM20	
12.	-50°C	-50°C	02.00	HM20	
13.	-50 °C	-50 °C	24.00	HM20	ON
14.	-50 °C	20 °C	14.00	HM20	ON
15.	20 °C	20 °C	24.00	HM20	ON

Table 7: *The protocol used for freeze substitution and Lowicryl HM20 low-temperature embedding of HP-frozen S. cerevisiae yeast cells by manual reagent handling*. T_{start} and T_{end} represent the temperatures at the beginning and at the end of each step, respectively. Total duration ~128 hours.

Step	T_{start}	T_{end}	Slope	Time (in hour)	Reagent	Transfer	Agitation	UV
1.	-90 °C	-90 °C	0	24.00	FS solution	Stay	On	
2.	-90 °C	-50 °C	5	08.00	FS solution	Exch/Fill	On	
3.	-50 °C	-50 °C	0	24.00	FS solution	Exch/Fill	On	
4.	-50 °C	-50 °C	0	00.01	Acetone	Exch/Fill	On	
5.	-50 °C	-50 °C	0	00.01	Acetone	Exch/Fill	On	
6.	-50 °C	-50 °C	0	00.01	Acetone	Exch/Fill	On	
7.	-50 °C	-50 °C	0	02.00	Acet/HM20 (25%)	Mix	On	
8.	-50 °C	-50 °C	0	03.00	Acet/HM20 (50%)	Mix	On	
9.	-50 °C	-50 °C	0	03.00	Acet/HM20 (75%)	Mix	On	
10.	-50 °C	-50 °C	0	02.00	HM20	Exch/Fill	On	
11.	-50 °C	-50 °C	0	02.00	HM20	Exch/Fill	On	
12.	-50 °C	-50 °C	0	02.00	HM20	Exch/Fill	On	
13.	-50 °C	-50 °C	0	24.00	HM20	Stay	Off	ON
14.	-50 °C	20 °C	5	14.00	HM20	Stay	Off	ON
15.	20 °C	20 °C	0	24.00	HM20	Stay	Off	ON

Table 8: *The protocol used for freeze substitution and Lowicryl HM20 low-temperature embedding of HP-frozen S. cerevisiae yeast cells using an automatic reagent handling system (Leica EM FSP).* T_{start} and T_{end} represent the temperatures at the beginning and at the end of each step, respectively. Slope = temperature raise (5 °C/hour). The processor was able to exchange/fill or to mix reagents and agitate the solution (if it was set). Total duration ~128 hours.

When ethanol:resin [3:1, 1:1, 1:3 (v:v)] infiltration mixtures were tested, additional washing with ethanol (1 min and 3 min step) was included after washing with acetone (step 6, Table 6 and 7).

The following protocol (see Table 9) was used for low-temperature dehydration and LR White resin embedding:

Step	T_{start}	T_{end}	Slope	Time (in hour)	Reagent	Transfer	Agitation
1.	-90 °C	-90 °C	0	24.00	FS solution	Stay	On
2.	-90 °C	-50 °C	5	08.00	FS solution	Exch/Fill	On
3.	-50 °C	-50 °C	0	24.00	FS solution	Exch/Fill	On
4.	-50 °C	0 °C	5	10.00	FS solution	Exch/Fill	On
5.	0 °C	0 °C	0	00.01	Acetone	Exch/Fill	On
6.	0 °C	0 °C	0	00.03	Ethanol	Exch/Fill	On
7.	0 °C	0 °C	0	00.03	Ethanol	Exch/Fill	On
8.	0 °C	0 °C	0	02.00	Ethanol:LR White (25%)	Mix	On
9.	0 °C	0 °C	0	02.00	Ethanol:LR White (50%)	Mix	On
10.	0 °C	0 °C	0	03.00	Ethanol: LR White (75%)	Mix	On
11.	0 °C	0 °C	0	03.00	LR White	Exch/Fill	On
12.	0 °C	0 °C	0	12.00	LR White	Exch/Fill	On
The samples were removed from the machine and further processed at room temperature							
13.	RT	RT		00.30	LR White		Shaker
14.	RT	RT		00.30	LR White		Shaker
15.	47 °C	47 °C		48.00	LR White		Thermostat

Table 9: *The protocol used for freeze substitution and LR White resin embedding of HP-frozen S. cerevisiae yeast cells.* T_{start} and T_{end} represent the temperatures at the beginning and at the end of each step, respectively. Slope = temperature raise (5 °C/hour). RT = room temperature. The last steps of infiltration and LR White embedding (13. – 15.) were performed as well as in the case of conventionally aldehyde-fixed samples (see Subchapter 3.1.3). Total duration ~137 hours.

3.2 CRYO-TEM OF LIPOSOMES AND OTHER VESICULAR STRUCTURES

The main approach encompasses the preparation of liposomes (Publication No.2, Subchapter 4.2) and/or similar nanoscopic vesicular structures (Publication No.3, Subchapter 4.3) for the cryo-TEM observation by the technique of a thin vitreous layer. As a description of the methods provided in Publications No.2 and No.3 of Chapter 4 (Subchapters 4.2.3 and 4.3.3, respectively) is only very brief, details of the sample preparation and cryo-TEM observation as well as data treatment follows in the next chapter.

3.2.1 NANOSCOPIC VESICULAR STRUCTURES

The materials were kindly provided by Mariusz Kepczynski research group from the Faculty of Chemistry, Jagellonian University in Krakow, in Poland. Details of their characteristics, purchase and preparation can be found in Publications No.2 and No.3.

Briefly, the samples under the study included the liposomes (made from egg yolk phosphatidylcholines), the cationic liposomes i.e., the liposomes covered with a dimethyldioctadecylammonium bromide (DODAB) surfactant, and the cationic liposomes covered with a novel silicone monomer tetra(methyldimethoxysilylethyl)-tetramethylcyclotetrasiloxane ($D_4^{ethyl\text{-}D}$). This silicone monomer was introduced to the cationic liposome dispersions at pH 8.5 or pH 10.2. The formed structures were characterized with different methods: dynamic light scattering, zeta potential measurements (not performed in our laboratory), and cryo-TEM analysis. Next, the catanionic DODAB/oleic acid (OA) dispersions (the cationic DODAB vesicles with integrated anionic OA surfactant) were analyzed with different methods such as differential interference contrast microscopy, differential scanning calorimetry and fluorescence anisotropy technique (not performed in our laboratory). The morphology of bilayer structures formed in the dispersions was inspected using cryo-TEM. It is worth to mention at least that the mole fractions of OA (X_{OA}) was equal to 0.0, 0.2, 0.4, 0.6, 0.8, and 1.0 and the total lipid content was constant and equal to 10 *mM*.

3.2.2 PREPARATION OF THE HOLEY-CARBON GRIDS FOR CRYO-TEM IMAGING

First, the glass slides were pre-cleaned with ethanol and placed for at least 5 min into a beaker containing 1% (w/v) aqueous benzalkonium chloride solution (OSVAN, Sigma-Aldrich, Czech Republic) in order to make their surface hydrophobic. Each slide was then

individually dipped into a beaker containing distilled water and slowly withdrawn by holding it at one end with a tweezers. The slide had to sort from the water perfectly dry, without water droplets sticking to its surface. If not, it was dipped again into OSVAN, and the procedure was repeated. Next, the slides were placed on a cold plate in order to get frozen droplets of water, which made holes in the OSVAN film after evaporation. The aluminum block was pre-cooled with liquid nitrogen to about -18 ºC. The OSVAN treated glass slides were then placed on the block for a while. It is known that the size of droplets of water condensing onto the cold support increases with relative humidity and the length of time the slide is on the cold plate (in our case, generally, each glass slide was placed onto the block for about 10 s). The slide was then removed and tilted at ~ 60° angle and a solution of plastic (0.25 % (w/v) cellulose acetate-butyrate in ethyl-acetate (TRIAFOL, Sigma-Aldrich) was poured over its surface using a Pasteur pipette. Slide with the cellulose film was then air-dried and checked under a phase contrast microscope at a 10x magnification for holes formation. If the holes had homogeneous shape and size, and were distributed on the entire length of the film, the slide was used for the next processing otherwise it was discarded. Metal block was wiped dry each time prior processing next slide.

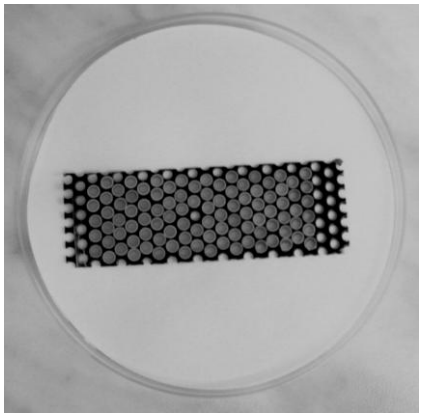

Figure 3-01: *A metal support with arranged copper EM grids covered with perforated cellulose film, after drying.*

Further, a special perforated metal support (see Figure 3-01) was dipped into a glass container filled with distilled water, and copper bare grids (Cat.# G200TT-Cu, Electron Microscopy Sciences) were arranged onto it. The film was loosened from the glass slide by immersion into a 1% (w/v) aqueous docusate sodium salt solution (PELEX, Sigma-Aldrich), for about 1 min. Then the slide was gently immersed into the water container, with the

cellulose film side up, at a ~30º angle with water. Film should detach from the slide and float at the water surface. If not, edges of the film on a slide should be gently scrubbed to facilitate its detachmend. Cellulose film was positioned above the grids and deposited on them by lowering the water level. After drying (Figure 3-01), the metal support with a film-coated grids was placed on a filter paper and coated with carbon to a 10 nm thick layer and then with platinum to a 3.5 nm layer using MED 020 Modular High Vacuum Coating System (BAL-TEC AG, Liechtenstein). Just before use, the cellulose film was dissolved by dipping the grid into pure ethyl-acetate and air-dried.

3.2.3 PLUNGE FREEZING

An EM grid with perforated carbon-platinum supporting film was mounted in a tweezers of the plunger (EMS-002 Plunge Freezer, Electron Microscopy Sciences). Typically 3 to 5 μL drop of the sample solution was placed onto the grid. The excess fluid was then blotted with the filter paper Whatman Grade No 1 (blotting time was about 1 - 3 s, depending on the sample), and the grid was quickly plunged into a liquid ethane bath, cooled with liquid nitrogen to about –182 ºC [91.15 K]. After freezing, the grid was rapidly transferred to a storage box under liquid nitrogen. To transfer the grid without rewarming into the cryo-electron microscope (TECNAI G20 SPHERA, FEI Company, Czech Republic), a single tilt cryo-transfer TEM specimen holder (Gatan 626, Gatan Inc., Pleasanton, USA) and a standard cryo-TEM transfer workstation (Gatan Inc.) was used.

3.2.4 LOW DOSE IMAGING

The images of vitrified samples were recorded at the lowest possible electron dose required to reduce radiation damage of the samples by cryo-TEM (typically<20 electrons/$Å^2$), at 120 kV accelerating voltage. Using the search mode, an area of interest was selected at low magnification, typically 5,000x and low intensity beam. Using the focus mode, the objective lenses were focused at high resolution (typically 14,500x for the DODAB/OA dispersions, and 25,000x for the liposome vesicles) on a neighboring area, close enough to have only small changes in the height and far enough to avoid irradiation of the area of interest. This was performed using an image shift (beam shift), whose angle and amplitude were selected. Underfocuses in the range of 1 to 3 μm were used to maintain adequate image contrast. The images were recorded on Gatan UltraScan^{TM} 1000 slow-scan CCD (CCD; charged coupled

device) camera using a Gatan DigitalMicrograph^{TM} software. The applied blotting conditions resulted in samples with thicknesses ranging from 100 to 300 nm.

3.2.5 DATA TREATMENT

Diameters of individual vesicles images extracted from cryo-TEM micrographs were estimated by standard Hough transformation and their distribution was subjected to probability density function analysis, which revealed and described the characteristic populations of vesicles present in the specimen (Hlaváč & Šonka, 1992).

Chapter 4 RESULTS

4.1 PUBLICATION No.1

Saccharomyces cerevisiae nuclear and nucleolar antigen preservation for immunoelectron microscopy

---

Authors: **V. Mistríková**[1,*], J. Bednár[1,2]

Published in*:* Folia Biologica (Praha) (2010), 56: 97-109

[1]Charles University in Prague, 1st Faculty of Medicine, Institute of Cellular Biology and Pathology and Institute of Physiology, Academy of Sciences of the Czech Republic, Department of Cell Biology, Prague, Czech Republic

[2]CNRS/UJF, Laboratoire de Spectrométrie Physique, UMR 5588, BP87, 140 Av. de la Physique, 38402 St. Martin d'Hères Cedex, Grenoble, France

[*]***Corresponding author:*** V. Mistrikova, e-mail: vmist@lf1.cuni.cz

Keywords: *Saccharomyces cerevisiae* · Nucleolus · Nucleus · Chemical fixation · High-pressure freezing · Freeze substitution · Immunoelectron microscopy

Funding sources: This work was supported by the Czech Grants no. MSM0021620806, LC535, AV0Z50110509, 303/03/H065 and 13308.

4.1.1 ABSTRACT

Yeast cells in general are known to be difficult to prepare for electron microscopy investigations particularly when the preservation of antigenicity is required. In this work, we compare various protocols for preparation of *Saccharomyces cerevisiae* cells for immunoelectron microscopy, ranging from classical chemical fixation to high-pressure freezing followed by freeze-substitution in different kinds of substitution media. Our aim was to establish a protocol giving optimal, routinely reproducible results for simultaneous retention of fine ultrastructural details and antigen immunoreactivity, with particular focus on the preservation of nuclear and nucleolar architecture. This was demonstrated by ultrastructural immunolocalization of various nucleolar (Nop1 and Nsr1), nuclear (Nsp1) and α-tubulin antigens. The protocol which we found to yield the best preserved *Saccharomyces cerevisiae* cells for both morphological and immunological studies included cryofixation by high-pressure freezing followed by freeze-substitution in acetone with 0.1% uranyl acetate and embedding in Lowicryl HM20. In addition, immunofluorescence detection of the antigens was performed and correlated with immunolabeling at the electron microscopy level.

4.1.2 INTRODUCTION

The nucleolus is known to be a highly dynamic nuclear subcompartment where the processes of rRNA synthesis and ribosome biogenesis take place (Hernandez-Verdun, 2006; Sirri *et al*, 2008). Mostly, the nucleoli of higher eukaryotes are more or less spherical regions, often without direct contact with the nuclear envelope, varying greatly in size, number and structure according to the cell type and metabolic state. Classical transmission electron microscopy (TEM) permits one to distinguish three basic nucleolar subcompartments characterized by specific ultrastructural arrangement: the electron lucent fibrillar centers (FCs) surrounded by highly contrasted dense fibrillar components (DFCs) and the granular components (GCs) formed by pre-ribosomal particles (Derenzini *et al*, 2009; Mosgoeller, 2004; Shaw & Doonan, 2005; Sirri *et al*, 2008). Nucleoli of both budding (*Saccharomyces cerevisiae*) and fission (*Schizosaccharomyces pombe*) yeast are considerably smaller than those of higher eukaryotes and their organization into clearly distinguishable domains is less apparent. TEM micrographs of chemically fixed *S. cerevisiae* cells generally reveal the nucleolus as a dense, crescent-shaped region occupying up to one-third of the nuclear volume, having extensive contacts with the nuclear envelope (Melese & Xue, 1995; Sicard *et al*, 1998;

Trumtel *et al*, 2000). Especially in the case of yeast cells, chemical fixation appears to be insufficient to uncover the fine structural organization of the nucleolus. Moreover, its use strongly compromises the antigenicity of nuclear and nucleolar epitopes. Considerably better results can be achieved by low-temperature preparation and processing techniques (cryo-methods) that allow for finer ultrastructural observations and improved immunocytochemical studies (Quintana, 1994). *S. cerevisiae* nucleolar subcompartments could only be distinguished in samples prepared in this way, though some morphological details (compared to higher eukaryotic cells) were still lost (Leger-Silvestre *et al*, 1999; Thiry & Lafontaine, 2005).

Nowadays, cryofixation by high-pressure freezing (HPF) followed by dehydration at subzero temperatures, i.e., freeze-substitution (FS), is the method of choice for the best preservation of cellular ultrastructure in numerous biological samples, e.g, Buser & Walther (2008); Hawes *et al* (2007); McDonald (2007); Vanhecke *et al* (2008). The cryo-preserved material displays an excellent morphology with considerably reduced numbers of artifacts when compared to chemically fixed samples. In this work, we apply these cryo-preparation methods to the study of the fine ultrastructure of *S. cerevisiae* nucleoli and to the immunolocalization of specific nuclear and nucleolar markers at the electron microscopy (EM) level. Although a number of protocols for chemical fixation (Mulholland & Botstein, 2002; Wright, 2000), cryofixation (Giddings, 2003; Humbel *et al*, 2001; McDonald, 2007; Murray, 2008; Walther & Ziegler, 2002) and Tokuyashu cryo-sectioning (Griffith *et al*, 2008) of yeast cells were proposed in the past, only a few have focused on fine nuclear and nucleolar antigen preservation in *S. cerevisiae* cells (Leger-Silvestre *et al*, 1999; Trumtel *et al*, 2000).

Here, we describe optimized recipes for *S. cerevisiae* preparation for immunoelectron microscopy (IEM) based on cryofixation by HPF followed by FS procedures and low-temperature embedding in Lowicryl HM20. Using these procedures, the cellular fine ultrastructure was retained to a great extent without loss of antigenicity. Their efficiency is demonstrated by direct comparison with equivalent immunolabeling experiments performed on conventionally chemically fixed and LR White embedded *S. cerevisiae* cells. Our results show that the immunoreactivity of two proteins that were analyzed (Nsr1 and Nsp1) was preserved exclusively in cryo-processed cells. Simultaneously, immunofluorescent visualization of the target antigens was performed at light microscopy (LM) level.

4.1.3 MATERIALS AND METHODS

4.1.3.1 Yeast strain, media and cultivation conditions

The *S. cerevisiae* haploid strain NOY 886 (*MATα rpa*135Δ::LEU2 *ade 2-1 ura3-1 his 3-11 trp1-1 leu2-3,112 can1-100 fob1Δ::HIS3* pNOY117 [*CEN RPA135 TRPI*]) (a kind gift of Yvonne S. Osheim, University of Virginia Health System, USA) was used throughout this study. Cells were grown at 26˚C in a standard YPD medium containing 1% yeast extract, 2% peptone, 2% D-(+)-glucose and 100 μg/ml adenine hemisulfate salt.

Unsynchronized yeast cells were used in each experiment. The day prior to fixation, a single colony of the yeast cells was used to inoculate 100 ml of YPD medium in a 250-ml Erlenmeyer flask and grown overnight with moderate shaking. The next day, the overnight culture was used to inoculate 5 ml of fresh YPD medium and grown to an early log phase (OD 600 0.2 - 0.4, corresponding to less than 10^7 cells/ml), then processed for the LM or EM studies.

4.1.3.2 Preparation of *S. cerevisiae* cells for immunoelectron microscopy

4.1.3.2.1 High-pressure freezing

Cryofixation was performed using a Leica EM PACT2 high-pressure freezer equipped with a rapid transfer system (Leica Microsystems, Vienna, Austria) as previously described (McDonald & Müller-Reichert, 2002). Approximately 5-ml aliquots of yeast culture (OD 0.2 – 0.4) were harvested by vacuum filtration using a 15-ml suction filtration apparatus (Millipore, Billerica, MA, USA) on 0.45 μm nitrocellulose membrane filters (Macherey Nagel, Düren, Germany), then placed on a plate with 1% agar in YPD medium in order to prevent dehydration of the yeast during the transfer. Using a sterile toothpick, the yeast paste was scraped off the filter onto a membrane carrier (1.5 mm in diameter, 0.1 mm deep, Cat.# 16707898, Leica instruments) under a stereomicroscope. Precautions were taken to thoroughly fill the entire volume of the carrier cavity. The samples were immediately high-pressure frozen (HP-frozen) and stored under liquid N_2 until FS. The time interval between the harvesting of the cells and freezing was kept under one minute.

4.1.3.2.2 Freeze substitution

Freeze substitution was performed using an automatic FS instrument (Leica EM AFS2, Leica Microsystems) equipped with an EM FS processor. HP-frozen samples were first placed into a reagent bath loaded with one of the FS solutions under test pre-cooled to -90 ˚C, and processed for 24 h. Next, the temperature was gradually increased at a rate of 5 ˚C/h (8 h in total) to -50 ˚C and held constant for 24 h. All successive processing steps were performed at this temperature. Samples were then washed three times with pure acetone and gradually infiltrated with 3:1, 1:1 and 1:3 acetone:resin (v:v) mixtures, 2 to 3 h for each step. Lowicryl HM20 (HM20 kit, Cat.# 14340, Electron Microscopy Sciences, Hatfield, PA, USA) was used for low-temperature embedding. Before use, the resin was degassed with a stream of dry nitrogen to remove oxygen which could interfere with the polymerization. The mixture was exchanged with pure resin at least three times, using 2 h for each incubation. Polymerization under UV light (using a UV LED lamp integrated in the FS processor) was performed for 24 h at -50 ˚C and for an additional 24 h at +20 ˚C (the temperature was gradually increased at a rate of 5 ˚C/h -14 h in total).

The following FS media were used: (1) anhydrous acetone (EM grade, Polysciences Europe GmbH, Eppelheim, Germany); (2) acetone with 0.1% glutaraldehyde (GA) - made from a 50% aqueous GA stock solution (Electron Microscopy Sciences); (3) acetone with 0.1% uranyl acetate (UA, Merck, Darmstadt, Germany) - prepared from a 10% methanolic stock solution a day prior to experiment, then filtered three times through a syringe filter (0.22 μm) before use and (4) acetone with 0.1% UA and 0.1% GA.

4.1.3.2.3 Chemical fixation

Yeast cells were fixed in a solution of 4% (w/v) formaldehyde (FA, Fluka, Buchs, Switzerland) in 0.1 M PIPES (pH 6.8), 1 *mM* $CaCl_2$, 1 *mM* $MgCl_2$ and 0.1 M D-Sorbitol with or without addition of various concentrations of GA (0.05 to 0.5%) for 1 h at room temperature (RT). The cells were washed twice, for 15 min, in 0.1 M PIPES with 0.1 M D-Sorbitol and once in 0.1 M PIPES alone and treated with 1% $NaIO_4$ and 50 *mM* NH_4Cl as described (Mulholland & Botstein, 2002). Dehydration was performed successively on ice in graded ethanol series (25, 50, 75, 95 and 100% ethanol) in 5 min steps. Three changes of 100% ethanol were applied and the final step was performed at RT. The dehydrated cells were infiltrated with 2:1, 1:1 and 1:2 ethanol:LR White resin (v:v) mixtures and twice with pure LR

White (Medium grade, kit, Cat.# 14380, Electron Microscopy Sciences), each step was for 1 h at RT. The third infiltration step was performed overnight at 4 °C. The next day, the resin was again exchanged, and incubated for about 30 min at RT. Finally, the samples were transferred into gelatin capsules (size 1, Leica instruments) containing fresh resin, allowed to settle for 15 min and polymerized at 47 °C for 2 or 3 days.

4.1.3.2.4 Microtomy, staining and electron microscopy

Ultrathin sections (60 nm) were prepared on a Reichert Ultracut S microtome using a diamond knife (45˚ Diatome, Ft. Washington, PA, USA) and collected on Formvar/carbon coated nickel or copper grids. Sections of chemically fixed yeast cells were post-stained using 2% aqueous uranyl acetate for 5 min and lead citrate (Reynolds, 1963) for 1 min. Sections of HP-frozen/acetone alone or acetone/GA substituted cells were post-stained similarly as described above, except that 2% uranyl acetate in 70% methanol was used. Sections of acetone/UA or acetone/UA/GA substituted cells were not post-stained. The samples were then imaged with a Tecnai G20 Sphera transmission electron microscope (FEI Company, Brno, Czech Republic) operating at 120 kV. Images were recorded with a Gatan Ultrascan 1000 CCD camera.

4.1.3.2.5 Immunolabeling

Thin sections mounted on nickel grids were first pre-blocked with 5% (w/v) normal goat serum (NGS) in phosphate-buffered saline (PBS, pH 7.4) for 30 min and then incubated with primary antibody diluted in 1% (w/v) bovine serum albumine (BSA) and 0.05% Tween-20 in PBS for 1 h and 45 min in a humid chamber at RT. Afterwards, the grids were first washed in 0.05% Tween-20 in PBS and then in PBS alone. Before the secondary antibody was applied, the grids were blocked with 1% NGS in PBS for 10 min. Gold-conjugated secondary antibody was diluted in PBS and incubation was performed for 1 h in a humid chamber at RT. Finally, the grids were washed in PBS and in double-distilled water, air-dried, and post-stained as described above or, alternatively, left unstained. In negative control experiments the incubation with primary antibody was omitted.

For quantification of immunogold labeling, Nop1 and Nsr1 antigens were selected due to their specific localization in nucleolus. Sets of 10 micrographs of yeast cell nuclei (nucleoli) at a magnification of x 7800 were chosen randomly for each of FS media and a

labeling density was determined in terms of a number of gold particles per square micrometer. For each set an average and standard deviation were determined. The density was evaluated for the nucleolus and for the rest of the cell section, giving thus the information about the level of nonspecific labeling. The measurements were performed using ImageJ software (Rasband, 1997-2009).

4.1.3.3 Immunofluorescence microscopy

The cells were fixed with 4% (w/v) FA in 0.1 M potassium phosphate buffer (KPi), pH 6.8 added directly to the growing culture as a 2x stock. Fixation was performed for 2 h at RT. Fixed cells were washed twice in 0.1 M KPi and once in 0.1 M KPi with 1.2 M D-Sortbitol (solution P). Cell walls were removed using zymolyase (Cat.# E1004, ZymoResearch, Orange, CA, USA) diluted 1:50 in solution P at 30 °C for 10 to 20 min. Digestion of the cell walls was monitored by phase contrast light microscopy using a 100x oil-immersion objective. The spheroplasted cells were washed again in solution P and left to sediment for 10 min on poly-L-lysine (0.01% solution, Sigma, Saint Louis, USA) treated coverslips. Permeabilization of the cells was performed as described by Pringle *et al* (1989), with 0.1% Triton X-100 in PBS for 30 min at RT or alternatively by dipping the coverslips into methanol for 6 min and subsequently into acetone for 30 s, both at -20 °C. Next, the samples were pre-blocked for 20 min with the blocking buffer (1% (w/v) BSA in PBS, pH 7.4), incubated for 1 h with primary antibody, washed in PBS and incubated for an additional 1 hour with fluorescent secondary antibody. Both antibodies were diluted in the blocking buffer and all steps were performed at RT. Finally, the cells were washed in PBS and in double-distilled water, embedded in Mowiol/DABCO mounting medium (Fluka) containing 0.4 μg/ml DAPI (4',6-diamidino-2-phenylindole) and placed onto slides. The cells were examined with a Leica TCS SP5 laser scanning confocal microscope (Leica Microsystems) using a 100x/1.4 NA oil immersion objective.

4.1.3.4 Antibodies

The following primary antibodies were used: (a) anti-fibrillarin (Abcam plc, Cambridge, UK), diluted 1:500 for LM and 1:5 for EM; (b) anti-Nsr1p (Abcam), diluted 1:400 for LM and 1:7 for EM; (c) anti-Nsp1p (Abcam), diluted 1:450 for LM and 1:5 for EM and (d) anti-α-tubulin (Sigma) diluted 1:2000 for LM and 1:50 for EM. All used primary

antibodies were mouse monoclonal, IgG isotype. Cy3-labeled donkey anti-mouse secondary antibody diluted 1:500 and 12 nm gold conjugated goat anti-mouse secondary antibody diluted 1:10 (both from Jackson ImmunoResearch, Suffolk, UK) were used for LM and EM detection, respectively.

4.1.4 RESULTS

4.1.4.1 Chemically fixed cells

4.1.4.1.1 Formaldehyde-fixed cells

Typically, 4% FA-fixed cells (Figure 4-01A) exhibited irregular shapes and most of the cellular organelles showed improper preservation. The cytoplasm was retracted and distinct plasma membrane invaginations into the cytoplasm were frequently observed (black arrows). The vacuoles were rather small and numerous in most cases and their contents were almost always lost. The mitochondria, Golgi cisternae, endoplasmatic reticulum (ER) and nucleus were distinguishable only due to the white profile of their membranes, very likely a consequence of omitting $KMnO_4$ and/or OsO_4 treatment (Wright, 2000). Prominently, the shape of the nuclear envelope was strongly irregular and nuclear organization, i.e., the presence of recognizable regions of heterochromatin and euchromatin, was almost invisible. In a majority of the nucleoli that were investigated, the FC/DFC/GC compartments were not recognizable, though zones of lower and higher electron densities were observed.

4.1.4.1.2 Formaldehyde/Glutaraldehyde-fixed cells

The ultrastructural preservation in FA/GA-fixed cells was apparently better (Figures 4-01B-D) despite the fact that the GA concentrations that were used were kept low (from 0.05 to 0.5%) due to the requirement of antigenicity preservation. Generally, the cytoplasmic organelles showed a morphology similar to those of FA-fixed cells and plasma membrane invaginations were still present (black arrows); however, the retractions of the cytoplasm were nearly eliminated. Preservation of the vacuolar content gradually improved with increasing concentration of GA, though without reaching an acceptable level. Nuclear shape was still strongly irregular and the nucleoplasm showed a homogeneous grainy texture. As in FA-fixed cells, the nucleolar subcompartments were hardly recognizable.

4.1.4.2 High-pressure freezing and freeze-substitution

We next performed cryofixation by HPF method and subsequently processed *S. cerevisiae* cells at low temperatures by FS procedure using various substitution solutions (see Subchapter 4.1.3.2.2). Low-viscosity non-polar Lowicryl HM20 was selected as an embedding medium as it permits processing of samples at subzero temperatures and has been used successfully for IEM procedures (Giddings, 2003; Hofmann *et al*, 1998; van Tuinen & Riezman, 1987).

4.1.4.2.1 FS medium 1: acetone alone

The substitution of *S. cerevisiae* cells in acetone alone (Figure 4-02A) resulted in structural and ultrastructural preservation noticeably superior to that generally observed in aldehyde-fixed cells (Figures 4-01A-D). Lowicryl HM20 (and K4M) is known to produce high contrast of the sections compared to other embedding media (Bendayan & Shore, 1982). Thus even in unstained sections (data not shown) the major morphological features of the cells (e.g., vacuoles, nuclei, etc.) were obvious but finer details were difficult to distinguish unless the post-staining procedure was applied (Figure 4-02A). The overall ultrastructural preservation of the cells was very good though infiltration with the resin was imperfect in many cases. Gaps between the resin and the cells were commonly observed. In some cases, whole cells popped out of the sections (data not shown).

4.1.4.2.2 FS medium 2: acetone with 0.1% glutaraldehyde

The cells substituted in acetone with 0.1 % GA (Figure 4-02B) showed better resin infiltration (no yeast cells were lost during the preparation of thin sections) and ultrastructural preservation was similar to that observed in acetone-only substituted yeast cells. As revealed by post-staining, all cytoplasmic structures in the cells (mitochondria, ERs, Golgi compartments, nuclei, etc.) were well preserved.

4.1.4.2.3 FS medium 3: acetone with 0.1% uranyl acetate

The best results were obtained with substitution in acetone with 0.1% UA (Figure 4-02C). Even at this concentration of UA, the overall contrast of the sections was notably

enhanced, in accordance with previous observations (van Donselaar *et al*, 2007; Walther & Ziegler, 2002). Moreover, fine contours of the membranes were emphasized thus the individual organelles were readily recognized even without the use of the post-staining procedure.

4.1.4.2.4 FS medium 4: acetone with 0.1% uranyl acetate and 0.1% glutaraldehyde

The results obtained when acetone containing both 0.1% UA and 0.1% GA (Figures 4-02D, 4-03A) was used were very similar to those of acetone/GA substituted samples. The quality of the structure preservation was the same, though the contrast was significantly better.

Overall, all the FS media that were used yielded well-preserved *S. cerevisiae* cells compared to conventionally aldehyde fixed cells (compare Figures 4-01 and 4-02). As shown in Figure 4-03, the cell walls, plasma membranes, vacuolar membranes, nuclear envelopes, etc. showed smooth and continuous contours. Moreover, the fine details of the cell walls were very well preserved in a great majority of the cells (Figure 4-03B). Plasma membrane invaginations were less pronounced. The vacuoles had a spherical shapes and contents of uniform density (Figures 4-03A, B). In the cytoplasm, the individual ribosomes, rough ER (Figure 4-03C), Golgi cisternae (Figure 4-03D), mitochondria (Figure 4-03E), multivesicular bodies (Figure 4-03F), etc. were clearly distinguishable. Regular and smooth profiles of the nuclei were always observed (Figures 4-03A and 4-04A). When UA was added to the FS solution it was much easier to observe the double membrane profile of the nuclear envelope (Figures 4-03C, 4-04A, B) and its interruption by nuclear pores (Figures 4-04A, B, arrowheads) than it was in acetone-only or acetone/GA substituted yeast cells. Microtubules (Figure 4-04C) and spindle pole bodies (SPB) were also easily localized (Figures 4-04D, E). Generally, substitution with acetone/UA FS medium yielded the best overall results but some particular structures, e.g. SPB mentioned above (compare Figures 4-04D and 4-04E), were better defined when the stain was not present in the FS medium and their contrast was obtained by post-staining. The nuclear and nucleolar chromatin was always well preserved and very dense in all four types of FS media described above (Figures 4-05A-D). In the nucleolar region, FCs were easily distinguished as the zones of lower electron densities (Figures 4-05, asterisks) surrounded by electron-dense areas in which both dense fibrils and pre-ribosomal particles were localized (arrowheads).

4.1.4.3 Immunofluorescence and immunoelectron microscopy

Next, the ultrastructural immunolocalization of various antigens related to nuclear and nucleolar function was examined on thin sections of both chemically fixed (data not shown) and HP-frozen/FS *S. cerevisiae* cells. Nop1 and Nsr1 were used as nucleolar markers, Nsp1 as a nuclear envelope marker and α-tubulin as a marker of microtubules. Each of the proteins that were analyzed was first specifically localized via indirect immunofluorescent (IF) staining of permeabilized yeast cells.

4.1.4.3.1 Nop1 protein

Nop1 is a yeast nucleolar protein known to be structurally and functionally homologous to vertebrate fibrillarin which is essential for viability and pre-rRNA processing (Schimmang *et al*, 1989; Tollervey *et al*, 1991). Nop1 was previously specifically localized both by indirect IF (Qiu *et al*, 2008; Schimmang *et al*, 1989; Tollervey *et al*, 1991) and IEM procedures (Leger-Silvestre *et al*, 1999; Trumtel *et al*, 2000). As expected, our experiments revealed a specific, intense and often crescent-shaped labeling pattern characteristic of the yeast nucleolus at the LM level (Figure 4-06A). Consistent with IF results, Nop1 was localized to the nucleolus at the EM level, predominantly to the dense areas surrounding the FCs of lower electron densities (Figure 4-06B, arrowheads). The pattern of labeling was similar on both chemically fixed and cryo-processed cells; however, the intensity of the labeling and localization with respect to the individual nucleolar subcomparments was more prominent on sections of HP-frozen/FS yeast cells.

4.1.4.3.2 Nsr1 protein

Nsr1 is a non-ribosomal nucleolar protein known as the vertebrate nucleolin ortholog (Lee *et al*, 1992; Yan & Melese, 1993) and functional homologue of *Schizosaccharomyces pombe* gar2 protein (Gulli *et al*, 1995). Similarly to Nop1, Nsr1 is involved in rRNA maturation, ribosome assembly and possibly in nucleo-cytoplasmic transport (Gulli *et al*, 1995; Kondo & Inouye, 1992; Lee *et al*, 1992). In agreement with previous results (Xu *et al*, 2003; Yan & Melese, 1993), we have specifically localized Nsr1 to the *S. cerevisiae* nucleolus using an indirect IF staining (Figure 4-06C). As reported earlier (Leger-Silvestre *et al*, 1997), *S. pombe* gar2 protein was localized at the EM level along the DFCs and around the FCs,

although nucleolin was detected in DFCs and rarely in both the GCs and FCs in vertebrate cells (Escande *et al*, 1985; Spector *et al*, 1984). However, the immunocytochemical detection of *S. cerevisiae* Nsr1 protein has not been reported. Here, thin sections of HP-frozen/FS and chemically fixed yeast cells were used for Nsr1 localization using on-section immunogold labeling. Gold particles were mainly distributed along and/or in the dense parts of the nucleolus, in agreement with (Leger-Silvestre *et al*, 1997) results. Importantly, no labeling was detected on thin sections of chemically fixed yeast cells.

4.1.4.3.3 Nsp1 protein

Nsp1 is one of the most abundant nucleoporins in yeast. It plays an important role in facilitating bidirectional transport of materials through nuclear pore complexes (NPC) (Bailer *et al*, 2001; Fahrenkrog *et al*, 2000). Previously, Nsp1 was specifically localized by a pre-embedding method at the EM level (Fahrenkrog *et al*, 2000). Here, indirect IF staining of Nsp1 revealed the *S. cerevisiae* nuclear envelope (Figure 4-07A). Next, we immunolocalized Nsp1 on thin sections of both chemically fixed and HP-frozen/FS *S. cerevisiae* cells. Consistent with previous results, most of the NPCs present in the sections of HP-frozen/FS yeast cells were specifically labeled. The gold particles were detected inside the NPCs and both on their nucleoplasmic and cytoplasmic sides (Figure 4-07B, arrowheads). No Nsp1 signal was detected on sections of chemically fixed cells.

4.1.4.3.4 α-Tubulin

Immunodetection of *α*-tubulin in *S. cerevisiae* cells is shown in Figures 4-08A, B. Microtubules running from the SPBs embedded in the nuclear envelope were specifically labeled both by indirect IF staining (Figure 4-08A) and by on-section immunogold labeling (Figure 4-08B). Both patterns were consistent with previous results (Kilmartin & Adams, 1984; Müller-Reichert *et al*, 2003; Sato *et al*, 1996). The intensity of the labeling was similar on both chemically fixed and HP-frozen/FS yeast cells sections though in the case of chemically fixed cells microtubules were not directly visible (data not shown).

4.1.5 DISCUSSION

In this study, we aimed to find optimal conditions for immunodetection of selected nuclear and nucleolar antigens in *S. cerevisiae* cells both at the LM and EM levels. The fine ultrastructural preservation and the efficiency of the IEM detection was compared on thin sections of cells prepared either by conventional fixation methods at RT or by HPF method followed by dehydration, infiltration and embedding performed at low (subzero) temperatures.

Chemical fixation was done using either 4% FA (Figure 4-01A) or combined FA/GA fixation (Figures 4-01B-D), followed by multiple centrifugation, washing and resuspension steps, including sodium metaperiodate and ammonium chloride treatment and LR White embedding (Mulholland & Botstein, 2002; Wright, 2000). Using these processing methods, the majority of the cells showed similar structural preservation and artifacts referred to as 'typical' for that kind of processing (see Subchapter 4.1.4.1). These cells can be used for routine morphological observations but in most cases they are not suitable for immunolocalization experiments due to improper preservation of both the fine ultrastructure and antigenicity. The use of even very weak chemical fixation can destroy some sensitive antigens. In our study, this was the case of Nsr1 and Nsp1 which were successfuly localized only in the HP-frozen/FS yeast cells.

An alternative to chemical fixation of the samples is a physical one, by vitrification, as performed by the HPF method (Dubochet, 2007; McDonald, 2007; Studer *et al*, 2008). It is well known that the specimen loading into the HP-freezer is one of the most critical steps for obtaining well-preserved samples (McDonald, 1999). Concentrating of *S. cerevisiae* cells using a vacuum filtration apparatus (McDonald, 2007; Murray, 2008), also used in our experiments (see Subchapter 4.1.3.2.1), proved to be superior to other procedures like centrifugation or aspiration of the yeast cells into the specimen tubes (Hohenberg *et al*, 1994). Using this approach it was not necessary to use additive cryo-protectants (e.g., BSA solution, 1-hexadecane, etc.) to achieve flawless cryofixation as the homogeneous yeast paste obtained by filtration entirely filled the cavity in the specimen carriers. Immediately after the freezing step, the specimens were dehydrated at low temperatures by the FS procedure (Schwarz *et al*, 1993). The details of the FS procedure are generally adapted for the type of material being investigated and for the main goal of the experiment, particularly fine ultrastructural or immunological studies. Different FS protocols for immunocytochemical studies of yeast cells have been published (Giddings, 2003; Hofmann *et al*, 1998; Chial *et al*, 1998; Müller-

Reichert *et al*, 2003). In our protocol we selected the substitution parameters of 24 h at -90 °C and 24 h at -50 °C in four different FS media (see Subchapters 4.1.3.2.2 and 4.1.4.2). To avoid the high temperatures neccessary for LR White embedding, we have opted for lowicryl resins designed for low-temperature embedding (Carlemalm *et al*, 1982). We preferred the non-polar Lowicryl HM20, which was previously successfully used for immunocytochemical studies (Giddings, 2003; Hofmann *et al*, 1998; Müller-Reichert *et al*, 2003) despite its hydrophobic properties. The hydrophilic Lowicryls K4M and HM23 were also reported as a convenient embedding media (Hofmann *et al*, 1998; Quintana, 1994).

The cells substituted in acetone alone (Figure 4-02A) or in acetone with 0.1% GA (Figure 4-02B) showed similar structural preservation. In both cases, however, post-staining was neccessary to reveal all the structural features typical of yeast cells. Several previous studies have described FS with acetone only as an approach that often gives unsatisfactory results (Porta & Lopez-Iglesias, 1998), but in others well preserved samples were obtained (Hawes *et al*, 2007; von Schack & Fakan, 1993). In our experiments, this procedure resulted in a very good overall ultrastructural preservation. The only drawback was the already mentioned detachment of the cells from the resin during the preparation of thin sections. This is often attributed to imperfect infiltration. As described previously (Murray, 2008), it is rather difficult to infiltrate yeast cells with lowicryls at low temperatures. Artifacts such as rupture of the cell wall and even rupture of the nuclear envelope can sometimes be observed. In our experiments, the ultrastructural preservation of the interior of the cells substituted in acetone alone was well preserved without the artifacts mentioned above. However, a complete detachment of these cells from the sections occurred frequently, similar to what was observed with LR White-embedded, chemically fixed yeast cells that were not treated with sodium metaperiodate (data not shown). We tried to solve this problem by replacing the acetone/Lowicryl mixtures during infiltration by ethanol/Lowicryl solutions since this was suggested to improve infiltration in tissues (Yanick Schwab – personal communication). However, results were not significantly better (data not shown). The presence of GA and/or UA in the FS media resulted in the elimination of cell detachments from the lowicryl sections and at the same time improved the preservation of the structure of the cell walls - their fine details became clearly visible in a great majority of cells (Figure 4-03A, B). Interestingly, the use of GA as a fixative in the FS media has previously been questioned in some studies, as the addition of aqueous GA increases the water content in the substitution mixture and decreases the quality of the ultrastructural preservation (Steinbrecht & Müller, 1987). It was shown later that the addition of GA could be profitable (Giddings, 2003). As the GA starts to be

chemically active only above -50 °C, the fixative can infiltrate the whole specimen during the first step of substitution (performed at -90 °C) without reacting (Schwarz et al, 1993). Moreover, the addition of water up to 5% was shown to markedly enhance membrane contrast without impairing ultrastructural preservation (Walther & Ziegler, 2002). In our experiments, cells substituted in the presence of GA were well preserved (Figures 4-02B, D and 3A) though occasionally the vacuolar content could be seen to be partially emptied into the cytosol. This phenomenon was also frequently observed in cells substituted in higher concentrations of GA (up to 0.7%) and in acetone/UA/GA substituted cells (data not shown). Since it was not generally observed in acetone/UA substituted cells, it can presumably not originate from the high-pressure shock applied during freezing. It is also not obvious to attribute its origin to the action of GA. To our knowledge, this 'artifact' has never been described in the literature.

In cells where UA was added to the FS medium, no post-staining was necessary as the UA present produced sufficient contrast (e.g., Figures 4-02C, D, 4-03A-F, 4-04A-D). The cells showed excellent ultrastructural preservation, which makes this type of specimen preparation very convenient for both immunocytochemical and morphological studies. Moreover, since the stain (UA) is distributed throughout the entire volume of the sample and not only at or in the vicinity of the surface as after post-staining, this type of preparation is optimal for electron tomography. On the other hand, because the image is a projection of the section volume onto a plane, the spatial distribution of stain can blur the details of structures with complex three-dimensional structural organization. This is probably the reason for the improved appearance of the SPB in post-stained samples (Figure 4-04E).

4.1.5.1 *S. cerevisiae* nuclear ultrastructure

Application of conventional chemical fixation methods that allowed subsequent immunolocalization resulted in nuclei with noticeably irregular shapes in both FA (Figure 4-01A) and FA/GA-fixed (Figures 4-01B-D) *S. cerevisiae* cells. The nucleoplasm appeared homogeneous without convincing contrast between the regions of heterochromatin and euchromatin.

In HP-frozen/FS *S. cerevisiae* cells, regular and smooth profiles of the nuclei were always observed (Figures 4-02A-D). It is known that well-preserved nuclei are the first indication of high quality cryofixation. If the freezing step is not performed adequately, a net-like pattern within the chromatin is often observed, referred to as ice crystal damage (Murray,

2008). In our samples, the material in the nuclei was well-preserved, and very dense. Generally, no reticulation of the chromatin was observed (Figures 4-05A-D). The nucleoplasm pattern was almost identical in the cells substituted in all four types of FS media described above. As reported earlier (von Schack & Fakan, 1993), in cryo-fixed samples of higher eukaryotic cells (not substituted in osmium-acetone mixtures) the chromatin contrast can be 'altered' depending on the embedding media that is used. For example, in acetone alone FS samples embedded in Epon or Lowicryl HM23, the heterochromatin regions were more electron-dense than the euchromatin regions. However, this contrast was reversed when e.g. Lowicryl K11M or LR White was used. In our experiments, the contrast between heterochromatin and euchromatin was visibly improved in HPF/FS samples compared to that observed in the chemically fixed cells, but it still remained rather weak. Neither addition of UA to the FS media (Figures 4-05C, D) nor additional post-staining of acetone/UA substituted cells (data not shown) led to any improvement. Combined with the particular ultrastructure of the yeast nucleoplasm, the identification of the heterochromatin/euchromatin regions was rather difficult. There were however some indications suggesting that contrast reversal occurred. More electron-dense chromatin was clearly observed in the nuclear pore areas (Figures 4-04A-B, arrowheads), which are generally considered to be devoid of heterochromatin (Fedorova & Zink, 2008).

4.1.5.2 *S. cerevisiae* nucleolar ultrastructure

Although the nucleolus of yeast cells is rather well visible at the EM level in most samples prepared by chemical fixation, it is more difficult to distinguish the three distinct nucleolar subcompartments (Leger-Silvestre *et al*, 1999; Melese & Xue, 1995; Sicard *et al*, 1998; Trumtel *et al*, 2000). The unambiguous identification of an electron-lucid zones resembling the FCs, surrounded by DFCs and GCs has been reported only for *S. cerevisiae* cells prepared by cryo-methods (Leger-Silvestre *et al*, 1999). This identification was questioned however (Thiry & Lafontaine, 2005), and it was proposed that *S. cerevisiae* nucleoli exhibit bipartite organization as only FC and GC compartments could be unambiguously discerned.

In our experiments, most of the investigated nucleoli in FA and FA/GA-fixed *S. cerevisiae* cells had barely detectable subnucleolar organization (Figures 4-01A-D). Electron-lucid zones surrounded by zones of higher electron densities were occasionally observed, although the pre-ribosomal particles that are known to form the GCs were not seen clearly. In

contrast, the nucleoli of HP-frozen yeast cells showed detailed nucleolar ultrastructure in all four types of FS media that were used (Figures 4-05A-D). The electron-lucid FCs could be clearly distinguished (Figures 4-05, asterisks) against the dense chromatin that formed the rest of the nucleolus and exhibited both granular and fibrillar aspects (Figures 4-05, arrowheads). Thus it was hard to identify the electron-dense areas as either DFCs or GCs though they are predicted to have different ultrastructural arrangements. Out of all four FS media, the nucleoli of acetone/UA substituted yeast cells were the most distinct with slightly coarser structure (Figure 4-05B). Since clear FC/DFC/GC compartmentalization was never observed in any of our samples, our findings are in agreement with the bipartite model of *S. cerevisiae* nucleolar organization (Thiry & Lafontaine, 2005).

4.1.5.3 Immunocytochemistry

Different proteins closely associated with nuclear (Nsp1) or nucleolar (Nop1 and Nsr1) functions as well as α-tubulin were selected as target antigens for both LM and EM detection. Immunocytochemical studies performed on thin sections of cells prepared with our HPF/FS protocol gave very satisfactory results, often revealing antigenic sites which were hardly or not at all detected in cells processed by conventional chemical fixation procedures. Due to the improved ultrastructural preservation it was much easier to simultaneously correlate the localization of specific antigenic sites with fine details preserved in the cell nucleus. Thus, Nop1 (Figure 4-06B) and Nsr1 (Figure 4-06D) were clearly localized to the dense parts of the yeast nucleolus, resembling mostly the DFCs. Interestingly, no Nsr1 labeling was detected on sections of both FA and FA/GA-fixed yeast cells. A similar situation was observed in the case of Nsp1, which was otherwise clearly detected on sections of HP-frozen/FS cells (Figure 4-07B). To determine whether the antigenicity of these proteins was impaired by fixation procedure or by heat polymerization (+47 °C in the case of LR White), the HP-frozen/FS yeast cells were embedded in LR White. Both antigens gave the same pattern and labeling intensity as in Lowicryl HM20 low-temperature embedded samples (data not shown), thus demonstrating that in this particular case the chemical fixation, despite being very weak, was probably the main cause of antigenicity loss, and not the heat polymerization. The pattern of α-tubulin labeling was the same in both HP-frozen/FS (Figure 4-08B) and FA and FA/GA-fixed yeast cells (data not shown).

Next, we compared the efficiency of on-section immunogold labeling of Nop1 and Nsr1 antigens between yeast cells substituted in the different FS media described in this study.

With the exception of acetone/GA, the immunolabeling efficiency revealed to be approximately equal (within the error bar) for all used FS media giving for the nucleolus area approximately 23 and 16 gold particles/μm^2 for Nop1 and Nsr1, respectively. On the other hand, the non-specific background labeling (outside the nucleolus) was increased in acetone-only and acetone/GA FS samples, 2 ± 5 gold particles/ μm^2 for Nop1 and 4 ± 5 for Nsr1, while in other two media it was below 0.5 for both antibodies. This would suggest a positive role of UA in suppresion of non-specific labeling. Similar results with increasing non-specific labeling were previously observed in cryo-fixed/FS tissue samples (von Schack & Fakan, 1993) and in HP-frozen and subsequently rehydrated samples (van Donselaar *et al*, 2007). Although efficient immunodetection of particular antigens was reported even after adding GA in FS media at a concentration of up to 0.25% (Giddings, 2003; Hawes *et al*, 2007; McDonald & Müller-Reichert, 2002), we decided to keep the concentrations of both GA and UA very low (0.1% final) in the present study in order to maximize retention of antigenicity for tested antigens. Even at this concentration, the addition of GA to acetone had an opposite effect on the localization of the two antigens. While for Nop1 the intensity of labeling doubled to 50 ± 12 gold particles/μm^2 in the case of Nsr1 it dropped to 8 ± 2 gold particles/μm^2. This suggests that use of GA as the only fixative in the substitution media can have an unpredictable impact on the immunolabeling efficiency. The addition of UA or combination of GA with UA to FS media therefore seems to be more recomendable choice.

In conclusion, we have compared in this study different ways to prepare *S. cerevisiae* cells for immunolocalization of proteins known to be closely related to nuclear and nucleolar functions, both at LM and EM level. An approach using weak chemical fixation was compared with a high-pressure freezing method followed by dehydration via freeze-substitution in different substitution media. Out of all tested combinations, we found the freeze-substitution in acetone with 0.1% UA and low-temperature embedding in Lowicryl HM20 to be the most universal and to give the best preserved *S. cerevisiae* cells for both morphological and immunological studies.

4.1.6 ACKNOWLEDGEMENTS

We are grateful to Yvonne S. Osheim and Ann L. Beyer from Department of Microbiology, University of Virginia Health System (USA) for providing the yeast cell strain NOY 886. We also thank Lubomír Kováčik for assistance with the preparation of figures and Christian Lanctôt and Guy Hagen for critical editing of the manuscript.

4.1.7 FIGURE LEGENDS

Figure 4-01: *Morphology of chemically fixed and LR White embedded S. cerevisiae cells.* Conventional fixation for TEM (IEM) with A - 4% FA alone, B - 4% FA in combination with 0.05% GA, C - with 0.3% GA, and D - with 0.5% GA. Black arrows point to plasma membrane invaginations. CW, cell wall; M, mitochondria; Np, nucleoplasm; Nu, nucleolus; V, vacuole. Sections were post-stained. Scale bar = 500 nm.

Figure 4-02: *Morphology of Lowicryl HM20 embedded S. cerevisiae cells after high-pressure freezing and freeze-substitution in different media.* Substitution in A - acetone alone, B - acetone with 0.1% GA, C - acetone with 0.1% UA, and D - acetone with 0.1% UA + 0.1% GA. M, mitochondria; Np, nucleoplasm; Nu, nucleolus; V, vacuole. Sections were post-stained (A, B) or left without post-staining (C, D). Scale bar = 500 nm.

Figure 4-03: *Details of various cell components preserved in S. cerevisiae cells after high-pressure freezing and freeze-substitution.* A - Budding yeast cell substituted in acetone with 0.1% UA + 0.1% GA. B - F - Fine ultrastructural details of the cells substituted in acetone with 0.1% UA. CW, cell wall; GC, Golgi cisternae; NE, nuclear envelope; Np, nucleoplasm; Nu, nucleolus; M, mitochondria; MVB, multivesicular body; PM, plasma membrane; rER, rough endoplasmatic reticulum; V, vacuole. Sections were not post-stained. Scale bar = 500 nm (A), 200 nm (B, C, E, F) and 100 nm (D).

Figure 4-04: *Details of selected nuclear structures demonstrating fine ultrastructure preservation obtained by high-pressure freezing and freeze-substitution of S. cerevisiae cells, embedded in Lowicryl HM20.* A - Overview of the nucleus. B - Nuclear pores (arrowheads) embedded in the nuclear envelope. C - Microtubules (arrows) in longitudinal section. D, E - A single spindle pole body. MT, microtubules; NE, nuclear envelope; Np, nucleoplasm; Nu, nucleolus. The cells were substituted either in acetone with 0.1% UA and sections left without post-staining (A-D) or in acetone with 0.1% GA and post-stained (E). Scale bar = 200 nm (A), 100 nm (B-E).

Figure 4-05: *Nucleolar ultrastructure preservation of high-pressure frozen S. cerevisiae cells substituted in different media.* The nuclei of the cells substituted in A - acetone alone, B - acetone with 0.1% GA, C - acetone with 0.1% UA and D - acetone with 0.1% UA + 0.1%

GA. Fibrillar centers are marked by asterisks, dense fibrillar and granular areas by arrowheads. HC, heterochromatin; EC, euchromatin; Nu, nucleolus. Sections were post-stained (A, B) or left without post-staining (C, D). Scale bar = 200 nm.

Figure 4-06: *Comparative immunolocalization of the nucleolar markers Nop1 and Nsr1 in S. cerevisiae cells at the LM and EM levels.* A, C - Differential interference contrast (DIC), indirect immunofluorescent localization of Nop1 and Nsr1 respectively (red), nuclear DNA staining with DAPI (blue) and their merge. The primary antibodies were visualized with a Cy3-conjugated secondary antibody. B, D - Post-embedding on-section immunogold (12 nm) labeling of Nop1 and Nsr1 respectively at the EM level (arrowheads). Nu, nucleolus. *S. cerevisiae* cells were freeze-substituted in acetone with 0.1% UA and embedded in Lowicryl HM20. Sections were not post-stained. Scale bar = 3 μm (A, C), 100 nm (B), 200 nm (D).

Figure 4-07: *Comparative LM and EM mapping of Nsp1 in S. cerevisiae cells.* A - DIC, an indirect immunofluorescent localization of the nuclear envelope marker protein Nsp1 (red), nuclear DNA staining with DAPI (blue), and their merge. The primary antibody was visualized with a Cy3-conjugated secondary antibody. B - Post-embedding on-section immunogold (12 nm) labeling of Nsp1 at the EM level. Gold particles decorate the nuclear pores in the nuclear envelope or are localized in their close proximity (arrowheads). Cy, cytoplasm; Np, nucleoplasm. *S. cerevisiae* cells were freeze-substituted in acetone with 0.1% UA and embedded in Lowicryl HM20. Sections were not post-stained. Scale bar = 3 μm (A), 200 nm (B).

Figure 4-08: *Immunolocalization of α-tubulin in S. cerevisiae cells.* Yeast cells in late stages of mitosis are shown. A - DIC, indirect immunofluorescent localization of α-tubulin (red), nuclear DNA staining with DAPI (blue), and their merge. The primary antibody was visualized with a Cy3-conjugated secondary antibody. Staining revealed both the intranuclear and cytoplasmic microtubules running from the spindle pole bodies embedded in the nuclear envelope. B - Post-embedding on-section immunogold (12 nm) labeling of α-tubulin at the EM level. Microtubules connecting the separated nuclei are specifically labeled (arrow). Mt, microtubule. *S. cerevisiae* were freeze-substituted in acetone with 0.1% UA and embedded in Lowicryl HM20. Sections were not post-stained. Scale bar = 3 μm (A), 200 nm (B).

4.1.8 FIGURES

Figure 4-01:

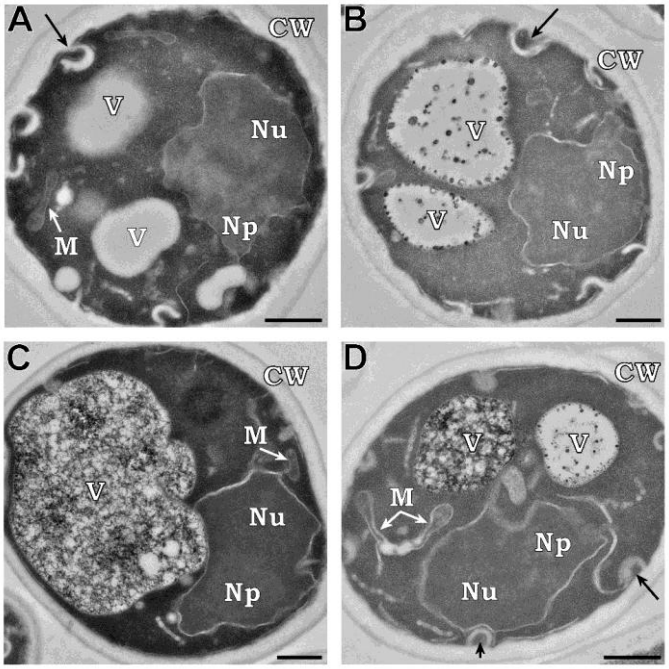

Figure 4-02:

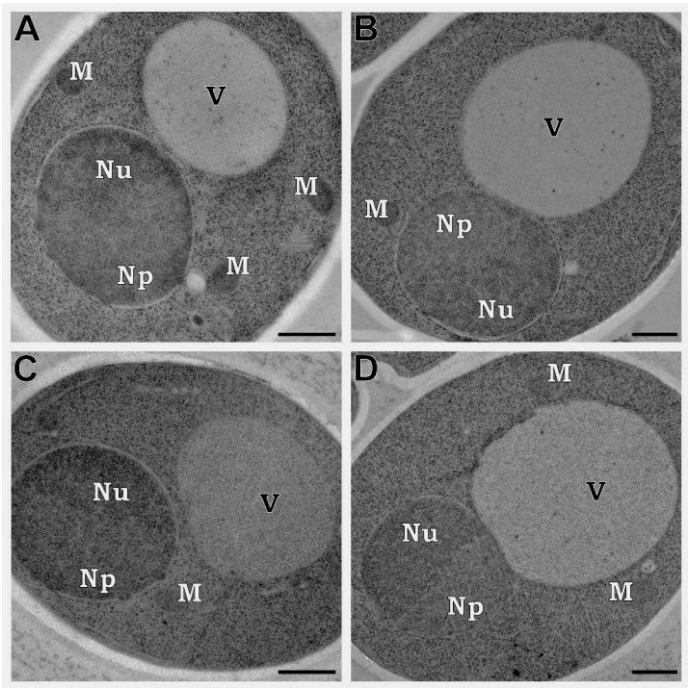

Figure 4-03:

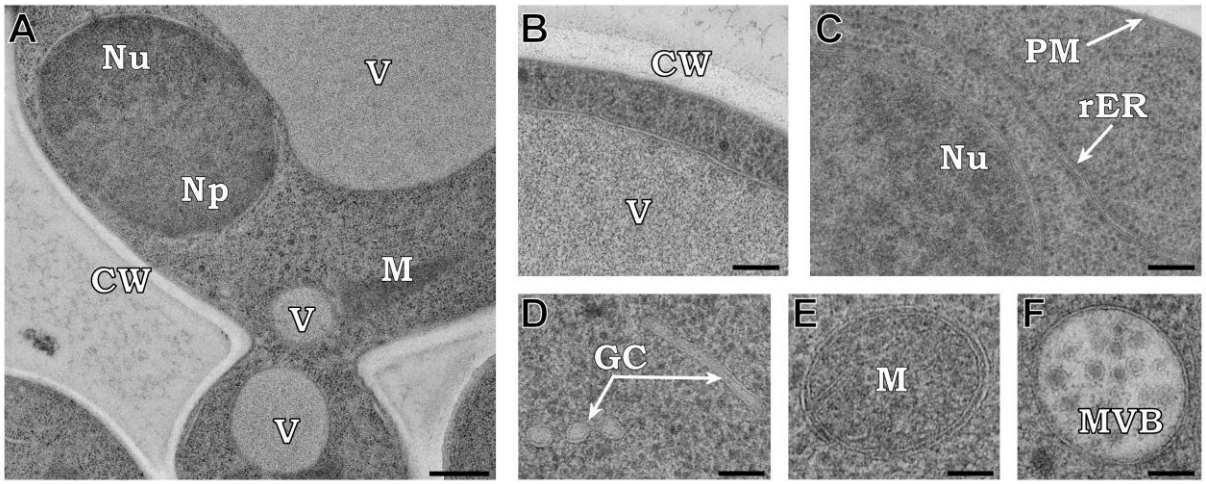

Figure 4-04:

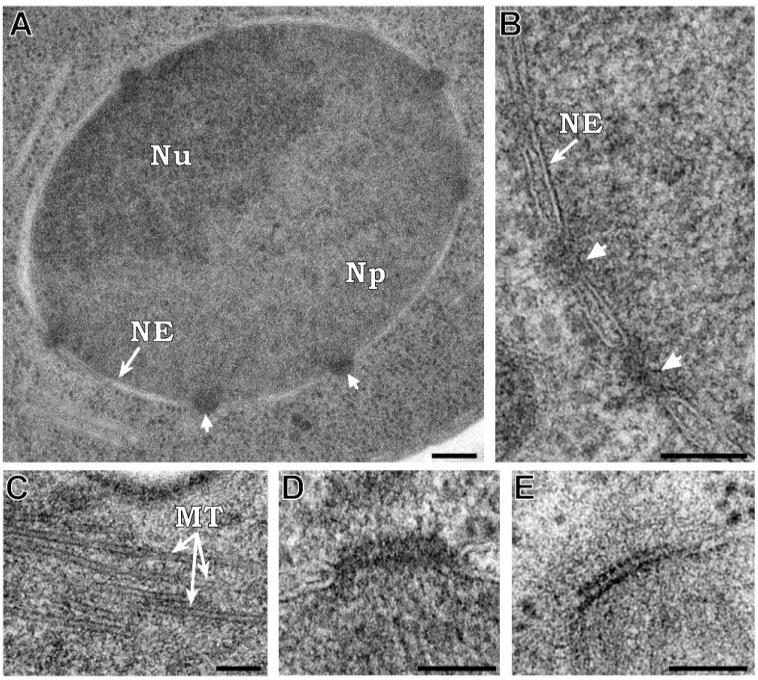

Figure 4-06:

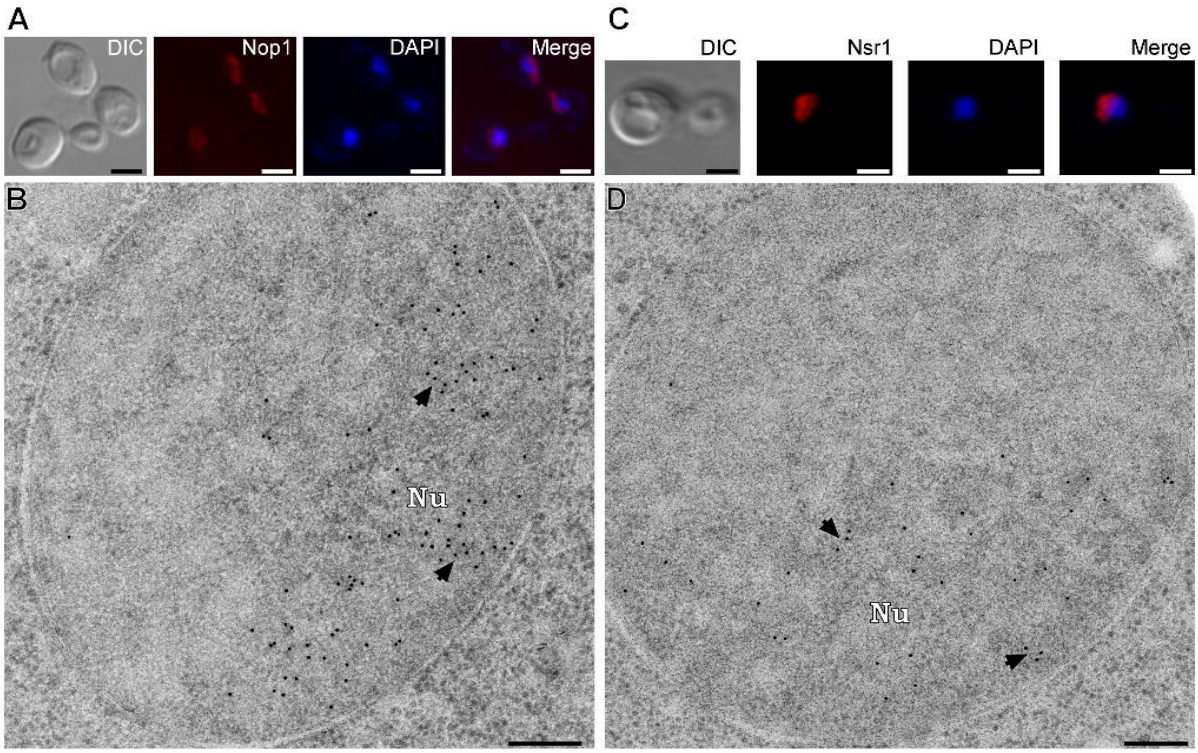

Figure 4-05:

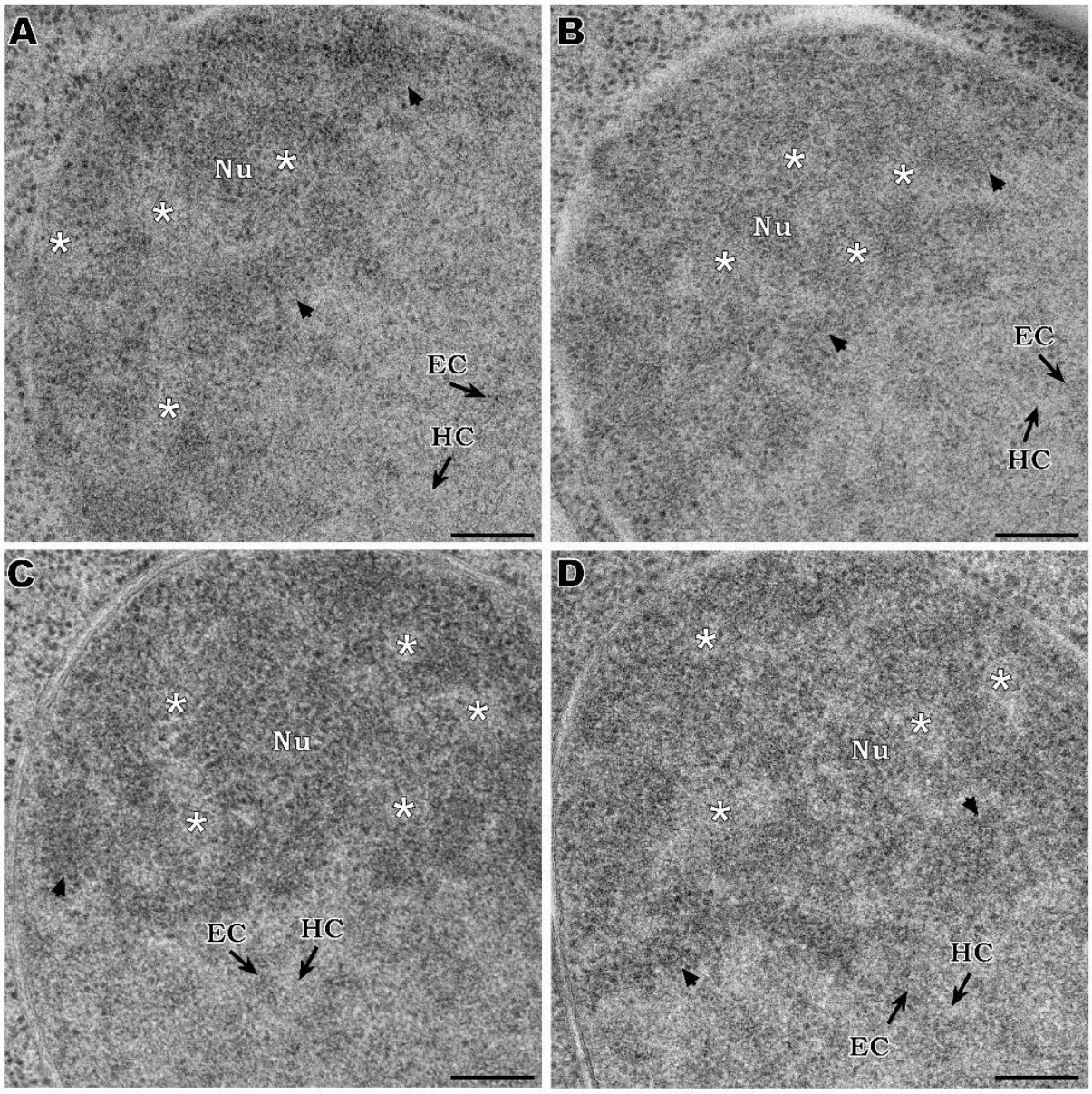

Figure 4-07:

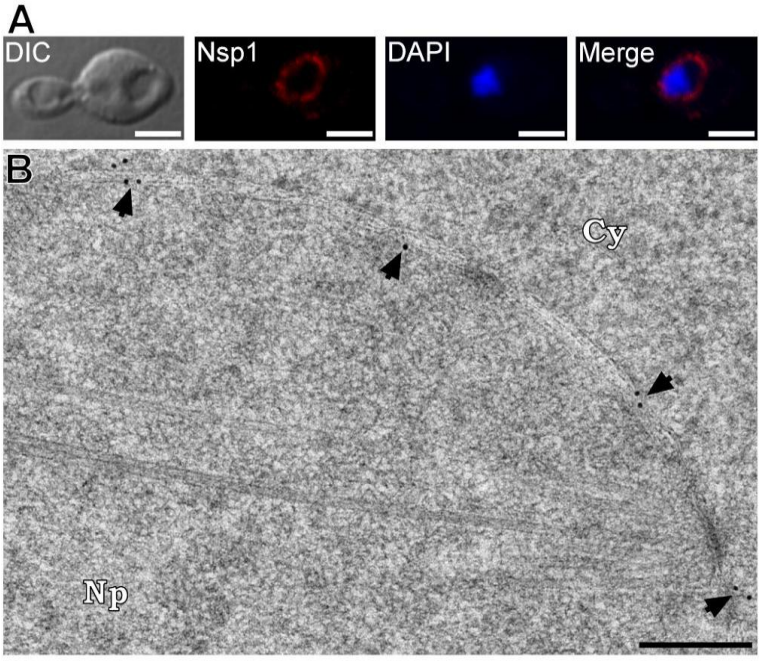

Figure 4-08:

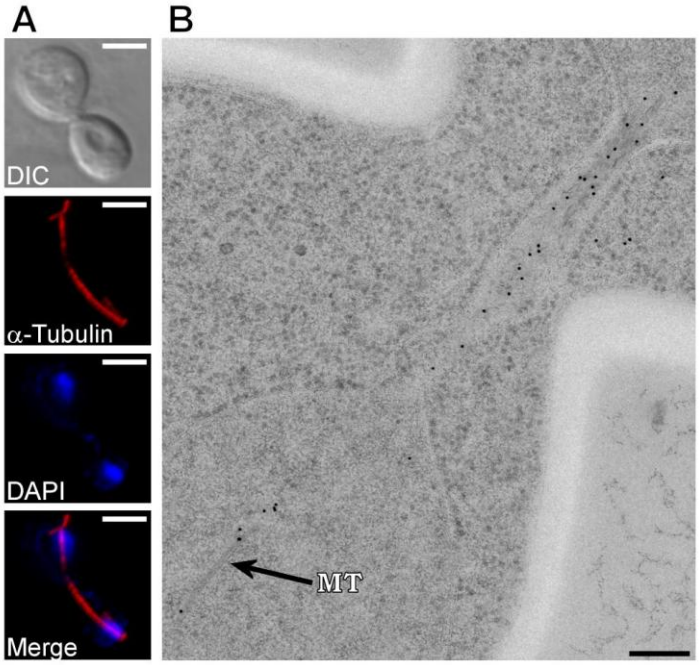

4.2 PUBLICATION No.2

Silicone-stabilized liposomes

Authors: Lewandowska J.[a], Kepczyński M.[a], Bednar J.[b,c], Rząd E.[a], **Moravcikova V.**[b], Jachimska B.[d], Nowakowska M.[a,*]

Published in: Colloid & Polymer Science (2010), 288 (1): 37-45

[a]Faculty of Chemistry, Jagiellonian University, Ingardena 3, 30-060 Krakow, Poland

[b]Charles University in Prague, First Faculty of Medicine, Institute of Cellular Biology and Pathology and Department of Cell Biology, Institute of Physiology, Academy of Sciences of the Czech Republic, Albertov 4, 128 01 Prague 2, Czech Republic

[c]CNRS/UJF, Laboratoire de Spectrométrie Physique, UMR 5588, BP87, 140 Av. de la Physique, 38402 St. Martin d'Hères Cedex, Grenoble, France

[d]Institute of Catalysis and Surface Chemistry, Polish Academy of Sciences, Niezapominajek 8, 30-239 Krakow, Poland

[*]***Corresponding author:*** M. Nowakowska, e-mail: nowakows@chemia.uj.edu.pl

Keywords: Liposomes · Silicones · Stabilization · Hydrosilylation · Cryo-transmission electron microscopy

4.2.1 ABSTRACT

The present work is focused on stabilization of liposomes by covering their surface with a thin silicone layer. The appropriate silicone monomer was obtained by the hydrosilylation of vinylmethyldimethoxysilane with 1,3,5,7-tetramethylcyclotetrasiloxane. The surface potential of egg yolk phosphatidylcholine vesicles was modified by incorporation of a cationic double-tailed surfactant, dimethyldioctadecylammonium bromide (DODAB), yielding cationic liposomes. The silicone material was deposited on the cationic liposomes in base-catalyzed polycondensation/polymerization processes of the monomer at the liposomal surface. In order to initialize the processes pH of the liposomal dispersion was adjusted to the values of 8.5 or 10.2. The formed structures were characterized using dynamic light scattering (DLS) and zeta potential measurements. The DLS measurements show that the size of covered liposomes decrease during the reaction and the zeta potential turned to negative value, as can be expected. The morphology of the structures was evaluated using transmission cryo-electron microscopy (cryo-TEM). The cryo-TEM micrographs revealed the presence of the covered liposomes of sizes lower than the initial liposomes, which is in line with DLS measurements. However, some disintegration of the liposomes occurred during the covering procedure, especially at high pH value. Using the surfactant lysis and calcein-release study it was shown that silicone covered liposomes are stable.

4.2.2 INTRODUCTION

Recently, the self-assembly of organized nanoscopic structures has been the subject of considerable interest (Bégu *et al*, 2007). Liposomes are among the most intensively studied nanosystems. That is due to their unique properties such as nontoxicity, biodegradability, as well as simplicity of preparation and control over the composition and size. Liposomes are able to encapsulate a hydrophilic solute inside their inner water cavity as well as hydrophobic compounds in the bilayer lipid membranes (Takeuchi *et al*, 2000; Takeuchi *et al*, 2001; Yaroslavov *et al*, 2008). Thus, they are frequently studied as possible vehicles for the delivery of therapeutic compounds, such as drugs or enzymes. Unfortunately, the major problem with liposomes is their low stability during storage which is due to their strong tendency for degradation, aggregation, and fusion leading to uncontrolled leakage of the entrapped compounds, e.g., a drug before administration (Takeuchi *et al*, 2001). There has been a considerable number of attempts to overcome those problems (Haidar *et al*, 2008; Takeuchi *et*

al, 2000). The main strategies proposed involve (1) optimization of the lipid composition in the membrane (Kokkona *et al*, 2000), (2) adsorption of polymeric material at the liposomal surfaces, both nonionic polymers (Hwang, 2001; Momekova *et al*, 2007) and polyelectrolytes (Ciobanu *et al*, 2007; Cho, 2007; Rinuado, 2009; Volodkin *et al*, 2007) especially using the layer-by-layer method (Michel *et al*, 2006), (3) covalent grafting of hydrophilic polymers onto the head groups of phospholipids (Mobed & Chang, 1998; Ruysschaert *et al*, 2006). Liposomes were also covered with inorganic siliceous shell (Bégu *et al*, 2007; Hentze, 2003; Hubert, 2000) or trapped into sol–gel silica materials (Besanger, 2002). Interesting concept of vesicle stabilization by applying the sol–gel process for an organo-alkoxysilane with a lipid-like structure leading to so called 'Cerasomes' was presented by Katagiri *et al* (2002a); Katagiri et al (2002b). However, no attempts were undertaken to stabilize the lipid vesicles by coating their surface with a thin layer of silicone.

Silicones are important biomaterials used in prosthetic devices as implant for breast enlargement, for tissue augmentation and for treatment of hydrocephalus. They are also good candidates for use in monolithic devices where the active agent is dispersed in a polymer matrix and its release is controlled by diffusion from the matrix (Rogero, 2005). They generally have a low toxicity, posses a good corrosion resistance, low surface tension, and excellent thermal stability over a broad temperature range that widens with length and branching of the substituents (Wei, 2008). In addition, silicones exhibit excellent permeability of gases, which results from the longer bonds compared to typical organic polymers (Rościszewski, 2002).

In this paper, we present the results of the first studies on stabilization of liposomes by covering their surface with a thin silicone layer. The new silicone monomer was synthesized for this purpose by a hydrosilylation reaction between vinylmethyldimethoxysilane and 1,3,5,7-tetramethylcyclotetrasiloxane. The obtained features after covering procedure were characterized with different methods: dynamic light scattering, zeta potential measurements, and cryo-transmission electron microscopy.

4.2.3 EXPERIMENTAL SECTION

4.2.3.1 Materials

1,3,5,7-tetramethylcyclotetrasiloxane (D_4^H), vinylmethyldimethoxysilane (VMS), and Karstedt's catalyst were purchased from ABCR. L-α-phosphatidylcholine from frozen egg

yolk type XIII-E (PC lipid, Sigma, 100 mg/mL solution in ethanol), dimethyldioctadecylammonium bromide (DODAB, Fluka), toluene (Sigma-Aldrich, anhydrous), and calcein (Aldrich) were used as received. Sephadex G-50, 20 – 50μm was obtained from Sigma.

4.2.3.2 Synthesis of the monomer

The monomer, tetra(methyldimethoxysilylethyl)-tetramethylcyclotetrasiloxane ($D_4^{ethyl-D}$), was prepared according to the reported procedure (Lin & Cabasso, 1999). Briefly, the mixture of D_4^H (2.2g), VMS (4.9g), and toluene (5.9g) were inserted into 50-mL three-necked flask fitted with a magnetic stirrer, reflux condenser, and a nitrogen inlet. The mixture was heated to 50 °C and 25 μl of catalyst was then added. The mixture was refluxed for 4 h at 70 °C under a gentle stream of nitrogen. The product was a pale brown viscous oil. Toluene was removed using a vacuum evaporator.

Elem. anal. calculated for $D_4^{ethyl-D}$ ($C_{24}H_{64}O_{12}Si_8$): C, 37.46%; H, 8.38%. Found: C, 37.40%; H, 8.36%. Spectral data: ^{1}H NMR (500 MHz, $CDCl_3$, δ) 0.031–0.058 (m, 24H, Si−CH_3), 0.438–0.504 (m, 14.04H, Si−CH_2−CH_2−Si and Si−$CH(CH_3)$−Si), 1.026 (d, 1.81H, Si−$CH(CH_3)$−Si), 3.452–3.464 (s, 24H, OCH_3). ^{13}C NMR (500 MHz, $CDCl_3$, δ) −6.004 (Si−$CH(CH_3)$−Si), −0.940 (Si−CH_3), 4.721 (Si−CH_2−CH_2−Si), 8.61 (Si−$CH(CH_3)$−Si), 50.804 (OCH_3). IR (film) 2,835 cm^{-1} (υ_s Si−OCH_3), 1,408 cm^{-1} (δ_{as} CH_3), 1,260 cm^{-1} (δ_s CH_3−Si), 1,139 cm^{-1} (υ Si−CH_2CH_2−Si), 1,083 cm^{-1} (υ_{as} Si−O−Si) (Anderson & Smith, 1974).

4.2.3.3 Preparation of cationic liposomes

DODAB surfactant (2.1 mg; 10 mol% of PC lipid) was dissolved in ethanol and added to the ethanol solution of the lipid (250 μl of the solution). The mixture was vortexed for about 5 min and then ethanol was evaporated under a gentle stream of nitrogen. The film formed after the complete removal of the solvent was hydrated and vortexed. The resulting multilamellar vesicle dispersion was subjected to five freeze–thaw cycles from liquid nitrogen temperature to 60 °C and then extruded six times through the membrane filters with 100-nm pores using a gas-pressurized extruder.

4.2.3.4 Covering with silicone

In the next step, the liposomes were coated with $D_4^{ethyl\text{-}D}$. To initiate the condensation/polymerization processes of the monomer at the liposome surface, the pH of the dispersion was adjusted to the value of 8.5 or 10 and then the appropriate amount of $D_4^{ethyl\text{-}D}$ was added (50% of molar content of lipids). The stirring was continued for 48 h at 70 °C. For characterization by FTIR spectroscopy, the silicone material was recovered by precipitation with methanol. 5 ml of the dispersion was poured into 10 ml of methanol, the mixture was vortexed for 5 min and centrifuged at 13,000 rpm for 30 min. The precipitate was dispersed in 5 ml of methanol/ water (3:1 *v/v*) mixture using sonic bath and the material was centrifuged. The procedure was repeated four times. Finally, the product was dried for 24 h in a vacuum and a white powder was obtained.

4.2.3.5 Calcein-release studies

Calcein-loaded liposomes (CL) were prepared according to the similar procedure as that described above for liposomes in pure buffer solution, with the only difference being that the lipid film was hydrated with 0.06 *M* solution of calcein (pH 8.5). CL liposomes were next covered with silicone in the same manner to that described above. Untrapped calcein molecules were separated from CL liposomes, both native and silicone-coated, by size-exclusion chromatography on a Sephadex G-50 column using PBS buffer as an eluent. The fluorescence intensity of the CL liposomes was measured and found to be low due to the self-quenching effect. The titration with 0.75% solution of Triton-X100 was performed. The change in fluorescence intensity due to calcein release from the vesicles after addition of each portion of surfactant was monitored with an SLM-AMINCO 8100 Instruments spectrofluorimeter. Excitation and emission wavelengths were set at 490 and 520 nm, respectively.

4.2.3.6 Cryo-transmission electron microscopy (cryo-TEM)

Three microliters of the sample dispersion was applied to an electron microscopy grid covered with perforated supporting film. Most of the sample was removed by blotting (Whatman No 1 filter paper) for approximately 1 s, and the grid was immediately plunged into liquid ethane held at -183 °C. The sample was then transferred without reheating into

Tecnai Sphera G20 electron microscope using Gatan 626 cryo-specimen holder. The images were recorded at 120 kV accelerating voltage and microscope magnification ranging from 5,000 to 25,000× using Gatan UltraScan™ 1000 slow-scan CCD camera and low-dose mode with a dose not exceeding 15 electrons per square Å. Typical value of applied underfocus ranged between 1.5 to 2.3 μm. The applied blotting condition resulted in a specimen with thickness ranging from 100 to 300 nm.

4.2.3.7 Light scattering and zeta potential measurements

A Malvern Nano ZS light-scattering apparatus (Malvern Instrument Ltd., Worcestershire, UK) was used for dynamic light scattering (DLS) and zeta potential measurements. The time-dependent autocorrelation function of the photocurrent was acquired every 10 s, with 15 acquisitions for each run. The sample of solutions was illuminated by a 633-nm laser, and the intensity of light scattered at an angle of 173° was measured by an avalanche photodiode. The *z*-averaged hydrodynamic mean diameters (dz), polydispersity (PDI) and distribution profiles of the samples were calculated using the software provided by Malvern. The zeta potential of liposomes was measured using the technique of laser Doppler velocimetry (LDV).

4.2.3.8 FTIR and NMR spectroscopy

FTIR spectra were obtained on a Bruker Equinox 55 FTIR spectrometer. For each sample, 32 scans were recorded with a resolution of 2 cm^{-1}. The KBr pressed disk technique (1.0 mg of sample and 150 mg of KBr) was used for solid substance. Liquid substance was deposited between two KBr plates. ^{1}H and ^{13}C NMR spectra were recorded on a Bruker AMX 500 Hz instrument.

4.2.4 RESULTS AND DISCUSSION

4.2.4.1 The monomer synthesis

The new monomer, tetra(methyldimethoxysilylethyl)tetramethylcyclotetrasiloxane ($D_4^{ethyl\text{-}D}$) was successfully synthesized as shown in Figure 4-09. The hydrosilylation reaction was followed by FTIR measurements. Based on the analysis of disappearance of the vibration

bands at 2,170 and 879 cm^{-1}, characteristic of Si–H bonds, it was concluded that the reaction was completed in 4 h. The hydrosilylation reaction usually leads to the formation of two isomers: –Si–CH_2–CH_2– (β isomer) and –Si–$CH(CH_3)$– (α isomer) (Lin & Cabasso, 1999). The molar ratio of these two isomers is dependent upon several parameters: the conversion degree, the type of solvent and catalyst, and the structure of unsaturated compound. We have found that the hydrosilylation of VMS with D_4^H under our experimental conditions resulted in formation of a mixture of α and β isomers of the pendant group. Based on the ^1H NMR measurement the ratio of α to β isomeric groups was determined to be 15:85 (see Subchapter 4.2.3). This is consistent with the result of the studies on the addition of D_4^H to vinylbenzyl chloride (Lin & Cabasso, 1999), which have shown that β isomer predominates in the reaction carried out in toluene with the Karstedt's catalyst.

4.2.4.2 Characterization of the cationic liposomes

In our studies, we have made liposomes from egg yolk phosphatidylcholines (PC) and a cationic double-tailed surfactant, dimethyldioctadecylammonium bromide (DODAB). The surfactant was introduced to modify the surface potential of the liposomes, so the base-catalyzed polymerization/polycondensation processes of the monomer would occur at the surface. In order to obtain the liposome dispersion of low polydispersity, the lipid vesicles were extruded through filters with 100-nm pores. The mean hydrodynamic diameter (dz) of the cationic liposomes measured by DLS was 125.4 nm and polydispersity was less than 0.1 (see Table 10). Figure 4-10 depicts the size distribution profiles of the liposomes determined from DLS measurements. The cryo-TEM visualization provided information regarding the morphology of the obtained structure. The typical cryo-TEM micrograph and the diameter of the initial vesicles are shown in Figure 4-11. The initial liposomes showed the good spherical structure with distinct bilayered phospholipid membrane surrounding an aqueous core. Although the unilamellar structure constitutes the main population some multilayered liposomes also can be observed. The mean size (diameter) of the liposomes observed on the micrographs is about 80±33 nm. This value is lower than that determined by DLS measurements. In the previous paper, we have shown that DLS method is heavily weighted toward the largest structures in the solution, since the intensity of the scattered light increases strongly with increasing size of objects (Kepczynski *et al*, 2009). Thus, the *z*-averaged hydrodynamic mean diameter obtained by cumulant analysis is overestimation of the object size.

The zeta potentials of the cationic liposomes were determined and the results are presented in Table 9. The increase in surface charge usually increases the values of the zeta potential of the molecules (the electric potential in the slipping plane) which are well correlated with the stability of suspensions. The zeta potential is a quantity well accessible experimentally, e.g., by using the microelectrophoretic method which was used in this study. It is known that the value of zeta potential of liposomes depends strongly on pH and ionic strength of solution. Depending on the ionic strength, the zeta potential of the liposomes from egg L-α-phosphatidylcholine is in the range between −22.5±1.0 and −12.1±1.0 mV (Kepczynski *et al*, 2006). That negative zeta potential may come from some acidic impurities, e.g., phosphatidylglycerol. As it can be noticed from the analysis of data presented in Table 10, the addition of DODAB to liposomal dispersion results in a drastic increase of zeta potential of lipid vesicles. That was expected because DODAB is the cationic surfactant and the addition of that compound (10 mol%) affected the surface potential. Dispersion of microparticles characterized by zeta-potential values above +30 mV or below −30 mV is generally considered to be well stabilized through strong repulsion forces operating between particles which prevent their aggregation (Haidar *et al*, 2008).

In order to initiate the crosslinking/polymerization processes of the monomer at the liposome surface, the pH of the dispersion was increased from the value of 6.67 to 8.5 or 10.2, respectively, and the temperature was raised to 70 °C. We have checked the effect of pH and temperature change on the size and zeta potential of the cationic liposomes. The results presented in Table 10 indicated that both the size and zeta potential have decreased when pH was increased. The case of the zeta potential can be explained considering that the counterions (hydroxyl anions) accumulated near the surface of particle screening the particle charges, thus reducing the zeta potential.

The observed effect of pH on the size of the liposomes can be explained in two different ways. The dissociation of an additional amount of acidic groups, due to a shift of pH, may cause the attenuation of the repulsive lateral interaction of the phospholipids. That will result in a decrease of their mean molecular area, and in this way will lead to the shrinkage of the liposome's membrane (Gibrat & Grignon, 1982). More trivial explanation is connected to the specificity of the DLS measurements. The size of a particle is calculated from a translational diffusion coefficient. The coefficient depends not only on the size of the particle "core", but also on any surface structure, as well as the concentration and type of the ions in the medium. Any change to the surface of a particle that affects the diffusion rate will correspondingly change the apparent size of the particle. The ions in the medium and the total

ionic concentration can affect the particle diffusion rate by changing the thickness of the electric double layer. Changing the pH by addition of NaOH resulted in an increase of the total ionic strength. A medium of higher conductivity suppresses the electrical double layer of ions around the particle, increasing the diffusion rate and resulting in a lower apparent hydrodynamic diameter.

As can be found from the results presented in Table 10, the temperature increase to the value of 70 °C had rather small effect on the liposome size. The mean hydrodynamic diameter decreased slightly for liposomes at both values of pH. Volodkin *et al* (2007) have reported the reversible reduction in liposome size upon heating above the solid liquid phase transition temperature for liposomes prepared from the synthetic lipids. Such size reduction upon heating was not found for liposomes build from the natural lipid, used in our studies, which is in agreement with our results.

4.2.4.3 Preparation of silicone-coated liposomes

The monomer, 50 mol% in respect to the total concentration of lipid and DODAB, was introduced to the cationic liposome dispersion at pH 8.5 or 10.2. An effect of the monomer presence on the size and zeta potential of liposomes was determined. When the silicone monomer was introduced to the liposomal dispersion, the reduction of the zeta potential was observed (see Table 10). This observation can be explained assuming the adsorption of the monomer on the liposome which results in shielding of the positively charged liposomal surface. Moreover, the distribution profiles of the hydrodynamic diameters became broader and the values of dz increased (see Figure 4-10 and Table 10). Those findings suggest that $D_4^{ethyl\text{-}D}$ has accumulated at the vesicle surface.

In order to start the polycondensation/polymerization processes the mixture was heated to 70 °C. The formation of crosslinked silicone material was confirmed by comparing FTIR spectra of the initial monomer and the polymeric material extracted from the vesicle templates solution (see Figure 4-12). During the processes the band at 1,083 cm^{-1}, distinctive for small-ring cyclosiloxanes, became much broader, suggesting the formation of longer or branched polysiloxane chains. The ring-opening polymerization of cyclotetrasiloxanes is well known (Barrére *et al*, 2001). The intensity of the vibrational band at 2,836 cm^{-1} assigned to $Si–OCH_3$ bond, decreased significantly. Considerable reduction of intensity of bands at 2,962 and 2,918 cm^{-1}, which are characteristic of C–H stretching vibrations, was also observed. These changes in the FTIR spectra were accompanied by the appearance of the new

absorption bands centered at 3,437 cm^{-1} and at 902 cm^{-1}, both assigned to hydrogen-bonded Si–OH (Lipp & Smith, 1991). This indicates that the methoxy groups are released during the processes. The silanol and methoxy groups undergo condensation under basic conditions forming siloxane bonds, which absorb in similar region of IR spectrum as the polysiloxanes. We have found that Si–O–Si bonds in silica nanoparticles show a single band at 1,102 cm^{-1}. Thus, the formation of such bonds is manifested as a shoulder of the polysiloxane band. As a result of the described reactions, the monomer created a densely crosslinked silicone network. This is schematically depicted in Figure 4-13.

DLS experiments were performed for the liposomes after modification. Thermally induced polycondensation of the silicone monomer results in considerable broadening of the distribution profiles of liposome size (data not shown). The increase of the size spread is also manifested by the significantly higher value of the PDI values (see Table 10). Cryo-TEM visualization of the formulation d and g gave some information of morphologies of features, which are formed after heating of the dispersions. Figure 4-14 presents cryo-TEM micrographs of the liposome dispersion after covering procedure at two different pH conditions. Figure 4-14a displays a variety of different structures obtained at pH 10.2. Empty features with a thicker membrane, which are liposomes covered by silicone material are present in the dispersion, but they are less numerous than the initial liposomes (see Figure 4-11). A part of liposomes undergoes disintegration at applied conditions with formation of the bilayer fragments, which appeared in the micrographs as a dark line and dots. The situation is quite different in a milder pH conditions. As can be seen in Figure 4-14b, the amount of silicone-coated liposomes is much higher compared to the previous micrograph, so under these experimental conditions, liposomes are more stable. The micrograph reveals the presence of liposome bilayer fragments, which form a kind of stack. The bilayer stacks are floating freely in the dispersion or stick to the coated liposomes. Sparse solid particles, which we have attributed to the formation of monomer droplets (o/w emulsion) in the system, can be noticed.

The cryo-TEM technique enabled us to distinguish the empty and the solid objects and to calculate statistics of the silicone-coated liposomes. The distribution profiles are presented in Figure 4-14. The size of the objects is in the range of 20 – 180 nm and 25 – 200 nm for pH 10.2 and 8.5, respectively. The mean diameters are equal to 41±26 nm (pH 10.2) and 53±13 (pH 8.5). The quantitative results showed that the average diameter of covered liposomes is almost twice lower compared to these characteristic of the initial liposomes. These values are also lower than that obtained by cumulant analysis from DLS experiments (see Table 10). As

was mentioned above, the mean hydrodynamic diameter obtained in DLS measurements is strongly influenced by the largest objects and is overestimated, especially in samples of high polydispersity. The reduction in size of the silicone coated during the coating processes is a rather unexpected result. As was shown above, the heating of the liposomes had limited effect on the mean hydrodynamic diameter of vesicles. Possible explanation of the size decrease is that the polymerization at the surface initiate a liposome fragmentation processes leading to the formation of larger number of smaller vesicles or fragments of lipid bilayer (especially at the higher pH).

Expected results were obtained from the measurements of zeta potential of liposomes. After initiation of crosslinking/polymerization process, the surface potential turn to the negative values (see Table 10, formulations d and g). The formation of the Si–OH bonds which might be exposed at the liposome surface leads to the drastic change of the zeta potential value, thus confirming the presence of the silicone coating at the liposome surface.

In order to determine the stability of liposomes before and after modification they were subjected to the treatment with surfactant, Triton X-100. The liposome dispersion was titrated with a 15% solution of Triton X-100 and the changes were followed by measurement of the optical density at λ=320 nm (Figure 4-15). Addition of the surfactant solution to the liposome dispersion leads primary to the incorporation of the surfactant into the liposome assembly (Jung *et al*, 2000b). After exceeding a certain critical concentration the surfactant induces destruction of the liposomes and formation of bilayer fragments. These undergo transformation into the mixed micelles, which results in a decrease of dispersion turbidity (De la Maza & Parra, 1995; Gustaffson *et al*, 1997; Silvander *et al*, 1996). For DODAB-modified liposomes, such a transition occurs when the molar ratio of Triton X-100 to lipid exceeds the value of 0.35.

In the case of the liposomes coated with $D_4^{ethyl\text{-}D}$ monomer in two different pH conditions (8.5 and 10.2), the turbidity of dispersion decreases gradually with an increase of surfactant concentration and the breakup of the liposome structure is completed at Triton/lipid molar ratio equal to 2.5. The higher stability of these liposomes can be explained considering that the coating of the monomer on the liposome membrane in some way increases their stability, but eventually the break up takes place. In the case of the modified liposomes obtained after crosslinking of $D_4^{ethyl\text{-}D}$ on the liposomes for which pH of the solution was about 10.2, there are no signs of destabilization on the surfactant addition. Moreover, with increasing surfactant concentration the turbidity of the dispersion increased. The crosslinked silicone material formed on the surface of the liposomes stabilizes the structure of the

liposomes and prevents the surfactant induced lysis. The increase in turbidity of the solution observed at higher Triton X-100 concentration can be explained considering the adsorption of the surfactant molecules on the surface of the covered liposome, which increases the size of the light scattering objects. In the case of the covered liposomes obtained in the lower pH value of the solution (about 8.5), the tendency seems to be a little bit different. At Triton/lipid molar ratio equal to about 2.0 there can be observed some decrease of the turbidity of the solution. Nevertheless, the complete breakup of the coated liposomes does not occur.

Integrity of the covered liposomes obtained at pH 8.5 was also tested using a common technique of calcein entrapment inside the liposome interior (Shimanouchi *et al*, 2009). Calcein was entrapped inside the liposomes, which were next covered with silicone layer. Calcein-loaded liposomes, both native and silicone-modified ones, were next titrated using 0.75% solution of Triton X-100. Figure 4-16 shows the changes in calcein fluorescence upon titration. Addition of the surfactant solution to the initial liposome dispersion led to gradual increase of the fluorescence intensity due to the release of the dye. When the molar ratio of Triton X-100 to the lipid exceeded the value of 0.3, the pronounced increase of the fluorescence intensity was observed, which is related to the disintegration of liposomes. This value is very close to that found by the turbidity measurements. In a case of the covered liposomes loaded with calcein, the results of the spectrofluorimetric titration are completely different. The fluorescence intensity did not change during the experiments. That can be explained assuming that the siliconecovered vesicles are stable and they sustained their structure after introduction of the surfactant.

4.2.5 CONSLUSIONS

Silicone-covered liposomes were obtained using base-catalyzed polycondensation/polymerization processes of tetra(methyldimethoxysilylethyl)-tetramethylcyclotetrasiloxane at the lipid vesicle surface. Two different pH conditions were used to initialize the processes, namely 8.5 and 10.2. The cryo-TEM micrographs clearly showed that silicone-coated liposomes can be obtained using the procedure presented above, but at the higher value of pH, liposomes are not stable and a part of them undergoes disintegration. The properties of these nanoparticles such as size and surface charge were determined. We found that the diameter of the silicone-coated vesicles is significantly lower compared to that for the initial liposomes, which is a rather unexpected result. But as one can

predict, the zeta potential of the particles turned to the negative value. The experiments with surfactant lysis showed that the siliconecoated liposomes are very stable.

4.2.6 ACKNOWLEDGEMENTS

The authors are grateful to the Polish Ministry of Science and Higher Education for financial support in the form of Grants N204 131 32/3320 and N N205 4000 33. JB acknowledges the support of the Grant Agency of the Czech Republic (Grant #304/05/2168), the Ministry of Education, Youth and Sports (MSM0021620806 and LC535) and the Academy of Sciences of the Czech Republic (Grant #AV0Z50110509).

4.2.7 FIGURE AND TABLE LEGENDS

Figure 4-09: *Synthesis of the monomer.*

Figure 4-10: *Distribution profiles of the hydrodynamic diameters obtained from DLS measurements for the different systems:* (a) liposomes at pH 6.67 (dotted line), liposomes at pH 8.5 (dashed line) and after introduction of $D_4^{ethyl\text{-}D}$ (solid line); (b) liposomes at pH 6.67 (dotted line), liposomes at pH 10.2 (dashed line) and after introduction of $D_4^{ethyl\text{-}D}$ (solid line).

Figure 4-11: *The cryo-TEM micrograph and the diameter profiles of the initial liposomes obtained by extrusion.*

Figure 4-12: *FTIR spectra of the polymeric material extracted from the liposomes after heating (solid line) and* $D_4^{ethyl\text{-}D}$ *(dotted line).*

Figure 4-13: *Polymerization / condensation processes of* $D_4^{ethyl\text{-}D}$ *catalyzed by hydroxide anion at the liposome surface.*

Figure 4-14: *The cryo-TEM micrographs of the silicone-coated liposomes obtained at pH 10.2 (a) and 8.5 (b) and the appropriate distribution profiles of the vesicle diameter.*

Figure 4-15: *Optical density traces for the surfactant titration of the liposome dispersions:* the liposomes (empty square), after introduction of $D_4^{ethyl\text{-}D}$ (filled inverted triangle pH 8.5;

empty upright triangle pH 10.2) and after heating (filled circle pH 8.5; empty circle pH 10.2). [Triton X-100]/[lipid] is a molar ratio.

Figure 4-16: *Changes in fluorescence intensity of calcein during titration of the liposome dispersions at pH 8.5:* the liposomes (empty circle) and the silicone-covered liposomes (empty square). [Triton X-100]/[lipid] is a molar ratio.

Table 10: *The values of mean hydrodynamic diameter (dz), polydispersity (PDI) and the zeta potential (ζ).*

4.2.8 FIGURES AND TABLE

Figure 4-09:

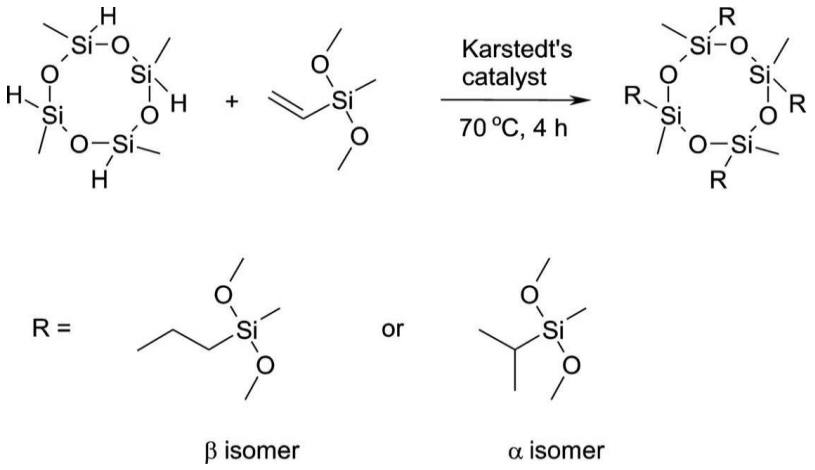

Figure 4-10:

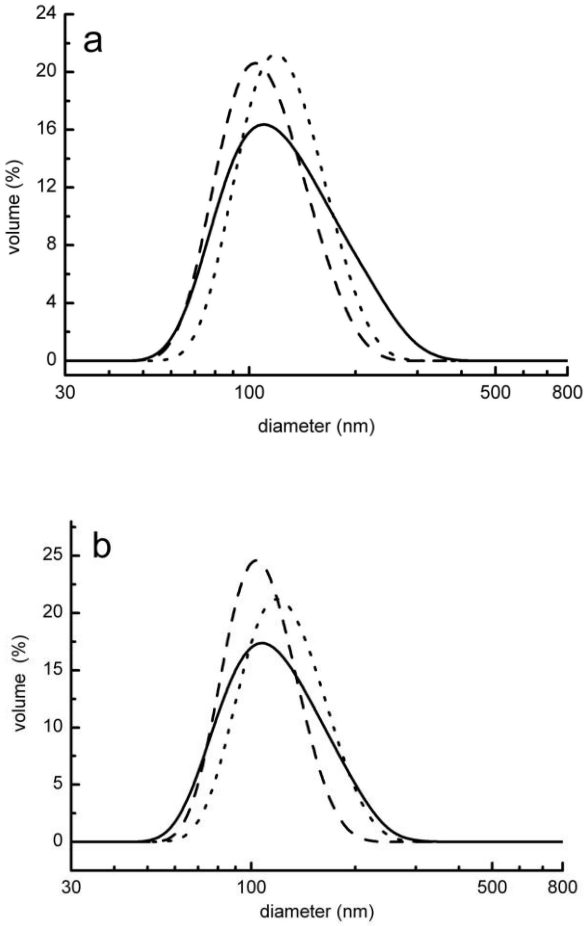

Figure 4-11:

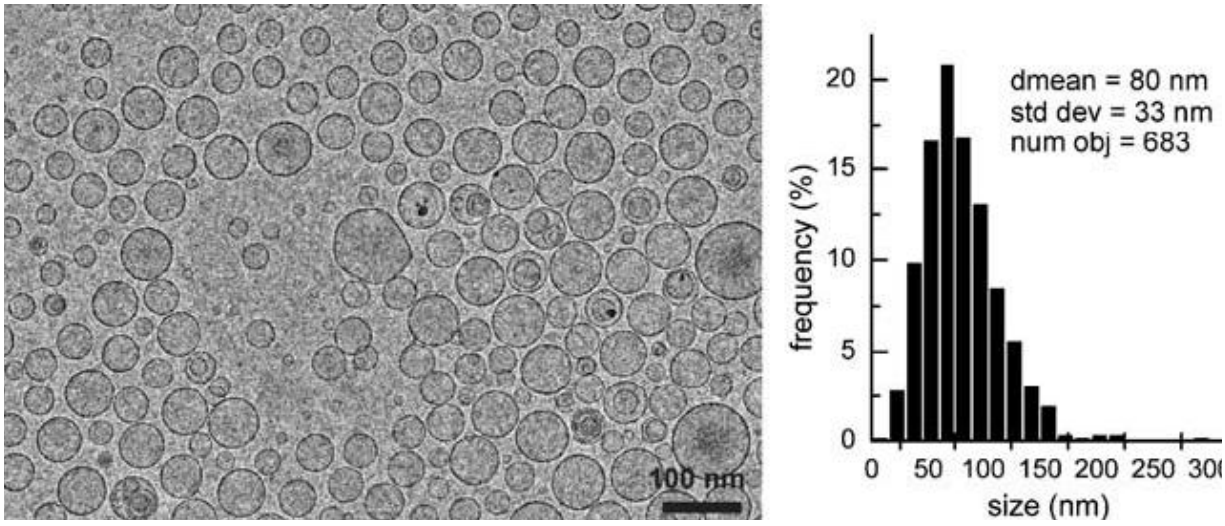

Figure 4-12:

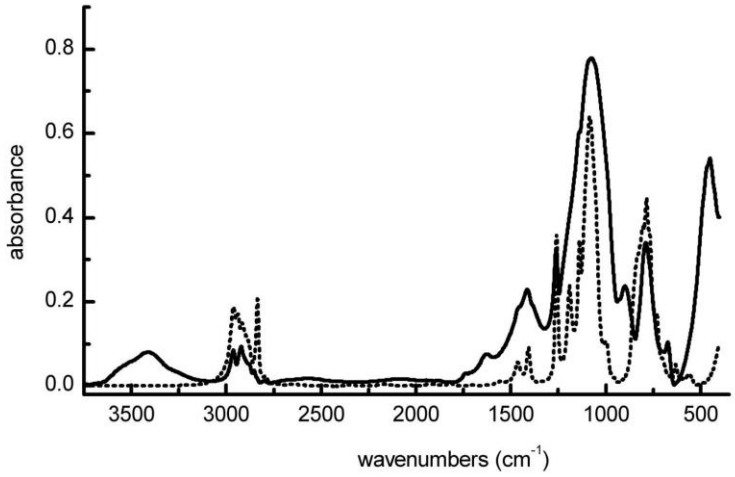

Figure 4-13:

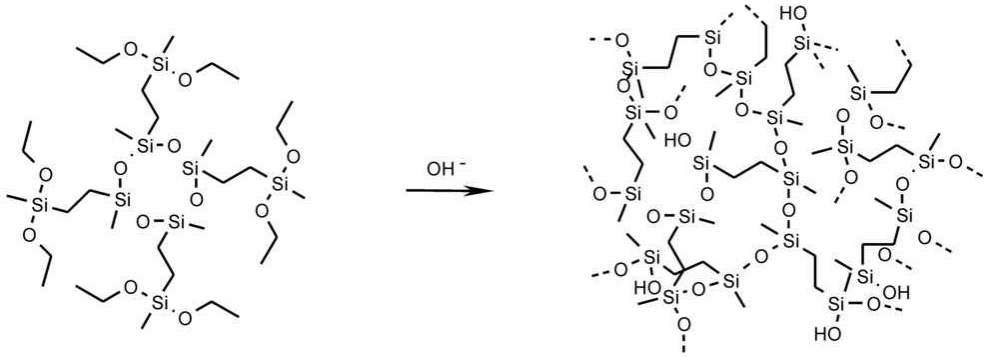

Figure 4-14:

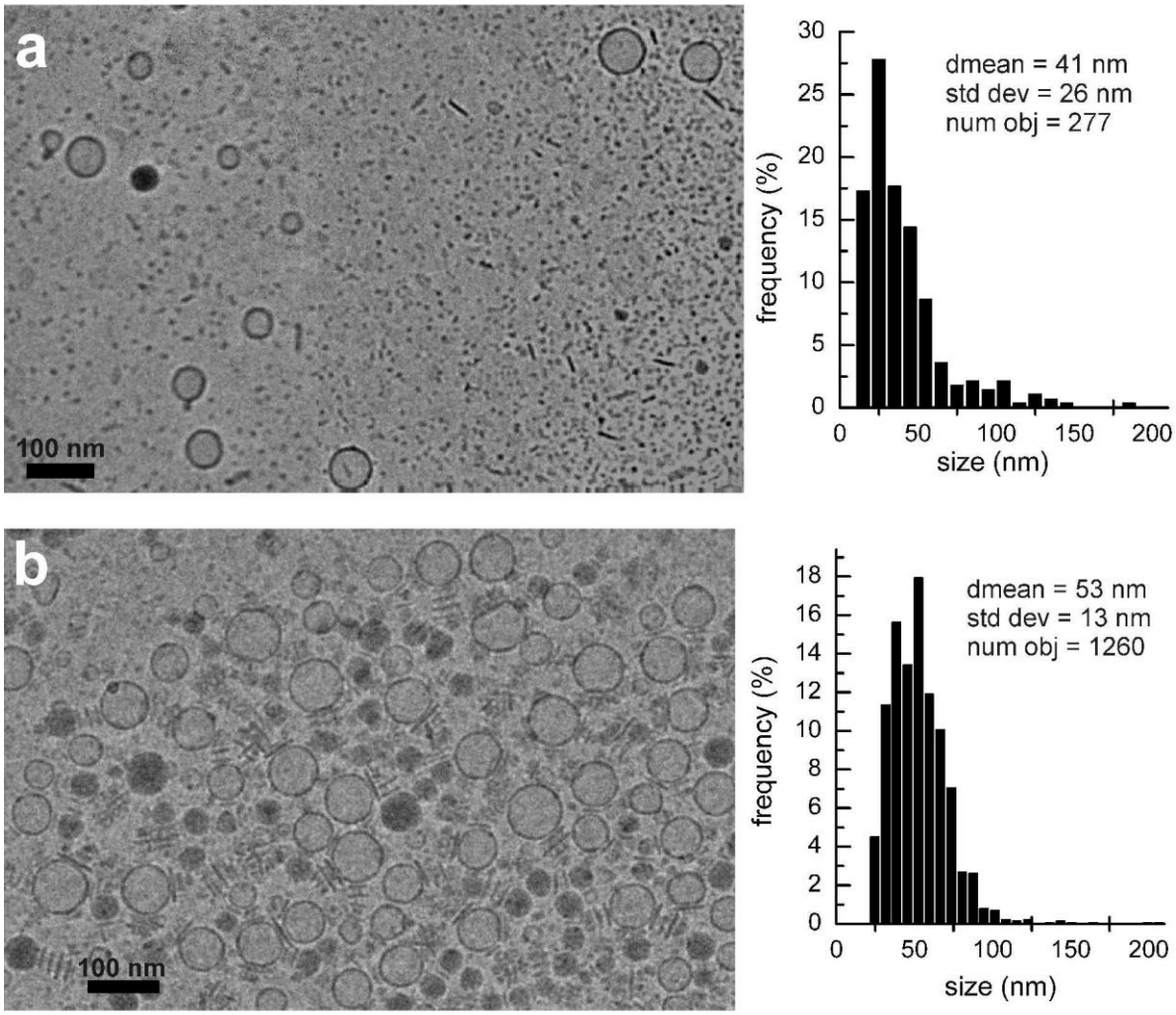

Figure 4-15:

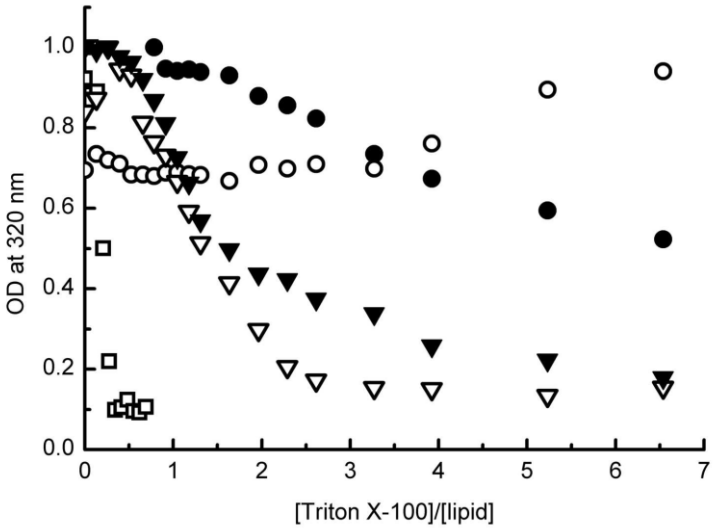

Figure 4-16:

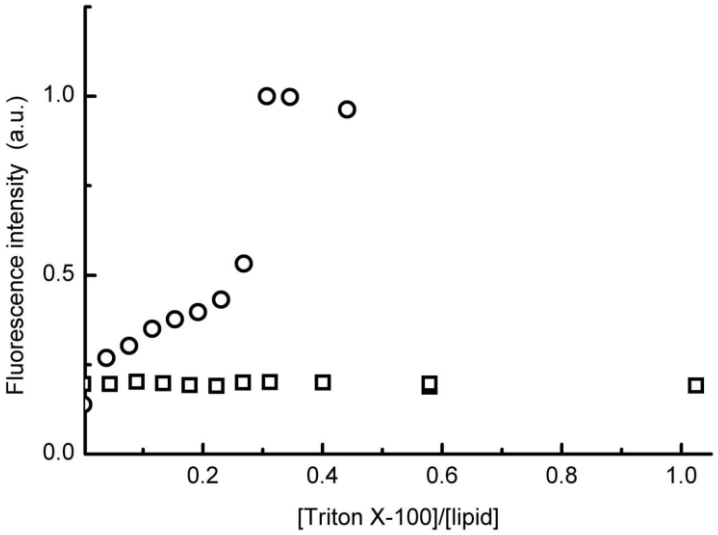

Table 10:

Formulation	pH	dz [nm]	PDI	ζ [mV]
Liposomes	6.67	125.4±0.4	0.09	51.7±0.5
Liposomes	8.5	119.7±0.3	0.077	
Liposomes at 70 °C	8.5	108.2±0.4	0.107	
Liposomes with $D_4^{ethyl\text{-}D}$ (50 mol%)	8.5	130.8±1.1	0.231	
Liposomes with $D_4^{ethyl\text{-}D}$ after heating	8.5	77.06±1.2	0.243	-49.4±1.8
Liposomes	10.2	114.8±1.2	0.08	35.3±0.8
Liposomes at 70 °C	10.2	111.4±0.9	0.174	
Liposomes with $D_4^{ethyl\text{-}D}$ (50 mol%)	10.2	115.7±0.5	0.12	29.9±1.1
Liposomes with $D_4^{ethyl\text{-}D}$ after heating	10.2	163.5±1.9	0.34	-65.8±1.8
Formulation	pH	dz [nm]	PDI	ζ [mV]
Liposomes	6.67	125.4±0.4	0.09	51.7±0.5

4.3 PUBLICATION No.3

Bilayer structures in dioctadecyldimethylammonium bromide/oleic acid dispersions

---

Authors: Kepczynski M.[a,*], Lewandowska J.[a], Witkowska K.[a], Kędracka-Krok S.[b], **Mistrikova V.**[c], Bednar J.[c,d], Wydro P.[a], Nowakowska M.[a]

Published in: Chemistry and Physics of Lipids (2011), 164 (5): 359-367

[a]Faculty of Chemistry, Jagiellonian University, Ingardena 3,30-060 Kraków, Poland

[b]Department of Physical Biochemistry, Faculty of Biochemistry, Biophysics and Biotechnology, Jagiellonian University, Gronostajowa 7, 30-387 Kraków, Poland

[c]Charles University in Prague, First Faculty of Medicine, Institute of Cellular Biology and Pathology and Department of Cell Biology, Institute of Physiology, Academy of Sciences of the Czech Republic, v.v.i., Albertov 4, 128 01 Prague 2, Czech Republic

[d]CNRS/UJF, Laboratoire de Spectrométrie Physique, UMR 5588, BP87, 140 Av. de la Physique, 38402 St. Martin d'Heres Cedex, Grenoble, France

*__Corresponding author:__ M. Kepczynski, tel.: +48 12 663 2020; fax: +48 12 634 0515; e-mail: kepczyns@chemia.uj.edu.pl

Keywords: Vesicles · DODAB · Cryo-transmission electronmicroscopy · Microcalorimetry · Langmuir monolayer

4.3.1 ABSTRACT

This paper reports on the properties of bilayers composed of dioctadecyldimethylammonium bromide (DODAB) and oleic acid (OA) at various molar ratios. The mole fraction of OA, X_{OA}, was varied in the range of 0–1 and the total lipid content was constant and equal to 10 mM. The DODAB/OA dispersions were extruded at a temperature higher than that of the gel–liquid transition of DODAB. The morphology of bilayer structures formed in the dispersions was inspected using a cryogenic transmission electron microscopy (cryo-TEM) and a differential interference contrast microscopy (DIC). The observations revealed that the incorporation of OA into DODAB bilayer results in a decrease of the membrane curvature. Anisotropy measurements using 1,6-diphenylhexatriene (DPH) as a rotator probe demonstrated that the DODAB/OA membrane microviscosity decreased considerably for $X_{OA} > 0.4$. The thermal behavior of DODAB/OA membranes has been studied by differential scanning calorimetry (DSC). In the case of the systems in which $X_{OA}<0.8$, the DODAB/OA membranes are in the gel phase at room temperature. Additionally, Langmuir monolayer experiments of the DODAB/OA mixtures showed that due to the electrostatic interactions between the oppositely charged head groups of DODAB and OA they get close to each other, which results in a decrease of the mean area per molecule. The results were next discussed based on the packing parameter concept. The reduction of the mean area per head group (*a*) in the DODAB/OA systems leads to subsequent increase in the so-called packing parameter (*S*), which governs themorphology of surfactant aggregates.

4.3.2 INTRODUCTION

Nanoscopic vesicular structures have been the subject of considerable interest in both colloid and materials science. Vesicles consist of one or multiple amphiphilic bilayer shells that enclose an aqueous phase. The amphiphilic bilayers can be spontaneously assembled in aqueous solution from compounds such as lipids (liposomes) (Bangham *et al*, 1965), double-tailed surfactants (Jung, 2000a; Lopes *et al*, 2008) or in the appropriate mixture of oppositely charged surfactants (the catanionic vesicles) (Kaler *et al*, 1992; Kaler *et al*, 1989). The catanionic vesicles, formed spontaneously in an aqueous solution after simple mixing of a cationic surfactant solution and an anionic one at the proper molar ratios, usually possess well-defined spherical morphologies as was shown using cryogenic transmission electron microscopy (cryo-TEM) (Kepczynski *et al*, 2009; Marques *et al*, 2008).

Dioctadecyldimethylammonium bromide (DODAB) is a synthetic double-chained cationic surfactant that tends to aggregate spontaneously in the aqueous solution with the formation of bilayer structures (Kunitake & Okahata, 1977). The DODAB vesicles, referred to in the literature as cationic liposomes, have found a widespread use in both the fundamental studies on interfacial phenomena (Goncalves da Silva *et al*, 2005), and practical applications; they may be used as DNA carrier systems for gene transfection (Barreleiro *et al*, 2002; Li *et al*, 2008) and as vehicles for drug delivery (Pacheco & Carmona-Ribeiro, 2003; Shi *et al*, 2002). Therefore, the DODAB dispersions have attracted substantial experimental interest over the last three decades. However, contrary to liposomes or the catanionic vesicles, the morphology of structures, which are formed in the DODAB dispersions at room temperature, strongly depends on the method of preparation (Andersson *et al*, 1995; Feitosa & Brown, 1997; Lopes *et al*, 2008). As was shown previously, upon sonication, bilayer fragments are preferably formed in the dispersion (Andersson *et al*, 1995; Feitosa & Brown, 1997; Kepczynski *et al*, 2010). Application of extrusion results in the formation of vesicle structures; however, they have non-spherical angular morphologies and are rather polydisperse in size and geometry (Lopes *et al*, 2008). The origin of that phenomenon can be related to the molecular structure of DODAB bilayer. In a previous paper, we have shown using the molecular dynamics (MD) simulations, that the molecular organization of DODAB surfactant in its membrane at room temperature is complicated (Jamróz *et al*, 2010). The bilayer arranges spontaneously into the rippled phase (P_{β}'). Its characteristic feature is the presence of two regions with very different molecular ordering patterns. In the first region, the hydrocarbon chains of the DODAB molecules in the upper and lower monolayers are interdigitated, which results in a reduced bilayer thickness. The hydrocarbon chains are stretched out and tightly packed in a manner characteristic of the gel phase. In the other region, the upper and lower monolayers are separated. The membrane thickness of this region equals to approximately double the chain length. Both domains alternate in a periodic manner, giving a characteristic, asymmetric sawtooth profile. Such arrangement of DODAB molecules in its membrane results in relatively high bending rigidity of the surfactant bilayer.

Oleic acid (OA), a *cis*-monounsaturated fatty acid, is a natural compound, which considerably affects the lipid membrane properties (Kepczynski *et al*, 2008). The unsaturated fatty acids in *cis*-conformation decrease acyl chain ordering of the lipid in the bilayer increasing in this way the membrane free volume. Thus, the presence of OA in lipid membranes leads to the reduction of microviscosity (increase in the fluidity) at all locations in the membrane. Moreover, OA can gain the negative charge due to dissociation and become an

anionic surfactant. In this way, the catanionic system can be obtained by the introduction of OA into DODAB membrane at the appropriate pH. The study of the DODAB/OA monolayer at the air–water interface by the surface pressure–area (π–A) measurements and by the Brewster angle microscopy (BAM) has been performed earlier (Goncalves da Silva & Romao, 2005). The results indicate miscibility between monolayer components in a wide range of film composition, and phase separation for monolayer of X_{OA} = 0.8 at high surface pressures (higher than the collapse surface pressure of the OA monolayer). Therefore, it seems that OA should be a good candidate for an additive improving the DODAB vesicle geometries.

The phase- and structural behavior of OA dispersion is known to be strongly dependent upon the protonation state of the fatty acid (Edwards *et al*, 1995; Ferreira *et al*, 2006). At 25 °C and physiological salt concentration pK_a values of fatty acids embedded into phosphatidylcholine vesicles was reported to be in the range of 7.2 - 8 (Edwards *et al*, 1995). Under the conditions at which the fatty acid is almost fully ionized (pH > 9), OA organizes into micelles, whose size and shape is very sensitive to the sample concentration. As the pH is lowered to the values just above 9, unilamellar vesicles begin to form. With decreasing pH the vesicles show an increasing tendency to aggregate, and at pH values close to 8, large clusters of aggregated vesicles dominate in the sample.

The purpose of present studies was to investigate the effect of OA on the morphology of structures formed in the DODAB/OA dispersion at room temperature. The morphology of the objects formed was analyzed using a cryo-transmission electron microscopy (cryo-TEM) and a differential interference contrast microscopy (DIC). Properties of the DODAB/OA bilayer were studied using fluorescence anisotropy of 1,6-diphenylhexatriene (DPH) molecular probe and differential scanning calorimetry (DSC). Additionally, Langmuir monolayer measurements of the DODAB/OA mixtures on a phosphate buffered saline (PBS) subphase were performed.

4.3.3 MATERIALS AND METHODS

4.3.3.1 Materials

Dioctadecyldimethylammonium bromide (DODAB, >99%, Fluka), *cis*-9-octadecenoic acid (oleic acid, OA, >98%, Fluka), 1,6-diphenyl-1,3,5-hexatriene (DPH, Fluka, for fluorescence, ≥97.5%), and *N*,*N*-dimethylformamide (DMF, spectrophotometric grade, ≥99.8%) were used as received. Chloroform (p.a.) and ethanol (96%, p.a.) were purchased

from POCh, Poland. Millipore-quality water was used for all solution preparations. All experiments were conducted in phosphate-buffered saline (PBS) at pH 9.0.

4.3.3.2 DODAB/OA dispersion

Stock solutions of DODAB and OA in ethanol were prepared. The appropriate volumes of the stock solutions were mixed in a vial and the solvent was evaporated. Buffer was added to obtain surfactant concentration of 10 *mM*. The dispersion was stirred for 2 days at 60 °C and next extruded five times through a 200 nm filter (Millipore) using a high-pressure extruder. The obtained dispersion was slowly cooled down to room temperature (20 - 25 °C) and aged for one week under these conditions.

4.3.3.3 Differential Scanning Calorimetry (DSC)

DSC experiments were performed on a Calorimetry Sciences Corporation (CSC) 6100 Nano II differential scanning calorimeter with a cell volume of 0.3228 mL. The heat capacities of dispersions were recorded relatively to that of pure water. The measurements for 10 *mM* total lipid concentration and varying DODAB and OA concentration were performed at a scan rate of 1 °C/min. T_m was defined as the temperature of the peak maximum. The enthalpy was obtained by integration of the area under transition peak.

4.3.3.4 Cryo-Transmission Electron Microscopy (cryo-TEM)

Cryo-TEM allows the direct imaging of the hydrated sample while limiting the perturbation of the object observed. Three microliters of the sample solution were applied onto an electron microscopy grid covered with perforated supporting film. Most of the sample was removed by blotting (Whatman No.1 filter paper) for approximately one second, and the grid was immediately plunged into liquid ethane held at -183 °C. The sample was then transferred without rewarming into Tecnai Sphera G20 electron microscope using Gatan 626 cryo-specimen holder. The images were recorded at 120 kV accelerating voltage and microscope magnification ranging from 5000x to 14,500x using Gatan UltraScan 1000 slow scan CCD camera (giving final pixel size from 2 to 0.7 nm) and low dose mode with the electron dose not exceeding 15 electrons per square Å. Typical value of applied underfocus

ranged between 1.5 to 2.7 μm. The applied blotting conditions resulted in specimen with thickness varying between 100 to ca 300 nm.

4.3.3.5 Differential interference contrast (DIC) microscopy

Ten microliters of the DODAB/OA dispersion were applied onto a microscopy slide and covered with a microscope cover glass. An inverted microscope Nikon Eclipse, Ti (Japan) equipped with a halogen lamp and a DIC slider was used for DIC analysis. A 40x objective lens (Nikon Plan Fluor 0.60) was applied.

4.3.3.6 Fluorescence anisotropy measurements and microviscosity calculations

A stock solution of DPH was prepared in DMF. For labeling, the vesicle suspension was incubated in the dark for 1 h with appropriate amount of the probe stock solution. The fluorescence anisotropies of the samples were determined using λ_{exc} = 350 nm and λ_{em} = 428 nm. The measurements were repeated ten times and the average value was calculated. Steady-state fluorescence spectra and anisotropies of the samples were recorded at room temperature on an SLM-AMINCO 8100 Instruments spectrofluorimeter. For anisotropy measurements the spectrofluorimeter worked in the L-format and was equipped with automatic polarizers. Emission spectra were corrected for the wavelength dependence of the detector response by using an internal correction function provided by the manufacturer. The steady state anisotropy (*r*) was calculated according to the equation (Lakowicz, 1999)

$$r = \frac{I_{vv} - GI_{vh}}{I_{vv} + 2GI_{vh}} \tag{1}$$

where *I* is the fluorescence intensity and the two subscripts refer to the settings of the excitation and emission polarizers, respectively; *v* and *h* denote the vertical and horizontal orientation, respectively. *G* is an instrumental correction factor, which takes into account the sensitivity of the monochromator to the polarization of light. *G*-factor can be easily determined according to the equation (Lakowicz, 1999)

$$G = \frac{I_{hv}}{I_{hh}} \tag{2}$$

G-factors were measured individually for each sample and automatically corrected anisotropy values were obtained.

The apparent microviscosity, η, was calculated by using the expression (Pandey & Mishra, 1999)

$$\bar{\eta} = \frac{2.4r}{0.362 - r} \tag{3}$$

4.3.3.7 Langmuir monolayer measurements

Spreading solutions were prepared by dissolving the compounds in freshly distilled chloroform. Mixed solutions were prepared from the stock solutions. *π-A* isotherms were recorded with a NIMA (U.K.) Langmuir trough (total area of 300 cm^2) placed on an anti-vibration table. The spreading solutions were deposited onto the subphase with the Hamilton micro syringe, precise to 1.0 μL. Upon spreading, the monolayers were left for 10 min. to allow the organic solvent to evaporate. Since in preliminary experiments no influence of the compression velocity (within the range of 5–30 cm^2/min) was found for the investigated compounds, monolayers were compressed with the barrier speed of 20 cm^2/min in all experiments. Surface pressure was measured with the accuracy of ± 0.1 mN/m using a Wilhelmy plate made of filter paper (ashless Whatman Chr1) connected to an electrobalance. The subphase temperature (20 °C) was controlled thermostatically within 0.1 °C by a circulating water system.

The basic characteristics of the Langmuir monolayers concerning their molecular organization and the miscibility of their components can be drawn from the course and position of the recorded *π-A* isotherms. Preliminary information on miscibility of film components can be obtained from the variation of the collapse surface pressure with the composition of mixed monolayers. To verify the state of the investigated films and possible phase transitions as well as to obtain the information on the ordering of molecules in a monolayer, the compression modulus, which is a reciprocal of the monolayer compressibility at a given monolayer composition, was calculated according to the following equation (Davies & Rideal, 1963):

$$C_S^{-1} = -A\left(\frac{d\pi}{dA}\right) \tag{4}$$

where A is an area per molecule at a surface pressure π. The states of monolayers are classified on the basis of the maximal values of C_S^{-1} in the following way: $(C_S^{-1})_{max}$ = 12.5-50 mN/m, liquid-expanded; $(C_S^{-1})_{max}$ = 50-100 mN/m, liquid; $(C_S^{-1})_{max}$ = 100-250 mN/m, liquid-

condensed; $(C_S^{-1})_{max}$ = 250-1000 mN/m, condensed; $(C_S^{-1})_{max}$ > 1000 mN/m, solid. The minima in the plots of C_S^{-1} versus π correspond to the phase transitions. The miscibility and the interactions between molecules in the mixed monolayers were analyzed according to the additivity rule. The mean areas per molecule in the mixed film (A_{12}) determined directly from the isotherms, at various surface pressure values (5, 10 and 32.5 mN/m), were compared with those assuming ideal miscibility of the molecules (Costin & Barnes, 1975; Gaines, 1966):

$$A_{12}^{id} = A_1X_1 + A_2X_2 \tag{5}$$

where A_{12}^{id} is the mean area per molecule for ideal mixing, A_1, A_2 are the molecular areas of the respective component in their pure films at a given surface pressure and X_1, X_2 are the mole fractions of components 1 and 2 in the mixed film. Moreover, based on the excess Gibbs energy of mixing (ΔG^{Exc}) values, calculated according to eq. 6 (Costin & Barnes, 1975; Gaines, 1966), quantitative information on the interactions existing between the molecules in the mixed monolayers was drawn.

$$\Delta G^{Exc} = N_A \int_0^{\pi} (A_{12} - X_1A_1 - X_2A_2)d\pi \tag{6}$$

4.3.4 RESULTS

In this work we analyze a binary system of DODAB and OA. The chemical structures of the studied compounds are presented in Figure 4-17. DODAB is a surfactant with double saturated chains, while OA is a *cis*-monounsaturated single-chained amphiphile. A series of DODAB/OA samples with total lipid concentration corresponding to 10 *mM* and different mole fractions of OA (X_{OA}) equal to 0.0, 0.2, 0.4, 0.6, 0.8 and 1.0, were prepared by extrusion at the temperature higher than that of the gel-liquid transition of DODAB. After aging for one week at room temperature they were analyzed by cryo-TEM, DIC, DSC and fluorescence anisotropy technique.

4.3.4.1 Cryo-TEM and DIC microscopy studies

The effect of X_{OA} on the morphology of structures formed in the DODAB/OA dispersion was examined with cryo-TEM and optical microscopy. A typical cryo-TEM micrograph of the extruded DODAB dispersion (X_{OA} = 0) is shown in Figure 4-18A. As can

be seen, the vesicle population does not show ideally spherical vesicle structures as known for liposomes or the cationic vesicles. Instead, the micrographs revealed a shape diversity of the vesicular structures with angular or ellipsoidal geometries and sizes between 100 and 200 nm. On the contrary, the micrograph presented in Figure 4-18F shows that samples of pure OA (X_{OA} = 1) buffered at pH 9.0 are dominated by uni- and bilamellar vesicles of predominantly spherical shape. The diameter of vesicles is close to 100 nm.

In the case of the system where X_{OA} = 0.2, the structures appeared as faceted vesicles with highly deformed wrinkled walls (Figure 4-18B). A closer inspection of the micrograph reveals that there is a population of bilamellar vesicles and not all structures are completely closed. The sizes of the features are similar to those for X_{OA} = 0, i.e. between 100 to 200 nm. As the OA mole fraction increased up to the value of 0.4 or 0.6, after cooling down to the room temperature the extruded dispersions became cloudy. This observation suggested formation of large objects in the DODAB/OA dispersions at those mole fractions. Figure 4-19 shows typical DIC micrographs of the dispersions with X_{OA} = 0.4 and 0.6. The DIC images revealed that the lipids organize into large planar membranes. Such membranes are arranged into a stack of several bilayers. The dimensions of those structures are in the order of tens or hundreds of micrometers. Such objects are too large to allow preparation of a specimen for cryo-TEM analysis. Therefore, for that experiment we shortly sonicated the DODAB/OA dispersions to obtain smaller fragments of the lipid bilayer. Figure 4-18C shows the cryo-TEM micrograph of the lipid dispersion at X_{OA} = 0.4. The mutually overlapping bilayer flakes were observed in the sample. Interestingly, the fragments of lipid membranes contain features that have lower contrast (are brighter) compared to the surroundings. That increase in brightness suggests that these sites might be holes in the membrane. Cryo-TEM analysis of the sample with X_{OA} = 0.6 (Figure 4-18D) confirms the presence of the planar membranes. In that case no holes were observed. With the further increase of OA content in the membrane up to X_{OA} = 0.8 unilamellar vesicles are formed in the DODAB/OA dispersion, as seen in Figure 4-18E. Those vesicles possess predominantly spherical shape and their sizes are close to 100 nm.

4.3.4.2 Differential scanning calorimetry studies

DSC curves for the mixed DODAB/OA bilayers with the various mole fractions of OA were obtained (Figure 4-20). The transition observed by DSC can be characterized by the chain melting temperature (T_m), enthalpy of transition (ΔH_m), and width at half-height ($\Delta T_{1/2}$),

of the transition peak. These experimentally determined thermodynamic data are summarized in Table 10. The thermogram for the neat DODAB exhibits a single and relatively sharp endothermic peak (Fig. 4-20). The temperature and enthalpy values for the main transition of DODAB measured in this study show a good agreement with the literature data (Feitosa *et al*, 2000).

In the DSC thermogram for the DODAB/OA system containing the lowest amount of OA (X_{OA} = 0.2), the main thermal transition occurs at 36.6 °C. The observed large temperature decline (8.6 °C) is associated with an enrichment of the system in the unsaturated compound. The enthalpy change for X_{OA} = 0.2 system is higher than for the pure DODAB liposomes. A noticeable increase of enthalpy is rather an unexpected effect considering the addition of unsaturated fatty acid. This effect can result from electrostatic interactions between cationic DODAB and anionic OA. At this concentration of OA, the DSC curve exhibits two additional small endotherms at 46.1 and 52.8 °C, which can be related to main and post-transition of the pure non-sonicated DODAB (see Subchapter 4.3.5), respectively. The observation of such transitions can indicate the existence of pure DODAB patches in the DODAB/OA mixture. Further increase of OA content (X_{OA} = 0.4) brings about little decrease in the transition temperature (only by 0.3 °C) and substantial reduction of the ΔH_m value, what indicates the loss of interaction strength. Nevertheless, the peak still remains sharp, therefore, the cooperativity of the transition is relatively high. Subsequent decrease in T_m and ΔH_m can be observed upon further increase of OA concentration (X_{OA} = 0.6). However, under such mixture composition, the thermal transition becomes considerably broader. The DSC curve obtained at X_{OA} = 0.8 is much more complex and difficult for interpretation. The endotherm consists of three partially overlapping peaks, which correspond to different DODAB/OA fluid states. The neat OA indicated no peaks in the temperature range of 10 - 70 °C.

4.3.4.3 Fluorescence anisotropy measurements

DPH is the most widely applied rotational probe for estimating microviscosity and fluidity of liposomal membrane in the acyl side chain region (Kepczynski *et al,* 2008). We have used that probe for fluorescence study of DODAB/OA membrane properties. The systems containing different amount of OA were labeled with DPH in the dark. There was no effect of membrane composition on the shape and location of the emission band of the incorporated probe. The measurement of the fluorescence polarization was done and the

steady-state anisotropy of DPH in the DODAB/OA membranes as a function of mole fraction of OA is shown in Figure 4-21. It is seen that the anisotropy of DPH increases slightly up to the OA mole fraction of 0.4, and then decreases abruptly with a further increase of OA level in the membrane. Feitosa *et al*. have previously studied the anisotropy of DPH in dispersions of DODAB at various temperatures (Feitosa *et al*, 2000). At 20 °C they have found the *r* values equal to 0.29 and 0.31 for sonicated and non-sonicated dispersion, respectively. The DPH anisotropy obtained in this study for the neat DODAB membrane is slightly lower than that reported in the literature, but that deviation could be attributed to the different method of the DODAB dispersion treatment.

The fluorescence anisotropy of the probe is a function of the environment microviscosity. Values of the apparent microviscosities were calculated from the measured anisotropies of DPH using the Perrin equation (Eq.(3)). The measured anisotropy of DPH and the calculated values of microviscosity are listed in Table 12. The neat DODAB bilayer is characterized by relatively high microviscosity. The addition of OA up to X_{OA} = 0.4 into DODAB membrane cause a significant increase of the microviscosity of the mixed bilayer. However, for higher concentrations of the fatty acid an abrupt decrease of microviscosity was noticed.

4.3.4.4 Langmuir monolayer measurements

The surface pressure (π) - area (A) isotherms for the DODAB/OA mixed systems were recorded on PBS subphase at pH 9 and are presented in Figure 4-22. Comparing the curves obtained for one-component monolayers it can be seen that in the case of a DODAB film the surface pressure increases at area ≈110 Å^2/molecule and the film collapses at $\pi_{coll.}$ ≈ 64 mN/m. In DODAB isotherms a pseudo-plateau regions can be observed π ≈ 11 mN/m. These pseudo-plateaus reflect a phase transition between liquid expanded (LE) and liquid condensed (LC) state, which is confirmed by maximal values of the compression modulus ((C_S^{-1})$_{max}$ = 34 mN/m and (C_S^{-1})$_{max}$ = 215 mN/m) in the plot of C_S^{-1} vs. Π (Figure 4-23A).The analysis of π - A dependence for OA showed that the surface pressure starts to rise at the area about 65 Å^2/molecule and then systematically increases up to the monolayer collapse ($\pi_{coll.}$= 41 mN/m) at the area of about 25 Å^2/molecule. The shape of the π -A curves for OA indicates liquid state of the investigated film, which is confirmed by maximal values of the compression modulus ((C_S^{-1})$_{max}$ = 64 mN/m). As it was found the maximal value of the compression modulus for

OA monolayer is much lower than that for the DODAB film proving fluidizing effect of the unsaturation of the hydrocarbon chain on the monolayer organization.

The addition of OA into DODAB film strongly influences both the shape and the position of the π -*A* curves (Figure 4-22). With the increase of OA mole fraction in the mixed film, the phase transition characteristic of the DODAB monolayer shifted towards higher values of surface pressure. Moreover, the increase of OA content in the monolayer provokes the shift of the isotherms for DODAB/OA monolayers towards the curve for OA monolayer. The incorporation of OA into DODAB film affects also the collapse surface pressure ($\pi_{coll.}$) of the mixed monolayers, which indicates the miscibility of the components in the whole range of film composition.

To verify the influence of OA on the fluidity of DODAB monolayer the values of compression modulus at π = 32.5 mN/m were plotted as a function of the membrane composition (Figure 4-23B). As can be seen a small amount (up to 30%) of OA in DODAB monolayer reduces almost linearly the monolayer rigidity. Further increase of OA content to X_{OA} = 0.5 causes the increase of the rigidity to the value comparable to that for the pure DODAB membrane. For mole fractions of OA higher than 0.7 the abrupt increase in fluidity of the mixed membrane was observed.

It is suggested that at a surface pressure between 30 and 35 mN/m the monolayer properties, such as area per molecule, lateral pressure and elastic compressibility modulus, correspond to the properties of bilayer (Marsh, 1996; Nagle & Tristram-Nagle, 2000). Figure 4-24A presents the plots of the mean area per molecule (A_{12}) vs. monolayer composition (X_{OA}). The A_{12} values were determined directly from the isotherms at surface pressures π = 5, 10 and 32.5 mN/m. The plots for ideal mixing are presented as dashed lines. As can be seen, in the whole range of the monolayer composition in the $A_{12} = f(X_{OA})$ plots the deviations from ideal behavior can be observed. This indicates mixing of the investigated compound in the monolayer. Since the observed deviations are negative, one can conclude that the addition of OA significantly condenses DODAB monolayer, which suggests more attractive (or less repulsive) interactions between OA and DODAB in the mixed films than OA-OA and DODAB-DODAB forces in their one-component monolayers.

To examine the magnitude of the interactions between molecules in the mixed system the excess Gibbs energy of mixing (ΔG^{Exc}) values were calculated and plotted as a function of the film composition (Fig. 4-24B). As can be observed the values of the excess Gibbs energy of mixing for the studied mixed systems are negative in the whole range of the monolayer composition. This demonstrates that in the mixed monolayer DODAB and OA molecules

attract stronger than in one component films formed by the investigated compounds. The minimum of ΔG^{Exc} at X_{OA} = 0.5 indicates the monolayer composition of the strongest attractions between molecules. Thus, the strongest interactions between DODAB and OA molecules occur at the ratio [DODAB]:[OA] of 1:1. Furthermore, the values of the ΔG^{Exc} decrease with the increase of the surface pressure. This is due to denser packing of molecules at higher values of π that provokes stronger interactions between molecules.

4.3.5 DISCUSSION

The main objective of this study was to explore the effect of incorporation of OA on the morphology and properties of DODAB bilayer. OA has in its structure the *cis*-double bond bending the hydrocarbon chain and carboxylic group bearing negative charge due to dissociation under our experimental conditions. Both of these groups should affect the arrangement of DODAB molecules in its bilayer. The bent hydrocarbon chain of OA should introduce disordering in dense DODAB chain packing, whereas the negative charge at the head group should result in appearance of the strong interactions between both lipids.

Cryo-TEM micrographs (Figures 4-18B-E) and DIC images (Figure 4-19) revealed the drastic effect of the OA inclusion on the morphology of the DODAB/OA membranes. The morphology of objects revealed that the incorporation of OA into DODAB bilayer results in a decrease of the membrane curvature. After introduction of 20 mol% of the fatty acid, the faceted vesicles were observed in the DODAB/OA dispersion, whereas at X_{OA} = 0.4 or 0.6 only fragments of planar bilayer were present. The vesicles having regular spherical morphology with a distinct surfactant membrane surrounding an aqueous core were formed only when the mole fraction of OA in the DODAB/OA dispersion was equal to 0.8 or higher (see Figures 4-18E and F).

To explain such influence of OA on the DODAB bilayer, the properties of DODAB/OA membranes having various compositions were studied using the fluorescence anisotropy, Langmuir monolayer, and microcalorimetry methods. The anisotropy measurements were used to determine a local microviscosity of the pure and mixed membranes. DPH is buried deeply in the hydrocarbon region and the viscosity of that environment has a significant effect on the rotational movement of these molecules (Kepczynski *et al*, 2008). The changes of microviscosity in the hydrocarbon part of vesicles are directly related to the changes of the free volume. Surprisingly, the introduction of OA up to X_{OA} = 0.4 causes significant increase in the value of the microviscosity. This may indicate

that the presence of OA in DODAB membrane at that range of concentrations entailed more densely packed structure of DODAB/OA mixed bilayers in comparison to the pure DODAB membrane. That can be a consequence of the electrostatic interactions between the oppositely charged lipid molecules (see below). Only a further increase of the content of OA results in the reduction of the DPH fluorescence anisotropy indicating a decrease of the local viscosity (Figure 4-21 and Table 12). This observation can be easily explained considering the 30° bend of oleoyl chains at the C9 position, which causes the steric nonconformability to the DODAB molecules. Thus, the densely packed DODAB hydrocarbon chains are loosened and the free volume in the membrane increases. The values of microviscosities characteristics of the DODAB/OA system at $X_{OA} \geq 0.8$ are similar to those reported for the saturated lipids bilayer in the fluid state (Bahri *et al*, 2007). The DSC experiments allowed determining the main phase transition temperature, which describes the transition between the rigid gel state and the fluidlike liquid-crystalline state of the lipids in the bilayer. Depending on the preparation method, buffer used, sample concentration, vesicle curvature and heating rate, the temperature of the main thermal transition for neat DODAB changes in broad range (43.5 – 47.8 °C) (Feitosa *et al*, 2000). Additionally, in the case of the non-extruded (nonsonicated) DODAB dispersions small endotherms of pre-transition (~36.3 °C) and post-transition (~52.6 °C) were observed (Brito & Marques, 2005; Feitosa *et al*, 2000). These pre- and post-transition peaks are probably related to the appearance of new structures in the dispersion and/or changes in the local structure of the vesicle bilayer as a result of intra- and intervesicular interactions. As was found in our studies, the value of T_m decreased from 45.2 °C for the pure DODAB to 34-36 °C (depending on the composition, see Table 11) in the DODAB/OA systems with $X_{OA} < 0.8$. This temperature range is very close to the pre-transition temperature of the neat DODAB membrane. Therefore, the incorporation of OA into the DODAB membrane induced changes in its molecular arrangement. However, the observed reduction of the T_m value is insufficient, and at room temperature the DODAB/OA membranes of $X_{OA} < 0.8$ form still the gel phase, where the hydrocarbon chains stretch and most molecular degrees of freedom are frozen, or at least dramatically slowed down. When heating above 34-36 °C, the chains of lipids are fluid and the membrane is in the liquid-crystalline state. Only the DODAB/OA systems with $X_{OA} \geq 0.8$ are in the liquid state at room temperature. These findings are in line with the microviscosity measurements.

A further insight into DODAB/OA membrane properties was obtained using Langmuir monolayer experiments. The Langmuir monolayers consisting of various lipids are frequently used as a model of biomembranes (Maget-Dana, 1999; Wagner & Brezesinski,

2008; Wydro & Hąc-Wydro, 2007). The obtained results indicate that in the mixed DODAB/OA films the beneficial interactions between molecules appear that shorten intermolecular distance, causing the film condensation. There are strong electrostatic attractions between oppositely charged polar groups of the investigated compounds, which are reflected in the negative values of the mean areas per molecule (Figure 4-24A) as well as in the excess of Gibbs energy (Figure 4-24B). Moreover, the maximum of the area condensation and minimum of ΔG^{Exc} appears for monolayers containing about 50% of OA, which indicate that interactions between molecules are the strongest when DODAB and OA are in proportion of 1:1. OA as the compound possessing *cis* double bond in the chain forms typical liquid monolayers and therefore it can be expected that the incorporation of OA molecules should have strongly fluidizing influence on DODAB monolayer. The fact that the addition of OA into DODAB film decreases the compression modulus only insignificantly (Figure 4-23B) indicates that electrostatic attractions between polar head group, which are responsible for strong condensation of the monolayer, prevail over the effect of unsaturated fatty acid chain. This is confirmed by the fact that the fluidity of the investigated monolayers increases when the mole fraction of OA is greater than its contents at which the strongest intermolecular forces are observed. The decrease of monolayers rigidity for $X_{OA} > 0.5$ is in good agreement with the DSC and anisotropy measurements.

According to the critical packing theory, the molecular packing parameter is a factor governing the morphology of surfactant aggregates formed in the aqueous solution (Israelachvili *et al*, 1976). That parameter (*S*) of the surfactant molecule is the ratio between a 'sterical' area naturally linked to fluid incompressibility, a_s, and the equilibrium area per molecule at the hydrophobic-hydrophilic interface, *a* (Kunz *et al*, 2009). The a_s area is equal to the ratio *V*/*l*, where *V* is the volume of the hydrocarbon chains and *l* is the length of the hydrocarbon chains. Therefore, the molecular packing parameter is given by $S = V/(al)$. It is commonly accepted that the formation of vesicles is preferred at $0.5 \leq S \leq 1$,and for $S \geq 1$ the flat bilayer is usually observed. DODAB molecule has the packing parameters close to one (Bronich *et al*, 2000). The electrostatic interactions of the opposite charged head groups of DODAB and OA cause the oncoming of those groups and the resultant decrease in the effective size of the head group in DODAB-OA complex, as was shown with the Langmuir monolayer experiments. This leads to the reduction of the value *a* and subsequent increases in *S* to values larger than 1. As a consequence, the DODAB/OA systems gain tendency to form the planar bilayer fragments, as was observed using the microscopy techniques.

4.3.6 CONCLUSIONS

In the current studies we have demonstrated that the incorporation of OA into DODAB bilayer has a significant effect on the morphology and properties of that membrane. The observed morphologies were strongly dependent on the membrane composition. The presence of OA in DODAB bilayer at X_{OA} lower than 0.8 results in a decrease of the membrane curvature and the faceted vesicles or the planar bilayer fragments are formed. The spherical vesicles are formed only when the mole fraction of OA in the DODAB/OA mixed membrane exceeds the value of 0.8. This phenomenon can be explained taking into account the strong electrostatic interactions between the head groups of OA and DODAB, which attained its maximum at X_{OA} = 0.5. These attractive interactions cause the reduction of the effective head group area at the hydrophobic-hydrophilic interface and more tight packing of the bilayer. As a consequence, the microviscosity of the membrane increases. An increase of OA content above X_{OA} = 0.5 results in the increase of the free volume (reduction of the microviscosity). Thus, the presence of OA causes disordering in dense DODAB chain packing and the fluidity of the bilayer increase. However, the DODAB/OA mixed membranes are in the gel state at room temperature for the systems with X_{OA} lower than 0.8, so the DODAB chains are stretched and their mobility is significantly reduced up to that content of OA. Our results have shown that OA is not an appropriate additive to improve the morphology of the DODAB vesicles. It seems that application of a compound devoid of the negative charge at head group should give better results.

4.3.7 ACKNOWLEDGEMENTS

The authors thank to the Polish Ministry of Science and Higher Education for financial support in the form of Grant No N N209 118937. The research was carried out with the equipment purchased thanks to the financial support of the European Regional Development Fund in the framework of the Polish Innovation Economy Operational Program (contract no. POIG.02.01.00-12-023/08). J.B. acknowledges the support to the Czech Grants LC535, MSM0021620806 and AV0Z50110509. P.W. wishes to thank the Foundation for Polish Science for financial support.

4.3.8 FIGURE AND TABLE LEGENDS

Figure 4-17: *Chemical structure of dioctadecyldimethylammonium bromide (DODAB) and oleic acid (OA).*

Figure 4-18: *Cryo-TEM micrographs of vitrified extruded DODAB/OA dispersions.* (A) X_{OA} = 0, (B) X_{OA} = 0.2, (C) X_{OA} = 0.4, (D) X_{OA} = 0.6, (E) X_{OA} = 0.8 and (F) X_{OA} = 1. The scale bar represents 100 nm for C, E and F panel, and 200 nm for A, B and D panel.

Figure 4-19: *Differential interference contrast (DIC) images of structures formed in the DODAB/OA dispersions at X_{OA} = 0.4 (A) and X_{OA} = 0.6 (B).* The scale bar represents 20 μm.

Figure 4-20: *DSC thermograms (second upscans) for 10 mM DODAB/OA aqueous dispersions as a function of OA mole fraction.* Mole fractions of OA are depicted on each curve.

Figure 4-21: *The effect of the OA mole fraction on the fluorescence anisotropy of the DPH probe incorporated into bilayer* (λ_{exc} = 350 nm, λ_{em} = 428 nm, $c_{DPH} = 1.4 \times 10^{-7}$ M).

Figure 4-22: *The surface pressure (π)–area (A) isotherms of DODAB/OA mixed monolayers formed at the air/water interface at 20 °C.* The subphase was a PBS buffer at pH 9.

Figure 4-23: (A) *The compression modulus versus surface pressure for the DODAB/OA mixed monolayer.* (B) The changes of the compression modulus values at π = 32.5 mN/m vs. composition of DODAB/OA monolayers.

Figure 4-24: (A) *The mean area per molecule (A_{12}) vs. composition plots for DODAB/OA mixed monolayers at various surface pressures.* (B) The excess Gibbs energy of mixing vs. Composition plots for DODAB/OA mixed monolayers at various surface pressures.

Table 11: *Thermodynamic data obtained by micro-DSC analysis for 10 mM mixture DODAB/OA in water; the melting temperature, T_m, the melting enthalpy, ΔH_m.*

Table 12: *Experimentally measured the fluorescence anisotropy of DPH and the calculated microviscosity.*

4.3.9 FIGURES AND TABLES

Figure 4-17:

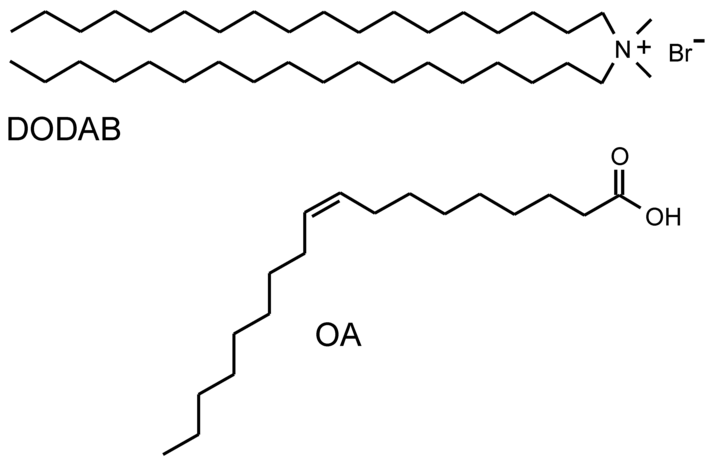

Figure 4-19:

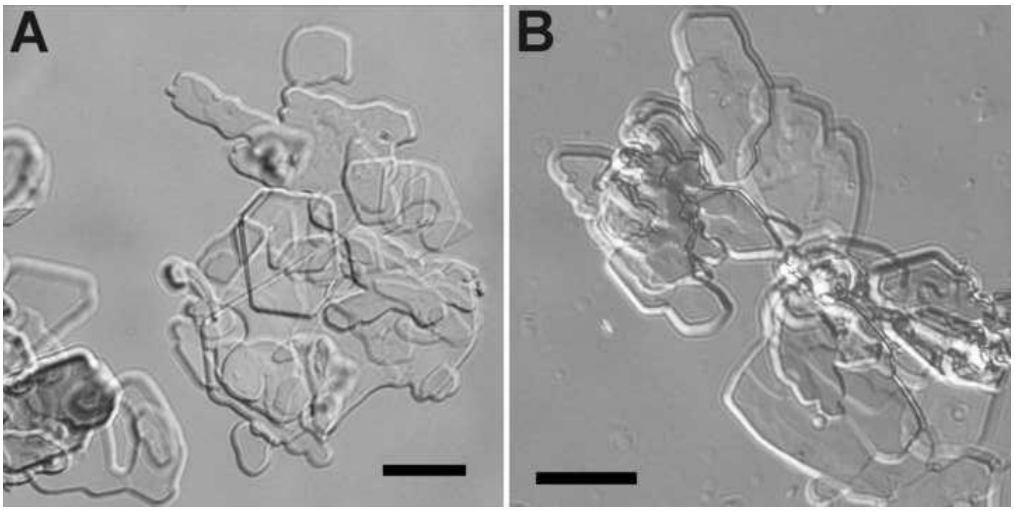

Figure 4-18:

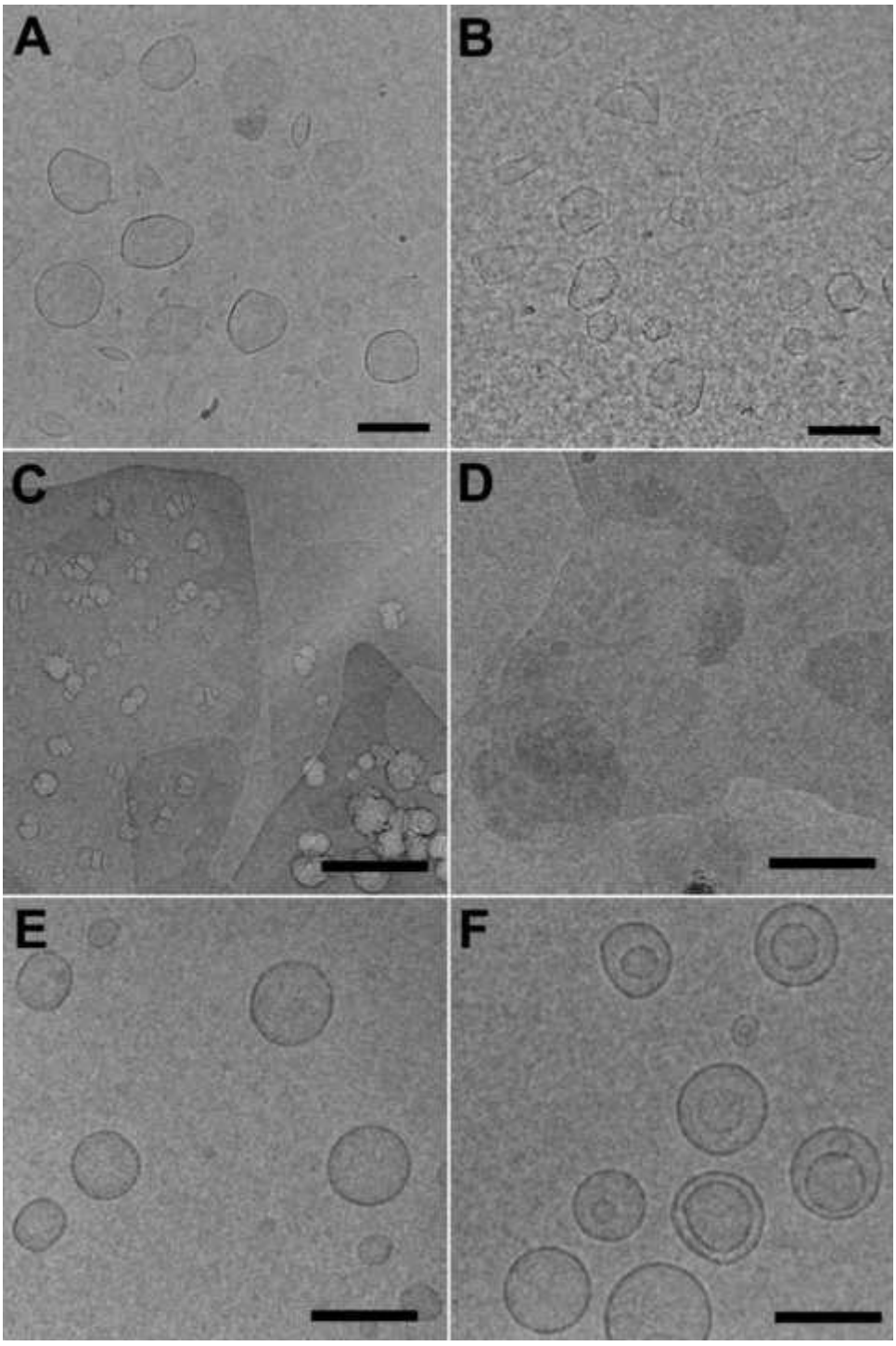

Figure 4-20:

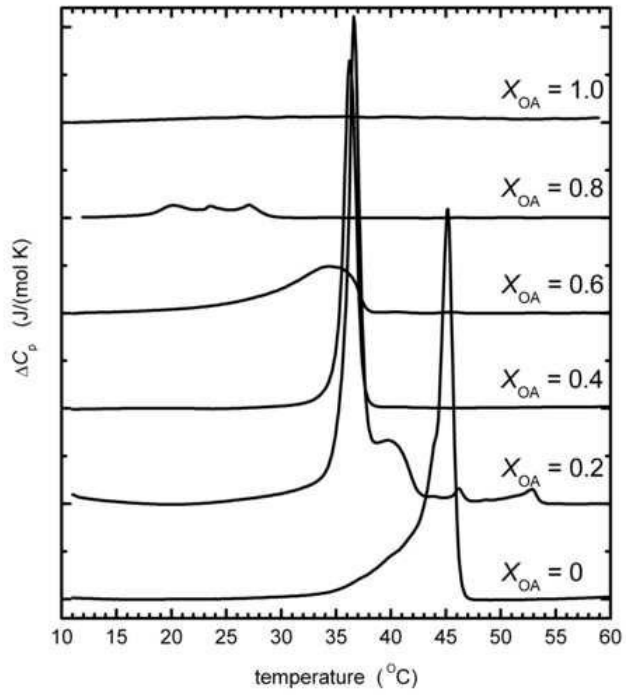

Figure 4-21:

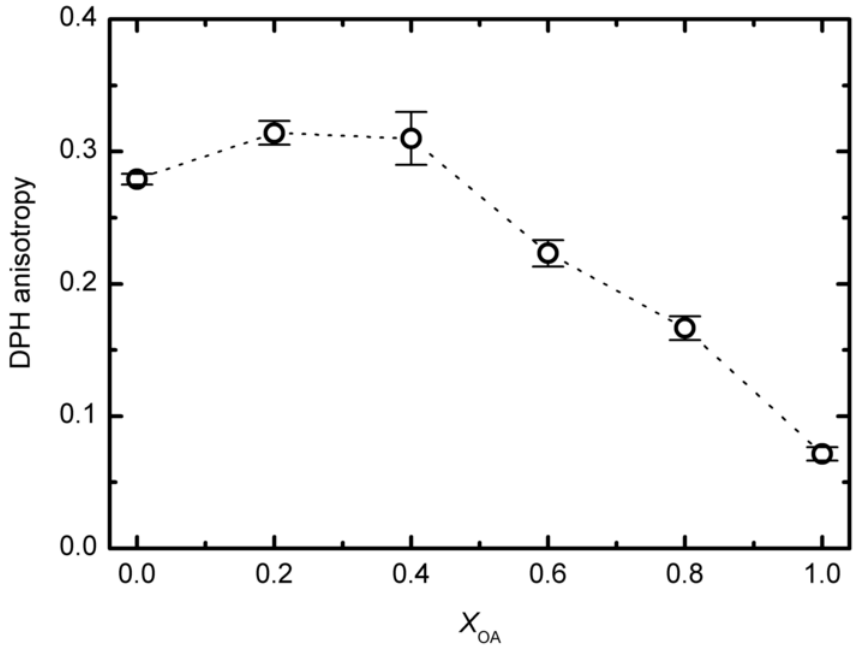

Figure 4-22:

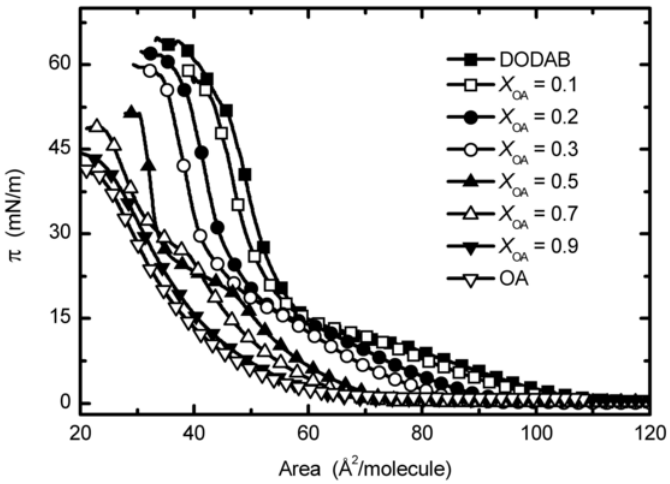

Table 11:

OA (mol%)	ΔH_m		T_m (°C)	$\Delta T_{1/2}$ (°C)
	(kJ/mol)	(kcal/mol)		
0	43,5	10,4	45,2[a]	1,3
		10,3[b]	44,6[b]	
20	51,5	12,3	36,6[a]	1,2
40	25,5	6,1	36,3	0,9
60	18,0	4,3	34,4	5,1
80	4,6	1,1	19,8; 23,1; 26,7[a]	9,2

[a] Temperature corresponding to main peak.
[b] Data taken from Feitosa et al. (2000).

Table 12:

X_{OA}	DPH anisotropy	Microviscosity (cP)
0	0,279 ± 0,004	805
0,2	0,314 ± 0,009	1570
0,4	0,31 ± 0,02	1430
0,6	0,223 ± 0,009	385
0,8	0,167 ± 0,009	205
1	0,0715 ± 0,0043	59

Figure 4-23:

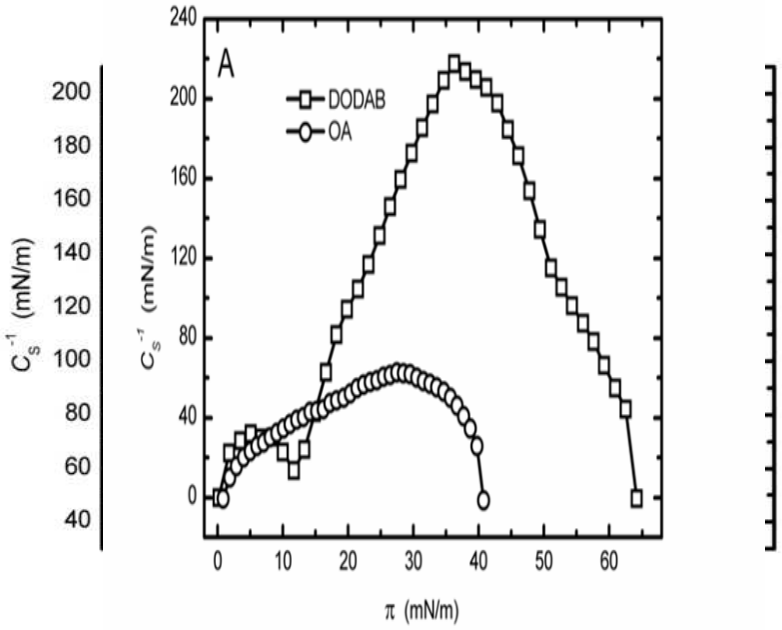

Figure 4-24:

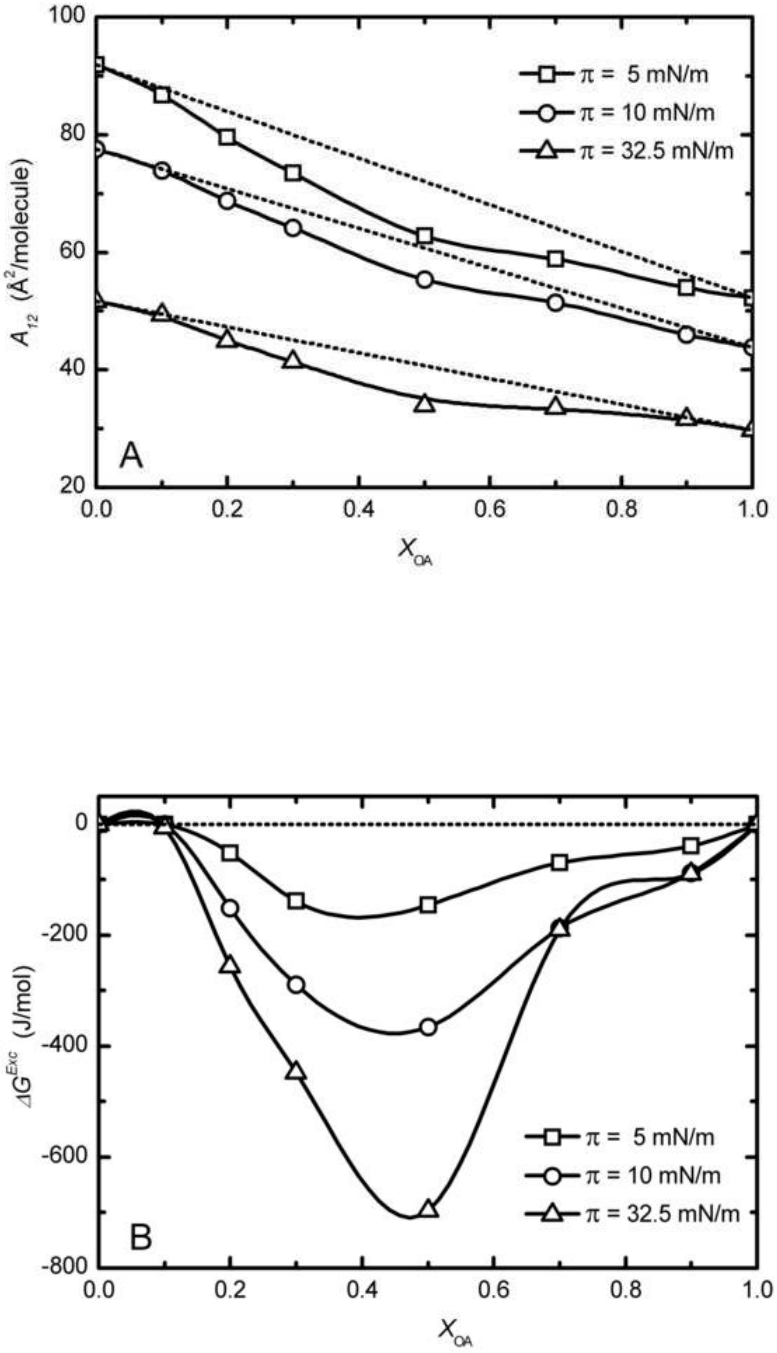
A
B
π = 5 mN/m
π = 10 mN/m
π = 32.5 mN/m
A_{12} (Å^2/molecule)
ΔG^{Exc} (J/mol)
X_{OA}
100
80
60
40
20
0
-200
-400
-600
-800
0.0
0.2
0.4
0.6
0.8
1.0

CHAPTER 5 GENERAL DISCUSSION

Electron microscopy has become an indispensable tool in many fields of life science research providing unique information about the biological structure-function relationships from the cellular to nearly atomic scale – the critical range in which molecular machines of living systems operate - since its invention in 1931 (Ernst Ruska – Autobiography, n.d.). Researchers were looking at the biological material for many years, and currently there is an enormous variety of experimental techniques, which allows us to look at biological material in many different ways. The chemical fixation, dehydration and embedding constitute the major pathways, by which the vast majority of biological sample processing is carried out for TEM, but also some LM observation (Bozzola, 2007; Glauert, 1974; Griffiths, 1993). These techniques, however, almost always involve the removal of water from the samples, which inevitably leads to changes in the native biological structure: a lot of soluble materials are extracted, and further *in vivo* distribution of ions and other mobile components is radically changed. Such considerations led to a much greater attention being paid to an alternative for the preparation of biological samples: that of cryo-immobilization. The catalyst for this 'revolution' was the development of new instruments (Moor & Riehle, 1968; Studer *et al*, 2001) and TEM imaging techniques (Adrian *et al*, 1984; Dubochet *et al*, 1988; Pierson *et al*, 2009).

The work presented in this thesis is devoted to the utilization of cryo-preparation methods in the processing of samples for conventional TEM and cryo-TEM image analysis.

In Publication No.1 (Subchapter 4.1), we described and compared different protocols of the processing of the yeast *S. cerevisiae* for fine ultrastructural and immunocytochemical TEM analysis. An approach using an aldehyde-based fixation, alcohol dehydration, LR White resin embedding, ultrathin sectioning and heavy metal post-staining was compared with that of cryo-fixation by high-pressure freezing, cryo-dehydration in the process of freeze substitution, Lowicryl HM20 low-temperature embedding, ultrathin sectioning with or without post-staining (as described above), in order to emphasize the importance and power of presented low-temperature processing methods.

The goal of fixation for the immunocytochemical TEM analysis is to preserve the fine ultrastructure of the cells as much as possible without destroying the antigen determinants recognized by antibodies (Griffiths, 1993). Thus, it is possible to simultaneously show the precise localization of a protein and the ultrastructure of the organelle and environment wherein it is embedded (Griffith *et al*, 2008). It is known that yeast cells are particularly

difficult to preserve for both the ultrastructural and immunocytochemical TEM analysis, mainly due to the presence of a thick cell wall that acts as a barrier against diffusion of fixatives (Mulholland & Botstein, 2002; Wright, 2000). Especially when yeasts are proccesed in a classical way, which includes conventional aldehyde-based fixation and dehydration at room temperature, significant ultrastructural artifacts are observed in TEM micrographs (Figure 4-01A-D from Subchapter 4.1). As a result, the preservation of antigens could be significantly influenced in a negative way in such preparations. As presented here, thin sections of aldehyde-fixed yeasts were on-section immunogold-labeled with antibodies recognizing nuclear (Nsp1), nucleolar (Nop1 and Nsr1) and α-tubulin antigens. According to our results (see Subchapter 4.1.3), the immunoreactivity of two antigens under the study (namely, Nsr1 and Nsp1) was not preserved in those samples, though Nop1 and α-tubulin were localized (data not shown). However, it was not an easy task to correlate the antigen localization with the subcellular arrangement in these samples. Fine ultrastructural details were not well visible or preserved (Figure 4-01A-D). Typically, the FA-fixed cells showed lower level of ultrastructural preservation compared to the FA/GA-fixed cells, but artifacts such as plasma membrane invaginations, irregular shape of the nuclei, etc. were still present. Moreover, the nucleolar sub-compartments were hardly recognizable in both the FA- and the FA/GA-fixed cells. It was not so suprising, since the TEM micrographs of aldehyde-fixed *S. cerevisiae* cells previously allowed to describe the nucleolus only as a strongly electron-dense and a crescent-shaped region of the nucleus (Melese & Xue, 1995; Sicard *et al*, 1998; Trumtel *et al*, 2000).

Cryo-preparation techniques are currently on the way to replace chemical fixation as a standard approach (Hurbain & Sachse, 2011). Among them, the cryo-fixation by HPF followed by low-temperature dehydration (FS) and low-temperature embedding is believed to be the method that preserves high-resolution details present in living cells in a state closely related to the native one (Moor & Riehle, 1968). The available evidence suggests that even the piece of an uncryoprotected tissue up to about 200 μm (600 μm theoretically) can be effectively vitrified by this approach (McDonald, 2007; McDonald, 2009; Studer *et al*, 2008). As presented in this thesis, we implemented HP-induced cryo-fixation followed by FS and embedding into Lowicryl HM20 with the objective to formulate a 'standard protocol', which can be applied to *S. cerevisiae* cells, and/or alternatively to a wide variety of other samples, with optimal preservation of both ultrastructure and antigenicity. We analyzed FS media of different composition i.e, the acetone, acetone/UA, acetone/GA and acetone/UA/GA media for their positive/negative impact on the preservation of cell morfology and immunoreactivity.

We compared the appearance of the TEM images of *S. cerevisiae* thin sections prepared by conventional method described above (Figure 4-01) with the TEM images of HP-frozen/FS samples (Figures 4-02). Differences remained considerably significant (see Figures 4-03, 4-04, and 4-05), though the primary goal to preserve mainly the antigenicity influenced the choice of reagents used for the substitution and resin embedding. Both types of preparation showed almost the same structural details in the sense that the cell constituents seen with one method were visible also with the other, e.g., organelles, membranes, nuclei. However, the higher magnification views of HP-frozen/FS cells (Figures 4-03 and 4-04, respectively), presented ultrastructural details that were greatly different from that observed in aldehyde-fixed cells (Figure 4-01). Beyond the notable superior high level of preservation of the ultrastuctural details (Figure 4-03), the sensitivity of the immunocytochemical localization of antigens on sections was unambiguosly increased contrary to samples processed in a conventional manner: Nop1 (Figure 4-06 B), α-Tubulin (Figure 4-08B) and Nsp1 (Figure 4-07B) antigens were clearly immunolocalized on sections of these cells. Moreover, the immunocytochemical detection of Nsr1 protein was reported for the first time. Altogether, HPF followed by FS in acetone with 0.1% UA gave the most satisfactory results from all tested media – both for the ultrastructural preservation (compare the fine details of nucleolar ultrastructure preservation of cells substituted in different FS media in Figure 4-05), and also for immunodetection of tested antigens (see Subchapter 4.1.5.3). However, since the 'clear' sub-nucleolar compartmentalization was never observed in any of HP-frozen/FS samples, our findings were in agreement with the bipartite model of *S. cerevisiae* nucleolar organization (Thiry & Lafontaine, 2005).

Undeniably, the cryo-fixation preserves cells as close as possible to the native cell structure and following low-temperature processing significantly minimizes the extraction of material. Therefore, the images generated by HPF can consequently serve as a 'gold standard', by which all other sample preparation methods for yeast or other biological objects can be judged (McDonald & Müller-Reichert, 2002). It should be mentioned that these cryo-preparation methods could also induce their own artefacts, but they are often more easily understandable than those arising during chemical treatment (Dubochet *et al*, 1983; Peters & Pierson, 2008). The so-called seggregation pattern can be seen in the cytoplasm and/or nucleus as a result of ice formation (Dubochet, 2007; Studer *et al*, 2008). In fact, the nature of the sample, its size and hydration, the sample pre-treatment before cryo-fixation, the quality of cryo-fixation, duration and temperature range in the FS procedure, and the choice of FS solvents (Nicolas & Bassot, 1993) are the main factors that could significantly influence the

result. For example, direct cryo-sectioning of a vitrified (HP-frozen) material followed by cryo-TEM examination in its hydrated state, can circumvent some of the 'factors' mentioned above (for details see Subchapter 1.2.4.4.1). The negative aspect of this method is the cutting-induced deformation of the sections, which remains the serious problem of the technique to these days (Al-Amoudi *et al*, 2005; Hsieh *et al*, 2006). Another example is the cryo-fixation and direct cryo-TEM analysis of cells that grew directly on an EM grid. Unfortunately, the cryo-TEM imaging is then possible only in thin fringe parts of the cell (Frederik *et al*, 2008). The hybrid approach of HPF/FS and low-temperature embedding followed by room temperature sectioning is therefore the only technique that offers ultrastructural and immunocytochemical analysis of sections of complex samples, e.g. cells, animal tissues, plant tissues, up to a thickness of 500 μm (McDonald, 1999; McDonald, 2007; McDonald, 2009). The situation should be however changed in the near future as promising new technologies are going to be applied in cell imaging. During the past few years were for example developed protocols that adapt HPF/FS for subsequent immunolabeling according to the Tokuyasu technique – the so-called rehydration technique (Slot & Geuze, 2007; Stierhof *et al*, 1991; van Donselaar *et al*, 2007). Though this method gave excellent results, more unspecific background labeling is present in the rehydrated samples (Griffith *et al*, 2008). Next, the correlative light and electron microscopy technique, which combines the advantages of both LM/FM and TEM in one experiment, has gained dominant position in the current research as well. The same cell (a cell culture) is examined *in vivo* in a confocal microscope (to locate features of interest at low resolution) and then immediately vitrified by HPF (instead of the standard chemical fixation) and FS, embedded in a resin and sectioned for analysis in TEM (to map their ultrastructure or specific antigen at high resolution) (Brown *et al*, 2009; Giepmans, 2008; McDonald, 2009; Shu *et al*, 2011; Verkade, 2008). The method has been successfully applied to cells cultured *in vitro*, frequently growing at monolayers (Agronskaia *et al*, 2008; Brown *et al*, 2009; Jimenez *et al*, 2010; Spiegelhalter *et al*, 2010; Verkade, 2008), and then to e.g., HIV particles bind to mammalian cell surface (Kukulski *et al*, 2011), and even to study of *Caenorhabditis elegans* (Kolotuev *et al*, 2009), yeast (Kukulski *et al*, 2011), etc. Recent technical developments (e.g. of a cryo-LM stage) have moreover allowed the accurate correlation of fluorescently labelled subcellular structures to cryo-TEM micrographs of frozen-hydrated samples (Lucic *et al*, 2008; Plitzko *et al*, 2009; Sartori *et al*, 2007; Schwarz & Humbel, 2007). The method has been optimized also for the Tokuyasu cryo-sections (Vicidomini *et al*, 2010). The same resin section can be imaged by FM and then transferred to TEM (Kukulski *et al*, 2011).

Unlike cryo-immobilization of a bulk samples by HPF, other types of rapid freezing methods operating at an ambient pressure can be successfully used for the cryo-fixation of e.g., suspensions of cells and microorganisms, organelles, and tissue cultures in a thickness range of about 5-20 μm (detailed description of these procedures was provided in Subchapter 1.2.4.2). Among them, the method of plunge freezing is currently widely used in combination with cryo-TEM imaging to study a range of macromolecular complexes and other types of biological nanomachines (Adrian *et al*, 1984; Dubochet *et al*, 1988). In this thesis we next presented the use of the technique of a thin vitreous layer performed by plunge freezing and cryo-TEM imaging for detailed study of the morphology, properties and/or stability of the liposomes and the silicone-coated liposomes (Publication No.2, Subchapter 4.2), and other vesicular structures such as bilayers composed of DODAB (the cationic liposomes) and OA at various molar ratios (Publication No.3, Subchapter 4.3). Different nanoscopic vesicular structures, e.g., dendrimers, polymers, liposomes, and polymeric/inorganic nanoparticles, have been studied over the last decades as potential drug delivery systems - nanocarriers - for the delivery of therapeutic compounds in the promising therapy approach for the treatment of cancers, systemic or local fungal infections (Jin *et al*, 2010; Schwendener, 2007; Takeuchi *et al*, 2000; Takeuchi *et al*, 2001; Yaroslavov *et al*, 2008). In the current research, the liposomes and the liposome-based formulations occupy a leading role among these systems due to their versatility and vast body of known properties (Jin *et al*, 2010; Schwendener, 2007). Molecular biology techniques have been used to elucidate certain physico-chemical and biological activities of such nanocarriers (Jin *et al*, 2010). Electron microscopy has also found its applications in measuring the nanoparticle sizes and shapes during drug manufacturing. However, conventional TEM, as well as atomic force microscopy and scanning electron microscopy can not unambiguously answer questions about their morphology (Jin *et al*, 2010) due to the destructive effects related to particles immobilization (adsorption on a support) or that of staining agents (Figure 1-20). In this thesis, we presented the results of the first studies on successful stabilization of liposomes by covering their surface with a thin silicone layer using a novel silicone precursor (Publication No.2, Subchapter 4.2). Next, we reported on the properties of bilayers composed of DODAB and OA at various molar ratios (Publication No.3, Subchapter 4.3). The formed structures were clearly characterized with different methods, i.e, dynamic light scattering, zeta potential measurements, fluorescence anisotropy (see Subchapters 4.2 and 4.3), cryo-TEM being no exception. The method of plunge freezing was used to produce thin vitrified aqueous films with the hydrated vesicles embedded in them. As the vesicles were directly visualized in a vitreous hydrated state, the perturbation of the

objects was limited. We are confident that the samples were observed in their *in vivo* conformation; thus we were able to clearly characterize their morphology (Figures 4-11 and 4-18, respectively) and distribution profiles (Figure 4-14). Thus, a unilamellar and multilamellar vesicles were clearly distinguished. A typical example of a cryo-TEM micrograph shows a distinct bilayered phospholipid membrane surrounding the aqueous core of liposome is illustrated in Figure 4-11. Similarly, Figure 4-18 shows clearly the morphology of vitrified extruded DODAB/OA dispersions. As shown, this method is practically unique and provides invaluable information neccessary for the development of these nanocarriers as well as other types of nanocarriers in a near future.

CHAPTER 6 CONCLUSIONS

Electron microscopic imaging of cells, animal and plant tissues, microorganisms, etc. in their 'close-to-native' state is not a trivial task. The samples must tolerate vacuum environment present in an electron microscope, and therefore the water present in the cells must be removed in such a way that will not cause significant alterations to the native biological structure. This is not possible with conventional methods based on chemical cross-linking of a biological material, drying and embedding in a plastic. However, development of new tools in the last two decades has changed the way of preparation of biological material and possibilities of its observation in TEM. Three studies included in this thesis were performed in order to expand our knowledge on the application of cryo-fixation and low-temperature processing techniques and electron cryo-microscopic imaging.

In the first part of thesis (Chapter 1), the conventional procedures of sample preparation were presented. We also gave insight into a variety of cryo-preparation techniques and finally the principles of electron cryo-microscopy were described in detail. In fact, a profound understanding of these methods is required for in-depth analysis and evaluation of TEM micrographs. In the second part of this thesis (Chapter 2), the objectives of our work were introduced. Materials and methods used in our study were described in the following Chapter 3. Results of our work were presented in Chapter 4 and discussed subsequently in Chapter 5. Thesis was terminated by conclusion (Chapter 6) and list of references (Chapter 7).

In this thesis, three publications were enclosed. In Publication No.1, we investigated and developed a new protocol that could be used for the successful preparation of yeast *Saccharomyces cerevisiae* for both fine ultrastructural and immunocytochemical TEM study. Described methods covered: i) conventional aldehyde-based fixation procedure, ii) cryo-fixation by HPF, substitution in four different media and embedding into Lowicryl HM20 – both performed at low temperatures, iii) thin sectioning, iv) immunogold labeling using antibodies recognizing nucleolar (Nsr1 and Nop1), nuclear (Nsp1) and α-tubulin antigens, v) post-staining, and vi) conventional TEM analysis. Each step of fixation and embedding protocol was assessed for its potential to retain both the morphology and antigenicity. As presented, the sensitive antigens, which have been altered by conventional way of sample processing, were preserved after cryo-fixation followed by our FS protocol. In addition, the ultrastructural preservation of *S. cerevisiae* cells was incomparable to that obtained with conventional processing method. Even though that only these yeast cells were investigated,

we are confident that similar results can be obtained with other cell types or tissues. In addition, the protocol allows variable alterations according to the desired aim of study.

In Publications No.2 and No.3 we tried to address the question of utilization and advantage of the technique of cryo-TEM in the study of different vesicular structures (the liposomes, silicone-covered liposomes and DODAB/OA vesicles) in the nanometer range scale. We described how the method of plunge freezing followed by cryo-TEM imaging helps to elucidate data that cannot be obtained by alternative methods that could be used to characterize these vesicles, including analysis by conventional TEM. The cryo-TEM was used for both the visualization of the formation of objects in solution and for their morphological characterization. As the method allows direct imaging of hydrated samples in the most natural environment currently possible, only limited perturbation of the objects was observed. The vitreous state of samples was maintained throughout the process. The cryo-TEM was therefore the only method that enabled us to clearly distinguish unilamellar and multilamellar vesicles.

Altogether, we wish to emphasize the importance of the methods presented in this thesis. Currently, biological samples prepared by HPF, followed by FS and low-temperature resin embedding, possess the highest level of ultrastructural preservation; and therefore these are the methods of choice for fine ultrastructural and immunocytochemical TEM analysis. For a high-resolution analysis of isolated macromolecular complexes or other types of biological nanomachines, the rapid freezing in a vitreous layer of water is currently the only technique that retains native state of the object before cryo-TEM imaging. Especially in structural biology, the imaging of biological sample in its most native state is a fundamental requirement. The development of currently presented methodologies is ongoing, and a number of improvements can be expected in a near future. We are therefore certain to gain invaluable cell biological insights. Unambiguously, these methods have a great potential to open new applications in a biomedical research.

CHAPTER 7 REFERENCES

1. Adrian M, Dubochet J, Fuller SD, Harris JR (1998) Cryo-negative staining. *Micron* **29:** 145-160
2. Adrian M, Dubochet J, Lepault J, McDowall AW (1984) Cryo-electron microscopy of viruses. *Nature* **308:** 32-36
3. Agronskaia AV, Valentijn JA, van Driel LF, Schneijdenberg CT, Humbel BM, van Bergen en Henegouwen PM, Verkleij AJ, Koster AJ, Gerritsen HC (2008) Integrated fluorescence and transmission electron microscopy. *J Struct Biol* **164:** 183-189
4. Al-Amoudi A, Chang JJ, Leforestier A, McDowall A, Salamin LM, Norlen LP, Richter K, Blanc NS, Studer D, Dubochet J (2004) Cryo-electron microscopy of vitreous sections. *Embo J* **23:** 3583-3588
5. Al-Amoudi A, Studer D, Dubochet J (2005) Cutting artefacts and cutting process in vitreous sections for cryo-electron microscopy. *J Struct Biol* **150:** 109-121
6. Alberts B, Johnson A, Lewis J, Raff M, Roberts K, Walter P (2008) *Molecular biology of the cell*, Garland Science, Taylor & Francis Group, New York, USA
7. Anderson DR, Smith AL (1974) *Analysis of silicones.* Wiley, New York, USA
8. Andersson M, Hammrstrom L, Edwards K (1995) Effect of bilayer phase transitions on vesicle structure and its influence on the kinetics of viologen reduction. *J Phys Chem* **99:** 14531-14538
9. Armbruster BL, Garavito RM, Kellenberger E (1983) Dehydration and embedding temperatures affect the antigenic specificity of tubulin and immunolabeling by the protein A-colloidal gold technique. *J Histochem Cytochem* **31:** 1380-1384
10. Bahri MA, Seret A, Hans P, Piette J, Deby-Dupont G, Hoebeke M (2007) Does propofol alter membrane fluidity at clinically relevant concentrations? An ESR spin label study. *Biophys Chem* **129:** 82-91
11. Bachmann L, Schmitt WW (1971) Improved cryofixation applicable to freeze etching. *Proc Natl Acad Sci U S A* **68:** 2149-2152
12. Bailer SM, Balduf C, Hurt E (2001) The Nsp1p carboxy-terminal domain is organized into functionally distinct coiled-coil regions required for assembly of nucleoporin subcomplexes and nucleocytoplasmic transport. *Mol Cell Biol* **21:** 7944-7955
13. Bangham AD, Standish MM, Watkins JC (1965) Diffusion of univalent ions across the lamellae of swollen phospholipids. *J Mol Biol* **13:** 238-252

14. Barreleiro PC, May RP, Lindman B (2002) Mechanism of formation of DNA-cationic vesicle complexes. *Faraday Discuss* **122:** 191-201
15. Barrére M, Ganachaud F, Bendejacq D, Dourges M-A, Maitre C, Hémery P (2001) Anionic polymerization of octamethylcyclotetrasiloxane in miniemulsion II. Molar mass analyses and mechanism scheme. *Polymer* **42:** 7239-7246
16. Baumeister W (2002) Electron tomography: towards visualizing the molecular organization of the cytoplasm. *Curr Opin Struct Biol* **12:** 679-684
17. Beck M, Forster F, Ecke M, Plitzko JM, Melchior F, Gerisch G, Baumeister W, Medalia O (2004) Nuclear pore complex structure and dynamics revealed by cryoelectron tomography. *Science* **306:** 1387-1390
18. Beginning an electron microscopy project (2009, February 11) Retrieved June 5, 2011, from http://cryoem.nysbc.org/cryoem-interested.html
19. Bégu S, Aubert Pouessel A, Lerner DA, Tourne-Peteilh C, Devoisselle JM (2007) Liposil, a promising composite material for drug storage and release. *J Control Release* **118:** 1-6
20. Bendayan M, Shore GC (1982) Immunocytochemical localization of mitochondrial proteins in the rat hepatocyte. *J Histochem Cytochem* **30:** 139-147
21. Besanger TR, Zang Y, Brennan JD (2002) Characterization of fluorescent phospholipid liposomes entrapped in sol-gel derived silica. *J Phys Chem* **106:** 10535-10542
22. Best B (n.d.) *Vitrification in cryonics.* Retrieved June 8, 2008, from http://www.benbest.com/cryonics/vitrify.html#nature
23. Betzig E, Patterson GH, Sougrat R, Lindwasser OW, Olenych S, Bonifacino JS, Davidson MW, Lippincott-Schwartz J, Hess HF (2006) Imaging intracellular fluorescent proteins at nanometer resolution. *Science* **313:** 1642-1645
24. Biggiogera M, Fakan S (2008) Visualization of nuclear organization by ultrastructural cytochemistry. *Methods Cell Biol* **88:** 431-449
25. Bleck CK, Merz A, Gutierrez MG, Walther P, Dubochet J, Zuber B, Griffiths G (2010) Comparison of different methods for thin section EM analysis of Mycobacterium smegmatis. *J Microsc* **237:** 23-38
26. Bozzola JJ (2007) Conventional specimen preparation techniques for transmission electron microscopy of cultured cells. *Methods Mol Biol* **369:** 1-18
27. Brenner S, Horne RW (1959) A negative staining method for high resolution electron microscopy of viruses. *Biochim Biophys Acta* **34:** 103-110

28. Brito RO, Marques EF (2005) Neat DODAB vesicles: Effect of sonication time on the phase transition thermodynamic parameters and its relation with incomplete chain freezing. *Chem Phys Lipids* **137:** 18-28

29. Bronnich TK, Popov AM, Eisenberg A, Kabanov VA, Kabanov AV (2000) Effects of block length and structure of surfactant on self-assembly and solution behavior of block ionomer complexes. *Langmuir* **16:** 481-489

30. Brorson SH, Roos N, Skjorten F (1994) Antibody penetration into LR-White sections. *Micron* **25:** 453-460

31. Brown E, Mantell J, Carter D, Tilly G, Verkade P (2009) Studying intracellular transport using high-pressure freezing and correlative light electron microscopy. *Semin Cell Dev Biol* **20:** 910-919

32. Buser C, Walther P (2008) Freeze-substitution: the addition of water to polar solvents enhances the retention of structure and acts at temperatures around -60 degrees C. *J Microsc* **230:** 268-277

33. Carlemalm E, Garavito RM, Villiger W (1982) Resin Development for Electron-Microscopy and an Analysis of Embedding at Low-Temperature. *J Microsc-Oxford* **126:** 123-143

34. Carlemalm E, Villiger W, Hobot JA, Acetarin JD, Kellenberger E (1985) Low temperature embedding with Lowicryl resins: two new formulations and some applications. *J Microsc* **140:** 55-63

35. Cavalier SD (2008) Progressive lowering of temperature for immunolabeling and in situ hybridization. In *Handbook of cryo-preparation methods for electron microscopy*, Cavalier ASD, Humbel BM (ed) pp 433-465 USA: CRC Press, Tailor & Francis Group

36. Ciobanu M, Heurtault B, Schultz P, Ruhlmann C, Müller CD, Frisch B (2007) Layersome: development and optimization of stable liposomes as drug delivery system. *Int J Pharm* **344:** 154-157

37. Conlon JM, Yano K, Chartrel N, Vaudry H, Storey KB (1998) Freeze tolerance in the wood frog Rana sylvatica is associated with unusual structural features in insulin but not in glucagon. *J Mol Endocrinol* **21:** 153-159

38. Conway JF, Cheng N, Zlotnick A, Wingfield PT, Stahl SJ, Steven AC (1997) Visualization of a 4-helix bundle in the hepatitis B virus capsid by cryo-electron microscopy. *Nature* **386:** 91-94

39. Costin IS, Barnes GT (1975) Two-component monolayers. II. Surface pressure-area relations for the octadecanol-docosyl sulphate system. *J Colloid Interface Sci* **51:** 106-121
40. Cox G, Sheppard CJ (2004) Practical limits of resolution in confocal and non-linear microscopy. *Microsc Res Tech* **63:** 18-22
41. Crucifix C, Papai G, Schultz P (2008) Frozen hydrated macromolecules for structural analysis. In *Handbook of cryo-preparation methods for electron microscopy*, Cavalier ASD, Humbel BM (ed) pp 159-189. USA: CRC Press, Tailor & Francis Group.
42. Crystallization (June 3, 2011) In *Wikipedia: The free encyclopedia.* Retrieved June 3, 2011, from http://en.wikipedia.org/wiki/Crystallization
43. Cyrklaff M, Risco C, Fernandez JJ, Jimenez MV, Esteban M, Baumeister W, Carrascosa JL (2005) Cryo-electron tomography of vaccinia virus. *Proc Nat Acad Sci USA* **102:** 2772-2777
44. Dahan M, Levi S, Luccardini C, Rostaing P, Riveau B, Triller A (2003) Diffusion dynamics of glycine receptors revealed by single-quantum dot tracking. *Science* **302:** 442-445
45. Dahl R, Staehelin LA (1989) High-pressure freezing for the preservation of biological structure: theory and practice. *J Electron Microsc Tech* **13:** 165-174
46. Davies JT, Rideal EK (1963) *Interfacial Phenomena.* Academic Press, New York and London
47. de Carlo S (2008) Plunge-freezing (holey carbon method). In *Handbook of cryo-preparation methods for electron microscopy,* Cavalier ASD, Humbel BM (ed) pp 49-68. USA: CRC Press, Tailor & Francis Group
48. De la Maza A, Parra JL (1995) Vesicle-micelle structural transitions of phospholipid bilayers and sodium dodecyl sulfate. *Langmuir* **11:** 2435-2441
49. Deerinck T, Martone M, Ellisman MH (2006) Preparative methods for transmission electron microscopy. In *Basic methods in microscopy*, Spector D, Goldman, RD (ed) pp 307 - 327. New York: Cold Spring Harbour Press
50. Derenzini M, Montanaro L, Trere D (2009) What the nucleolus says to a tumour pathologist. *Histopathology* **54:** 753-762
51. Dubochet J (1995) High-pressure freezing for cryoelectron microscopy. *Trends Cell Biol* **5:** 366-368
52. Dubochet J (2007) The physics of rapid cooling and its implications for cryoimmobilization of cells. *Methods Cell Biol* **79:** 7-21

53. Dubochet J (2008) Vitreous water. In *Handbook of cryo-preparation methods for electron microscopy,* Cavalier ASD, Humbel BM (ed) pp 1-14. USA: CRC Press, Tailor & Francis Group
54. Dubochet J, Adrian M, Chang JJ, Homo JC, Lepault J, McDowall AW, Schultz P (1988) Cryo-electron microscopy of vitrified specimens. *Q Rev Biophys* **21:** 129-228
55. Dubochet J, Lepault J, Freeman R, Berriman JA, Homo, JC (1982) Electron microscopy of frozen water and aqueous solutions. In: Friedrich H, Frederik PM, de With G, Sommerdijk NAJM (2010) Imaging of self-assembled structures: Interpretation of TEM and Cryo-TEM images Angew Chem Int Ed **49:** 7850-7858.
56. Dubochet J, McDowall AW, Menge B, Schmid EN, Lickfeld KG (1983) Electron microscopy of frozen-hydrated bacteria. *J Bacteriol* **155:** 381-390
57. Dubochet J, Sartori Blanc N (2001) The cell in absence of aggregation artifacts. *Micron* **32:** 91-99
58. Ebersold HR, Cordier JL, Luthy P (1981) Bacterial mesosomes: method dependent artifacts. *Arch Microbiol* **130:** 19-22
59. Edelmann L (2008) Freeze-drying and embedding of biological material. In *Handbook of cryo-preparation methods for electron microscopy,* Cavalier ASD, Humbel BM (ed) pp 367-390 USA: CRC Press, Tailor & Francis Group
60. Edwards K, Silvander M, Karlsson G (1995) Aggregate structure in dilute aqueous dispersions of oleic acidsodium oleate and oleic acid sodium oleate/egg phosphatidylcholine. *Langmuir* **11:** 2429-2434
61. Echlin P, Skaer HB, Gardiner BO, Franks F, Asquith MH (1977) Polymeric cryoprotectants in the preservation of biological ultrastructure. II. Physiological effects. *J Microsc* **110:** 239-255
62. Elands J, Hax W (2004) CryoEM as a complement to current techniques in protein structural analysis. Retrieved June 10, 2009, from www.currentdrugdiscovery.com
63. Ellis EA (2007) Poststaining grids for transmission electron microscopy: conventional and alternative protocols. *Methods Mol Biol* **369:** 97-106
64. Ellisman MH (2006) Image production using transmission electron microscopy. In: *Basic methods in microscopy,* Spector DL, Goldman RD (ed) pp. 303-306. Cold Spring Harbor, New York
65. Ernst Ruska - Autobiography (n.d.) In *Nobelprize.org.* Retrieved September 15, 2011, from http://www.nobelprize.org/nobel_prizes/physics/laureates/1986/ruska-autobio.html

66. Escande ML, Gas N, Stevens BJ (1985) Immunolocalization of the 100 K nucleolar protein in CHO cells. *Biol Cell* **53:** 99-109
67. Fahrenkrog B, Aris JP, Hurt EC, Pante N, Aebi U (2000) Comparative spatial localization of protein-A-tagged and authentic yeast nuclear pore complex proteins by immunogold electron microscopy. *J Struct Biol* **129:** 295-305
68. Fedorova E, Zink D (2008) Nuclear architecture and gene regulation. *Biochim Biophys Acta* **1783:** 2174-2184
69. Feitosa E, Barreleiro PC, Olofsson G (2000) Phase transition in dioctadecyldimethylammonium bromide and chloride vesicles prepared by different methods. *Chem Phys Lipids* **105:** 201-213
70. Feitosa E, Brown W (1997) Fragment and vesicle structures in sonicated dispersions of dioctadecyldimethylammonium bromide. *Langmuir* **13:** 4810-4816
71. Fernandez-Moran H (1960) Low-temperature preparation techniques for electron microscopy of biological specimens based on rapid freezing with liquid helium II. *Annals NY Acad Sci* 85, 689-713. In McDonald K (2007) Cryopreparation methods for electron microscopy of selected model systems. *Methods Cell Biol* 79: 23-56
72. Fernandez-Moran H, Dahl AO (1952) Electron microscopy of ultrathin frozen sections of pollen grains. *Science* **116:** 465-467
73. Ferreira DA, Bentley MV, Karlsson G, Edwards K (2006) Cryo-TEM investigation of phase behaviour and aggregate structure in dilute dispersions of monoolein and oleic acid. *Int J Pham* **310:** 203-212
74. Finck H (1960) Epoxy resins in electron microscopy. *J Biophys Biochem Cytol* **7:** 27-30
75. Fox CH, Johnson FB, Whiting J, Roller PP (1985) Formaldehyde fixation. *J Histochem Cytochem* **33:** 845-853
76. Franks F, Asquith MH, Hammond CC, Skaer HB, Echlin P (1977) Polymer cryoprotectants in the preservation of biological ultrastructure. I. Low temperature states of aqueous solutions of hydrophilic polymers. *J Microsc* **110:** 223-228
77. Frederik PM, de Haas F, Storms MMH (2008) Controlled vitrification. In *Handbook of cryo-preparation methods for electron microscopy*, Cavalier ASD, Humbel BM (ed) pp 69-99. USA: CRC Press, Tailor & Francis Group
78. Freezing (June 6, 2011) In *Wikipedia: The free encyclopedia.* Retrieved June 7, 2011, from http://en.wikipedia.org/wiki/Freezing
79. Freeze-fracturing and Etching (n.d.) Retrieved June 5, 2011, from http://www.udel.edu/biology/Wags/b617/ffe/ffe7.gif

80. Friedrich H, Frederik PM, de With G, Sommerdijk NA (2010) Imaging of self-assembled structures: interpretation of TEM and cryo-TEM images. *Angew Chem Int Ed Engl* **49:** 7850-7858
81. Gaines GL (1966) Insoluble monolayers at liquid/gas interfaces (Chapter 6). *Wiley-Interscience, New York*
82. Gibrat R, Grignon C (1982) Effect of pH on the surface charge density of plant membranes. Comparison of microsomes and liposomes. *Biochim Biophys Acta* **692:** 462-468
83. Giddings TH (2003) Freeze-substitution protocols for improved visualization of membranes in high-pressure frozen samples. *J Microsc* **212:** 53-61
84. Giepmans BN (2008) Bridging fluorescence microscopy and electron microscopy. *Histochem Cell Biol* **130:** 211-217
85. Glaeser RM, Taylor KA (1978) Radiation damage relative to transmission electron microscopy of biological specimens at low temperature: a review. *J Microsc* **112:** 127-138
86. Glauert AM (1974) *Fixation, dehydration and embedding of biological specimens: Practical methods in electron microscopy*, vol 3, part 1, North-Holland, Amsterdam
87. Goncalves da Silva AM, Romao RIS (2005) Mixed monolayers involving DPPC, DODAB and oleic acid and their interaction with nicotinic acid at the air-water interface. *Chem Phys Lipids* **137:** 62-76
88. Gounon P (1999) Low-temperature embedding in acrylic resins. *Methods Mol Biol* **117:** 111-124
89. Grassucci RA, Taylor DJ, Frank J (2007) Preparation of macromolecular complexes for cryo-electron microscopy. *Nat Protoc* **2:** 3239-3246
90. Griffith J, Mari M, De Maziere A, Reggiori F (2008) A cryosectioning procedure for the ultrastructural analysis and the immunogold labeling of yeast *Saccharomyces cerevisiae. Traffic* **9:** 1060-1072
91. Griffith J, Penalva MA, Reggiori F (2011) Adaptation of the Tokuyasu method for the ultrastructural study and immunogold labeling of filamentous fungi. *J Electron Microsc* **60:** 211-216
92. Griffiths G (1993) *Fine structure immunocytochemistry*. Springer Verlag, Heidelberg
93. Griffiths G (2001) Bringing electron microscopy back into focus for cell biology. *Trends Cell Biol* **11:** 153-154

94. Grigorieff N, Harrison SC (2011) Near-atomic resolution reconstructions of icosahedral visuses from electron cryo-microscopy. *Curr Op Struct Biol* **21**: 265-273.
95. Gruska M, Medalia O, Baumeister W, Leis A (2008) Electron tomography of vitreous sections from cultured mammalian cells. *J Struct Biol* **161:** 384-392
96. Gulli MP, Girard JP, Zabetakis D, Lapeyre B, Melese T, Caizergues-Ferrer M (1995) gar2 is a nucleolar protein from *Schizosaccharomyces pombe* required for 18S rRNA and 40S ribosomal subunit accumulation. *Nucleic Acids Res* **23:** 1912-1918
97. Gustafsson J, Oradd G, Almgren M (1997) Disintegration of the lecithin lamellar phase by cationic surfactants. *Langmuir* **13:** 6956-6963
98. Hagler HK (2007) Ultramicrotomy for biological electron microscopy. *Methods Mol Biol* **369:** 67-96
99. Haidar ZS, Hamdy RC, Tabrizian M (2008) Protein release kinetics for core-shell hybrid nanoparticles based on the layer-by-layer assembly of alginate and chitosan on liposomes. *Biomaterials* **29:** 1207-1215
100. Harris JR (2007) Negative staining of thinly spread biological samples. *Methods Mol Biol* **369:** 107-142
101. Hawes P, Netherton CL, Mueller M, Wileman T, Monaghan P (2007) Rapid freeze-substitution preserves membranes in high-pressure frozen tissue culture cells. *J Microsc* **226:** 182-189
102. Hayat M (1989) *Principles and techniques of electron microscopy: biological applications.* CRC Press, Boca Raton, FL
103. Hayles MF, Matthijs de Winter DA, Schneijdenberg CT, Meeldijk JD, Luecken U, Persoon H, de Water J, de Jong F, Humbel BM, Verkleij AJ (2010) The making of frozen-hydrated, vitreous lamellas from cells for cryo-electron microscopy. *J Struct Biol* **172:** 180-190
104. Hell SW (2003) Toward fluorescence nanoscopy. *Nat Biotechnol* **21:** 1347-1355
105. Hemmerich P, von Mikecz A (2000) Antinuclear autoantibodies: fluorescent highlights on structure and function in the nucleus. *Int Arch Allergy Immunol* **123:** 16-27
106. Hentze HP, Raghavan SR, McKelvey SA, Kaler EW (2003) Silica hollow speres by templating of catanionic vesicles. *Langmuir* **19:** 1069-1074
107. Hernandez-Verdun D (2006) The nucleolus: a model for the organization of nuclear functions. *Histochem Cell Biol* **126:** 135-148
108. Hess MW (2007) Cryopreparation methodology for plant cell biology. *Methods Cell Biol* **79:** 57-100

109. Hlaváč V, Šonka M (1992) Počítačové vidění. *Grada*, Praha. ISBN 80-85424-67-3
110. Hobot JA, Carlemalm E, Villiger W, Kellenberger E (1984) Periplasmic gel: new concept resulting from the reinvestigation of bacterial cell envelope ultrastructure by new methods. *J Bacteriol* **160:** 143-152
111. Hobot JA, Villiger W, Escaig J, Maeder M, Ryter A, Kellenberger E (1985) Shape and fine structure of nucleoids observed on sections of ultrarapidly frozen and cryosubstituted bacteria. *J Bacteriol* **162:** 960-971
112. Hofmann C, Cheeseman IM, Goode BL, McDonald KL, Barnes G, Drubin DG (1998) Saccharomyces cerevisiae Duo1p and Dam1p, novel proteins involved in mitotic spindle function. *J Cell Biol* **143:** 1029-1040
113. Hohenberg H, Mannweiler K, Müller M (1994) High-pressure freezing of cell suspensions in cellulose capillary tubes. *J Microsc* **175:** 34-43
114. Hsieh CE, Leith A, Mannella CA, Frank J, Marko M (2006) Towards high-resolution three-dimensional imaging of native mammalian tissue: electron tomography of frozen-hydrated rat liver sections. *J Struct Biol* **153:** 1-13
115. Hubert DHW, Jung M, German AL (2000) Vesicle templating. *Adv Mater* **12:** 1291-1295
116. Humbel BM, Konomi M, Takagi T, Kamasawa N, Ishijima SA, Osumi M (2001) In situ localization of beta-glucans in the cell wall of *Schizosaccharomyces pombe*. *Yeast* **18:** 433-444
117. Humbel BM, Stierhof YD (2008) Cryo-sectioning according to Tokuyasu. In *Handbook of cryo-preparation methods for electron microscopy,* Cavalier ASD, Humbel BM (ed) pp 467-498. USA: CRC Press, Tailor & Francis Group
118. Hurbain I, Sachse M (2011) The future is gold: cryo-preparation methods for tranmission electron microscopy of cells. *Biol Cell* **103(9):** 405-420
119. Hwang ML, Prud´homme RK, Kohn J, Thomas JL (2001) Stabilization of phosphatidylserine/phosphatidylethanolamine liposomes with hydrophilic polymers having multiple "Sticky Feet". *Langmuir* **17:** 7713-7716
120. Chial HJ, Rout MP, Giddings TH, Winey M (1998) *Saccharomyces cerevisiae* Ndc1p is a shared component of nuclear pore complexes and spindle pole bodies. *J Cell Biol* **143:** 1789-1800
121. Chiu W, Baker ML, Jiang W, Dougherty M, Schmid MF (2005) Electron cryomicroscopy of biological machines at subnanometer resolution. *Structure* **13:** 363-372

122. Chiu W, Chen D, Jakana J, Chang J, Jiang W, Ludtke SJ, Baker ML (2006) Visualization of biological nano-machines at subnanometer resolutions. *JEOL news* **41:** 12-17

123. Cho EC, Lim HJ, Shim J, Kim J, Chang IS (2007) Improved stability of liposome in oil/water emulsion by association of amphiphilic polymer with liposome and its effect on bioactive skin permeation. *Colloids Surf A Physicochem Eng Asp* **299:** 160-168

124. Indi S, Wakley G, Stebbings H (1986) Effects of glycerol and freezing on the appearance and arrangement of microtubules in three different systems: A freeze-substitution study. *Tissue Cell* **18:** 331-339

125. Israelachvili JN, Mitchell DJ, Ninham BW (1976) Theory of self-assembly of hydrocarbon amphiphiles into micelles and bilayers. *J Chem Soc Faraday Trans 2* **72:** 1525-1568

126. Jamróz D, Kepczynski M, Nowakowska M (2010) Molecular structure of the dioctadecyldimethylammonium bromide (DODAB) bilayer. *Langmuir* **26:** 15076-15079

127. Jiang W, Ludtke SJ (2005) Electron cryomicroscopy of single particles at subnanometer resolution. *Curr Opin Struct Biol* **15:** 571-577

128. Jimenez N, Van Donselaar EG, De Winter DA, Vocking K, Verkleij AJ, Post JA (2010) Gridded Aclar: preparation methods and use for correlative light and electron microscopy of cell monolayers, by TEM and FIB-SEM. *J Microsc* **237:** 208-220

129. Jin SE, Bae JW, Hong S (2010) Multiscale observation of biological interactions of nanocarriers: from nano to macro. *Microsc Res Tech* **73:** 813-823

130. Jung M, Hubert DHW, van Veldhoven E, Frederik PM, Blandamer MJ, Briggs B, Visser AJWG, van Herk AM, German AL (2000a) Interaction of styrene with DODAB bilayer vesicles. Influence on vesicle morphology and bilayer properties. *Langmuir* **16:** 968-979

131. Jung M, Hubert DHW, Veldhoven E, Frederik P, Herk AM, German AL (2000b) Vesicle-polymer hybrid architectures: a full account of the parachute architecture. *Langmuir* **16**: 3165-3174

132. Kaler EW, Herrington KL, Murthy AK, Zasadzinski JAN (1992) Phase behaviour and structures of mixtures of anionic and cationic surfactants. *J Phys Chem***:** 6698-6707

133. Kaler EW, Murthy AK, Rodriguez BE, Zasadzinski JA (1989) Spontaneous vesicle formation in aqueous mixtures of single-tailed surfactants. *Science* **245:** 1371-1374

134. Kang BH (2010) Electron microscopy and high-pressure freezing of Arabidopsis. *Methods Cell Biol* **96:** 259-283.

135. Katagiri K, Hamasaki R, Ariga K, Kikuchi J (2002a) Layered paving of vesicular nanoparticles formed with cerasome as a bioinspired organic-inorganic hybrid. *J Am Chem Soc* **124:** 7892-7893
136. Katagiri K, Hamasaki R, Ariga K, Kichiki J (2002b) Layer-by-layer self-assembling of liposomal nanohybrid "Cerasome" on substrates. *Langmuir* **18:** 6709-6711
137. Kepczynski M, Bednar J, Kuzmicz D, Wydro P, Nowakowska M (2010) Spontaneous formation of densely stacked multilamellar vesicles in dioctadecyldimethylammonium bromide/oleosiloxane mixtures. *Langmuir* **26:** 1551-1556
138. Kepczynski M, Bednar J, Lewandowska J, Staszewska M, Nowakowska M (2009) Hybrid silica-silicone nanocapsules obtained in catanionic vesicles. Cryo-TEM studies. *J Nanosci Nanotechnol* **9:** 3138-3143
139. Kepczynski M, Nawalany K, Jachimska B, Romek M, Nowakowska M (2006) Pegylated tetraarylporphyrin entrapped in liposomal membranes. A possible novel drug-carrier system for photodynamic therapy. *Colloids Surf* **49:** 22-30
140. Kepczynski M, Nawalany K, Kumorek M, Kobierska A, Jachimska B, Nowakowska M (2008) Which physical and structural factors of liposome carriers control their drug-loading efficiency? *Chem Phys Lipids* **155:** 7-15
141. Kiernan JA (2000) Formaldehyde, formalin, paraformaldehyde and glutaraldehyde: What they are and what they do. *Micros Today* **00-1:** 8-12
142. Kilmartin JV, Adams AE (1984) Structural rearrangements of tubulin and actin during the cell cycle of the yeast Saccharomyces. *J Cell Biol* **98:** 922-933
143. Kokkona M, Kallinteri P, Fatouros D, Antimisiaris SG (2000) Stability of SUV liposomes in the presence of cholate salts and pancreatic lipases: effect of lipid composition. *Eur J Pharm Sci* **9:** 245-252
144. Kolotuev I, Schwab Y, Labouesse M (2009) A precise and rapid mapping protocol for correlative light and electron microscopy of small invertebrate organisms. *Biol Cell* **102:** 121-132
145. Kondo K, Inouye M (1992) Yeast NSR1 protein that has structural similarity to mammalian nucleolin is involved in pre-rRNA processing. *J Biol Chem* **267:** 16252-16258
146. Koning RI, Koster AJ (2009) Cryo-electron tomography in biology and medicine. *Ann Anat* **191:** 427-445
147. Korn ED, Weisman RA (1966) I. Loss of lipids during preparation of amoebae for electron microscopy. *Biochim Biophys Acta* **116:** 309-316

148. Kukulski W, Schorb M, Welsch S, Picco A, Kaksonen M, Briggs JA (2011) Correlated fluorescence and 3D electron microscopy with high sensitivity and spatial precision. *J Cell Biol* **192:** 111-119

149. Kunitake T, Okahata Y (1977) A totally synthetic bilayer membrane. *J Am Chem Soc* **99:** 3860-3861

150. Kunz W, Testard F, Zemb T (2009) Correspondence between curvature, packing parameter, and hydrophilic-lipophilic deviation scales around the phase-inversion temperature. *Langmuir* **25:** 112-115

151. Kurner J, Medalia O, Linaroudis AA, Baumeister W (2004) New insights into the structural organization of eukaryotic and prokaryotic cytoskeletons using cryo-electron tomography. *Exp Cell Res* **301:** 38-42

152. Lakowicz JR (1999) *Principles of fluorescence spectroscopy.* Springer, New York, USA

153. Lee WC, Zabetakis D, Melese T (1992) NSR1 is required for pre-rRNA processing and for the proper maintenance of steady-state levels of ribosomal subunits. *Mol Cell Biol* **12:** 3865-3871

154. Leger-Silvestre I, Gulli MP, Noaillac-Depeyre J, Faubladier M, Sicard H, Caizergues-Ferrer M, Gas N (1997) Ultrastructural changes in the *Schizosaccharomyces pombe* nucleolus following the disruption of the gar2+ gene, which encodes a nucleolar protein structurally related to nucleolin. *Chromosoma* **105:** 542-552

155. Leger-Silvestre I, Trumtel S, Noaillac-Depeyre J, Gas N (1999) Functional compartmentalization of the nucleus in the budding yeast *Saccharomyces cerevisiae. Chromosoma* **108:** 103-113

156. Leunissen JL, Yi H (2009) Self-pressurized rapid freezing (SPRF): a novel cryofixation method for specimen preparation in electron microscopy. *J Microsc* **235:** 25-35

157. Li P, Li D, Zhang L, Li G, Wang E (2008) Cationic lipid bilayer coated gold nanoparticles-mediated transfection of mammalian cells. *Biomaterials* **29:** 3617-3624

158. Lin S, Cabasso I (1999) Synthesis of poly(phosphonosiloxane) and its cyclic monomer via hydrosilytation and phosphonylation of vinylbenzyl chloride. *J Polym Sci A* **37:** 4043-4053

159. Liou W, Geuze HJ, Slot JW (1996) Improving structural integrity of cryosections for immunogold labeling. *Histochem Cell Biol* **106:** 41-58

160. Lipp ED, Smith AL (1991) *In the analytical chemistry of silicones.* Wiley, New York, USA

161. Lopes A, Edwards K, Feitosa E (2008) Extruded vesicles of dioctadecyldimethylammonium bromide and chloride investigated by light scattering and cryogenic transmission electron microscopy. *J Colloid Interface Sci* **322:** 582-588

162. Lucic V, Leis A, Baumeister W (2008) Cryo-electron tomography of cells: connecting structure and function. *Histochem Cell Biol* **130:** 185-196

163. Maget-Dana R (1999) The monolayer technique: a potent tool for studying the interfacial properties of antimicrobial and membrane-lytic peptides and their interactions with lipid membranes. *Biochim Biophys Acta* **1462:** 109-140

164. Marko M, Hsieh CE (2007) Three-dimensional cryotransmission electron microscopy of cells and organelles. *Methods Mol Biol* **36:** 407-429

165. Marques EF, Brito RO, Silva SG, Rodriguez-Borges JE, do Vale ML, Gomes P, Araujo MJ, Soderman O (2008) Spontaneous vesicle formation in catanionic mixtures of amino acid-based surfactants: chain length symmetry effects. *Langmuir* **24:** 11009-11017

166. Marsh D (1996) Lateral pressure in membranes. *Biochim Biophys Acta* **1286:** 183-223

167. Mayhew TM (2007) Quantitative immunoelectron microscopy: alternative ways of assessing subcellular patterns of gold labeling. *Methods Mol Biol* **369:** 309-329

168. McDonald K (1999) High-pressure freezing for preservation of high resolution fine structure and antigenicity for immunolabeling. *Methods Mol Biol* **117:** 77-97

169. McDonald K (2007) Cryopreparation methods for electron microscopy of selected model systems. *Methods Cell Biol* **79:** 23-56

170. McDonald K (2009) A review of high-pressure freezing preparation techniques for correlative light and electron microscopy of the same cells and tissues. *J Microsc* **235:** 273-281

171. McDonald K, Webb RI (2011) Freeze substitution in 3 hours or less. *J Microsc* **243:** 227-233.

172. McDonald K, Müller-Reichert T (2002) Cryomethods for thin section electron microscopy. *Methods Enzymol* **351:** 96-123

173. McEwen BF, Marko M, Hsieh CE, Mannella C (2002) Use of frozen-hydrated axonemes to assess imaging parameters and resolution limits in cryoelectron tomography. *J Struct Biol* **138:** 47-57

174. Mears JA, Hinshaw JE (2008) Visualization of dynamins. *Methods Cell Biol* **88:** 237-256

175. Medalia O, Weber I, Frangakis AS, Nicastro D, Gerisch G, Baumeister W (2002) Macromolecular architecture in eukaryotic cells visualized by cryoelectron tomography. *Science* **298:** 1209-1213

176. Melese T, Xue Z (1995) The nucleolus: an organelle formed by the act of building a ribosome. *Curr Opin Cell Biol* **7:** 319-324

177. Mercogliano CP, DeRosier DJ (2007) Concatenated metallothionein as a clonable gold label for electron microscopy. *J Struct Biol* **160:** 70-82

178. Michel M, Arntz Y, Fleith G, Toquant J, Haikel Y, Voegel JC, Schaaf P, Ball V (2006) Layer-by-layer self-assembled polyelectrolyte multilayers with embedded liposomes: immobilized submicronic reactors for mineralization. *Langmuir* **22:** 2358-2364

179. Mobed M, Chang TM (1998) Comparison of polymerically stabilized PEG-grafted liposomes and physically adsorbed carboxymethylchitin and carboxymethyl/glycolchitin liposomes for biological applications. *Biomaterials* **19:** 1167-1177

180. Momekova D, Rangelov S, Yanev S, Nikolova E, Konstantinov S, Romberg B, Storm G, Lambov N (2007) Long-circulating, pH-sensitive liposomes sterically stabilized by copolymers bearing short blocks of lipid-mimetic units. *Eur J Pharm Sci* **32:** 308-317

181. Moor H, Riehle U (1968) Snap-freezing under high-pressure: a new fixation technique for freeze-etching. *Proc 4th Eur Elect Microsc* **2:** 33-34

182. Moor H (1987) Theory and practise of high pressure freezing. In *Cryotechniques in Biological Electron Microscopy*, Steinbrecht RA, Müller-Reichert R, Zierold, K (ed), pp 175-191. Berlin, Heidelberg: Springer-Verlag

183. Morphew MK (2007) 3D immunolocalization with plastic sections. *Methods Cell Biol* **79:** 493-513

184. Morphew MK (n.d.) *Practical methods in high-pressure freezing, freeze-substitution, embedding and immunocytochemistry for electron microscopy.* Retrieved June 5, 2011, from http://bio3d.colorado.edu/docs/mmanual.pdf

185. Mosgoeller W (2004) Nucleolar ultrastructure in vertebrates. In *The Nucleolus*, Olson MOJ (ed), pp 10-20. USA: New York: Landes Bioscience/ Kluwer Academic

186. Mulholland J, Botstein D (2002) Immunoelectron microscopy of aldehyde-fixed yeast cells. *Methods Enzymol* **351:** 50-81

187. Müller-Reichert T, Sassoon I, O'Toole E, Romao M, Ashford AJ, Hyman AA, Antony C (2003) Analysis of the distribution of the kinetochore protein Ndc10p in *Saccharomyces cerevisiae* using 3-D modeling of mitotic spindles. *Chromosoma* **111:** 417-428

188. Murray S (2008) High pressure freezing and freeze substitution of *Schizosaccharomyces pombe* and *Saccharomyces cerevisiae* for TEM. *Methods Cell Biol* **88:** 3-17

189. Nagle JF, Tristram-Nagle S (2000) Structure of lipid bilayers. *Biochim Biophys Acta* **1469:** 159-195

190. Nicastro D, McIntosh JR, Baumeister W (2005) 3D structure of eukaryotic flagella in a quiescent state revealed by cryo-electron tomography. *Proc Nat Acad SciUSA* **102:** 15889-15894

191. Nicastro D, Schwartz C, Pierson J, Gaudette R, Porter ME, McIntosh JR (2006) The molecular architecture of axonemes revealed by cryoelectron tomography. *Science* **313:** 944-948

192. Nickell S, Hegerl R, Baumeister W, Rachel R (2003) Pyrodictium cannulae enter the periplasmic space but do not enter the cytoplasm, as revealed by cryo-electron tomography. *J Struct Biol* **141:** 34-42

193. Nickell S, Kofler C, Leis AP, Baumeister W (2006) A visual approach to proteomics. *Nat Rev* **7:** 225-230

194. Nicolas MT, Bassot JM (1993) Freeze substitution after fast-freeze fixation in preparation for immunocytochemistry. *Microsc Res Tech* **24:** 474-487

195. Nisman R, Dellaire G, Ren Y, Li R, Bazett-Jones DP (2004) Application of quantum dots as probes for correlative fluorescence, conventional, and energy-filtered transmission electron microscopy. *J Histochem Cytochem* **52:** 13-18

196. Ochs R (2006) Immunoelectron microscopy. In *Basic methods in microscopy*, Spector D, Goldman, RD (ed), **21**: 343-350. New York: Cold Spring Harbor Laboratory Press

197. Pacheco LF, Carmona-Ribeiro AM (2003) Effects of synthetic lipids on solubilization and colloid stability of hydrophobic drugs. *J Coll Interface Sci* **258:** 146-154

198. Pandey BN, Mishra KP (1999) Radiation induced oxidative damage modification by cholesterol in liposomal membrane. *Radiat Phys Chem* **54:** 481-489

199. Peters PJ, Pierson J (2008) Immunogold labeling of thawed cryosections. *Methods Cell Biol* **88:** 131-149

200. Pierson J, Sani M, Tomova C, Godsave S, Peters PJ (2009) Toward visualization of nanomachines in their native cellular environment. *Histochem Cell Biol* **132:** 253-262

201. Plitzko JM, Rigort A, Leis A (2009) Correlative cryo-light microscopy and cryo-electron tomography: from cellular territories to molecular landscapes. *Curr Opin Biotechnol* **20:** 83-89

202. Porta D, Lopez-Iglesias C (1998) A comparison of cryo- versus chemical fixation in the soil green algae Jaagiella. *Tissue Cell* **30:** 368-376
203. Pringle JR, Preston RA, Adams AE, Stearns T, Drubin DG, Haarer BK, Jones EW (1989) Fluorescence microscopy methods for yeast. *Methods Cell Biol* **31:** 357-435
204. Qiu H, Eifert J, Wacheul L, Thiry M, Berger AC, Jakovljevic J, Woolford JL, Jr., Corbett AH, Lafontaine DL, Terns RM, Terns MP (2008) Identification of genes that function in the biogenesis and localization of small nucleolar RNAs in *Saccharomyces cerevisiae*. *Mol Cell Biol* **28:** 3686-3699
205. Quintana C (1994) Cryofixation, cryosubstitution, cryoembedding for ultrastructural, immunocytochemical and microanalytical studies. *Micron* **25:** 63-99
206. Rasband WS (1997-2009) *ImageJ*. U. S. National Institutes of Health, Bethesda, Maryland, USA. Retrieved June 7, 2009, from http://imagej.nih.gov/ij/
207. Raska I, Ochs RL, Salamin-Michel L (1990) Immunocytochemistry of the cell nucleus. *Electron Microsc Rev* **3:** 301-353
208. Rebhun LI, Sawada N (1969) Augmentation and dispersion of the *in vivo* mitotic apparatus of living marine eggs. *Protoplasma* **68:** 1-22
209. Reynolds ES (1963) The use of lead citrate at high pH as an electron-opaque stain in electron microscopy. *J Cell Biol* **17:** 208-212
210. Riemersma JC (1968) Osmium tetroxide fixation of lipids for electron microscopy. A possible reaction mechanism. *Biochim Biophys Acta* **152:** 718-727
211. Rinuado M, Quemeneur, F., Pepin-Donat, B. (2009) Stabilization of liposomes by polyelectrolytes:mechanism of interaction and role of experimental condtítions. *Macromol Symp* **278:** 67-79
212. Robards AW, Sleyter UB (1985) *Low temperature methods in biological electron microscopy*. In: Practical methods in electron microscopy, Glauert, AM (ed) Elsevier Amsterdam **10:** 19
213. Robertson D, Monaghan P, Clarke C, Atherton AJ (1992) An appraisal of low-temperature embedding by progressive lowering of temperature into Lowicryl HM20 for immunocytochemical studies. *J Microsc* **168:** 85-100
214. Rogero O, Sousa JS, Alario DJr, Lopergolo L, Lugao AB (2005) Silicone crosslinked by ionizing radiation as potential polymeric matrix for drug delivery. *Nucl Instrum Methods Phys Res B* **236:** 521-525
215. Rościszewski P, Zielecka M (2002) *Silikony*. Wydawnictwo Naukowo-Techniczne, Warszawa, Poland

216. Ruysschaert T, Paquereau L, Winterhalter M, Fournier D (2006) Stabilization of liposomes through enzymatic polymerization of DNA. *Nano Lett* **6:** 2755-2757
217. Sali A, Glaeser R, Earnest T, Baumeister W (2003) From words to literature in structural proteomics. *Nature* **422:** 216-225
218. Sandin S, Ofverstedt LG, Wikstrom AC, Wrange O, Skoglund U (2004) Structure and flexibility of individual immunoglobulin G molecules in solution. *Structure* **12:** 409-415
219. Sartori A, Gatz R, Beck F, Rigort A, Baumeister W, Plitzko JM (2007) Correlative microscopy: bridging the gap between fluorescence light microscopy and cryo-electron tomography. *J Struct Biol* **160:** 135-145
220. Sato M, Kobori H, Ishijima SA, Feng ZH, Hamada K, Shimada S, Osumi M (1996) Schizosaccharomyces pombe is more sensitive to pressure stress than Saccharomyces cerevisiae. *Cell Struct Funct* **21:** 167-174
221. Severs NJ (2007) Freeze-fracture electron microscopy. *Nat Protoc* **2:** 547-576
222. Severs NJ, Robenek H (2008) Freeze-fracture cytochemistry in cell biology. *Methods Cell Biol* **88:** 181-204
223. Shaw P, Doonan J (2005) The nucleolus. Playing by different rules? *Cell cycle* **4:** 102-105
224. Shi G, Guo W, Stephenson SM, Lee RJ (2002) Efficient intracellular drug and gene delivery using folate receptor-targeted pH-sensitive liposomes composed of cationic/anionic lipid combinations. *J Control Release* **80:** 309-319
225. Shimanouchi T, Ishii H, Yoshimoto N, Umakoshi H, Kuboi R (2009) Calcein permeation across phosphatidylcholine bilayer membrane: effects of membrane fluidity, liposome size, and immobilization. *Colloids Surf* **73:** 156-160
226. Shu X, Lev-Ram V, Deerinck TJ, Qi Y, Ramko EB, Davidson MW, Jin Y, Ellisman MH, Tsien RY (2011) A genetically encoded tag for correlated light and electron microscopy of intact cells, tissues, and organisms. *PLoS Biol* **9:** e1001041
227. Schimmang T, Tollervey D, Kern H, Frank R, Hurt EC (1989) A yeast nucleolar protein related to mammalian fibrillarin is associated with small nucleolar RNA and is essential for viability. *EMBO J* **8:** 4015-4024
228. Schwartz CL, Sarbash VI, Ataullakhanov FI, McIntosh JR, Nicastro D (2007) Cryo-fluorescence microscopy facilitates correlations between light and cryo-electron microscopy and reduces the rate of photobleaching. *J Microsc* **227:** 98-109
229. Schwarz H, Humbel BM (2007) Correlative light and electron microscopy using immunolabeled resin sections. *Methods Mol Biol* **369:** 229-256

230. Schwarz H, Hohenberger H, Humbel BM. (1993) Freeze-substitution in virus research: a preview. In *Immuno-gold electron microscopy in virus diagnosis and research*, Hyatt AD, Eaton BT (ed) pp 349-376. USA: CRC Press, Boca Raton

231. Schwendener RA (2007) Liposomes in biology and medicine. *Adv Exp Med Biol* **620:** 117-128

232. Sicard H, Faubladier M, Noaillac-Depeyre J, Leger-Silvestre I, Gas N, Caizergues-Ferrer M (1998) The role of the *Schizosaccharomyces pombe* gar2 protein in nucleolar structure and function depends on the concerted action of its highly charged N terminus and its RNA-binding domains. *Mol Biol Cell* **9:** 2011-2023

233. Silvander M, Karlsson G, Edwards K (1996) Vesicle solubilization by alkyl sulfate surfactants: a Cryo-TEM study of the vesicle to micelle transition. *J Coll Interface Sci* **179:** 104-113

234. Sirri V, Urcuqui-Inchima S, Roussel P, Hernandez-Verdun D (2008) Nucleolus: the fascinating nuclear body. *Histochem Cell Biol* **129:** 13-31

235. Slot JW, Geuze HJ (2007) Cryosectioning and immunolabeling. *Nat Protoc* **2:** 2480-2491

236. Spector DL, Ochs RL, Busch H (1984) Silver staining, immunofluorescence, and immunoelectron microscopic localization of nucleolar phosphoproteins B23 and C23. *Chromosoma* **90:** 139-148

237. Spehner D, Edelmann L (2008) Slam-freezing, metal-mirror freezing. In *Handbook of cryo-preparation methods for electron microscopy*, Cavalier ASD, Humbel BM (ed) pp 16-47. USA: CRC Press, Tailor & Francis Group

238. Spiegelhalter C, Tosch V, Hentsch D, Koch M, Kessler P, Schwab Y, Laporte J (2010) From dynamic live cell imaging to 3D ultrastructure: novel integrated methods for high pressure freezing and correlative light-electron microscopy. *PloS One* **5:** e9014

239. Steere RL (1957) Electron microscopy of structural detail in frozen biological specimens. *J Biophys Biochem Cyt* **3:** 45-60

240. Steinbrecht RA, Müller M (1987) Freeze substitution and freeze-drying. In *Cryotechniques in biological electron microscopy*, Steinbrecht RA, Zierold K (ed), pp 149-172. Berlin: Springer-Verlag

241. Stierhof YD, Humbel BM, Schwarz H (1991) Suitability of different silver enhancement methods applied to 1 nm colloidal gold particles: an immunoelectron microscopic study. *J Electron Microsc Tech* **17:** 336-343

242. Stoffler D, Feja B, Fahrenkrog B, Walz J, Typke D, Aebi U (2003) Cryo-electron tomography provides novel insights into nuclear pore architecture: implications for nucleocytoplasmic transport. *J Mol Biol* **328:** 119-130

243. Studer D, Graber W, Al-Amoudi A, Eggli P (2001) A new approach for cryofixation by high-pressure freezing. *J Microsc* **203:** 285-294

244. Studer D, Humbel BM, Chiquet M (2008) Electron microscopy of high pressure frozen samples: bridging the gap between cellular ultrastructure and atomic resolution. *Histochem Cell Biol* **130:** 877-889

245. Studer D, Michel M, Müller M (1989) High pressure freezing comes of age. *Scanning Microsc* **3:** 253-268; discussion 268-259

246. Studer D, Michel M, Wohlwend M, Hunziker EB, Buschmann MD (1995) Vitrification of articular cartilage by high-pressure freezing. *J Microsc* **179:** 321-332

247. Takeuchi H, Kojima H, Yamamoto H, Kawashima Y (2000) Polymer coating of liposomes with a modified polyvinyl alcohol and their systemic circulation and RES uptake in rats. *J Control Release* **68:** 195-205

248. Takeuchi H, Kojima H, Yamamoto H, Kawashima Y (2001) Evaluation of circulation profiles of liposomes coated with hydrophilic polymers having different molecular weights in rats. *J Control Release* **75:** 83-91

249. Thiry M, Lafontaine DL (2005) Birth of a nucleolus: the evolution of nucleolar compartments. *Trends Cell Biol* **15:** 194-199

250. Tokuyasu KT (1973) A technique for ultracryotomy of cell suspensions and tissues. *J Cell Biol* **57:** 551-565

251. Tollervey D, Lehtonen H, Carmo-Fonseca M, Hurt EC (1991) The small nucleolar RNP protein NOP1 (fibrillarin) is required for pre-rRNA processing in yeast. *EMBO J* **10:** 573-583

252. Trumtel S, Leger-Silvestre I, Gleizes PE, Teulieres F, Gas N (2000) Assembly and functional organization of the nucleolus: ultrastructural analysis of Saccharomyces cerevisiae mutants. *Mol Biol Cell* **11:** 2175-2189

253. van Donselaar E, Posthuma G, Zeuschner D, Humbel BM, Slot JW (2007) Immunogold labeling of cryosections from high-pressure frozen cells. *Traffic* **8:** 471-485

254. van Tuinen E, Riezman H (1987) Immunolocalization of glyceraldehyde-3-phosphate dehydrogenase, hexokinase, and carboxypeptidase Y in yeast cells at the ultrastructural level. *J Histochem Cytochem* **35:** 327-333

255. Vanhecke D, Graber W, Studer D (2008) Close-to-native ultrastructural preservation by high pressure freezing. *Methods Cell Biol* **88:** 151-164
256. Vanhecke D, Herrmann G, Graber W, Hillmann-Marti T, Muhlfeld C, Studer D, Ochs M (2010) Lamellar body ultrastructure revisited: high-pressure freezing and cryo-electron microscopy of vitreous sections. *Histochem Cell Biol* **134:** 319-326
257. Vanhecke D, Studer L, Studer D (2007) Cryoultramicrotomy: cryoelectron microscopy of vitreous sections. *Methods Mol Biol* **369:** 175-197
258. Verkade P (2008) Moving EM: the Rapid Transfer System as a new tool for correlative light and electron microscopy and high throughput for high-pressure freezing. *J Microsc* **230:** 317-328
259. Vicidomini G, Gagliani MC, Cortese K, Krieger J, Buescher P, Bianchini P, Boccacci P, Tacchetti C, Diaspro A (2010) A novel approach for correlative light electron microscopy analysis. *Microsc Res Tech* **73:** 215-224
260. Vitrification (September 1, 2011) In *Wikipedia: The free encyclopedia.* Retrieved September 15, 2011, from http://en.wikipedia.org/wiki/Vitrification
261. Volodkin D, Ball V, Schaaf P, Voegel JC, Mohwald H (2007) Complexation of phosphocholine liposomes with polylysine. Stabilization by surface coverage versus aggregation. *Biochim Biophys Acta* **1768:** 280-290
262. von Schack ML, Fakan S (1993) The study of the cell nucleus using cryofixation and cryosubstitution. *Micron* **24:** 507-519
263. Wagenknecht T, Hsieh CE, Rath BK, Fleischer S, Marko M (2002) Electron tomography of frozen-hydrated isolated triad junctions. *Biophys J* **83:** 2491-2501
264. Wagner K, Brezesinski G (2008) Phospholipases to recognize model membrane structures on a molecular lenght scale. *Curr Opin Coll Interface Sci* **13:** 47-53
265. Walther P, Ziegler A (2002) Freeze substitution of high-pressure frozen samples: the visibility of biological membranes is improved when the substitution medium contains water. *J Microsc* **208:** 3-10
266. Watanabe S, Punge A, Hollopeter G, Willig KI, Hobson RJ, Davis MW, Hell SW, Jorgensen EM (2011) Protein localization in electron micrographs using fluorescence nanoscopy. *Nat Methods* **8:** 80-84
267. Watson ML (1958) Staining of tissue sections for electron microscopy with heavy metals. *J Biophys Biochem Cyt* **4:** 475-478
268. Webster P, Webster A (2007) Cryosectioning fixed and cryoprotected biological material for immunocytochemistry. *Methods Mol Biol* **369:** 257-289

269. Wei S-Q, Bai Y-P, Shao L (2008) A novel approach to graft acrylates onto commercial silicones for release film fabrications by two-step emulsion synthesis. *Eur Polym J* **44:** 2728-2736
270. *Wikipedia: The free encyclopedia*. (2004, July 22). FL: Wikimedia Foundation, Inc. Retrieved June 5, 2011, from http://www.wikipedia.org
271. Wright R (2000) Transmission electron microscopy of yeast. *Microsc Res Tech* **51:** 496-510
272. Wydro P, Hac-Wydro K (2007) Thermodynamic description of the interactions between lipids in ternary Langmuir monolayers: the study of cholesterol distribution in membranes. *J Phys Chem* **111:** 2495-2502
273. Xu C, Henry PA, Setya A, Henry MF (2003) In vivo analysis of nucleolar proteins modified by the yeast arginine methyltransferase Hmt1/Rmt1p. *RNA* **9:** 746-759
274. Yakovlev S, Downing KH (2011) Crystalline ice as a cryoprotectant: theoretical calculation of cooling speed in capillary tubes. *J Microsc* **243:** 8-14
275. Yamaguchi K, Suzuki K, Tanaka K (2010) Examination of electron stains as a substitute for uranyl acetate for the ultrathin sections of bacterial cells. *J Electron Microsc (Tokyo)* **59(2):** 113-118
276. Yan C, Melese T (1993) Multiple regions of NSR1 are sufficient for accumulation of a fusion protein within the nucleolus. *J Cell Biol* **123:** 1081-1091
277. Yaroslavov AA, Rakhnyanskaya AA, Yaroslavova EG, Efimova AA, Menger FM (2008) Polyelectrolyte-coated liposomes: stabilization of the interfacial complexes. *Adv Colloid Interface Sci* **142:** 43-52
278. Zhao Q, Ofverstedt LG, Skoglund U, Isaksson LA (2004) Morphological variation of individual Escherichia coli 30S ribosomal subunits in vitro and in situ, as revealed by cryo-electron tomography. *Exp Cell Res* **297:** 495-507